

Inaugural dissertation
for
obtaining the doctoral degree
of the
Combined faculty of Mathematics, Engineering and Natural Sciences
of the
Ruprecht-Karls-University
Heidelberg

presented by
M. Sc. Sarah Göllner
born in Reutlingen, Germany
Oral examination: 14.02.2023

**FUNCTIONAL AND BIOCHEMICAL
CHARACTERIZATION OF
VIRAL AND HOST FACTORS INVOLVED IN THE
ZIKA VIRUS REPLICATION CYCLE**

Referees:

1. Prof. Dr. Dr. h.c. Ralf Bartenschlager
2. Prof. Dr. Britta Brügger

ACKNOWLEDGEMENTS

This present work was performed in the Department of Molecular Virology at the University Hospital Heidelberg under the supervision of **Prof. Dr. Dr. h.c. Ralf Bartenschlager**, between May 2018 and February 2023.

First, I would like to express my deepest gratitude to Ralf for his outstanding support during my time in his laboratory. I greatly appreciated your offer to join your group as a PhD student and for your supervision throughout the years. Thank you for your openness and for giving me the chance to explore my own creativity to develop new projects and ideas, but also for providing guidance and expertise when I got stuck on the way. Although your schedule is super busy, you always found time to meet and discuss urgent matters or difficulties.

Furthermore, I want to thank **Prof. Dr. Britta Brügger** for her willingness to serve as my second supervisor and for reviewing this work. Thank you for being part of my PhD TAC committee as your input helped shaping the story and for initiating the collaboration with **Prof. Dr. Ilpo Vattulainen** in Helsinki, Finland, who together with **Dr. Giray Enkavi** and **Dr. Waldemar Kulig**, performed molecular dynamics simulations confirming my results at the bench. Additionally, I want to express my gratitude to **Prof. Dr. Friedrich Frischknecht** and **Dr. Viet Loan Dao Thi** for being part of my PhD defense committee.

I would also like to express my deepest gratitude to **Dr. Mirko Cortese** and **Dr. Christopher John Neufeldt** for introducing me to the lab. I am forever indebted to you two as you have always shared your knowledge and ideas, provided outstanding support, and for sharing your contagious enthusiasm for science. I want to extend my thanks to all other past and present members of the **Dengue/SARS-CoV2 group** for open discussions in the lab.

I am thankful to Uta Haselmann for her excellent support and expertise in electron microscopy. Thank you for having taught me each step in the process of EM sample preparation and your patience when I was learning how to cut samples. I want to thank Marie Bartenschlager and Micha Fauth for their technical assistance in the lab and Ulrike Herian for her helping hands in cell culture. I would like to acknowledge our IT and administrative team which keep the lab running.

Further, I want to say a big thank you to Vera and Julia for your presence and your encouraging support of keeping me going when I hit rock bottom. In you I have found two close friends without whom my PhD time would not have been as pleasant as it has turned out in the end. I want to say a big thank you to all other members of AGR, AGU and AGL that I did not name here for space reasons. You created a unique place to work, and it was an honor to work side by side with you.

Finally, I want to thank my parents, my sister and her husband, and little Noah, for their support during those years. Thank you for providing me get aways such as wellness weekends and lots of laughter during family meetings. And last, my husband and best friend, Vishnu, thank you for your endless encouragement, unlimited patience, your company in the lab when I had to go back at night and for everything that you are - ഞാൻ നിന്നെ ഒരുപാട് സ്നേഹിക്കുന്നു (ñān ninne orupāṭ snēhikkunnu).

SUMMARY

Arboviruses are one of the greatest threats to human health since they cause millions of infections each year. The mosquito-borne flavivirus Zika virus (ZIKV), which is listed as a priority disease, has been declared a public health emergency of global concern by the World Health Organization (WHO) in 2016. Even though most infections are asymptomatic or manifest only moderate symptoms, infections have been related to neurological disorders such as the Guillain-Barré syndrome and microcephaly. Despite years of intensive research, there are presently no effective antiviral therapies or vaccines. Their development requires further studies of the fundamental principles of the ZIKV life cycle to provide the necessary knowledge for the development of effective therapeutic measures.

Upon ZIKV infection, the cell's endoplasmic reticulum (ER) is significantly remodeled resulting in the formation of defined ER membrane invaginations termed vesicle packets (VPs), which are thought to be the sites where viral RNA replication takes place. Since their formation is coupled to viral replication, it has been challenging to retrieve mechanistic information on VP biogenesis thus far, as perturbations that reduce viral replication inevitably impact VP formation. To overcome this hurdle, my first project was to develop an expression system supporting the formation of ZIKV VPs to enable research focusing entirely on their biogenesis and the factors involved. I was able to demonstrate that ZIKV VPs are forming upon expression of the viral replicase (NS1-NS5) via a construct comprising in addition the 5' and 3' untranslated region (UTRs). Ultrastructural characterization of VPs in transfected cells revealed that the VPs are morphologically identical to those produced in infected cells. This newly created system was given the name pIRO (plasmid-induced replication organelle). A thorough deletion mutagenesis study focusing on RNA elements contained in the 5' and 3'UTR revealed that for VP formation the 5'UTR is largely dispensable. In contrast, the 3'UTR was required as deletion of distinct RNA elements contained therein decreased the efficiency of VP induction. In conclusion, I was able to show that ZIKV VP formation occurs independent of RNA elements with the size and morphology of VPs being independent of the length of the viral RNA.

The second part of my PhD thesis was devoted to characterizing the mode-of action of a novel ZIKV NS4A inhibitor. This topic was a perfect fit to the first part of my thesis, given the essential role of NS4A in VP formation. The inhibitor was developed by a collaborator who did a large-scale cell-based high-content screen, resulting in the identification of (2E)-N-benzyl-3-(4-butoxyphenyl) prop-2-enamide (SBI-0090799). This compound exhibits potent and widespread antiviral activity against numerous ZIKV strains *in vitro*. Using a combination of biochemical, virological, and imaging-based techniques, I confirmed that SBI-0090799 inhibits ZIKV replication by blocking the *de novo* formation of ZIKV VPs. Resistance mutations mapping to NS4A rescued viral RNA replication and restored VP formation in cells treated with high concentrations of the compound. These findings suggest that SBI-0090799 perturbs VP formation by interfering with NS4A, either by preventing it from inducing ER membrane curvature or inhibiting it from binding viral or cellular factors contributing to VP formation. Thus, the mechanism of action of SBI-0090799 is comparable to the one of hepatitis C virus NS5A inhibitors that are in clinical use.

The third part of my PhD study aimed to unravel the role of cholesterol in the viral replication cycle. Although it has already been shown that cholesterol plays a critical role in virus entry, particularly at the stage of viral envelope fusion with the endosome, as well as virion assembly, direct viral protein-cholesterol interactions have not been determined thus far. To fill this gap in knowledge I performed chemo-proteomics in ZIKV-infected human cells, using a photoactivatable and clickable cholesterol probe, to identify cholesterol binding viral proteins. I discovered that both the structural protein prM and its cleavage product, the M protein, can be efficiently cross-linked to cholesterol. Combining bioinformatics analyses and site-directed mutagenesis, alongside with cholesterol binding assays, I was able to show that the M protein has two functional cholesterol binding domains (CRAC motifs) in its transmembrane domains (TMD) 2 and 3 (CRAC2 and CRAC3, respectively). Using reverse genetics studies, I could show that the M protein's ability to bind cholesterol is not required for the processing of the viral polyprotein, viral RNA replication, and subcellular localization of the uncleaved prM protein. However, mutations affecting the cholesterol binding motif 2 (CRAC2) significantly impaired viruses in their ability to infect cells having low cholesterol levels. Furthermore, I was able to show that complete exchange of the cholesterol binding motif 3 (CRAC3) severely affected virus particle assembly. In line with these results, atomistic molecular dynamics simulations confirmed cholesterol binding to membrane-associated wild type M protein, whereas M proteins containing mutations in CRAC2 and CRAC3 lost cholesterol interactions. In conclusion, I was able to uncover a bifunctional role for the cholesterol interaction of the M protein in the ZIKV life cycle: facilitating virus entry requiring CRAC2 and virus particle assembly requiring CRAC3.

ZUSAMMENFASSUNG

Arboviren sind eine der größten Bedrohungen für die menschliche Gesundheit, da sie jedes Jahr Millionen von Infektionen verursachen. Das durch Mücken übertragene Flavivirus Zika-Virus (ZIKV), das als prioritäre Krankheit eingestuft ist, wurde 2016 von der Weltgesundheitsorganisation (WHO) zu einem weltweit besorgniserregenden öffentlichen Gesundheitsnotstand erklärt. Obwohl die meisten Infektionen asymptomatisch verlaufen oder nur mäßige Symptome aufweisen, wurden Infektionen mit neurologischen Störungen wie dem Guillain-Barré-Syndrom und Mikrozephalie in Verbindung gebracht. Trotz jahrelanger intensiver Forschung gibt es derzeit noch keine wirksamen antiviralen Therapien oder Impfstoffe. Ihre Entwicklung erfordert weitere Studien zu den grundlegenden Prinzipien des ZIKV-Lebenszyklus, um die notwendigen Kenntnisse für die Entwicklung wirksamer therapeutischer Maßnahmen zu gewinnen.

Bei einer ZIKV-Infektion wird das endoplasmatische Retikulum (ER) der Zelle erheblich umgebaut, was zur Bildung von definierten ER-Membraneinstülpungen führt, die als Vesikelpakete (VP) bezeichnet werden und von denen man annimmt, dass sie der Ort sind, an dem die virale RNA-Replikation stattfindet. Da ihre Bildung an die virale Replikation gekoppelt ist, war es bisher schwierig, mechanistische Informationen über die VP-Biogenese zu erhalten, da Störungen, die die virale Replikation reduzieren, unweigerlich die VP-Bildung beeinflussen. Um diese Hürde zu überwinden, bestand mein erstes Projekt darin, ein Expressionssystem zu entwickeln, das die Bildung von ZIKV-VPs unterstützt, damit sich die Forschung ganz auf ihre Biogenese und die daran beteiligten Faktoren konzentrieren kann. Ich konnte zeigen, dass sich ZIKV-VPs bei der Expression der viralen Replikase (NS1-NS5) über ein Konstrukt bilden, das zusätzlich die 5'- und 3'-untranslatierte Region (UTRs) umfasst. Die ultrastrukturelle Charakterisierung der VPs in transfizierten Zellen ergab, dass die VPs morphologisch identisch mit denen sind, die in infizierten Zellen produziert werden. Dieses neu geschaffene System erhielt den Namen pIRO (Plasmid induzierte Replikation Organelle). Eine gründliche Deletionsmutagenesestudie, die sich auf RNA-Elemente in der 5'- und 3'-UTR konzentrierte, ergab, dass die 5'-UTR für die VP-Bildung weitgehend entbehrlich ist. Im Gegensatz dazu fand ich heraus, dass die 3'UTR erforderlich ist, da die Deletion bestimmter darin enthaltener RNA-Elemente die Effizienz der VP-Induktion verringerte. Zusammenfassend konnte ich zeigen, dass die VP-Bildung bei ZIKV unabhängig von RNA-Elementen erfolgt und die Größe und Morphologie der VP unabhängig von der Länge der viralen RNA ist.

Der zweite Teil meiner Doktorarbeit war der Charakterisierung der Wirkungsweise eines neuen ZIKV NS4A-Inhibitors gewidmet. Dieses Thema passte perfekt zum ersten Teil meiner Arbeit, da NS4A eine wesentliche Rolle bei der VP-Bildung spielt. Der Hemmstoff wurde von einem Kollaborationspartner entwickelt, der einen groß angelegten zellbasierten High-Content-Screen durchführte, der zur Identifizierung von (2E)-N-Benzyl-3-(4-butoxyphenyl) prop-2-enamid (SBI-0090799) führte. Dieser Wirkstoff zeigt im Zellkultursystem eine starke und weit verbreitete antivirale Aktivität gegen zahlreiche ZIKV-Stämme. Mithilfe einer Kombination aus biochemischen, virologischen und bildgebenden Verfahren habe ich bestätigen können, dass SBI-0090799 die ZIKV-Replikation hemmt, indem es die Neubildung von ZIKV-VPs blockiert. Resistenzmutationen, die in NS4A auftreten, retteten die virale RNA-Replikation

und stellten die VP-Bildung in Zellen wieder her, die mit hohen Konzentrationen des Wirkstoffs behandelt wurden. Diese Ergebnisse deuten darauf hin, dass SBI-0090799 die VP-Bildung stört, indem es NS4A entweder daran hindert, die ER-Membrankrümmung zu induzieren, oder es an der Bindung viraler oder zellulärer Faktoren hindert, die zur VP-Bildung beitragen. Somit ist der Wirkmechanismus von SBI-0090799 vergleichbar mit dem der NS5A-Inhibitoren des Hepatitis-C-Virus, die bereits klinisch angewendet werden.

Der dritte Teil meiner Doktorarbeit zielte darauf ab, die Rolle von Cholesterin im viralen Replikationszyklus zu entschlüsseln. Obwohl bereits gezeigt wurde, dass Cholesterin eine entscheidende Rolle beim Viruseintritt spielt, insbesondere in der Phase der Fusion der Virushülle mit dem Endosom, sowie beim Zusammenbau des Virions, wurden direkte Wechselwirkungen zwischen viralen Proteinen und Cholesterin bisher nicht untersucht. Um diese Wissenslücke zu schließen, habe ich Chemo-Proteomik in ZIKV-infizierten menschlichen Zellen unter Verwendung einer photoaktivierbaren und klickbaren Cholesterin-Sonde durchgeführt, um Cholesterin-bindende virale Proteine zu identifizieren. Ich entdeckte, dass sowohl das Strukturprotein prM als auch sein Spaltprodukt, das M-Protein, effizient Cholesterin binden können. Durch die Kombination von Bioinformatik-Analysen und gezielter Mutagenese mit Cholesterin-Bindungsversuchen konnte ich zeigen, dass das M-Protein zwei funktionelle cholesterinbindende Domänen (CRAC-Motive) in seinen Transmembrandomänen (TMD) 2 und 3 (CRAC2 bzw. CRAC3) besitzt. Mithilfe von Studien zur reversen Genetik konnte ich zeigen, dass die Fähigkeit des M-Proteins, Cholesterin zu binden, nicht für die Verarbeitung des viralen Polyproteins, die virale RNA-Replikation und die subzelluläre Lokalisierung des ungespaltenen prM-Proteins erforderlich ist. Mutationen, die das Cholesterinbindungsmotiv 2 (CRAC2) betreffen, beeinträchtigen jedoch die Fähigkeit der Viren, Zellen mit niedrigem Cholesterinspiegel zu infizieren. Außerdem konnte ich zeigen, dass der vollständige Austausch des Cholesterinbindungsmotivs 3 (CRAC3) den Zusammenbau der Viruspartikel stark beeinträchtigt. In Übereinstimmung mit diesen Ergebnissen bestätigten atomistische Molekulardynamiksimulationen die Cholesterinbindung an das membranassoziierte Wildtyp-M-Protein, während M-Proteine mit Mutationen in CRAC2 und CRAC3 die Cholesterininteraktionen verloren. Zusammenfassend konnte ich eine bifunktionelle Rolle für die Cholesterin-Interaktion des M-Proteins im ZIKV-Lebenszyklus aufdecken: Erleichterung des Viruseintritts, wofür CRAC2 erforderlich ist, und Zusammenbau der Viruspartikel, wofür CRAC3 erforderlich ist.

TABLE OF CONTENTS

ACKNOWLEDGEMENTS	I
SUMMARY	III
ZUSAMMENFASSUNG	V
TABLE OF CONTENTS	VII
LIST OF FIGURES	XI
LIST OF TABLES	XIII
1. INTRODUCTION	1
1.1. ZIKA.....	1
1.1.1. Classification, origin, and emergence	1
1.1.2. ZIKV – a virus with epidemic and PHEIC potential.....	3
1.1.3. Symptoms, pathogenesis, and treatments.....	4
1.1.4. Control measures of ZIKV spread and disease	6
1.2. MOLECULAR BIOLOGY OF ZIKV	8
1.2.1. Virus genome organization	8
1.2.1.1. RNA structures in the ZIKV genome and their function.....	9
1.2.1.2. Viral proteins and their function.....	11
1.2.2. ZIKV transmission routes	15
1.2.3. ZIKV life cycle	17
1.2.4. ZIKV infectious replication cycle	18
1.2.4.1. Attachment, uptake, and fusion	18
1.2.4.2. Translation	19
1.2.4.3. Replication and replication organelles.....	20
1.2.4.4. ZIKV assembly, maturation, and egress.....	22
1.2.4.5. Zika virus particle structure.....	23
1.3. FLAVIVIRUSES INFECTION AND THE HOST LIPID METABOLISM.....	24
1.3.1. Lipidomic profiles of flavivirus infected cells	24
1.3.2. <i>De novo</i> lipid synthesis and flavivirus infection.....	26
1.3.3. Specific roles of lipids during the viral replication cycle.....	26
1.3.3.1. Lipids, virus entry, and membrane fusion.....	26
1.3.3.2. Lipids and virus replication	27
1.3.3.3. Lipids, virus assembly, and the lipid envelope	27
2. AIMS OF THIS STUDY	29
2.1. GENERATION OF A REPLICATION-INDEPENDENT SYSTEM PHENOCOPYING ZIKV REPLICATION ORGANELLES	29
2.2. DISSECTING THE MODE OF ACTION OF THE ANTIVIRAL COMPOUND SBI- 0090799	29

2.3.	THE IMPORTANCE OF VIRAL PROTEIN-CHOLESTEROL INTERACTIONS IN THE ZIKV REPLICATION CYCLE	30
3.	MATERIALS AND METHODS	31
3.1.	MATERIALS.....	31
3.1.1.	Chemicals and Expendables.....	31
3.1.2.	Recipes for buffers and solutions	34
3.1.3.	Technical Equipment and Software.....	35
3.1.4.	Oligonucleotides	36
3.1.5.	Bacteria and Cell Lines.....	37
3.2.	METHODS.....	37
3.2.1.	Cell culture	37
3.2.1.1.	Cell culture of mammalian and mosquito cells.....	37
3.2.1.2.	Transient transfection of RNA and DNA.....	38
3.2.1.3.	Generation of lentiviruses and stable cell lines.....	40
3.2.1.4.	Cell viability assays.....	40
3.2.1.5.	Luciferase activity assays	41
3.2.2.	Virology	41
3.2.2.1.	ZIKV stock production and purification	41
3.2.2.2.	Determination of virus titers by plaque assay	42
3.2.2.3.	Determination of virus titers by TCID50	43
3.2.2.4.	Quantification of cell associated infectious ZIKV	43
3.2.2.5.	Viral binding assays.....	44
3.2.2.6.	Viral entry inhibition assay	44
3.2.3.	Cloning	44
3.2.3.1.	Polymerase Chain reaction	44
3.2.3.2.	Restriction digest of DNA plasmids	45
3.2.3.3.	Agarose gel electrophoresis	45
3.2.3.4.	Gel extraction.....	46
3.2.3.5.	Ligation	46
3.2.3.6.	Transformation of chemically competent bacteria	46
3.2.3.7.	Isolation and analysis of plasmid DNA from bacteria	47
3.2.4.	Molecular biology.....	47
3.2.4.1.	Extraction and purification of total intracellular RNA.....	47
3.2.4.2.	Viral RNA Assay.....	47
3.2.4.3.	cDNA synthesis and SYBR Green-based quantitative real-time PCR.....	48
3.2.4.4.	One-Step probe-based RT-qPCR	49
3.2.4.5.	ZIKV RNA detection by agarose gel electrophoresis.....	49
3.2.4.6.	<i>In vitro</i> transcription	50
3.2.5.	Biochemistry	51
3.2.5.1.	Cell lysis.....	51
3.2.5.2.	Bradford assay	52
3.2.5.3.	SDS-PAGE and western blot analysis.....	52

3.2.5.4.	Photoaffinity crosslinking of proteins to cholesterol.....	53
3.2.5.5.	Coimmunoprecipitation of Env and prM proteins.....	54
3.2.5.6.	Quantification of cholesterol content in cells.....	54
3.2.6.	Microscopy.....	55
3.2.6.1.	Immunofluorescence microscopy.....	55
3.2.6.2.	Transmission electron microscopy (TEM).....	55
3.2.6.3.	Correlative light-electron microscopy.....	56
3.2.7.	Statistical analysis.....	56
4.	RESULTS	57
4.1.	GENERATION OF A REPLICATION-INDEPENDENT SYSTEM TO STUDY THE BIOGENESIS OF ZIKV REPLICATION ORGANELLES.....	57
4.1.1.	Formation of ZIKV ROs is independent of the stem loop structures in the 5'UTR.....	57
4.1.2.	The essential role of the 3'UTR in the formation of ZIKV ROs.....	61
4.1.3.	Requirement of an authentic 3'end.....	65
4.2.	PIRO-Z AND ITS APPLICATION TO UNRAVEL THE MODE OF ACTION OF A ZIKV NS4A INHIBITOR.....	67
4.2.1.	SBI-0090799 and its antiviral activity against ZIKV-H/PF/2013.....	67
4.2.2.	SBI-0090799 impairs the formation of ZIKV replication organelles....	68
4.2.3.	Mutations within NS4A confer resistance to SBI-0090799 and restore RO formation.....	71
4.3.	CHOLESTEROL AND ITS ROLE DURING ZIKV ENTRY AND VIRUS PARTICLE PRODUCTION.....	75
4.3.1.	ZIKV entry and particle production are cholesterol dependent.....	75
4.3.2.	Probing ZIKV structural proteins for cholesterol interaction.....	77
4.3.3.	Identification of potential cholesterol binding domains in the structural protein prM.....	79
4.3.4.	Functional characterization of cholesterol binding domains within the M domain of the structural prM protein.....	81
4.3.5.	Atomistic molecular dynamics simulations confirm the interaction between the M protein and cholesterol.....	82
4.3.6.	Mutant CARC ZIKV are significantly impaired in spread.....	85
4.3.7.	Mutant CARC2 ZIKV are sensitive to cholesterol levels in mammalian cells.....	87
4.3.8.	Cholesterol is required during virus entry into mammalian but not insect cells.....	90
4.3.9.	Mutant CARC3 Zika virions are defective in assembly.....	91
4.3.10.	Evidenve that the CARC3 motif is required for the recruitment of capsid to virus assembly sites.....	93
5.	DISCUSSION	99
5.1.	A NEW SYSTEM TO STUDY FLAVIVIRUS RO FORMATION INDEPENDENT OF VIRAL RNA REPLICATION.....	99

5.2.	<i>DE NOVO</i> FORMATION OF THE ZIKV RO IS SUPPRESSED BY THE NOVEL NS4A INHIBITOR SBI-0090799.....	102
5.3.	THE INTERACTION BETWEEN THE M DOMAIN OF THE PRM PROTEIN AND HOST CELLULAR CHOLESTEROL DRIVES ZIKV ENTRY AND PARTICLE ASSEMBLY...	104
6.	BIBLIOGRAPHY	111
7.	APPENDIX	134
7.1.	ABBREVIATIONS.....	134
7.2.	ADDITIONAL PROJECTS	137
7.2.1.	A pIRO-Z reporter system for CLEM analyses	137
7.3.	SUPPLEMENTARY INFORMATION	139
7.3.1.	Plasmids	139
7.3.2.	Oligonucleotides	143
8.	PUBLICATIONS AND PRESENTATIONS	147
8.1.	PUBLICATIONS AND MANUSCRIPTS IN PREPARATION.....	147
8.2.	PRESENTATIONS	147

LIST OF FIGURES

Figure 1	Phylogenetic tree of pathogenic flaviviruses	2
Figure 2	Global distribution of ZIKV and its vector <i>A. aegypti</i>	3
Figure 3	The course of human and mosquito infection	4
Figure 4	ZIKV genome organization and polyprotein structure	9
Figure 5	Secondary RNA structures in the UTRs of the ZIKV genome	10
Figure 6	Structure of capsid, membrane, and envelope proteins of ZIKV	12
Figure 7	Transmission routes of ZIKV	16
Figure 8	The mosquito arbovirus life cycle	17
Figure 9	Infectious replication cycle of flaviviruses	19
Figure 10	Morphology and architecture of the ZIKV replication organelle	21
Figure 11	Structural changes of the ZIKV particle during maturation	23
Figure 12	ZIKV and its interaction with the lipid metabolism	25
Figure 13	Expression and processing of the viral replicase is comparable between transfected and infected cells	58
Figure 14	Deletion mutations in the 5' and 3' UTR do not affect subcellular localization of ZIKV NS proteins	59
Figure 15	The ZIKV 5' UTR is dispensable for replication organelle biogenesis	60
Figure 16	Role of RNA elements in the domain III of the ZIKV 3' UTR in replication organelle formation	62
Figure 17	The ZIKV 3' UTR contributes to, but is not essential for, replication organelle formation	64
Figure 18	ZIKV replication organelle formation does not require an authentic 3' end	66
Figure 19	Assessment of antiviral activity and cytotoxicity of SBI-0090799	68
Figure 20	ZIKV replication organelle formation is suppressed by SBI-0090799	69
Figure 21	SBI-0090799 does not affect the subcellular localization of ZIKV NS proteins	70
Figure 22	NS4A mutations do not affect ZIKV replication fitness yet provide resistance against SBI-0090799	71
Figure 23	Mutations in NS4A restore ZIKV replication organelle formation in the presence of SBI-0090799	73
Figure 24	M β CD and lovastatin have antiviral activity against ZIKV	76
Figure 25	Cholesterol photoaffinity labeling in ZIKV infected Huh7-Lunet cells probes prM, NS2B, NS4A, and NS4B as cholesterol binding proteins	78
Figure 26	Identification of cholesterol binding domains in the prM protein of Zika	80
Figure 27	Mutagenesis of the cholesterol binding domains in the TMD2 and TMD3 of the M domain of the structural prM protein block cholesterol binding	82
Figure 28	Atomistic molecular dynamics simulations	84

Figure 29	Mutagenesis of cholesterol binding domains within the M domain affects viral spread	86
Figure 30	Functionality of the CARC2 motif in the M domain depends on cellular cholesterol levels	88
Figure 31	Mutagenesis of the CARC3 domain affects virus assembly	92
Figure 32	Polyprotein processing and protein abundance	94
Figure 33	Cholesterol interaction with the M domain recruit capsid proteins to virus assembly sites	95
Figure 34	Subcellular localization of prM and E proteins	96
Figure 35	Mutations in the M domain of the prM protein do not affect the prM-Env interaction	97
Figure 36	Replication organelles of the flavivirus and hepatitis virus	101
Figure 37	Proposed function of the M domain in virus entry	107
Figure 38	Proposed function of the M domain in virus assembly	109
Figure S1	A reporter pIRO construct for CLEM approaches	138

LIST OF TABLES

Table 1	List of approved vaccines against flaviviruses and developmental state of ZIKV vaccine candidates	7
Table 2	Composition of a mature flavivirus particle	28
Table 3	Overview of expendables	31
Table 4	Primary antibodies used in this study	33
Table 5	Secondary antibodies used in this study	33
Table 6	Probes, resins, and beads used in this study	33
Table 7	Commercial kits and systems	34
Table 8	Recipes for buffers used in this study	34
Table 9	Overview of centrifuges, PCR cyclers and other technical appliances	35
Table 10	Software	36
Table 11	Overview of cell lines used in this study	37
Table 12	RT-PCR cycling program used for cDNA synthesis using the high-capacity RT kit	48
Table 13	Cycling program used for SYBR-based qPCR	49
Table 14	Cycling program used for One-Step probe-based RT-qPCR	49
Table 15	RT-PCR cycling program used for cDNA synthesis using the Super-script III RT polymerase kit	50
Table 16	PCR cycling program used for detecting secreted viral RNA	50
Table 17	Relative replication of WT and NS4A mutant ZIKV replicons in the presence of various concentrations of SBI-0090799	72
Table S1	List of plasmids used and generated in this study	139
Table S2	List of oligos used in this study for qPCR and cloning	143

1. INTRODUCTION

1.1. Zika

1.1.1. Classification, origin, and emergence

Zika virus (ZIKV), along with dengue virus (DENV), Japanese encephalitis virus (JEV), tick-borne encephalitis virus (TBEV), yellow fever virus (YFV), and West Nile virus (WNV), is a member of the *Flavivirus* genus within the *Flaviviridae* family. Flaviviruses are small, enveloped viruses with genomes consisting of a non-segmented single-stranded RNA molecule with positive polarity. At present, the genus *Flavivirus* consists of over 50 virus species¹, of which many represent medically important human pathogens. These are considered a global health problem due to high morbidity and mortality^{2,3}. In general, human pathogenic flaviviruses can be transmitted via hematophagous arthropods such as mosquitos or ticks. In this context, ZIKV was found to be transmitted by mosquitos belonging to the genus *Aedes* (*A.*) including the species *A. africanus*⁴, *A. aegypti*⁵, *A. albopictus*⁶ and *A. hensilli*⁷.

Although ZIKV was first isolated in 1947 from a sentinel rhesus monkey in the Zika forest in Uganda⁴, it was in 1954 that the ZIKV infection was first associated with disease in humans⁸. The first evidence of ZIKV geographical spread was obtained in 1966, when for the first time outside of Africa, ZIKV was isolated from *A. aegypti* in Malaysia⁵, giving rise to the Asian lineage. Even though sequence and phylogenetic analyses indicate that the Asian lineage is distinct from the African lineage, it is still assumed that both lineages share the same origin^{9,10} (Figure 1). Interestingly, between 1954 and 1977 no human (clinical) ZIKV cases were reported in Asia. This low clinical detection rate was likely due to the lack of diagnostic testing at that time¹¹. It was eleven years after its discovery in Asia when the first ZIKV clinical cases were reported in Central Java, Indonesia¹². During the 1950s to 1970s, serosurveys were performed to monitor ZIKV infections, revealing that the geographic distribution of ZIKV was broader than suspected in both tropical Africa and Asia^{10,13}. However, interpretation of the results from these serosurveys were difficult due to extensive cross-reactivity among antibodies produced by infection with related flaviviruses which coexist in the same geographical areas¹³⁻¹⁶.

1. Introduction

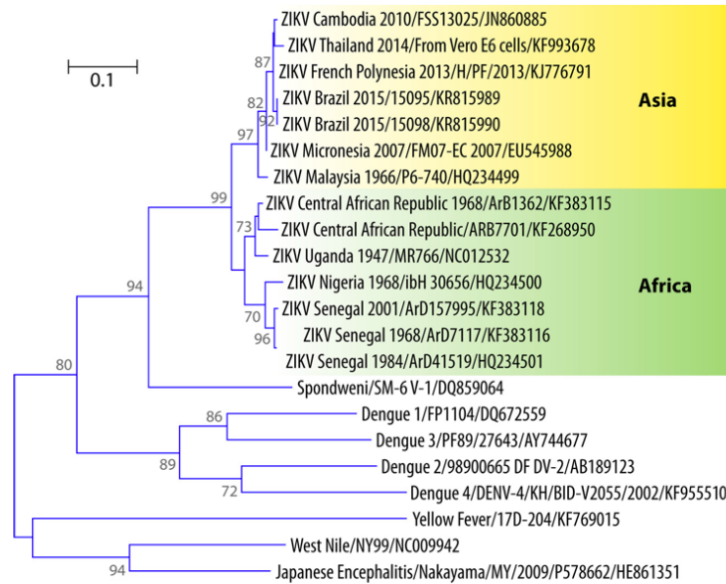


Figure 1. Phylogenetic tree of pathogenic flaviviruses.

Phylogenetic analysis was performed using nucleotide sequences of the envelope-encoding gene. The ZIKV African and Asian lineages are displayed. (Figure taken from [10])

Human population growth, urbanization, and globalization, together with the rapid geographic expansion of the arthropod vectors, created an environment in which human-mosquito-human transmission of ZIKV was sustainable, which led to several epidemic outbreaks. The first known outbreak of ZIKV occurred in 2007 on the YAP islands, Federated States of Micronesia, with a total of 5,000 infections which corresponded to 75% of the population^{17,18}. For years after this incident no further outbreaks were recorded. However, a major epidemic outbreak occurred in 2013 in French Polynesia with more than 30,000 cases^{19,20}. During this time the link between ZIKV infection and neurological complications such as the Guillain-Barré syndrome (GBS)²¹ was made. As ZIKV continued to spread, several small outbreaks were reported in New Caledonia²², the Cook Islands²³, and the Easter Island²⁴. The most severe series of ZIKV outbreaks, however, occurred in the Americas in 2015/16 with its origin in Bahia, Brazil²⁵. Within only 6 months, the virus spread rapidly through the Americas with over 37,000 symptomatic or probable cases²⁶. During this string of events, evidence grew that ZIKV infection during pregnancy caused severe neurological malformations including microcephaly and congenital ZIKV syndrome²⁷⁻³⁰. Thus, on February 1, 2016, the World Health Organization (WHO) declared ZIKV a Public Health Emergency of International Concern (PHEIC)³¹. The most recent outbreak with over 200 confirmed cases occurred in 2021 in India³². Although ZIKV infections had already been reported in 2018 in Gujarat, Madhya Pradesh and Rajasthan, cases from

1. Introduction



Figure 2. Global distribution of ZIKV and its vector *A. aegypti*.

ZIKV is found in 86 countries and territories mainly restricted to the Americas, sub-Saharan Africa, and Southeast Asia (dark orange). Furthermore, the global map displays countries and territories with confirmed *A. aegypti* but no ZIKV transmission cases (light orange). (Figure taken from [34])

Kerala and Maharashtra in 2021 have demonstrated that ZIKV is still on the rise, invading regions which have previously not been reported to be affected³². Overall, mapping ZIKV transmissions has revealed that since its emergence, a total of 86 countries and territories have been affected^{33,34} (Figure 2).

1.1.2. ZIKV – a virus with epidemic and PHEIC potential

Taken together, the data collected from serosurveys in tropical Africa and Asia suggest that the silent transmission of ZIKV among humans, animals and mosquitos has occurred during the last 70 years. As of January 4, 2018, a total of 223,477 confirmed cases have been reported worldwide with approximately 3,700 babies born with severe malformations³⁵. However, it is believed that the actual number of infections is much higher, as 70-80% of infections are asymptomatic and therefore remain undetected and unrecorded^{17,26,36}. Furthermore, many ZIKV infections may be misdiagnosed, due to overlapping symptoms with other infectious diseases caused by bacteria, parasites, or related flaviviruses³⁷. Even though the total number of infections is low when compared to DENV infections, with an estimate of 3.2 million infections per year^{38,39}, 2.2 billion people are living in areas known to contain the vector and the virus, and therefore are at risk of ZIKV infection⁴⁰. As of now, no vaccine

1. Introduction

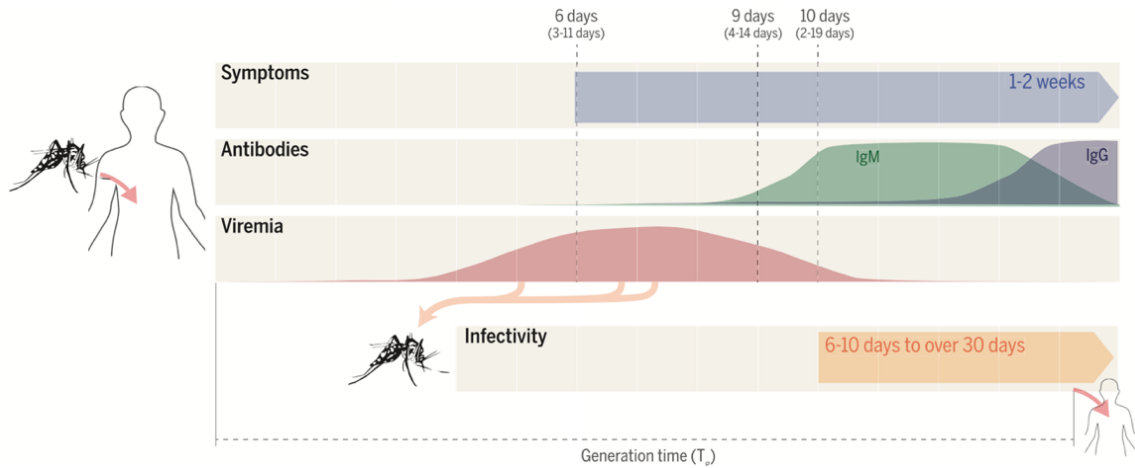


Figure 3. The course of human and mosquito infection.

Symptoms after ZIKV infection often occur in 3-12 days. IgM antibodies are the first to be detected, which start to rise about 9 days after infection. Later, as IgG antibodies rise and persist indefinitely, IgM antibodies start to decline. The likelihood of susceptible mosquitos contracting the disease while feeding on blood of infected hosts depends on the severity and length of the viremia. Viremia is likely to increase before to the onset of symptoms. After an incubation period of 10 to 30 days, infected mosquitos can transmit the virus to susceptible humans. (Figure taken from [48])

or antiviral therapy is available and together with the continuous silent spread and mutagenesis of the virus there is an increased risk of a bigger and even more severe outbreak. Therefore, understanding the viral replication cycle and its molecular mechanisms is important to combat the spread of this infectious disease.

1.1.3. Symptoms, pathogenesis, and treatments

Before 2013, the majority of Zika virus infections were asymptomatic, and Zika fever was known to be a mild, self-limiting febrile disease. Only a few patients developed clinical symptoms which included low-grade fever, maculopapular rash, arthralgia, fatigue, non-purulent conjunctivitis or conjunctival hyperemia, myalgia, and headache^{17,24,25,41-45}. Symptoms usually occur within 3-12 days after the bite of *Aedes* mosquito and typically resolve within 2-7 days⁴⁶⁻⁴⁸ (Figure 3). After its appearance in Brazil in 2015/16, ZIKV infection has been causally associated with various neurological complications comprising of congenital microcephaly, GBS, and even fetal losses in women who were infected during pregnancy^{49,50}. Retrospective analyses of the outbreak in French Polynesia in 2013 has demonstrated that even then ZIKV infections caused a significant increase in clinical cases involving neurological complications⁵¹⁻⁵³.

1. Introduction

Guillain-Barré Syndrome

Since the emergence of the Asian lineage, clinical cases showing neurological complications such as the GBS have significantly increased in number^{10,21,50}. Generally, GBS represents an acute self-limiting polyneuropathy which causes damage to the peripheral nervous system⁵⁴. The molecular mechanism of how ZIKV induces GBS is believed to be molecular mimicry^{55,56}. Recent studies have shown that the envelope glycan loop includes an IVNDT motif which is also found in the voltage-dependent L-type calcium channel subunit alpha-1C and Heat Shock 70 kDa protein (HSP70) 12A in humans⁵⁷. Both proteins have previously been identified to be associated with neurological autoimmune diseases of the central nervous system^{58,59}. Since immunogenic epitopes of the ZIKV polyprotein share similarities with host neuronal membrane gangliosides, antibodies produced upon ZIKV infection can cross react, therefore causing an auto-immune-like response^{60,61}. GBS symptoms can range from mild cases with brief weakness to devastating paralysis resulting in the inability of the patient to breathe independently⁶².

Microcephaly and congenital Zika syndrome

The most devastating feature of ZIKV is its ability to cause microcephaly, congenital malformations in neonates, and/or even fetal demise⁶³. In fact, approximately 30% of ZIKV-infected pregnancies showed ultrasound abnormalities^{45,64}. In addition, dysfunction of the placenta has also been reported^{65,66}. In general, the structural abnormalities and functional disabilities of the central and peripheral nervous system, which occur after ZIKV infection, are summarized in the term congenital Zika syndrome. Apart from the above-mentioned consequences of a ZIKV infection during pregnancy, imaging studies have revealed a much broader clinical phenotype which includes cerebral calcifications, cortical disorders, cortical development errors, hydrocephaly, and intrauterine growth restriction, to name just a few^{27,67}. However, within the last couple of years extensive research has been conducted with its main focus on how ZIKV causes microcephaly. For this, four different approaches using human induced pluripotent stem cells, brain organoids, mouse models, and non-human primate models have provided insight into the molecular mechanisms underlying the ZIKV-induced microcephaly^{68,69}. Combined research from all four models revealed that ZIKV preferentially infects neuronal progenitor cells (NPCs)⁷⁰⁻⁷². Although ZIKV can infect other brain cells such as mature neurons, their infectability is lesser⁷². Furthermore, it was shown that ZIKV inhibits NPC proliferation, differentiation, and migration, causing an increase in dysregulated cells, which are eliminated via apoptosis⁷¹⁻⁷⁴. Using *in vivo*

1. Introduction

models, findings from *in vitro* studies have been confirmed, and have shown the ultimate consequence of dysregulated NPC proliferation, differentiation, and migration on the brain development. In these studies, infected animals showed cortical thinning, reduced surface folding, and microcephaly, when compared to uninfected animals^{70,73,75-77}.

Treatments

To date there are no specific medicines, antivirals, or vaccines available for treating and preventing ZIKV disease and infection. Thus, current treatments are focused on reducing signs and symptoms by using analgesics and antipyretics drugs^{33,78,79}. Symptomatic patients are advised to rest and to drink plenty of fluids to prevent dehydration due to sweating and/or vomiting. As symptoms of ZIKV disease overlap with symptoms of closely-related flaviviruses such as DENV, patients are advised to not use aspirin or other non-steroidal anti-inflammatory drugs as they can increase the risk of hemorrhage⁸⁰.

1.1.4. Control measures of ZIKV spread and disease

Antivirals

Generally, three strategies can be employed to discover inhibitors of ZIKV. First, already clinically approved drugs can be repurposed⁸¹⁻⁸⁴. Such an approach is time- and cost-saving, as these drugs have already been identified and approved for human use. In this context, drugs including ivermectin⁸¹, pyrimethamine⁸¹, mevastatin⁸², and lovastatin⁸³ have been found to inhibit ZIKV infection. Second, viral replication-based phenotypic approaches can be used for screening novel compound libraries⁸⁵⁻⁸⁸. Here, the following three assays can be used: ZIKV infection assay; ZIKV replicon assay; Zika virus-like particle (VLP) infection assay. While ZIKV infection assays include each step of the viral replication cycle (from attachment to release of new progeny virus particles)^{85,88}, ZIKV replicon assays focus solely on the steps of translation and replication of the viral genome⁸⁹⁻⁹³. The VLP-based assay analyzes viral entry, translation, and RNA synthesis, as virus particles can only be formed by *trans* supplementation of the viral structural proteins^{87,94}. So far, VLP systems have been used for antiviral screening, vaccine development, and serological diagnosis of flaviviruses^{86,87,94-98}. However, VLP screening approaches have been found to be the least productive⁹⁹. The third and last strategy for discovering new antiviral drugs is based on viral proteins as targets¹⁰⁰. Here, enzymatic activity and crystal structure of viral proteins, and *in silico* docking to viral proteins are the most useful targets or processes¹⁰¹⁻¹⁰⁷. In this

1. Introduction

context, the two non-structural (NS) proteins NS3 and NS5 represent good targets as their enzymatic activity is well preserved among flaviviruses. Furthermore, the crystal structure of both proteins has been resolved, therefore providing valuable information for structure-based rational design and *in silico* docking of antiviral drugs. To this end, several potent inhibitors of flaviviruses have been identified *in vitro*; however, antiviral activity was not observed *in vivo* due to the lack of permeability or poor pharmacokinetics^{108–110}. Current advancements regarding the development of antivirals against ZIKV infection are summarized in the review by Li and colleagues¹¹¹.

Vaccines

Within the last decades, outstanding research has contributed to the development of vaccines against several different flaviviruses. Currently, clinically-approved vaccines are available for four flaviviruses: (i) live, attenuated vaccine against YFV; (ii) live, attenuated and inactivated-virus vaccine against JEV; (iii) inactivated-virus vaccine against TBEV, and (iv) chimeric, live, attenuated vaccine against DENV^{80,112} (Table 1).

After the release of Dengvaxia, safety studies have shown that vaccination in children who have previously not been exposed to dengue, caused an increased risk of cytoplasmic leakage syndrome¹¹³. This complication has illustrated that vaccines against related flaviviruses could exhibit cross-reactivity, causing a more severe outcome of Zika or dengue infections¹¹⁴. After the outbreak in 2015/16 and the declaration of ZIKV to be a PHEIC, a total of 45 vaccine candidates have been introduced by the scientific community. In 2019, the WHO Global Observatory on Health R&D listed eight projects for ZIKV vaccine development alone. While six projects focused on the two structural proteins prM-E as immunogens, the remaining two projects used live, attenuated viruses as immunogens. However, as of now only two projects have progressed to clinical phase II trials for testing their efficacy: mRNA-1325 (Moderna) and VRC-ZKAD-NA085-00-VP (NIH/NIAID)⁸⁰ (Table 1).

Table 1. List of approved vaccines against flaviviruses and developmental state of ZIKV vaccine candidates. (Adapted from [80])

Virus	Name of vaccine	State	Immunogen	Sponsor
DENV	Dengvaxia ^{80, 112}	Approved	Attenuated virus	Sanofi-Pasteur
JEV	IXIARO ¹¹⁵	Approved	Inactivated virus	Valneva
TBEV	Encepur ¹¹⁶	Approved	Inactivated virus	CC-Pharma GmbH
YFV	Stamaril ¹¹⁷	Approved	Attenuated virus	Sanofi-Pasteur
ZIKV	mRNA-1325 ⁸⁰	Phase II	prM-E (mRNA)	Moderna Therapeutics
ZIKV	VRC-ZKAD-NA085-00-VP ⁸⁰	Phase II	prME	NIH/NIAID

1. Introduction

Although the first steps towards a ZIKV vaccine have been taken, vaccine development projects are still having difficulties in recruiting subjects for the clinical trials. Due to the continuous decline in the number of ZIKV cases, as well as the geographic unpredictability of epidemics and the large variety of clinical symptoms, it is difficult to evaluate vaccine candidates, therefore potentially jeopardizing current and future clinical trials for a ZIKV vaccine.

Vector control

As vaccines and antivirals remain unavailable, the most efficient approach to control and prevent ZIKV infections is by reducing the contact between mosquitos and humans. Within the last couple of years campaigns were made aiming to eliminate or reduce mosquito populations in affected countries and territories. Although these eradication campaigns were promising, they relied heavily on the use of DDT and other persistent, highly toxic insecticides, and are therefore today considered by many to be environmentally unacceptable^{118,119}. Generally, the reduction of the arthropod vector can be achieved by the following approaches: (i) destruction of mosquito breeding sites¹²⁰; (ii) larvicides and insecticide aerosols¹²¹; (iii) release of genetically modified male mosquitos which express a dominant lethal gene at the larval stage¹²²; (iv) release of mosquitos infected with the endosymbiotic bacteria *Wolbachia*¹²³; and (v) usage of autocidal gravid ovitraps¹²⁴.

1.2. Molecular biology of ZIKV

1.2.1. Virus genome organization

The genome of flaviviruses is a single-stranded RNA molecule of positive polarity^{125,126}. As of 2007, for the first time, the entire genome of the African prototype (ZIKV strain MR766) was fully sequenced, revealing that the Zika viral RNA (vRNA) genome is 10.8 kb in length, contains a single open reading frame (ORF) which is flanked at both ends by untranslated regions (UTR) (Figure 4a). The 5'UTR comprises 106 nucleotides, whereas the 3'UTR is 428 nucleotides in length^{125,127}. The ORF is translated into a precursor polyprotein which upon processing forms the three structural proteins [capsid (C), precursor membrane (prM) and envelope (E)] and the seven non-structural proteins [NS1, NS2A, NS2B, NS3, NS4A, NS4B and NS5] (Figure 4b)^{125,128}. These non-structural proteins are involved in viral genome replication, virus morphogenesis, and host cell immune response evasion³. Forming

1. Introduction

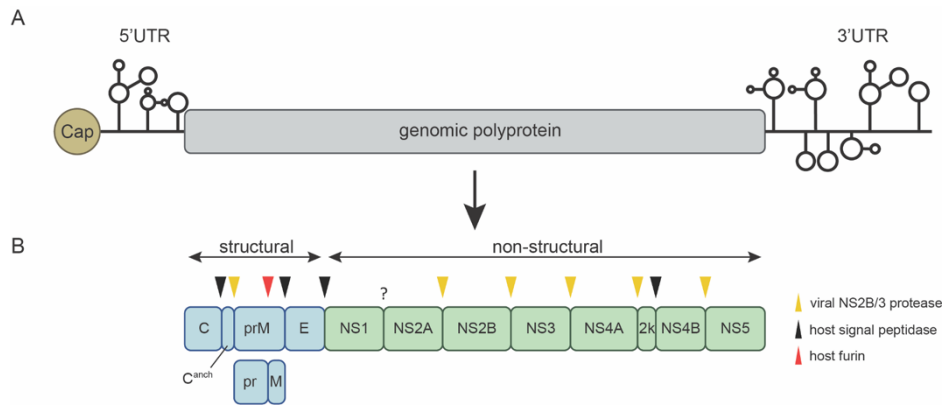


Figure 4. ZIKV genome organization and polyprotein structure.

(A) Schematic diagram of the viral genomic RNA. The positive, single-stranded RNA genome of ZIKV has a 5' type I cap, one open reading frame (ORF) encoding the polyprotein, and untranslated regions (UTRs) on either side of the ORF. Characteristic features of the UTRs are the secondary stem loop structures. (B) Host cellular (black arrowheads) and viral (yellow arrowheads) proteases co- and post-translationally process the polyprotein forming the three structural proteins [capsid (C), the precursor membrane (prM), and envelope (E)] and the seven non-structural (NS) proteins, numbers NS1 to NS5. The red arrowhead designates the location of the furin cleavage site for virus particle maturation.

of the individual viral proteins is achieved by co- and/or post-translational cleavage by the host signal peptidase (anchor C/prM; prM/E; E/NS1; 2k/NS4B)^{127,129,130}, the viral protease NS2B/3 (C/prM; NS2A/2B; NS2B/NS3; NS3/NS4A; NS4A/2k; NS4B/NS5)^{130–133} and an unknown host protease (NS1/NS2A)^{130,134}. The final cleavage occurs in the *trans*-Golgi network when immature viruses are processed by furin (pr/M) to generate fully mature infectious virus particles^{135,136}. Infectious virions are composed of the structural proteins and vRNA.

1.2.1.1. RNA structures in the ZIKV genome and their function

During the life cycle of positive-strand RNA viruses, the genome participates in three distinct processes: serving as a template for viral protein synthesis^{137–141}, serving as a template for virus genome amplification^{142–145}, and serving as vRNA which gets packaged into virions during virus assembly^{146–148}. Within the last decade noteworthy research has revealed that *cis*-acting RNA elements, located within the highly structured 5' and 3'UTR, regulate and control the utilization of the viral RNA genome in each step of the viral life cycle.

The 5'UTR contains a Y-shaped stem-loop (SL) A (Figure 5a), which binds to the viral RNA polymerase NS5, thus acting as the vRNA promoter^{127,142,145}. Initiation of viral replication requires the transfer of the viral polymerase to the RNA synthesis initiation site

1. Introduction

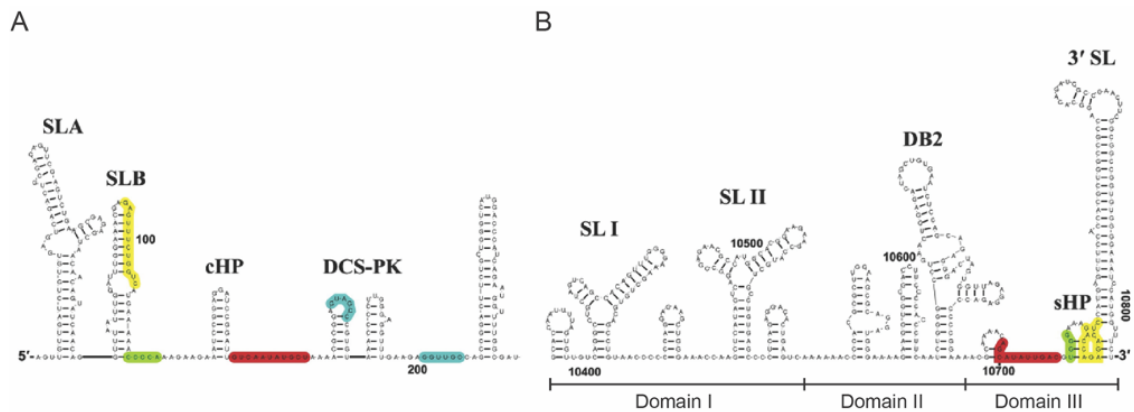


Figure 5. Secondary RNA structures in the UTRs of the ZIKV genome.

The secondary structures and sequences displayed derive from the ZIKV strain MR766 (NC_012532). **(A)** The 5' end contains the SLA, SLB, the capsid hair pin (cHP), and pseudoknots (PK) downstream of the 5' cyclization sequence (DCS). **(B)** The 3' end folds into three domains. Domain I contains the stem loop (SL) I and SL II. Domain II contains the DB2 element. Domain III contains the sHP and 3'SL structures. Cyclization of the viral RNA genome is accomplished by complementary sequences such as 5'-3'CS (red), 5'-3'UAR (yellow), and 5'-3'DAR (green). (Adapted from [127])

located within the 3' end. This transfer is accomplished by genome cyclization, which requires long-range RNA-RNA interactions^{149–151} for bringing both termini, which are separated by several thousand nucleotides, into proximity. These long-range interactions are based on the hybridization of complementary sequences which are found in conserved RNA structural elements including the SLB, the upstream AUG region (5'UAR)^{149,152}, the downstream AUG region (5'DAR)^{153,154}, and the cyclization sequence (5'CS)¹⁵⁵. Notably, these RNA structural elements are located in the ZIKV genome at classical positions which have previously been reported for other mosquito-borne flaviviruses^{149,152,153,155}.

The 3'UTR generally folds into three domains¹²⁷ (Figure 5b). Although Domain I is the least conserved domain among flaviviruses and its function remains mostly unclear, previous studies have shown that Domain I in the ZIKV genome contains two SL elements (referred to as SL I and SL II) which are required for the production of sRNAs and host adaptation^{156–158}. For most flaviviruses the Domain II contains two dumbbell structures (DB1 and DB2). However, Domain II of ZIKV consists of only one dumbbell structure (DB2) and two upstream small hairpin structures. To this end, DB elements were identified to play a role during translation, replication, and/or species tropism^{159–161}. The last domain, Domain III, is the most conserved domain among flaviviruses and consists of the long terminal 3'SL, a short hairpin stem-loop (sHP), the 3'CS, the 3'DAR and the 3'UAR sequences. To date, studies have demonstrated that the 3'SL is indispensable for flaviviruses

1. Introduction

replication^{162–165}. While the sHP structure is suggested to be required for balancing the genomes' conformations¹⁶⁶, the complementary sequences (3'CS, 3'DAR, and 3'UAR) are required for viral genome cyclization. Overall, the 3' RNA structural elements are found at classical locations as demonstrated for related flaviviruses.

1.2.1.2. Viral proteins and their function

The structural proteins

The **capsid (C)** protein is 122 amino acids (aa) in length and has a molecular weight of approximately 14 kDa. Structural analyses of the ZIKV capsid protein have revealed that its N-terminus is positively charged, forming a loop which is followed by five alpha helices ($\alpha 1$ - $\alpha 5$; Figure 6a)^{167,168}. Moreover, it was shown that the junction site between $\alpha 4$ and $\alpha 5$ gets cleaved by the viral protease NS2B/3, thus releasing mature C proteins into the cytosol. Monomeric mature C proteins assemble into dimers, a process which is mediated by the hydrophobic helix $\alpha 1$. In addition, helix $\alpha 1$ was also found to mediate the interaction with the viral lipid membrane^{167,168}. The helix $\alpha 4$ contains basic residues, forming a highly positively charged interface, which facilitates the binding to vRNA. The capsid-RNA complex, also referred to as nucleocapsid (NC), is enveloped by a lipid membrane containing prM and E proteins, resulting in the production of immature virus particles^{133,168,169}. Upon cleavage, helix $\alpha 5$ resides in the endoplasmic reticulum (ER) membrane and serves as a signal peptide, guiding prM to enter the lumen of the ER¹⁶⁷. Just recently, Morando and colleagues have shown that the dynamics of the structural elements respond to the structure-driven regulation based on the interaction with cellular hydrophobic interfaces, thus contributing to NC assembly¹⁷⁰.

Aside from its role during virus assembly, previous studies have shown that C proteins can bind to host proteins forming stable complexes, blocking the formation of stress granules and thus promoting translation of the viral genome¹⁷¹.

The **precursor membrane (prM)** protein is 178 aa in length and consists of three domains: the soluble pr peptide at the N-terminus, a central ectodomain, and a transmembrane domain (TMD) at the C-terminus^{172,173} (Figure 6b). So far studies have shown that prM is involved in the following three steps which are required for virus assembly: (i) interaction with E proteins in the ER membrane; (ii) envelopment of the viral NC; and (iii) maturation of virus particles^{174–177}. Together with the envelope the outer proteinaceous

1. Introduction

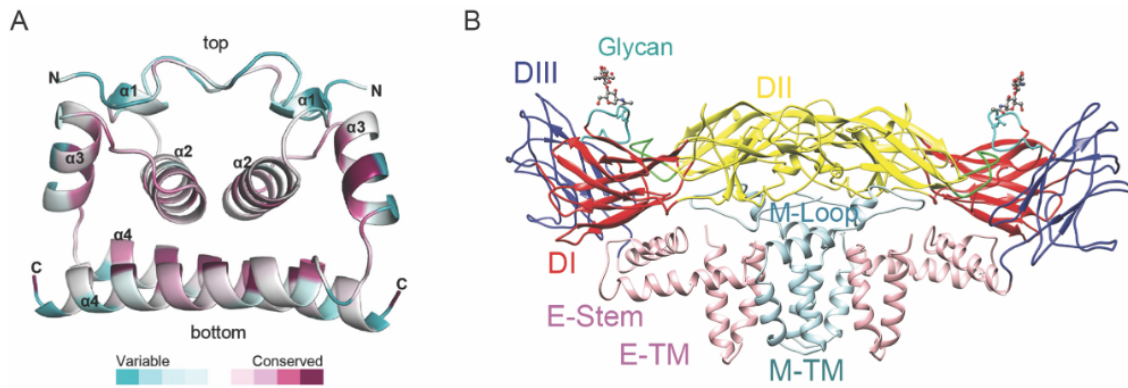


Figure 6. Structure of the capsid, membrane, and envelope proteins of ZIKV.

(A) A dimer representation of the mature Zika capsid with its secondary protein structures. Sequence conservation among flaviviruses is given by colors from the most conserved (dark magenta) to most divergent (dark cyan). The mature capsid contains 4 alpha helices ($\alpha 1$ - $\alpha 4$). Helix $\alpha 1$ mediates capsid dimerization and interaction with the viral lipid membrane. The nucleocapsid is formed when helix $\alpha 4$ binds to the vRNA via its highly positively charged interphase. (Figure taken from [168]) (B) Side view representation of Zika E-M dimers. The three ectodomains (DI: red; DII: yellow; and DIII: blue) and the stem-transmembrane (TM) domains (pink) are shown for envelope. The Asn154 within the envelope protein is glycosylated and shown for one monomer. For the small membrane protein, the M loops and stem-TM domains (turquoise) are shown. TM domains of E and M are embedded into the viral lipid membrane. (Figure taken from [173])

shell of virus particles is formed, which in immature viruses appears as protruding spike-like trimeric complexes (prM_3E_3)^{178,179}. While immature viruses follow the secretory pathway through the *trans*-Golgi network, pr peptides bind to E proteins, shielding the fusion loop and thereby protecting the virus from premature fusion^{175,180}. The M domain is embedded into the ER membrane and is connected to the pr peptide via a linker which comprises the furin cleavage site. Within the *trans*-Golgi network maturation of virus particles occurs, which involves conformational changes of trimeric prM_3E_3 spikes, revealing the furin cleavage site which subsequently gets cleaved by host furin or furin-like protease¹⁸¹⁻¹⁸³. Upon exocytosis, the neutral pH triggers the dissociation of pr from virions, whereby the virus becomes infectious¹⁸¹.

Apart from its role in virus assembly and maturation, studies have suggested that mutations within the prM protein are related to the ZIKV neurovirulence. When amino acid substitutions within the prM protein were studied, Yuan and colleagues identified an amino acid substitution (S139N) which is present in epidemic strains. Pre-epidemic Asian strains or revertant mutant viruses (N139S) showed lower neurovirulence¹⁸⁴. In the following years, Li and colleagues have demonstrated that prM and pr peptides can trigger apoptosis of human brain glial cells¹⁷⁶.

1. Introduction

The **envelope (E)** protein is the largest structural protein with approximately 500 aa and consists of three ectodomains (DI, DII and DIII) and a transmembrane domain^{173,185–188} (Figure 6b). Structural analyses of E proteins have revealed that the two ectodomains (DII and DIII) are connected via the β -barrel shaped domain I (DI). While ectodomain II (DII) contains the dimerization interface and the fusion loop, ectodomain III (DIII) contains the receptor binding site, mediating attachment and entry of the target cell. The transmembrane domain consists of two α -helices, forming a stem and a transmembrane region, which serve as anchor to the ER membrane^{189,190}. So far, E proteins were described to mediate virus attachment, entry into host cells, host adaptation, immune recognition, and virus pathogenesis^{189,191,192}. With its immunogenic properties, E proteins are the major component involved in the production of neutralizing antibodies^{186,187,193}. Within the last years studies have shown that E proteins are post-translationally modified through ubiquitination and glycosylation. While ubiquitination was found to be a determinant for ZIKV entry, tissue tropism and pathogenesis¹⁹¹, glycosylation was found to be requisite for ZIKV infection in mosquitos¹⁹³. In addition, evolutionary mutations, such as V473M, have been shown to enhance ZIKV neurovirulence, mother-to-child transmission, and viremia¹⁹².

The non-structural proteins

The **nonstructural protein 1 (NS1)** is 352 aa in length with a molecular weight of 46-55 kDa¹⁹⁴. NS1 exists in two forms which are involved in three processes during the infectious replication cycle. Its dimeric form is located within the lumen of the ER where it regulates the host cell immune response and supports virus replication, as it can induce membrane remodeling and thus contribute to the formation of virus replication organelles (ROs)^{194–196}. In addition, NS1 can form hexamers which are secreted into the extracellular space, where they trigger the host immune response^{197,198} and promote virus spread due to the ability to induce hyperpermeability in tissues¹⁹⁹. At present, studies have indicated that adaptive mutations within NS1 increased the virus infectivity towards mosquitos and enhanced viral prevalence in mosquitos²⁰⁰. In this context, Liu and colleagues found that pre-epidemic (before 2012) ZIKV strains exhibit an alanine at position 188 in NS1, whereas epidemic ZIKV strains exhibit a valine. While viruses exhibiting an alanine at position 188 were weak regarding infectivity and prevalence in mosquitos, a valine at position 188 increased ZIKV infectivity and prevalence. Therefore, such mutations are presumed to ease transmission which could explain the epidemic outbreaks since 2013²⁰¹.

1. Introduction

The **nonstructural 2A (NS2A)** protein is a small, hydrophobic, membrane-associated protein with a length of 226 aa and a molecular weight of approximately 22 kDa²⁰². Although its structure remains unresolved, functional studies of dengue and Zika NS2A have provided insights into its membrane topology and function during the viral replication cycle^{202,203}. Biochemical structure analysis of NS2A showed that its N-terminus is located on the luminal side of the ER and is comprised of two membrane-associated segments, whereas its C-terminus is located on the cytoplasmic side and comprised of four membrane-associated segments. Both termini are connected via a transmembrane segment which spans the ER membrane²⁰². Functional characterization of NS2A demonstrated its association with viral genome replication and virus particle assembly^{204,205}. Regarding the latter, the molecular mechanism of how NS2A contributes to virus assembly is described in detail in Section 1.2.2.4. Like other viral proteins, NS2A is involved in regulating the host immune response. NS2A antagonizes the RIG-I/MDA5 pathway mediated production of interferon beta (IFN- β) by inhibition of RIG-I and IRF3²⁰⁶.

The **nonstructural 2B (NS2B)** protein is a small, ER-associated, transmembrane protein with a length of 130 aa and a molecular weight of 14 kDa²⁰⁷. To date, no enzymatic function has been identified for NS2B, however, existing research describes NS2B as cofactor for the **nonstructural 3 (NS3)** protein. Its binding to NS3 stabilizes its structure, anchors NS3 to ER membranes via its transmembrane domain^{207–209}, and activates the protease domain^{207,209}. NS3 is a multi-domain protein with a length of 617 aa and a molecular weight of 72 kDa, which exerts two functions in the viral replication cycle. Its N-terminus consists of a serine protease domain which processes the precursor polyprotein²⁰⁷. Its C-terminus consists of two enzymatic functions including the nucleoside triphosphatase and RNA helicase domain^{209,210}. While the former provides energy via ATP hydrolysis, the latter uses the energy to dissociate double-stranded RNA during viral genome replication²¹¹. As the enzymatic functions of NS2B/3 are highly conserved among flaviviruses, research has focused on them for the development of antiviral compounds^{208,210–212}.

The two **nonstructural 4A** and **4B (NS4A and NS4B)** proteins are hydrophobic, ER-associated transmembrane proteins with a length of 127 aa and 252 aa, respectively. To date, both proteins have been shown to be essential components facilitating the formation of flavivirus replication complexes^{88,213–215}. However, to this end no enzymatic activity has been found nor their structural organization has been resolved.

1. Introduction

Like NS2A, NS4A antagonizes the production of type I IFN via the RIG-I/MDA5 signaling pathways by blocking the phosphorylation of the IRF3^{206,216–218}. A direct interaction has also been observed between NS4A and MAVS which prevents the interaction between RIG-I and MAVS required for producing type I IFN^{216,217}. In addition to NS4A, NS4B also regulates the host immune response, inhibiting the production of type I IFN by binding to TBK1^{218,219}.

Finally, the **nonstructural 5 (NS5)** protein is with 903 aa and a molecular weight of approximately 95 kDa the largest viral protein. NS5 consists of two domains with enzymatic activity including the RNA-dependent RNA polymerase (RdRp) at the C-terminus and the methyltransferase (MTase) at the N-terminus^{220,221}. While the RdRp is responsible for synthesizing new vRNA²²², the MTase mediates 5' capping and methylation of the genome²²³. In addition to its role during virus replication, recent studies have demonstrated that NS5 regulates the host immune response. In this context, ZIKV NS5 was found to antagonize the production of type I IFN by binding and inducing the ubiquitin-mediated degradation of the human transcription activator STAT2^{224,225}. Upon expression and processing of the polyprotein, NS5 relocates to the nucleus, where it interferes with host mRNA splicing²²⁶. Moreover, recent findings suggest that accumulation of NS5 in the nucleus protects cytosolic NS5 from degradation, promoting its biological functions in the virus replication cycle. Given its conserved enzymatic function among flaviviruses, NS5 is also considered as target for developing antiviral compounds.

1.2.2. ZIKV transmission routes

Vector borne transmission

As an arthropod-borne virus (arbovirus), ZIKV is transmitted via two distinct cycles: (i) a sylvatic cycle and (ii) an urban cycle^{112,227} (Figure 7), which both involve mosquitos belonging to the genus *Aedes*. While the former describes the transmission cycle between non-human primates, the latter refers to the transmission cycle between humans. Although several different *Aedes* species have been identified to be potential vectors, the primary vector is considered *A. aegypti*. This is demonstrated by the following evidence: (i) isolation of ZIKV from *A. aegypti* mosquitos^{5,228,229}; (ii) *A. aegypti* are susceptible to ZIKV infection^{230–232}; and (iii) artificially infected *A. aegypti* mosquitos are capable of transmitting ZIKV to rhesus

1. Introduction

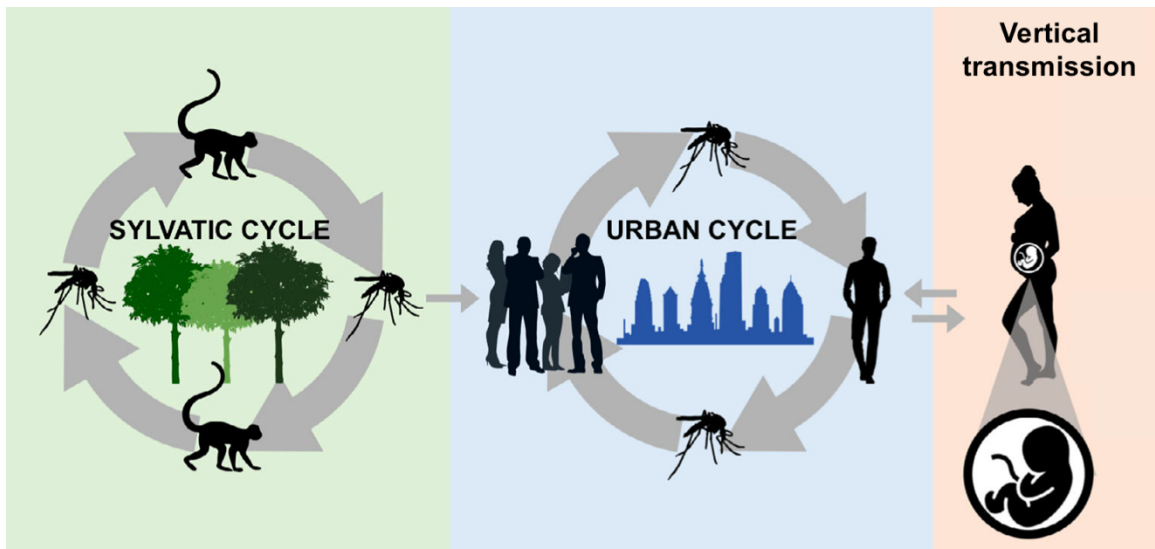


Figure 7. Transmission routes of ZIKV.

The ZIKV life cycle can occur via two distinct transmission cycles: a sylvatic cycle, which involves arboreal mosquitos and non-human primates (green); and an urban cycle, which involves urban mosquitos and humans (blue). Although transmission via its arthropod vector is considered the main transmission route, ZIKV can be transmitted vertically from mother to child (pink). (Adapted from [227])

monkeys and mice²³⁰. Overall, transmission via its arthropod vector is considered to be the most common mode of ZIKV transmission.

Non-vector-borne transmission

Besides its vector-borne transmission, several cases have been documented describing transmission of ZIKV directly from human-to-human. Possible routes that have been described include sexual transmission^{233,234}, transplacental and perinatal transmission^{27,45,49,64,235,236}, and blood transfusion or organ transplantations^{237,238}. In the context of sexual transmission, ZIKV was detected in vaginal fluids²³⁹ and semen²³⁴. In semen, infectious Zika virus particles and vRNA were detected at 24 days and 6 months after the onset of symptoms, respectively^{240,241}. To date, sexual transmission appears to be a unique feature of ZIKV which has not been reported for other vector-borne flaviviruses²⁴². During the outbreaks in French Polynesia and the Americas, research concerning mother-to-child transmissions highlighted that ZIKV transmissions can occur prenatally as well as postnatally. Here, ZIKV RNA was detected in breastmilk²³⁵, amniotic fluid^{49,236}, fetal and placental tissues²⁴³, cerebral spinal fluid^{244,245}, and brain of microcephalic fetuses^{27,64,235}. Finally, as the majority of ZIKV infections are asymptomatic there is a risk of ZIKV transmission during blood transfusion or organ transplantations^{237,238}.

1. Introduction

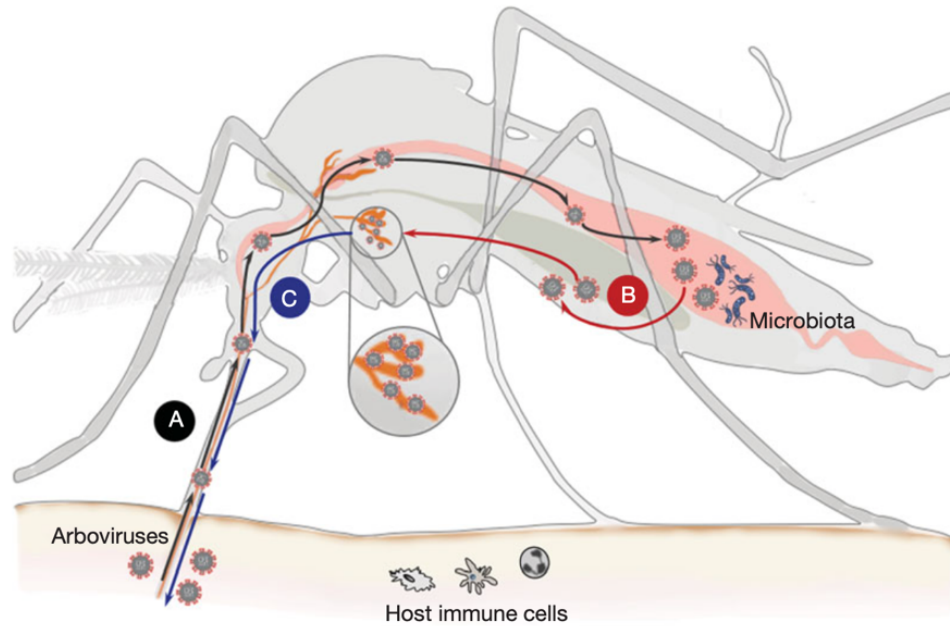


Figure 8. The mosquito arbovirus life cycle.

(A) The arbovirus initially infects the midgut following consumption of an infected blood meal. Here, the mosquito's intestinal defenses and commensal microbiome regulate its propensity to contract an infection. (B) Arboviruses pass via intestinal epithelial cells to reach the hemocoel, where they induce systemic infection in the mosquito. (C) New infectious viruses are produced within the salivary glands and are then stored in the apical cavity. The bite of an infected mosquito into human skin results in re-transmission. Here, the initial infection's primary targets are intradermal immune cells. (Figure taken from [251])

1.2.3. ZIKV life cycle

At the present time it is well established that ZIKV replicates and propagates in two distinct hosts - the mosquito and mammals (non-human primates and humans). While the infectious replication cycle in humans has been extensively studied and is therefore well described, little is known about the infectious replication cycle within the mosquito host.

At present, only a few studies have investigated the infectious replication cycle within the mosquito host for Zika and other arboviruses²⁴⁶⁻²⁴⁸. The arbovirus infectious replication cycle starts when female mosquitos feed on infected blood, thus retrieving the virus. The first organ to get infected is the digestive tract, as it receives and processes the infected blood²⁴⁹. In the midgut, the virus traverses through the intestinal epithelial cells before reaching the hemocoel. From that point, the virus spreads systematically throughout the arthropod's body, reaching its replication site the mosquito salivary glands^{246,250}. Within the salivary glands, new infectious viruses are produced which are subsequently stored in the apical cavity alongside the saliva of the mosquito^{246,247,251} (Figure 8). The extrinsic

1. Introduction

incubation in the arthropod vector takes 8-12 days before the virus can be re-transmitted to another human during the next blood meal^{252,253}.

The human infectious life cycle starts when the virus is injected into the skin where primary dermal fibroblasts, epidermal keratinocytes, and immature dendritic cells are infected and serve as initial replication sites for ZIKV^{254–257}. Following replication at its injection site, ZIKV spreads to the draining lymph node, from where it disseminates to peripheral tissues and visceral organs via the blood stream.

1.2.4. ZIKV infectious replication cycle

1.2.4.1. Attachment, uptake, and fusion

The ZIKV infectious replicative cycle starts with binding to the surface of susceptible cells including skin cells (e.g., epidermal keratinocytes, dermal fibroblasts, Langerhans cells)^{254,257}, blood cells (e.g., monocytes, dendritic cells)^{258–260}, brain cells (e.g., astrocytes, glial cells, and NPCs)^{72,261–264}, placenta cells (e.g., endothelial cells, Hofbauer cells, trophoblasts)^{265–271}, testicular cells (e.g., spermatozoa, Sertoli cells)^{272–275}, and retina cells (e.g., retinal pericytes, retinal microvascular endothelial cells)²⁷⁶. Initial binding occurs via attachment factors, which tether the virions onto the cell surface, followed by further specific interactions between ectopic envelope proteins and secondary receptors. Currently, the receptors and attachment factors which have been identified include DC-SIGN²⁷⁷, HSP70²⁷⁸, TIM receptor family, TAM receptor family (Tyro3, Axl, and Mer)^{254,261,262,279}, glucose-regulating protein 78²⁸⁰, integrin- α V/ β 5²⁸¹ and neural cell adhesion molecule²⁸² (Figure 9a). Upon binding to cell surface receptors, virions are internalized via clathrin-mediated (Figure 9b) or clathrin-independent endocytosis^{283–285}. As the endosome is transported a vacuolar ATPase pumps protons into the interior, causing its acidification. Acidification triggers irreversible conformational changes in the ectopic E protein, uncovering the fusion loop which is subsequently inserted into the endosomal membrane inducing virus fusion^{286–289} (Figure 9c). Once the fusion pore is formed, the NC is released into the cytosol. Upon capsid degradation, the vRNA is released into the cytosol where it gets translated by the host cellular translation machinery^{285,290}.

1. Introduction

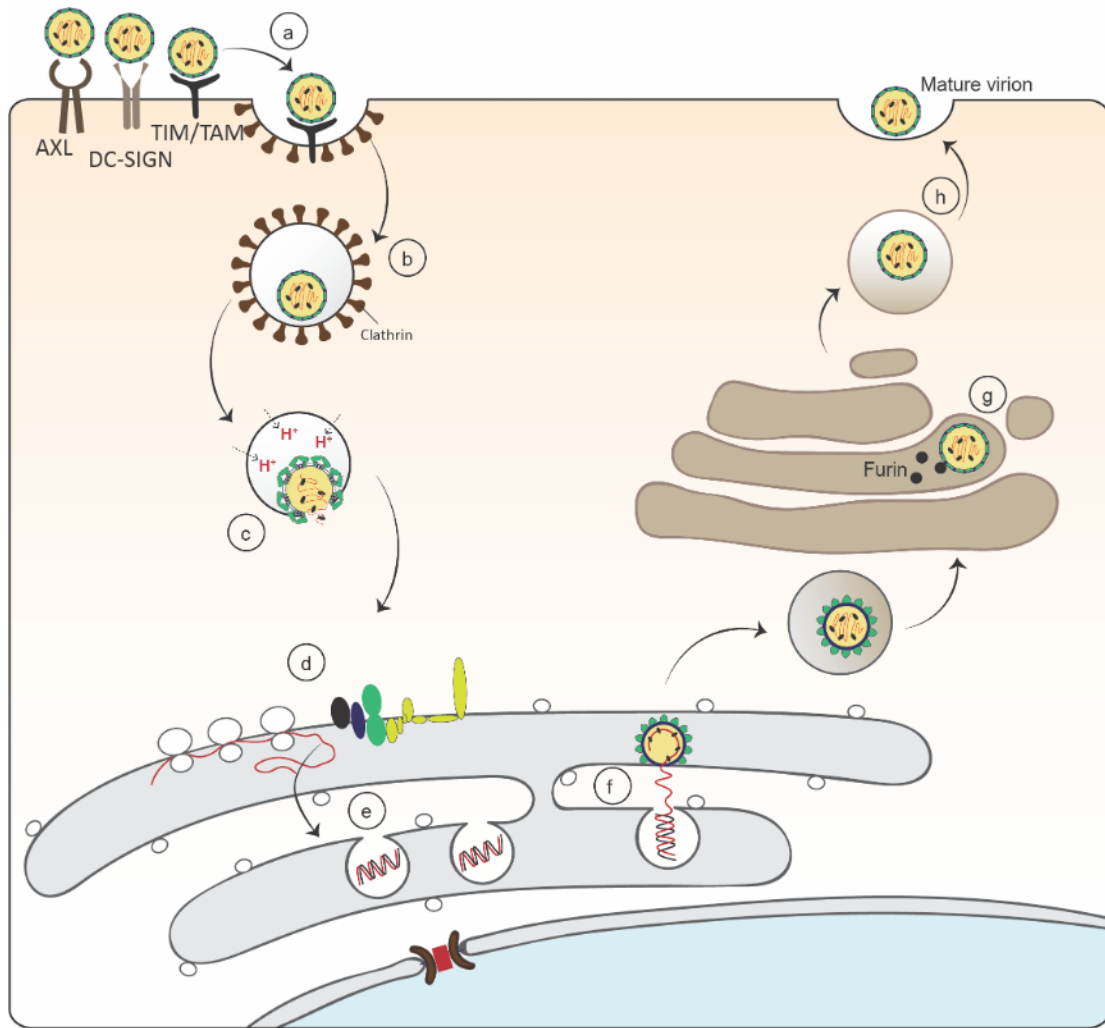


Figure 9. Replication cycle of flaviviruses.

Virus particles binding to the surface of target cells via receptors and attachment molecules (a). Viruses are thereafter internalized via clathrin-mediated endocytosis (b). The viral proteinaceous shell undergoes conformational changes in response to endosomal acidification, which is followed by the fusion of the viral and endosomal membranes, which releases the nucleocapsid into the cytosol (c). At the rough ER the ZIKV genomes is translated (d) resulting in the formation of distinct membranous structures, termed vesicle packets (VPs), in which viral replication occurs (e). New immature virus particles are formed via budding into the lumen of the ER at nearby sites (f). As immature viral particles traffic through the *trans*-Golgi, furin cleavage occurs resulting in conformational changes of E-prM. Via the conventional secretory pathway mature virions are released into the extracellular space, where pr peptides dissociate rendering infectious virus particles (h).

1.2.4.2. Translation

Upon release of the vRNA into the cytoplasm, the encoded methylguanosine cap at the 5'UTR initiates translation²⁹¹. First, the 43S pre-initiation complex is formed, which consists of the 40S ribosomal subunit, eukaryotic initiation factor (eIF)3, ternary complex (eIF2/GTP/Met-tRNA_i), eIF1 and eIF1A²⁹². This complex is thereafter recruited to vRNA via the 5'cap-binding complex eIF4F. Unwinding of the highly structural 5'UTR occurs via

1. Introduction

the helicase eIF4A/4B complex, thus allowing the scanning of the vRNA for a suitable AUG start codon²⁹³. Once the start codon is recognized, hydrolysis of the bound GTP occurs, resulting in the formation of the stable 48S complex. Initiation factors then dissociate and the 60S ribosomal subunit is recruited for polypeptide elongation²⁹⁴. During polypeptide elongation the precursor polyprotein is formed which contains an ER localization sequence at its N-terminus, resulting in its translocation to the ER²⁹⁵. As polypeptide elongation continues the polyprotein is inserted into the ER membrane, resulting in the location of prM, E, NS1, parts of NS2A, NS4A, and NS4B onto the ER luminal side, and C, NS3, and NS5 onto the cytoplasmic site (Figure 9d). Processing of the precursor polyprotein by host cellular and the viral proteases forms the 10 individual viral proteins. Viral proteins can change entire global cell metabolic profiles, generating a virus replication friendly environment and initiating the formation of the viral ROs (Figure 9e) which are required for virus replication.

1.2.4.3. Replication and replication organelles

As mentioned in Section 1.2.1.1., the viral RNA serves as a template during translation, replication and vRNA packaging into new virions within the infected host cell. While translation occurs in a 5'-3' direction, viral replication occurs in a 3'-5' direction, thus suggesting that these processes occur sequentially. Currently, the molecular switches involved in regulating the use of vRNA remain largely elusive. However, recent work by Sanford and colleagues has shown that RNA cyclization facilitates vRNA replication and simultaneously inhibits *de novo* translation initiation²⁹⁶. Within ROs, new vRNA is synthesized by the RdRp, which initially binds to the 5'SLA and thereafter is transferred to the RNA replication initiation site at the 3'end upon genome cyclization. RdRp synthesizes an intermediate, double-stranded RNA (dsRNA) which consists of a negative and positive strand RNA molecule. This intermediate is subsequently unwound by the NS3 helicase to generate both single-stranded RNA (ssRNA) of positive and negative polarity²⁹⁵. While the negative ssRNA serves as template for further transcription, the positive ssRNA serves either as template for protein synthesis or as genomic RNA which is packaged into new virions²⁹⁵. Newly synthesized positive ssRNA gets post-transcriptionally modified through 5'capping and methylation, which protects the vRNA from degradation²⁹⁷. Via its interaction with NS2A and capsid, vRNA is packaged into new virions which are assembled at adjacent sites to ROs.

1. Introduction

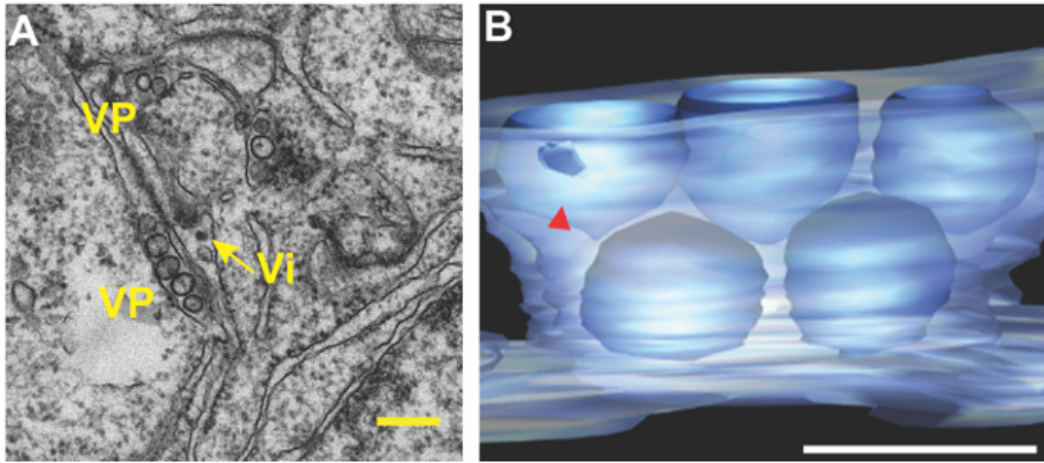


Figure 10. Morphology and architecture of the ZIKV replication organelle.

(A) Thin-section TEM picture of ZIKV strain H/PF/2013-infected Huh7-cells reveal virus-induced membrane changes. Virus-induced vesicle packets (VP) are invaginations into the lumen of the rough ER. In proximity to VPs a virus particle (Vi) can be discovered. Scale bar: 200 nm. (B) Ultrastructural analyses of the ZIKV-induced replication organelle. The reconstructed 3D model in its side view shows the pore-like opening (red arrow) connecting the interior of VPs to the cytoplasm. Scale bar: 100 nm. (Adapted from [301])

Viral RNA replication occurs in close association with virus-induced intracellular membrane structures, the so-called replication organelles (ROs), which consist of multiple invaginated vesicles that are found within the lumen of the ER^{298–301} (Figure 10). Flavivirus ROs have a diameter of approximately 90 nm and are connected to the cytoplasmic space via a pore which measures approximately 11 nm in diameter. This pore allows the continuous exchange of materials including proteins, nucleic acids, nucleotides, and other molecules³⁰¹. ROs form enclosed environments that serve three functions: (i) concentration of enzymes and substrates, enhancing viral replication/transcription; (ii) spatial separation of replication, translation, and virus assembly; and (iii) protection of the viral genome from degradation and recognition by host cellular immune responses^{302–304}. Although their morphology and architecture have been extensively studied and are well described, the molecular mechanisms and required host and viral factors remain largely elusive. To date, several non-structural proteins including NS1^{196,305–307}, NS4A^{215,308–314}, and NS4B^{315–317} have been described to function in RO formation in the context of virus infection and replicon transfected cells. However, to specifically evaluate their role in the biogenesis of ROs has been challenging, as disturbance of their function cause replication defects. Even though single viral protein expression has given insights into membrane-bending activity^{310,318}, such approaches failed to phenocopy RO formation. Furthermore, apart from the viral NS proteins, host cellular factors including proteins and lipids have also been identified to play

1. Introduction

crucial roles during the assembly of ROs. In this context several ER resident proteins such as reticulon (RTN), atlastins, and BPI fold containing family N member 3 (BPIFB3) were found to promote the formation of ROs. Previous studies have shown that RTN is recruited to viral replication sites³¹⁹, atlastins affect the morphology³²⁰, and BRIFB3 is involved in ER morphology contributing to RO biogenesis³²¹. Additionally, the silencing of these ER proteins has resulted in attenuation of virus replication. Moreover, lipidomic analyses of flavivirus-infected cells have shown that global lipid landscapes are significantly changed, indicating their involvement in RO biogenesis^{322,323}. To this end, however, no direct interaction between lipids and NS proteins in the RO has been demonstrated; therefore, further investigation is needed to understand the interplay between viral proteins and lipids and their contribution to RO formation.

1.2.4.4. ZIKV assembly, maturation, and egress

For completing the infectious replication cycle, new virions are produced and released into the extracellular space, where they disseminate to infect new naïve cells, and thus starting a new round of infectious replication cycle. Virus assembly occurs in adjacent sites to ROs (Figure 9f) and is dependent on viral proteins such as C, prM, E, NS2A, and NS2B/3²⁰⁵. A study by Zhang and colleagues has provided first evidence for the molecular mechanism by showing that NS2A recruits the vRNA and the NS2B/3 protease to virus assembly sites. Upon processing of the polyprotein C-prM-E, mature C proteins bind to vRNA via the positively charged helix $\alpha 4$, forming the nucleocapsid. Nucleocapsid is thereafter enveloped by the lipid bilayer containing the prM and E proteins²⁰⁵. How NC is recruited and incorporated into virus particles, however, remains to be determined.

Once new immature virions are formed, they are secreted via the secretory pathway³²⁴. While moving through the *trans*-Golgi network virus immature particles are glycosylated and subsequently processed by trimming of the glycans³²⁵. In addition, as immature particles encounter an acidic environment in the *trans*-Golgi, conformational changes of the trimeric prM-E spike are triggered, unveiling the furin cleavage site at the pr-M junction site, causing maturation cleavage (Figure 9g). Once cleaved, pr peptides remain associated with E proteins, thus protecting virions from premature fusion. Upon release into the extracellular matrix, pr peptides dissociate due to the neutral pH environment, releasing mature infectious particles¹⁸² (Figure 9h).

1. Introduction

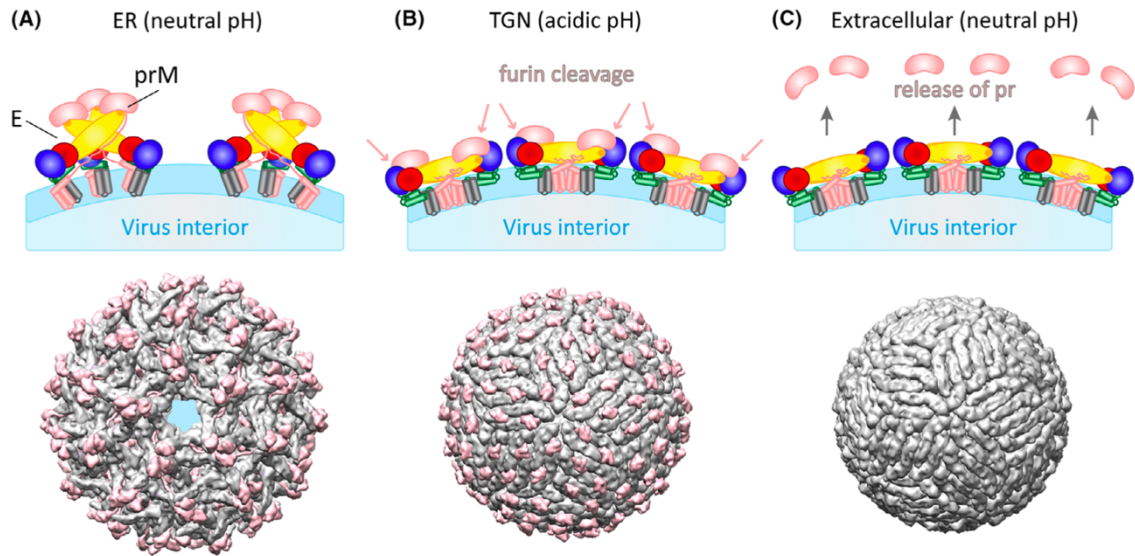


Figure 11. Structural changes of the ZIKV particle during maturation.

Schematic representations (upper panel) and cryo-EM reconstructions (lower panel) showing the rearrangements of viral surface proteins while traversing through the *trans*-Golgi network. **(A)** At the ER membrane immature virions are formed with trimeric prM/E spike-like protrusions on the surface. **(B)** In the *trans*-Golgi, changes in pH coincides with conformational changes of the structural proteins exposing the furin cleavage site. Furin cleavage forms smooth-surface particles. The soluble pr peptide remains associated. **(C)** Mature infectious virions are released, upon which the neutral pH causes the dissociation of pr from particles. (Figure taken from [328])

1.2.4.5. Zika virus particle structure

Although the precise mechanism of how ZIKV particles are formed is not yet fully understood, cryo-electron microscopy (EM) studies have provided detailed insight into the structure of immature and mature ZIKV particles^{167,179,326–328} (Figure 11). Here it was shown that immature virus particles have a spiky appearance with a diameter of 600Å, whereas mature virus particles are smooth with a diameter of approximately 460 nm^{179,327}. Prasad and colleagues found that within the inner shell in immature ZIKV particles, capsid proteins are associated with the inner viral membrane in proximity to the transmembrane domains of E and M proteins. This finding suggests that an interaction between these three proteins exists which is required for virus assembly¹⁷⁹. The outer proteinaceous shell of virus particles is composed of 60 copies consisting of prM-E trimeric complexes, which initially form spiky protrusions. Upon maturation in the *trans*-Golgi, E proteins undergo conformational changes forming antiparallel dimers which almost entirely cover the lipid bilayer³²⁷. In the context of virus maturation, cryo-electron microscopy analyses have identified a pocket-like gap which is located between the helices of the transmembrane domains^{326,327}.

1. Introduction

Examination of this pocket revealed incorporation of lipids which are presumed to fix and stabilize E proteins with respect to their distance and position. Furthermore, a guided mutagenesis study has shown that the lipid pocket is critical for the ZIKV life cycle³²⁶.

1.3. Flaviviruses infection and the host lipid metabolism

Within the last several years, research has provided detailed insights into the changes of the host lipidomic profile upon flavivirus infection^{322,323,329,330}. Today, it is well established that flaviviruses share an intimate union with host cellular lipids, as they play essential roles during each step of the viral replication cycle (from attachment and fusion to replication and virus assembly) (Figure 12). So far, virus-lipid interactions have been reported to occur in two ways: exploitation and reprogramming. While viruses utilize pre-existing host cellular lipids to mediate virus entry and trafficking^{331,332}, both extensive reprogramming of lipid metabolic pathways and redistribution of lipids occur during later stages, facilitating viral replication and virus assembly³³³.

1.3.1. Lipidomic profiles of flavivirus infected cells

The best evidence uncovering the effects of flavivirus infection on host cellular lipid metabolism derives from comparative lipidomic analyses via high-resolution mass spectrometry of flavivirus- and mock-infected cells^{322,323,329,330}. In this context, global lipidomic profiles have been established for the vector and mammalian host. Lipidomic analyses of DENV- and ZIKV-infected mosquito cells have revealed that 15% of the detected lipid metabolites³²⁹ and a total of 13 lipid species³²³, respectively, were significantly altered when compared to mock-infected mosquito cells. Interestingly, detailed analysis of DENV-infected mosquito cells revealed that 85% of the detected lipid metabolites were present in membrane fractions associated with viral ROs³²⁹. In addition, lipidomic profile analyses of mammalian cells infected with WNV and ZIKV have shown that intracellular levels of various lipid species were either significantly enriched or depleted^{322,330}. Taken together, these findings demonstrate a strong connection between flaviviruses and the host lipid metabolism in both the vector and mammalian host.

1. Introduction

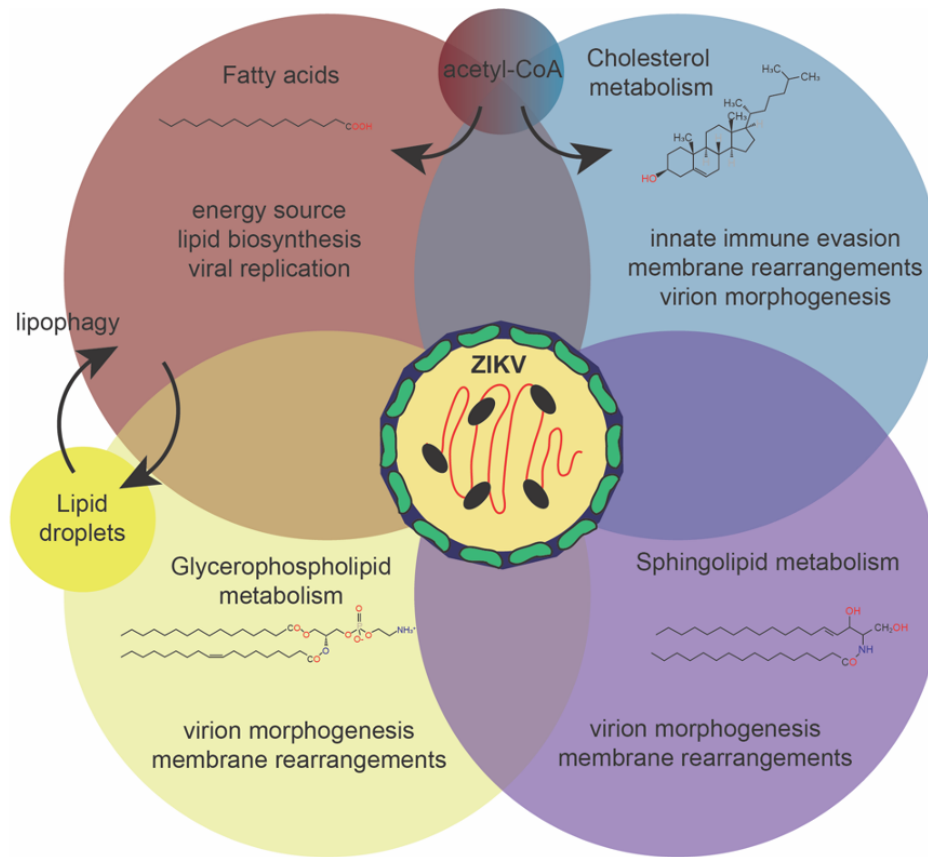


Figure 12. ZIKV and its interaction with the lipid metabolism.

ZIKV, like other flaviviruses, shares an intimate relationship with cholesterol, fatty acids, glycerophospholipids, lipid droplets, and sphingolipids to promote its infectious replication cycle. Only one typical metabolite from each lipid class is depicted (Fatty acids: palmitic acid; Cholesterol metabolism: cholesterol; Sphingolipid metabolism: ceramide; glycerophospholipid metabolism: phosphatidylethanolamine). (Adapted from [359])

Comparative analyses of the lipidomic profiles from mosquito and mammalian cells have revealed that several lipids are shared and similarly dysregulated within both hosts, including glycerophospholipids (e.g., phosphatidylcholine and phosphatidylethanolamine) and sphingolipids (e.g., ceramide and sphingomyelin)^{322,323,329,330}. Interestingly, analyses of individual lipid species within a lipid class and the effects of flavivirus infection on lipid classes over time have revealed that not all species within a lipid class were identically altered, and changes in levels varied over time, suggesting a fine-tuned rearrangement and dynamic interaction between the virus and the host lipid metabolism^{322,323,329,330}. Specifically, alterations regarding sphingolipids (mainly ceramides and sphingomyelin) occur at earlier time points, suggesting their contribution to the establishment of viral ROs due to their ability to induce membrane curvature³³⁴. Although ceramides and sphingomyelin can be interconverted by cellular enzymes, lipidomic analyses suggest that elevated levels are actually

1. Introduction

due to *de novo* synthesis instead of degradation, as both classes are significantly enriched^{329,330}. Although an increase in intracellular levels of cholesterol were observed in DENV, WNV, and ZIKV-infected cells^{322,333,335}, detailed mechanistic insights still remain largely unknown. However, lipidomic profile analysis of ZIKV-infected cells revealed that cholesterol is significantly enriched at later time points (48 hours post infection (h.p.i.)), suggesting a role during virus assembly and egress³²².

1.3.2. *De novo* lipid synthesis and flavivirus infection

As previously mentioned, flavivirus infection induces significant alterations with respect to the global lipid landscape of host cells. In fact, it was shown that flavivirus infection relies on lipogenesis^{333,335}, as interference with the lipid metabolism significantly inhibited flavivirus infection. For instance, inhibition of enzymes involved in the fatty acid synthesis, such as the fatty acid synthase and acetyl-CoA carboxylase, and the cholesterol biosynthesis, such as the mevalonate diphospho decarboxylase, squalene synthase, and hydroxyl methyl glutaryl-CoA reductase (HMG-CoA reductase), or 7-dehydrocholesterol reductase, significantly impaired flavivirus multiplication^{333,336–338}. Moreover, sphingolipid biogenesis was found to be a requisite process for WNV and ZIKV, as inhibition of the sphingomyelin synthases, the serine palmitoyl transferase, and ceramide synthase greatly reduced viral replication and production of infectious viruses^{322,330,339}. Taken together, the findings that inhibition of *de novo* lipid biosynthesis greatly impairs flavivirus infection suggests that elevation of intracellular levels of various lipid species is not a mere consequence of infection but also represents a necessity for efficient viral multiplication.

1.3.3. Specific roles of lipids during the viral replication cycle

1.3.3.1. Lipids, virus entry, and membrane fusion

To date, several lipids including cholesteryl esters, negatively charged phospholipids, and gangliosides^{340–343} were identified to be involved in virus entry and intracellular trafficking. In this respect, virus attachment factors are enriched in lipid rafts, which are cholesterol-enriched lipid ordered membrane domains^{344–347}. Following uptake, flaviviruses must escape the endosome which occurs via a fusion event involving both the viral lipid bilayer and the endosomal membrane. Previous research has highlighted that this step in the viral

1. Introduction

life cycle is cholesterol dependent, as it triggers fusion activity of DENV, TBEV, WNV, and ZIKV^{285,348–350}. As viruses rely on cholesterol to promote infection, it is of no surprise that alterations of the cholesterol content within host cellular membranes using the cholesterol solubilizing drug methyl- β -cyclodextrin (M β CD) reduces virus infection^{285,345,351}. Furthermore, host cells have developed antiviral strategies based on cholesterol interaction or resemblance. Studies have shown that interferon-inducible transmembrane proteins^{352–354} as well as 25-hydroxycholesterol³⁵⁵ inhibit virus entry. Upon fusion, the nucleocapsid is released into the cytoplasm which requires late endosomal specific lipids such as bis(monoacylglycerol)phosphate³⁵⁶. Taken together, it demonstrates that the lipid composition of host cellular target membranes determines flavivirus fusion and release of the nucleocapsid. However, the specific role of cholesterol during viral entry and membrane fusion remains an open question.

1.3.3.2. Lipids and virus replication

It is well established that the flavivirus replication cycle is intimately associated with host cellular membranes. Upon infection the ER is enlarged and undergoes extensive rearrangements giving rise to membrane structures known as vesicle packets (VPs)^{298,299,301}. Although the biosynthesis of glycerophospholipids, sterols, and sphingolipids occurs in the ER, the content of these lipids within the ER membrane is low as they are rapidly transported to other cellular membranes. In this context, however, flavivirus infection coincides with changes in the host cellular lipidomic profile, showing a specific enrichment of fatty acids, phospholipids, sphingolipids, and cholesterol in membranes associated with viral ROs^{329,333,336,357–359}. Although the contribution of individual lipids to viral replication is still unclear, there is a suggestion that various lipids are required for negative membrane curvature, a pre-requisite for forming VPs³⁶⁰.

1.3.3.3. Lipids, virus assembly, and the lipid envelope

Given the findings within the last couple of years, analyzing virus particles using cryo-electron tomography and lipidomic analyses have demonstrated that lipids represent the most abundant component with an estimate of ~ 8000 molecules³⁶¹ (Table 2). While cryo-electron tomography identified a lipid-pocket between the transmembrane domain helices, which is occupied by phosphatidylethanolamine^{326,327}, analysis of the lipid composition of

1. Introduction

WNV virions has shown an enrichment of sphingolipids (sphingomyelin)³³⁰. Because sphingolipid content in membranes was found to determine biophysical properties such as membrane curvature^{360,362}, it is suggested that sphingolipids determine virion architecture³³⁰. And while the conversion of sphingomyelin and ceramide was found to contribute to vectorial budding of vesicles^{363,364}, it is proposed that virion budding follows a similar mechanism. Apart from structural and lipidomic analysis, functional studies have indicated an incorporation of cholesterol³⁴⁸, phosphatidylserine³⁶⁵, and phosphatidylethanolamine³⁶⁶. With regards to cholesterol, treatment with the lipophilic agent lovastatin significantly reduced dengue and Zika extracellular infectious viral titers via decreasing virion assembly^{337,338}. However, understanding the contribution of cholesterol to virus particle assembly and envelope organization remains as an important milestone to be determined.

Table 2. Composition of a mature flavivirus particle. (Adapted from [359])

Component	Estimated number of molecules per virion
Genomic viral RNA	1
Viral structural proteins ^{173,190}	>360 (180 copies of E, 180 copies of M, multiple copies of C)
Sugar moieties of E proteins ³²⁵	Variable
Lipids within lipid bilayer ³⁶¹	~8000

2. AIMS OF THIS STUDY

2.1. Generation of a replication-independent system phenocopying ZIKV replication organelles

It is well established that the infectious replication cycle of ZIKV shares an intimate union with the endomembranous network of its host cell. In this context, it was shown that the ER undergoes distinct rearrangements and extensive expansion, resulting in the formation of vesicles, which are invaginations into the lumen of the ER and are also known as the viral replication organelle. Although the morphology and architecture of the ZIKV ROs have been well described, underlying molecular mechanisms, and required host and viral factors remain as an important milestone to be determined. The first part of my PhD thesis aimed to generate a replication-independent system to study the mechanisms and factors required for RO biogenesis. Initially, the focus was set on the contribution of viral RNA secondary structures within the 5' and 3'UTR in RO formation by consecutive deletion mutations. For authentic 3'UTRs the system was optimized by insertion of the hepatitis D virus (HDV) ribozyme downstream of the ZIKV sequence. Last, to facilitate correlative light and electron microscopy to specifically analyze transfected cells a reporter system was generated by insertion of a fluorescent protein along with a 2A peptide upstream of the viral polyprotein.

2.2. Dissecting the mode of action of the antiviral compound SBI-0090799

As of today, no specific medicine, antiviral drug or vaccine are available to treat or prevent ZIKV infection and its associated disease. As Zika continues to silently spread and given the unpredictability of new geographic epidemic outbreaks, encourages the ongoing search for new antiviral compounds. In this context, the second part of my PhD thesis was aiming to analyze the mode of action of a novel antiviral compound, referred to as SBI-0090799. This drug was identified during a screen of a novel compound library at the Sanford Burnham Prebys Medical Discovery Institute in California, USA. Given previous results by Riva and colleagues, SBI-0090799 was found to exhibit potent inhibitory effects when provided

prior, during or shortly after virus infection, suggesting a mode of action during virus translation or formation of Zika ROs. Given the system, which I have generated within my first PhD project, I investigated the impact of SBI-0090799 on viral polyprotein processing and protein abundance, subcellular localization of viral proteins, and the biogenesis of the ZIKV ROs via western blotting, immunofluorescence microscopy, and transmission electron microscopy, respectively.

2.3. The importance of viral protein-cholesterol interactions in the ZIKV replication cycle

Within the last years “omics” studies have provided new insights into how ZIKV modulates its host cells. Although it is well established that flaviviruses interact with host cellular lipids at any step of their replication cycle, yet direct virus protein-lipid interactions have been poorly studied. Hence, my third PhD project aimed to unravel a direct viral protein-lipid interaction and its contribution to the viral replication cycle. Initially, the focus was set on identifying cholesterol binding viral proteins by performing chemo-proteomics in ZIKV infected cells using a bifunctional chemically modified cholesterol probe. Thereafter, cholesterol-binding viral proteins were bioinformatically analyzed with respect to determine potential cholesterol amino acid recognition consensus sequences (CARC/CRAC motifs), which were functionally characterized via site-directed mutagenesis alongside with cholesterol binding assays. The importance of the interaction between viral proteins and cholesterol was assessed via kinetic viral replication studies using WT and mutated ZIKV making use of the reverse genetics system of Zika. Last, *in vitro* results were confirmed by collaborators who performed atomistic molecular dynamics simulations.

3. MATERIALS AND METHODS

3.1. Materials

3.1.1. Chemicals and Expendables

Table 3. Overview of expendables.

REAGENT or RESOURCE	SOURCE
Agarose (ultrapure)	Invitrogen
Agarose	VWR Life Science
Ammonium persulfate	VWR Life Science
Ampicillin	Roche
Anti-reverse cap analog (ARCA)	New England Biolabs
Beta-Mercaptoethanol	Carl Roth GmbH
Benzonase	Merck Millipore
Blasticidin	ThermoFisher Scientific
Bovine serum albumin (BSA)	Sigma Aldrich
Bromophenol Blue	Waldeck
Cacodylate acid sodium trihydrate (CaCo)	Serva
Calcium chloride (CaCl ₂)	Sigma-Aldrich
Calf Intestinal Phosphatase (CIP)	New England Biolabs
Carbenicillin Disodium Salt	Carl Roth GmbH
Carboxymethylcellulose	Sigma-Aldrich (Merck)
Chloroform	Sigma-Aldrich
Coelenterazine	PJK
cOmplete, EDTA free, protease inhibitor	Roche
Copper (II) sulfate pentahydrate (CuSO ₄)	Sigma Aldrich
DBA hardener	Carl Roth GmbH
Delipidated (DL) FBS	C-C-Pro
Dimethyl sulfoxide (DMSO)	Carl Roth GmbH
DNA loading dye (6x)	ThermoFisher Scientific
Dulbecco's Modified Eagle Medium (DMEM)	Gibco (ThermoFisher Scientific)
DMP 30	Carl Roth GmbH
Dithiothreitol (DTT)	Roche
Ethanol absolute	Sigma-Aldrich
Ethylenediaminetetraacetic acid (EDTA)	Sigma-Aldrich
Fetal Bovine Serum (FBS)	Gibco (ThermoFisher Scientific)
Fluoromount-G (DAPI)	Invitrogen
Formaldehyde	Carl Roth GmbH
Formvar	Electron Microscopy Sciences
Gene ruler 1kb DNA ladder	ThermoFisher Scientific
Glutaraldehyde EM grade	Electron Microscopy Sciences
Glycerol	Honeywell
Glycidyl ether	Carl Roth
Glycine	Labochem International
GlycoBlue Coprecipitant	Invitrogen (ThermoFisher Scientific)

3. Materials and Methods

HEPES buffer solution (1 M)	ThermoFisher Scientific
HPLC water	Sigma-Aldrich
Hydrogen peroxide (H ₂ O ₂)	Merck Millipore
Isopropanol	Honeywell
iTaq™ Universal SYBR® Green Supermix	Bio-Rad
L(+)-Ascorbic Acid	PanReac AppliChem
LB Medium/Agar	Carl Roth GmbH
Lead citrate	Electron Microscopy Sciences
Leibovitz's L-15 medium	Gibco (ThermoFisher Scientific)
lovastatin	Sigma-Aldrich (Merck)
Magnesium chloride (MgCl ₂)	Sigma Life Science
Methanol	Honeywell
Methyl-β-cyclodextrin	Sigma-Aldrich
MG132 proteasome inhibitor	AdipoGen Life Sciences
Minimum Essential Medium (MEM)	Gibco (ThermoFisher Scientific)
Milk powder	Carl Roth GmbH
Midori Green Advanced/direct	Nippon Genetics
MirusIT-LT1 transfection reagent	Mirus
MNA	Carl Roth GmbH
Non-essential amino acids	Gibco (ThermoFisher Scientific)
NP-40	AppliChem
NP LDS Sample Buffer 4X	ThermoFisher Scientific
OptiMEM Reduces Serum Medium	Gibco (ThermoFisher Scientific)
Osmium tetroxide	Electron microscopy science
Paraformaldehyde 16% EM grade	Science Services
Paraformaldehyde	Sigma-Aldrich
Penicillin-Streptomycin (100x)	Gibco (ThermoFisher Scientific)
PerfeCTa qPCR ToughMix	Quantabio
Phenol	Sigma-Aldrich
Photo-reactive clickable trans-sterol probe	Sigma-Aldrich
PhusionFlash High Fidelity master mix	ThermoFisher Scientific
Polybrene	Sigma Aldrich
Polyethylenimine (PEI)	Polyplus Transfection
Potassium chloride (KCl)	Sigma-Aldrich
Potassium hydroxide (KOH)	Honeywell
Pre-stained protein marker	GeneTex
Protease inhibitor cocktail	Sigma-Aldrich
Protein Assay Dye Reagent Concentrate	Bio-Rad
Puromycin	Sigma-Aldrich
PVDF membrane (0.2 μm pore size)	Cytiva
Restriction enzymes	New England Biolabs
RNasin Ribonuclease inhibitor	Promega
RNase A/T1 Mix	Thermo Scientific
Rotiphorese NF-Acrylamid/Bis-Solution 30	Carl Roth GmbH
rNTPs	Roche
RQ DNase I	Promega
Sodium chloride (NaCl)	Bernd Kraft
Sodium dodecyl sulfate (SDS)	Serva
Sucrose	Carl Roth GmbH

3. Materials and Methods

T4 Ligase	Fermentas
tris[(1-benzyl-1H-1,2,3-triazol-4-yl)methyl]amine (TBTA)	Carl Roth GmbH
TEMED	Applichem
TRIS base	Carl Roth GmbH
Triton X-100	Merck Millipore
TRIzol	ThermoFisher Scientific
Trypsin-EDTA	Gibco (ThermoFisher Scientific)
Tryptose B Phosphate (TBP)	Gibco (ThermoFisher Scientific)
Tween-20	Carl Roth GmbH
Uranyl acetate dihydrate	Serva
Zeocin	ThermoFisher Scientific

Table 4. Primary antibodies used in this study.

Target	Specificity	Source	Identifier
DENV NS3	Rabbit polyclonal	Homemade	Miller et al, 2006
ZIKV C	Rabbit polyclonal	GeneTex	GTX133317
ZIKV prM	Rabbit polyclonal	GeneTex	GTX133314
ZIKV E	Rabbit polyclonal	GeneTex	GTX133584
panFlavi E	Mouse monoclonal	Homemade	ATCC (HB-112)
ZIKV NS1	Mouse monoclonal	GeneTex	GTX634158
ZIKV NS2B	Rabbit polyclonal	GeneTex	GTX133318
ZIKV NS3	Rabbit polyclonal	GeneTex	GTX133320
ZIKV NS4A	Rabbit polyclonal	GeneTex	GTX133704
ZIKV NS4B	Rabbit polyclonal	GeneTex	GTX133321
ZIKV NS5	Rabbit polyclonal	GeneTex	GTX133327
HA	Rabbit polyclonal	Sigma Aldrich	PA1-985
RTN-3	Mouse monoclonal	Santa Cruz	Sc-374599
GAPDH	Mouse monoclonal	Santa Cruz	Sc-47724

Table 5. Secondary antibodies used in this study.

Antibody	Specificity	Source	Identifier
Alexa Fluor 488	Donkey anti-mouse	ThermoFisher	A-21202
Alexa Fluor 568	Donkey anti-rabbit	ThermoFisher	A-10042
Alexa Fluor 647	Donkey anti-mouse	ThermoFisher	A-31571
HRP conjugated	Goat anti-mouse	Sigma-Aldrich	A-4416
HRP conjugated	Goat anti-rabbit	Sigma-Aldrich	A-6154

Table 6. Probes, resins, and beads used in this study.

Agent	Specificity	Source	Identifier
Anti-HA agarose beads	Mouse, monoclonal	Sigma-Aldrich	A2095
Bodipy 493/503	Lipid droplets	Invitrogen	D3922
DAPI	DNA	Invitrogen	D3571
NeutrAvidin Agarose beads	Biotin specific	Thermo Scientific	29200

3. Materials and Methods

Table 7. Commercial kits and systems.

Name	Manufacturer
Amplex Red Cholesterol Assay kit	Invitrogen
CellTiter-Glo® 2.0 Assay	Promega
High-Capacity cDNA Reverse Transcription	Applied Biosystems
Mini Protean Tetra system	Bio-Rad
NucleoSpin Gel and PCR Clean-up	Macherey-Nagel
NucleoBond Plasmid	Macherey-Nagel
NucleoBond PC 500	Macherey-Nagel
NucleoSpin RNA II	Macherey-Nagel
SuperScript III RT	ThermoFisher Scientific
Western Lightning Plus-ECL	Perkin Elmer

3.1.2. Recipes for buffers and solutions

Table 8. Recipes for buffers used in this study.

Buffer/Solution	Composition
3 M Sodium Acetate (pH 4.5)	3 M Sodium Acetate, pH adjusted to 4.5 with Glacial Acetic acid
4% Paraformaldehyde (PFA)	4 g paraformaldehyde dissolved stirring in 60°C in 100 mL PBS
Acetatos (TCID ₅₀ detection substrate solution II)	37.5 mM sodium acetate, 15 mM acetic acid, storage 4°C
Ampicillin (1000x)	100 mg/mL in double distilled water, filter sterilized
Binding buffer	DMEM containing 20 mM HEPES, 0.2% BSA, 1 mM CaCl ₂ , 1 mM MgCl ₂ , adjusted to pH 7.4
Carbazol (TCID ₅₀ detection substrate solution I)	0.32% (w/v) carbazole dissolved in N,N-dimethylformamide, storage at 4°C in the dark
Carbenicillin (1000x)	100 mg/mL in double distilled water, filter sterilized
Coelenterazine	0.043% (w/v) coelenterazine dissolved in methanol, stored at -80°C
Cryomedium	90% FBS (v/v), 10% DMSO (v/v)
Cytomix for transfection via electroporation	120 mM KCl, 0.15 mM CaCl ₂ , 100 mM Potassium phosphate buffer (pH 7.6), 25 mM HEPES, 2 mM EGTA, 5 mM MgCl ₂ , adjust pH to 7.6 using KOH, freshly add 2 mM ATP, 5 mM Glutathione
DDM lysis buffer for co-immunoprecipitation	0.5% (w/v) DDM, 150 mM NaCl, 20 mM Tris-HCl (pH 6.9), 1 tablet complete protease inhibitor (in 50 mL)
EM fixative buffer	2.5% glutaraldehyde, 1% PFA, 2% sucrose in 50 mM sodium cacodylate buffer (50 mM cacodylate, 50 mM KCl, 2.6 mM CaCl ₂ , 2.6 mM MgCl ₂ , adjusted to pH 7.4)
Immunofluorescence blocking buffer	1% skim milk in PBS

3. Materials and Methods

Laemmli (6x)	600 mM Tris-HCl (pH 6.9), 15 mM EDTA, 0.1% (w/v) bromophenol blue, 10% SDS, 7.5% β -mercaptoethanol, 30% (v/v) glycerol
LB Agar	10 g Bacto-Trypton, 5 g Yeast extract, 2.5 g NaCl, 20 g Agar in 1 ml deionized water, autoclaved
NTE-buffer	100 mM NaCl, 10 mM Tris (pH 7.4), and 1 mM EDTA
Phosphate buffer saline (10X) (PBS)	80 mM Di-Sodium Hydrogen Phosphate, 20 mM Monosodium Phosphate, 1.4 M NaCl
Photoaffinity labeling lysis buffer	1X PBS, 1% (v/v) Triton X-100, 0.1% (w/v) SDS, and 1:500 protease inhibitor cocktail
Plaquing medium	1.5% (w/v) carboxymethylcellulose in 450 mL MEM medium, autoclaved,
<i>Renilla</i> luciferase assay buffer	25 mM glycine-glycine (pH 7.8), 15 mM Potassium phosphate buffer (pH 7.8), 15 mM MgSO ₄ , 4 mM EGTA, and 1.42 μ M coelenterazine
<i>Renilla</i> luciferase lysis buffer	0.1% (v/v) Triton-X-100, 10% (v/v) glycerol, 25 mM glycine-glycine (pH 7.8), 15 mM MgSO ₄ , 4 mM EGTA, stored at 4°C, freshly add 1 mM DTT
Resolving buffer (western blot)	1.5 M Tris-HCl, pH 8.8, 0.4% (w/v) SDS
RIPA lysis buffer	50 mM Tris-HCl (pH 6.9), 150 mM NaCl, 1% (w/v) Sodium deoxycholate, 1% (v/v) Nonident P-40, 0.1% (w/v) SDS
RRL buffer (5X)	400 mM HEPES (pH 7.5), 60 mM MgCl ₂ , 10 mM spermidine, 200 μ M DTT
Stacking buffer (western blot)	1 M Tris-HCl, pH 6.8., 0.8% (w/v) SDS
Sucrose cushion TNE buffer	12 mM Tris-HCl (pH 8.0), 120 mM NaCl, 2 mM EDTA, and 20% sucrose
TAE (50X) (TAE)	2 M Tris, 2 M Acetic acid, and 50 mM EDTA, pH 8.3
TGS (10X)	250 mM Tris (pH 8.6), 1920 mM glycine, 1% (w/v) SDS
Western blot blocking buffer	5% skim milk in PBS
Western blot transfer buffer	20% (v/v) methanol, 150 mM Glycine, 20 mM Tris (pH 8.0)
Western blot wash buffer	1X PBS, 0.1% (w/v) Tween20

3.1.3. Technical Equipment and Software

Table 9. Overview of centrifuges, PCR cycler and other technical appliances.

Name	Manufacturer
Agarose gel documentation table	INTAS
Automated Cell Counter TC20	Bio-Rad
Centrifuge (Multifuge 3s-e)	Heraeus
CFX PCR Cycler	Bio-Rad
ECL Chemocam Imager	INTAS
Fridges/Freezers	Liebherr
Fluorescent microscope Eclipse Ti	Nikon

3. Materials and Methods

Gene Pulser II Electroporation System	Bio-Rad
Incubator (insect cells)	Memmert
Incubator (mammalian cells; C200)	Labotec
Microscope DMIL LED	Leica
Microwave	Bosch
Minishaker	IKA MS2
NanoDrop	ThermoScientific
PCR cycler (Flex Cycler ²)	Analytik Jena
pH meter	inoLab
Plate reader (Mithras LB940)	Berthold Technologies
Scale	Sartorius Entris
Sorvall Lynx 6000	ThermoScientific
Spectrophotometer (Ultraspec 2100)	Amersham Biosciences
Tabletop centrifuges	Eppendorf
Thermomixer	Eppendorf
Tube luminometer	Berthold Lumat
Ultracentrifuges (Optima XE-90/LE-80k)	Beckman Coulter
UVP crosslinker	Analytik Jena

Table 10. Software.

Name	Developer
Adobe Illustrator	Adobe
A plasmid editor (Ape)	M. Wayne Davis
CFX Maestro V2	Bio-Rad
ChemoStar	INTAS
GelDoc	INTAS
Image composite editor	Microsoft
ICE Berthold	Berthold Technologies
LabImage 1D	INTAS
MikroWin 2000	Berthold Technologies
Nikon NIS Elements Viewer (V 5.30.06)	Nikon
Prism 8	GraphPad (La Jolla, CA, USA)
Primer3plus	Untergasser et al, 2012 ³⁶⁷

3.1.4. Oligonucleotides

All cloning and sequencing primers were designed using the tool ‘A plasmid editor’ (Ape) (by M. Wayne Davis). Primer pairs and probes used for one-step and two-step qRT-PCR were designed using the online software Primer3Plus (<https://www.bioinformatics.nl/cgi-bin/primer3plus/primer3plus.cgi>). Primers and probes were purchased from Sigma Aldrich/Merck. A complete list of primers and probes can be found in the Supplementary Table 3.

3. Materials and Methods

3.1.5. Bacteria and Cell Lines

The bacterial strain *E. coli* DH5 α (Invitrogen) was used for transformation during cloning. For amplification of plasmids the bacterial strain *E. coli* HB101 (Promega) was used. All *in vivo* experiments were performed using the cell lines listed below (Table 11).

Table 11. Overview of cell lines used in this study.

Name	Type
Aag2	Adherent mosquito embryonic cell line from <i>Aedes aegypti</i> , obtained from A. Kohl, Glasgow, UK
A549	Adherent adenocarcinomic human alveolar basal epithelial cell line, obtained at University of Heidelberg, "Campus"
C6/36	Adherent larval mosquito cell line from <i>Aedes albopictus</i> , obtained from ECACC 89051705
HB-112	Hybridoma Mouse b lymphocytes, obtained from ATCC D1-4G2-4-15, production of panFlavi Envelope antibody
HEK 293T	Adherent human embryonic kidney cell line, obtained from Birke Bartosch, Ens Lyon, France
Huh7-Lunet naïve	Adherent human hepatoma cell line, HCV cured
Huh7-Lunet T7 zeocin	Adherent human hepatoma cell line, HCV cured, stably expressing the T7 polymerase
Huh7-Lunet ZIKV RC	Adherent human hepatoma cell line, HCV cured, stably expressing a ZIKV reporter construct
JEG3	Adherent human placenta epithelial cell line, obtained from Udo Markert, University of Jena, Germany
VeroE6	Adherent African green monkey kidney cell line, obtained from Progen

3.2. Methods

3.2.1. Cell culture

3.2.1.1. Cell culture of mammalian and mosquito cells

In this study several different mammalian cell lines were used: (i) the human embryonic kidney cell line HEK 293T³⁶⁸, (ii) the human hepatoma cell line Huh7-Lunet naïve^{369,370}, (iii) the human hepatoma cell line Huh7-Lunet T7 cell line³⁷¹, (iv) the African green monkey kidney cell line VeroE6³⁷², (v) the lung carcinoma cell line A549³⁷³, and (vi) the placental JEG3 cell line. HEK 293T, Huh7-Lunet naïve, Huh7-Lunet T7, VeroE6, and A549 cells were cultured under normal conditions in polystyrene culture dishes (Falcon) and maintained in DMEM supplemented with 10% FBS, 1% non-essential amino acids, 100 U/mL penicillin, and 100 μ g/mL streptomycin. Cell lines were kept below 90% confluency in an

3. Materials and Methods

incubator (37°C, 5% CO₂), and were split as required. To maintain a stable expression of the T7 polymerase in Huh7-Lunet T7 cells the antibiotic zeocin was added to culture media at a final concentration of 5 µg/mL. The choriocarcinoma-derived human placental JEG-3 cell line was cultured under normal conditions in polystyrene culture dishes and maintained in Ham's F-12 Nutrient Mix supplemented with 10% FBS, 100 U/mL penicillin, and 100 µg/mL streptomycin. All cells were counted prior to seeding for experiments using the automated cell counter system from Bio-Rad (TC20).

To produce the panFlavi envelope antibody, the commercially available mouse hybridoma b lymphocytes were used (ATCC HB-112). Cells were cultured under normal conditions in 75 cm² cell culture flasks and maintained in Hybri-Care Medium supplemented with 10% FBS and 1.5 g/L sodium bicarbonate. Cells were kept at a density of 5x10⁵ cells/mL. On day 7 and 8 post thawing, medium was collected and sterile filtered using 0.2 µm Filter for the collection of freshly produced antibodies. Antibody solutions were tested by immunofluorescence-based visualization of ZIKV infected cells (see section 3.2.6.1.) and stored at 4°C.

The mosquito cell lines Aag2^{374,375} (obtained from A. Kohl, Glasgow University, United Kingdom) and C6/36³⁷⁶ were grown at 28°C (without CO₂), in 75 cm² cell culture flasks. Aag2 were maintained in Leibovitz's L-15 medium supplemented with 10% FBS, 10% TBP, 100 U/mL penicillin and 100 µg/mL streptomycin. C6/36 were maintained in Leibovitz's L-15 medium supplemented with 10% FBS, 100 U/mL penicillin and 100 µg/mL streptomycin. To recover Aag2 cells from thawing 20% FBS were initially used. C6/36 cells were used to produce stocks of ZIKV strain H/PF/2013.

3.2.1.2. Transient transfection of RNA and DNA

Electroporation of cells

In this study, Huh7-Lunet naïve, Huh7-Lunet T7, and VeroE6 cells were transfected with infectious ZIKV RNA, either encoding the sub-genomic replicon (sgR2A H/PF/2013) or the full-length infectious virus cassette (synZIKV H/PF/2013 and synZIKV-R2A H/PF/2013)³⁷⁷, by electroporation. Sub-confluent (80-90% confluency) cells were detached by trypsinization, centrifuged at 700xg for 5 minutes at room temperature, and washed with sterile PBS. Cells were counted using the automated cell counter from Bio-Rad. Cells were pelleted by centrifugation and resuspended in cytomix buffer to a final concentration of 1x10⁷ cells/mL or 1.5x10⁷ cells/mL for Huh7-Lunet or VeroE6 cells,

3. Materials and Methods

respectively. For electroporation, 4×10^6 or 6×10^6 Huh7-Lunet or VeroE6 cells, respectively, were mixed with 10 μg of *in vitro* transcribed (IVT) ZIKV RNA and transferred into an electroporation cuvette with a 0.4 cm gap. Using the Gene Pulser II system, a pulse of 270 V and 975 μF was applied, resulting in a time constant of 16-20 msec. Thereafter, cells were transferred into 20 mL pre-warmed DMEM complete and seeded as required for individual experiments. For experiments using the reporter constructs encoding the *Renilla* luciferase, transfection efficiency was determined at 4 hours post transfection (h.p.t.) by measuring *Renilla* activity (see section 3.2.1.5.).

Transient transfection using Polyethylenimine

Transfection using PEI was performed to produce lentiviruses (see section 3.2.1.3.) and to study protein-protein interactions. For both, HEK 293T cells were seeded one day prior to transfection in 10-cm dishes at a density of 5×10^6 cells per dish. On the day of transfection, medium was changed at least 30 minutes prior to transfection to a defined volume of 8 mL. For one 10-cm dish 15 μg of plasmid vector encoding the gene of interest was mixed with 800 μL of serum reduced OptiMEM and 45 μL of PEI by vortexing. Complex formation was allowed for 18 minutes at room temperature. Thereafter, transfection mixture was added to the cells in a dropwise manner. In the case of multiple transfections, a master mix of OptiMEM and PEI was prepared to avoid variability in transfection efficiency.

Transient transfection using Mirus TransIT-LT1

In this study, transient transfection using Mirus TransIT-LT1 was performed to characterize the pIRO-Z system, to determine the impact of the antiviral compound SBI-0090799 on ZIKV replication organelle formation, and to functionally characterize potential cholesterol binding domains in the structural M domain. For all experiments performed, Huh7-Lunet T7 cells were either seeded in 6-well or on glass coverslips in 24-well cell culture plates at a density of 2×10^5 or 3×10^4 cells per well, respectively. On the following day, medium was changed 30 minutes prior to transfection. For one well of a 24-well plate 500 ng of DNA plasmid was mixed with 200 μL of serum reduced OptiMEM and 1.5 μL Mirus TransIT-LT1 by vortexing. For a well of a six well plate, amounts were quadrupled. Complex formation was allowed during an incubation period of 18 minutes at room temperature. Thereafter, transfection mixture was added to the cells in a dropwise manner. At 4 h.p.t., medium was replaced by fresh DMEM complete. Regarding experiments investigating the effect of the antiviral compound SBI-0090799, DMEM complete was

3. Materials and Methods

supplemented with 12.5 μM of the drug, thus transfection and polyprotein expression occurred in the presence of the drug.

3.2.1.3. Generation of lentiviruses and stable cell lines

In this study the following stable cell line was generated via lentivirus transduction: Huh7-Lunet ZIKV reporter cell line (referred to as Huh7-Lunet ZIKV RC). For generating lentiviruses, HEK 293T cells were seeded in 10-cm cell culture dishes at a density of 5×10^6 cells per dish. One day post seeding, cells were transfected with the packaging plasmids pCMV-GAG-Pol and pMD.G2-VSV-G (kind gifts from D. Trono, EPFL, Lausanne) and the pWPI vector encoding the gene of interest. The ratio of pCMV-GAG-Pol - pWPI - pMD.G2-VSV-G was 6:6:3. For one 10-cm dish, 15 μg of total DNA was mixed with 800 μL of serum reduced OptiMEM and 32 μL of PEI by vortexing. Complex formation was allowed for 18 minutes at room temperature. Subsequently transfection mix was added to the cells in a dropwise manner. To reduce cytotoxic effects of PEI, medium was changed at 4 h.p.t.³⁷⁸. Supernatants were collected at 48 h.p.t., filtered using a 0.45 μm syringe tip filter, and either stored at -80°C for long term storage or used immediately to generate stable cell lines. On the day of transduction, 3×10^5 Huh7-Lunet cells were mixed with the respective lentivirus in the presence of polybrene at a final concentration of 4 $\mu\text{g}/\text{mL}$ and subsequently seeded into 6-well plates. On the following day, the medium was changed, and generation of stable cell lines was achieved by adding the antibiotic puromycin. Non-transduced cells were used as killing control. Once selection was performed cells were expanded as required and stocks of stable cell lines were frozen in cryomedium. After one hour of freezing at -20°C cells were transferred into liquid nitrogen tank.

3.2.1.4. Cell viability assays

To determine cell viability and cytotoxicity of the antiviral compound SBI-0090799, the lipophilic statin lovastatin, and the cholesterol extracting drug methyl- β -cyclodextrin (M β CD), the commercially available kit CellTiter-Glo® 2.0 Assay was used.

In general, white 96-well optical bottom plates were prepared by seeding target cells, in this study Huh7-Lunet T7 cells (SBI-0090799), Huh7-Lunet naïve cells (lovastatin) or VeroE6 cells (M β CD), at a density of 1×10^4 cells per well in a total volume of 100 μL DMEM complete. On the next day, two-fold serial dilution series were prepared with a starting

3. Materials and Methods

concentration of 100 μ M for SBI-0090799, 200 μ M for lovastatin, and 20 mM for M β CD. Cell viability was measured at 24 hours post treatment. Within each cell viability assay, each concentration was evaluated in triplicates. At given timepoints cell viability was determined by measuring ATP levels following the manufacturers' protocol. Once the substrate was added, plates were placed in the Mithras LB940 plate reader and luminescence was measured at 560 nm. Within each cell viability assay treatment with DMSO served as control.

3.2.1.5. Luciferase activity assays

Within the framework of this study, *Renilla* luciferase assays were performed to assess the replication dynamics of the sub-genomic ZIKV replicon in the presence of the antiviral compound SBI-0090799, and to assess the effect of mutated cholesterol binding domains in the structural M domain on virus replication kinetics. At given timepoints post electroporation cells were washed once with PBS, lysed directly in the plate by adding 100 μ L of *Renilla* luciferase lysis buffer, and stored at -20°C. Upon thawing, lysates were resuspended by pipetting and 20 μ L of lysate were mixed with 50 μ L of *Renilla* luciferase assay buffer. Luciferase activity was measured in a tube luminometer for 10 seconds. All luciferase measurements were done as technical duplicates.

3.2.2. Virology

3.2.2.1. ZIKV stock production and purification

ZIKV stocks were produced in two ways: amplification of the ZIKV strain H/PF/2013 (obtained from the European Virus Archive) using the mosquito cell line C6/36, and collection of supernatants containing synZIKV-H/PF/2013 (WT prM and mutant CARC2 prM ZIKV) from transfected Huh7-Lunet naïve cells.

For the former, C6/36 cells were seeded in 75 cm² flasks at a density of 1x10⁷ cells per flask. On the next day cells were infected with ZIKV at a multiplicity of infection (MOI) of 0.01. Parental virus stocks were diluted in Leibovitz's L-15 medium complete (see section 3.2.1.1.) for infection. Infection was allowed for 1 hour at 28°C (without CO₂), with occasional rocking. Thereafter inoculum was replaced with complete Leibovitz's L-15 medium supplemented with 10 mM HEPES and cells were kept at 28°C (without CO₂). Virus containing

3. Materials and Methods

supernatants were collected on day 5, 6, 7, 8, and 9 post-infections, filtered using a 0.45 µm syringe-tip filter and stored at -80°C. Aliquots of 500 µL were prepared to determine titers by plaque assay (PFU/mL) (see section 3.2.2.2.).

For the latter, Huh7-Lunet naïve cells were transfected via electroporation (see section 3.2.1.2.) with individual synZIKV-H/PF/2013 constructs. Virus containing supernatants were collected at day 5 post-transfections and filtered using a 0.45 µm syringe-tip filter. To concentrate virus stocks via sucrose cushion, ultracentrifuge tubes (Beckman Coulter, ultra-clear thin wall) were washed with sterile PBS followed by the addition of 2.5 mL 20% sucrose in TNE buffer. Next, ~33 mL of virus stock was carefully added on top of the sucrose. Tubes were filled up to a total volume of 36 mL followed by weighing and balancing of the tubes (\pm 0.01 g). After centrifugation for 2 hours at 96,589xg and 4°C, supernatants were carefully aspirated. Pellets were resuspended in NTE-buffer corresponding to a concentration of 100-fold. Aliquots of 100 µL were prepared and stored at -80°C. Viral RNA was extracted from 20 µL virus stock for quantifying viral genome copies/µL by qPCR (see section 3.2.4.4.) and infectious viral titers were determined by TCID50 assay (FFU/mL) (see section 3.2.2.3.).

3.2.2.2. Determination of virus titers by plaque assay

To determine the virus concentration of stocks raised in the mosquito cell line C6/36, plaque assays were performed. For this purpose, VeroE6 cells were seeded in 24-well plates at a density of 2.5×10^5 cells per well. On the following day, virus-containing supernatants were 10-fold serially diluted and 200 µL were added as inoculum. Each virus dilution was analyzed in duplicates. Infection was allowed at 37°C for at least 1 hour before infectious inoculum was removed and replaced with plaquing medium. Thereafter, plates were kept at 37°C (5% CO₂) for 4 days. To allow the quantification of plaques, samples were fixed with 10% formaldehyde for >1 hour at room temperature. Fixed plates were thoroughly washed with water. To visualize plaques, cell monolayers were stained for 20 minutes with crystal violet solution. Excess of crystal violet solution was removed by thoroughly washing the plates with water. After plates have dried, plaques were counted manually, and viral titers (PFU/mL) were estimated using the following formula:

$$\text{Titer (PFU/mL)} = \frac{\text{mean of plaques counted}}{\text{Volume of inoculum (ml)} * \text{dilution}}$$

3. Materials and Methods

3.2.2.3. Determination of virus titers by TCID₅₀

In the framework of this study, tissue culture infection dose₅₀ (TCID₅₀) assays were performed to determine infectious viral titers of synZIKV cholesterol binding mutants. Therefore, Huh7-Lunet naïve cells were seeded in 96-well plates at a density of 8×10^3 cells per well. The day after, virus-containing supernatants were diluted 1:2 initially followed by 10-fold serial dilution series in a total volume of 200 μ L. Each supernatant was analyzed in sextuplicate. After infection plates were kept at 37°C (5% CO₂) for 48 hours. For fixation, supernatants were replaced with ice cold methanol and immediately stored at -20°C for >30 minutes. Thereafter, methanol was discarded, plates were briefly air dried, washed with PBS, and permeabilized with 0.5% Triton X-100 in PBS for 5 minutes. Permeabilized cells were washed thrice with PBS and subsequently incubated with the panFlavi anti-envelope primary antibody (30 μ L/well). After a 3 hours incubation period at room temperature plates were washed thrice with PBS, incubated for 1 hour at room temperature with the HRP-coupled anti-mouse secondary antibody (diluted 1:200; 30 μ L/well), washed thrice with PBS, and finally incubated with substrate solution for visualizing positive cells. HRP substrate solution was prepared fresh shortly before usage by mixing 5 mL Acetatos, 1.5 mL Carbazole, and 20 μ L H₂O₂. To remove crystals, solution was filtrated using a 0.45 μ m syringe-tip filter. Once cells started showing a prominent red cytoplasmic stain reaction was stopped by replacing the substrate with water. Using a light microscope, positive wells were identified, and virus titers were calculated using the following excel sheet: <https://www.klinikum.uni-heidelberg.de/Downloads.126386.0.html>

3.2.2.4. Quantification of cell associated infectious ZIKV

To quantify intracellular infectious virus particles, ZIKV-transfected cell cultures were washed thrice with PBS, scraped in 1 mL DMEM complete supplemented with 15 mM HEPES, and subsequently transferred into 1.5 mL reaction tubes. Samples were frozen and thawed in three consecutive cycles using liquid nitrogen and a heat block pre-warmed to 37°C. Samples were then centrifuged for 5 minutes at 3,000xg and 4°C to remove cell debris. Clarified supernatants were transferred to a fresh 1.5 mL reaction tube and infectious titers were determined by performing TCID₅₀ assays (see section 3.2.2.3.). Alternatively, supernatants were stored at -80°C.

3. Materials and Methods

3.2.2.5. Viral binding assays

Viral binding assays were performed on VeroE6 cells. For this purpose, 1×10^5 cells were seeded in each well of a 24-well plate. On the following day, cells were pre-cooled at 4°C and washed once with binding buffer. Virus inoculums were prepared by dilution using 200 µL of binding buffer and a total of 2×10^8 viral genome copies per well. Binding was performed at 4°C for 1 ½ hours. To remove unbound virus, cells were washed three times with cold PBS. Thereafter, cells were lysed in 350 µL LBP RNA lysis buffer and either stored at -20°C or immediately processed for RNA extraction and qRT-PCR analysis (see section 3.2.4.4.).

3.2.2.6. Viral entry inhibition assay

For assessment of the mutations' influence on virus entry, VeroE6 cells were seeded in standard medium in 24-well plates at a density of 1×10^5 cells per well. On the following day cell monolayers were pre-treated with the entry inhibitor ammonium chloride for hour prior to infection at a final concentration of 50 mM. Afterwards, cells were pre-cooled at 4°C and washed with binding buffer. Virus inoculums were prepared as described in section 3.2.2.5. Virus binding was performed for 1 ½ hours at 4°C in the presence of ammonium chloride. Following, cells were warmed up to 37°C to allow uptake of the virus via the endocytic pathway. At given time points cells were washed thrice with PBS and thereafter lysed in 350 mL LBP RNA lysis buffer and either stored at -20°C of immediately processed for RNA extraction and qRT-PCR analysis (see section 3.2.4.4.).

3.2.3. Cloning

3.2.3.1. Polymerase Chain reaction

The polymerase chain reaction (PCR) is a commonly used technique in molecular biology to exponentially amplify DNA sequences. To accomplish amplification, single-stranded DNA is used as template and oligonucleotides, known as forward and reverse primers, are used to define the start and the end of amplicons. In this study, PCR was used to generate new constructs and for site-directed mutagenesis in the context of the viral genome. In a total volume of 50 µL the following components were mixed: 25 µL of 2X Phusion High-

3. Materials and Methods

Fidelity Master Mix, 2.5 μ L of forward primer (final concentration 500 nM), 2.5 μ L of reverse primer (final concentration 500 nM), 1.5 μ L of DMSO, 1 μ L of DNA template (100 ng), and 18.5 μ L of water. A complete list of primers used for cloning can be found in the Supplementary Table 3. All PCRs were performed on a thermal cycler with individualized cycling programs based on primer annealing temperatures and fragment length.

For site-directed mutagenesis in the context of the viral genome, a two-step overlap PCR was performed. For this purpose, two primer pairs were designed. While the “outer” primer pair was designed as usual, comprising the entire amplicon, and harboring unique restriction sites, the “inner” primer pair were designed with 5' complementary overhangs of approximately 15-20 nucleotides and harboring the desired mutations. Using the corresponding inner and outer primers, the first round of PCR generated two fragments with complementary sequences. Based on these complementary sequences, amplification products of the first-round PCR were fused in the second-round PCR, which was performed using the “outer” primer pair.

3.2.3.2. Restriction digest of DNA plasmids

Restriction digest was performed in this study to on the one hand clone new constructs and on the other hand validate newly generated constructs. For the former, to facilitate ligation of PCR products with vector backbones restriction digests were performed using respective restriction enzymes. For removing the 5' phosphates from each restriction site in vector backbones, 1 U of CIP was added to the reaction. Treatment with CIP was performed to counteract spontaneous re-ligation of the vector backbones. For validating newly generated constructs, \sim 1 μ g of DNA was subjected to restriction digest. For this purpose, 1 U per μ g of restriction enzyme was used. Each restriction digest was performed at 37°C for 1-2 hours followed by agarose gel electrophoresis for analysis (see section 3.2.3.3.).

3.2.3.3. Agarose gel electrophoresis

In this study, agarose gel electrophoresis was performed to resolve PCR products, restriction enzyme digest products, and IVT RNAs (see section 3.2.4.6.) based on their molecular size and charge. Depending on the size of nucleic fragments, 0.8-1.5% agarose gels were prepared in 1X TAE buffer with 3 μ L of Midori Green dye per 100 mL.

3. Materials and Methods

Electrophoresis was run in 1X TAE buffer for 20-30 minutes at 120 V. To estimate the sizes of nucleic fragments, the 1-kb DNA ladder was applied in parallel to loaded samples. Analysis was performed using the INTAS system.

3.2.3.4. Gel extraction

Following agarose gel electrophoresis, bands of interest were cut and purified using the commercially available NucleoSpin Gel and PCR clean-up kit. Extraction of DNA fragments was done according to the manufacturers' protocol. DNA fragments were eluted in 20 μ L of water. Fragments exceeding a length of >1000 bp were incubated at 70°C for 5 minutes.

3.2.3.5. Ligation

For ligating DNA fragments with compatible ends, the T4 DNA ligase kit was used. Usually, a molar ratio of 1:3 (Vector:Insert) was used ensuring a high insertion rate, whilst preventing multiple insertions. For each reaction 100 ng of vector was used. The corresponding amount of insert was calculated using the following formula:

$$m_{\text{insert}} \text{ (ng)} = \frac{m_{\text{vector}} \text{ (ng)} * l_{\text{insert}} \text{ (kbp)} * 5}{l_{\text{vector}} \text{ (kbp)}}$$

Ligation reaction was set up in a total volume of 10 μ L. Finally, ligation was performed either for 1-2 hours at room temperature or for 16 hours at 16°C. Thereafter, ligation products were transformed into competent bacteria (see section 3.2.3.6.).

3.2.3.6. Transformation of chemically competent bacteria

The bacterial strain *E. coli* DH5 α was thawed on ice, and 50 μ L of bacteria suspension were mixed with 10 μ L ligation mix. After an incubation period of 30 minutes on ice, bacteria were transformed for 40 seconds at 42°C in a thermomixer. Cultures were cooled for 2 minutes on ice and subsequently plated on LB agar plates supplemented with the antibiotic carbenicillin. Bacterial growth was allowed for 16 hours at 37°C, followed by clone picking with sterile pipet tips and amplification in 5 mL LB medium supplemented with ampicillin at 37°C and 180 rpm for 16 hours.

3. Materials and Methods

3.2.3.7. Isolation and analysis of plasmid DNA from bacteria

Plasmid DNA was extracted from bacteria using the NucleoBond PC 500 plasmid isolation kit. Extraction was done according to the manufacturer's protocol. Purified DNA plasmids were reconstituted in water with a final concentration of 1 µg/mL. Initial validation of plasmids was done by analytical restriction digest (see section 3.2.3.2.). To ensure correct sequences and proper reading frames, samples were sequenced by the commercial service provider Microsynth Seqlab GmbH, Göttingen, Germany. Primers used for sequencing are listed in the Supplementary Table 3. Validation of sequences was done by alignment using the tool Ape.

3.2.4. Molecular biology

3.2.4.1. Extraction and purification of total intracellular RNA

For monitoring replication kinetics of WT viruses and mutated viruses in mammalian and mosquito cell lines, intracellular ZIKV RNA levels were quantified by qRT-PCR (see section 3.2.4.3). For this, the human hepatoma cell line Huh7-Lunet naive was transfected with *in vitro*-transcribed RNA of the individual synZIKV-H/PF/2013 constructs and seeded in 12-well plates at a density of 2×10^5 cells per well. At 8 h.p.t. cells were washed once with PBS to remove contaminating free viral RNA. For replication kinetics in the mosquito cell line Aag2, cells were seeded one day prior to infection in 24-well plates at a density of 3.5×10^5 cells per well. At given time points, cells were washed thrice with PBS followed by the addition of 350 µL of RNA lysis buffer. Lysed cells were stored at -20°C until further processed. RNA was extracted using the NucleoSpin RNA II Purification Kit. RNA extractions were performed according to the manufacturer's protocol. RNA was eluted in a final volume of 60 µL RNase-free water. Samples were stored at -80°C or directly used for cDNA synthesis (see section 3.2.4.3.).

3.2.4.2. Viral RNA Assay

To allow the detection of secreted viral genome RNA associated with virus particles in the set-up of electroporation, a RNase protection assay was performed to remove residual RNAs from the electroporation procedure. For this 250 µL of supernatant collected at

3. Materials and Methods

96 h.p.t. was mixed with 5 μ L of RNase A/T1 and subsequently incubated for at least 1 hour at 37°C. Thereafter, viral RNA was extracted by adding 750 μ L of cold TRIzol. To allow complete disintegration of virus particles, samples were mixed by inversion and incubated at room temperature for 5 minutes. Next, 150 μ L of chloroform was added and samples were mixed by inversion. Separation of nucleic acids and proteins was achieved by centrifugation for 15 minutes at 12,000xg and 4°C. After centrifugation, the upper aqueous phase was carefully transferred to a fresh 1.5 mL RNase-free reaction tube, followed by the addition of 375 μ L isopropanol along with 1.5 μ L of GlycoBlue Coprecipitant for visualizing RNA pellets. After mixing samples by inversion, precipitation was performed at room temperature for 15 minutes. RNA was pelleted by centrifugation for 10 minutes at 12,000xg and 4°C, washed in 200 μ L of 70% ethanol in RNase-free water, air-dried briefly, and subsequently reconstituted in 30 μ L RNase-free water. RNA samples were either stored at -80°C or subjected to cDNA synthesis and analysis by agarose gel electrophoresis (see section 3.2.3.3.).

3.2.4.3. cDNA synthesis and SYBR Green-based quantitative real-time PCR

For quantifying intracellular viral and cellular RNA levels, the two-step reverse transcription quantitative PCR (RT-qPCR) was performed. First, complementary DNA (cDNA) was generated using the High-Capacity cDNA Reverse Transcription Kit. In a total volume of 10 μ L the following components were mixed: 1.6 μ L of RNase-free water, 1 μ L of 10X RT buffer, 0.4 μ L of 25X dNTP Mix (100 mM), 1 μ L of 10X RT Random Primers, 0.5 μ L of RNase inhibitors, 0.5 μ L of MultiScribe RT enzyme (50 U/mL), and 5 μ L of RNA. cDNA synthesis was performed on a thermal cycler running the cycling program shown below (Table 12).

Table 12. RT-PCR cycling program used for cDNA synthesis using the high-capacity RT kit.

Number of cycles	Temperature	Time [min]
1x	25°C	10
1x	37°C	120
1x	85°C	5
	4°C	∞

Following cDNA synthesis, expression levels of viral and cellular RNAs were assessed by quantitative real-time PCR using the iTaq Universal SYBR Green Kit. For this, in a total volume of 15 μ L the following components were mixed: 7.5 μ L of 2X iTaq Universal SYBR

3. Materials and Methods

Green Supermix, 0.75 μL of forward primer (final concentration: 500 nM), 0.75 μL of reverse primer (final concentration: 500 nM), 1.5 μL of RNase-free water, and 3 μL of cDNA (diluted 1:20 in RNase-free water). Sequences of primers used are displayed in Supplementary Table 3. Each sample was analyzed in triplicate wells. GAPDH was used for normalization in mammalian cells. RsP17 was used for normalization in mosquito cells. Quantitative real-time PCR was performed on a CFX96 Real-Time System using the cycling program displayed in Table 13.

Table 13. Cycling program used for SYBR-based qPCR.

Number of cycles	Temperature	Time
1x	95°C	3 min
44x	95°C	10 sec
	60°C	30 sec

3.2.4.4. One-Step probe-based RT-qPCR

For quantifying the number of viral RNA copies in binding (see section 3.2.2.5.), and acid-bypass assays (see section 3.2.2.6.) the PerfeCTa qPCR ToughMix was used. In a total reaction volume of 15 μL the following components were mixed: 7.5 μL 2x PerfeCTa mix, 400 nM of each primer (Supplementary Table 3), 200 nM of each probe (Supplementary Table 3), and 3 μL of extracted RNA (see section 3.2.4.1.). For absolute quantification, a 10-fold serial dilution series (10^3 to 10^9 copies) of ZIKV transcripts were added as standard to each plate. Each sample was analyzed in triplicate wells. GAPDH was used for normalization. Quantitative reverse transcription PCR was performed on a CFX96 Real-Time System using the cycling program displayed in Table 14.

Table 14. Cycling program used for One-Step probe-based RT-qPCR.

Number of cycles	Temperature	Time
1x	50°C	10 min
1x	95°C	1 min
40x	95°C	10 sec
	60°C	1 min

3.2.4.5. ZIKV RNA detection by agarose gel electrophoresis

For detecting secreted viral RNA associated with virus particles, extracted RNA was first subjected to first-strand cDNA synthesis using the Superscript III reverse-transcriptase kit. In a total volume of 20 μL the following components were mixed: 6 μL of RNase-free water,

3. Materials and Methods

1 μL of 25X dNTP Mix (100 mM), 4 μL of 5X First strand buffer, 1 μL of 0.1 M DTT, 1 μL of RNase inhibitor, 1 μL of SuperScript III RT (200 U/ μL), 1 μL of site-specific primer (Supplementary Table 3), and 5 μL of extracted RNA (see section 3.2.4.2.). cDNA synthesis was performed on a thermal cycler running the cycling program shown in Table 15.

Table 15. RT-PCR cycling program used for cDNA synthesis using the Superscript III RT polymerase kit.

Number of cycles	Temperature	Time [min]
1x	65°C	5
1x	25°C	5
1x	55°C	60
1x	70°C	15
	4°C	∞

Following cDNA synthesis, viral RNA was detected by amplification of the structural genes C-prM-E of ZIKV corresponding to an amplicon of 1000 bp in length. For this purpose, in a total volume of 25 μL the following components were mixed: 12.5 μL of 2X Phusion High-Fidelity Master Mix, 0.75 μL DMSO, 1.25 μL of forwards primer (final concentration: 500 nM), 1.25 μL of reverse primer (final concentration: 500 nM), 6.25 μL of water, and 3 μL of cDNA. Sequences of primers used for PCR are listed in the Supplementary Table 3. RNAs extracted from NS5-deficient and mock transfected cells were used as negative control. PCR was performed on a thermal cycler using the cycling program displayed below (Table 16).

Table 16. PCR cycling program used for detecting secreted viral RNA.

Number of cycles	Temperature	Time
1x	95°C	2 min
	95°C	15 sec
40x	55°C	10 sec
	72°C	45 sec
1x	72°C	3 min
	4°C	∞

3.2.4.6. *In vitro* transcription

To study the effect of mutations within the context of the viral genome the reverse genetics system was used³⁷⁷. *In vitro* transcripts were generated for transfecting mammalian cells by electroporation (see section 3.2.1.2.). Briefly, 10 μg of pFK-plasmids were linearized by XhoI, followed by DNA purification using the Nucleo-Spin extraction kit. Elution of

3. Materials and Methods

linearized templates was achieved in a two-step procedure by using 22 μL of RNase-free water. In a total reaction volume of 100 μL the following components were mixed: 41 μL of linearized DNA template, 12.5 μL of rNTP (3.125 mM of ATP, CTP, UTP; 1.56 mM of GTP), 20 μL of the ARCA cap (1 mM), 20 μL of 5X RRL buffer, 4 μL of the T7 polymerase (2 U/ μL), and 2 μL of RNasin (1 U/ μL). IVT was performed at 37°C for 2.5 hours, followed by the addition of 1 U/ μL T7 polymerase and an additional incubation period of up to 16 hours at 37°C. The DNA template was removed by adding 20 μL of RNase-free DNase I (RQ1) and incubation at 37°C for 1 hour. *In vitro*-transcribed RNA was purified through acidic phenol-chloroform extraction and isopropanol precipitation. Purified RNA was resuspended in RNase-free water to a final concentration of 1 $\mu\text{g}/\mu\text{L}$, and its quality was checked by agarose gel electrophoresis (see section 3.2.3.3.). IVT RNA were stored at -80°C until needed.

3.2.5. Biochemistry

3.2.5.1. Cell lysis

In the framework of this study, western blot analysis was done to study polyprotein and furin processing and to quantify protein abundance. For this purpose, cell lysis was achieved by either using RIPA buffer supplemented with 1X protease inhibitor cocktail or 2X Laemmli sample buffer.

Western blot samples for characterizing the pIRO-Z system were generated by seeding 2×10^5 Huh7-Lunet T7 cells in 6-well plates followed by transfection with individual constructs (see section 3.2.1.2.). At 18 h.p.t. cells were washed with PBS and lysed in 100 μL 2X Laemmli sample buffer. To reduce the viscosity of the lysate, DNA was digested for 10 minutes at room temperature by adding 1 μL of Benzonase (10 kU stock). Samples were thereafter subjected to SDS-PAGE and western blot analysis (see section 3.2.5.3.).

For generating western blot samples for characterizing polyprotein and furin processing in the context of synZIKV-H/PF/2013 transfection, Huh7-Lunet naïve cells were electroporated with individual constructs (see section 3.2.1.2.) and seeded in 10-cm cell culture dishes at a density of 1×10^6 cells per dish. At 48 hours post electroporation, cells were washed with PBS and subsequently lysed in 200 μL of RIPA lysis buffer. Lysis was performed at 4°C for ≥ 1 hour followed by centrifugation for 8 minutes at 16,000xg and 4°C for removing cell debris. Clarified supernatants were transferred to a fresh 1.5 mL reaction

3. Materials and Methods

tube, protein concentrations were determined via Bradford assay (see section 3.2.5.2.) and analyzed by western blot (see section 3.2.5.3.).

3.2.5.2. Bradford assay

Protein concentrations in whole cell lysates were determined by using the spectroscopic analytical Bradford assay³⁷⁹. For this purpose, a working solution of 1X Bradford reagent was prepared in deionized water. Thereafter, 1 mL of Bradford solution was mixed with 2 μ L of whole cell lysate, transferred into polystyrene cuvettes (Sarstedt), and measured using a spectrophotometer with an adsorption spectrum maximum at 595 nm. For correction, Bradford solution mixed with lysis buffer was used as reference for background signal. For absolute quantification, a 2-fold serial dilution series of BSA was prepared ranging from 0 to 10 μ g/mL.

3.2.5.3. SDS-PAGE and western blot analysis

For SDS gel electrophoresis samples were denatured at 95°C for 5 minutes prior to loading. Protein samples for characterizing the pIRO-Z system were separated on 12% polyacrylamide gels and blotted onto a methanol activated polyvinylidene difluoride (PVDF; 0.45 μ m pore size) membranes over 16 hours at 90 mA and 4°C using the wet blotting system. Protein samples for characterizing polyprotein and furin processing of synZIKV-H/PF/2013 were separated on 5-18% gradient polyacrylamide gels and blotted onto a methanol activated PVDF (0.2 μ m pore size) membranes over 45 minutes at 350 mA and room temperature using the wet blotting system. For the separation of proteins according to their size, electrophoresis was performed at a constant voltage of 100 V in 1X TGS running buffer. For identification of protein sizes, a pre-stained standard protein marker was applied in parallel to loaded samples. Following transfer membranes were blocked in blocking buffer for at least 1 hour at room temperature. Primary antibodies (Table 4) were diluted in 1X blocking buffer (1:1000) and added to membranes with an incubation period of >16 hours at 4°C. Thereafter membranes were washed thrice with washing buffer, followed by an incubation period of 1 hour at room temperature with HRP-conjugated secondary antibodies (1:5,000-10,000) (Table 5). Next, membranes were washed thrice with washing buffer and chemiluminescence was measured in an ECL Chemocam Imager using the ChemoStar software, after the ECL Western Lightning substrate was added. Analysis and

3. Materials and Methods

processing of western blots were done using the LabImage 1D and Fiji software packages, respectively.

3.2.5.4. Photoaffinity crosslinking of proteins to cholesterol

Identification of cholesterol binding ZIKV proteins in living mammalian cells was performed as previously described^{354,380–382}. Briefly, 2×10^5 Huh7-Lunet naïve cells were seeded in six-well plates and infected with ZIKV-H/PF/2013 at a MOI of 10. At 24 h.p.i, cells were treated for 1 hour at 37°C with 10 μ M PAC-cholesterol in DMEM supplemented with 10% DL-FBS (DL: delipidated). Cells were washed thrice with cold PBS, treated with ultraviolet (wavelength: 365 nm) for 5 minutes at $2000 \times 100 \mu\text{J}/\text{cm}^2$ and 4°C, and lysed in 100 μ L photoaffinity labeling lysis buffer for 1 hour at 4°C rotating. Clarification of lysates was achieved by centrifugation for 8 minutes at 16,000xg and 4°C. Clarified supernatants were transferred to fresh 1.5 mL reaction tubes and protein concentrations were determined via Bradford assay (see section 3.2.5.2.). Equal protein amounts were then subjected to copper catalyzed azide-alkyne cycloaddition (CuAAC) click chemistry. In a total volume of 100 μ L the following components were mixed: 75 μ L of protein lysate, and 5 μ L of each: 1% SDS in PBS, 25 mM freshly prepared CuSO_4 in water (final concentration 1.25 mM), 25 mM freshly prepared ascorbic acid in water (final concentration 1.25 mM), 2.5 mM of freshly prepared tris[(1-benzyl-1H-1,2,3-triazol-4-yl)methyl]amine (TBTA) in DMSO (final concentration 125 μ M), and 2.5 mM freshly prepared azide-biotin in DMSO (final concentration 125 μ M). Click chemistry was performed for 3 hours at 37°C. Proteins were precipitated overnight at -80°C in methanol. Pelleting of proteins was achieved by centrifugation for 10 minutes at 16,000xg and 4°C, followed by one washing step in methanol. Washed and pelleted proteins were reconstituted in 4% SDS in PBS at 37°C for 10 minutes. Thereafter, proteins were diluted to a final concentration of 0.2% SDS with PBS. Neutravidin beads, which were used for affinity purification, were equilibrated by three consecutive washing steps using 0.2% SDS in PBS. After each washing step, beads were pelleted by centrifugation for 1 minute at 500xg. Binding to the beads was allowed for 3 h at room temperature while rotating, followed by 10 consecutive wash steps with 1% SDS in PBS and centrifugation steps at 500xg for 1 minute. Finally, co-purified proteins were eluted using 2X Laemmli sample buffer and analysis was done by western blot (see section 3.2.5.3.).

3. Materials and Methods

3.2.5.5. Coimmunoprecipitation of Env and prM proteins

To assess whether mutations within the M domain affect the interaction between the two structural proteins envelope and prM of ZIKV, co-immunoprecipitation assays alongside with western blot analysis were performed. Briefly, HEK 293T cells were seeded in 10-cm dishes at a density of 5×10^6 cells per dish. One day post seeding, cells were transfected with pcDNA3.1 vector encoding the gene of interest. For one 10-cm dish, 15 μg of total DNA was mixed with 800 μL of serum reduced OptiMEM and 45 μL of PEI by vortexing. Complex formation was allowed for 18 minutes at room temperature. Subsequently transfection mix was added to the cells in a dropwise manner. At 18 h.p.t. cells were washed once with PBS, scraped, and transferred into 2 mL reaction tubes followed by centrifugation at 3,000xg for 5 minutes. Supernatants were thereafter aspirated and cell pellets were lysed in 200 μL of DDM lysis buffer for 1 hour on ice. Clarification of lysates was achieved by centrifugation for 8 minutes at 16,000xg and 4°C. Clarified supernatants were transferred to fresh 1.5 mL reaction tubes and protein concentrations were determined via Bradford assay (see section 3.2.5.2.). Cell lysates were normalized to the sample with lowest total protein concentration. 20% of total normalized cell lysate was saved as input and the remaining lysate was loaded onto HA-specific agarose beads slurry. After an incubation period of 16 hours at 4°C, rotating, resin beads were washed thrice with DDM lysis buffer followed by two wash steps with PBS. Samples were eluted using with 2X Laemmli sample buffer by boiling at 95°C for 15 minutes. Finally, efficacy of co-immunoprecipitation of prM with envelope was assessed and analyzed by western blot (see section 3.2.5.3.).

3.2.5.6. Quantification of cholesterol content in cells

Cellular cholesterol content was determined using the Amplex Red Cholesterol Assay kit. In this study cholesterol was quantified for mammalian cell lines including Huh7-Lunet naïve, VeroE6, A549, and JEG3 as well as for the mosquito cell lines Aag2 and C6/36. Briefly, 1×10^6 cells were washed with PBS, pelleted by centrifugation at 3,000xg for 5 minutes, and lysed in 100 μL photoaffinity labeling lysis buffer. In a total volume of 100 μL per well the following components were mixed: 10 μL of cell lysate, 40 μL of 1X reaction buffer, and 50 μL of the working solution (4.82 mL 1X reaction buffer, 75 μL of 300 μM Amplex Red stock solution, 50 μL of HRP stock solution (2 U/mL), 50 μL of the cholesterol oxidase stock solution (2 U/mL), and 5 μL of the cholesterol esterase stock

3. Materials and Methods

(0.2 U/mL)). For absolute quantification, a cholesterol standard curve was prepared ranging from 0 to 8 µg/mL. Fluorescence was measured at multiple time points (0 and 30 minutes after substrate addition) using a plate reader (CLARIOstar, BMG Labtech) using an excitation wavelength of 540 nm and emission detection wavelength of 590 nm. For correction, background fluorescence was subtracted using values derived from the no cholesterol control.

3.2.6. Microscopy

3.2.6.1. Immunofluorescence microscopy

In this study, immunofluorescence microscopy was performed to analyze the following aspects: (i) transfection efficiency; (ii) subcellular localization of viral proteins; (iii) colocalization of viral proteins; (iv) viral spread. For all experiments, cells were seeded on glass coverslips in a 24-well plate at a density of 3×10^4 cells per well. At 18 h.p.t. transfection efficiency and subcellular localization of viral non-structural proteins for the pIRO-Z system were determined. Subcellular localization of prM proteins and E proteins was determined at 48 hours post electroporation (h.p.e.), and viral spread was monitored in 24-hour intervals over the period 72-120 h.p.e. At each given time point, cells were washed with PBS, fixed with 4% PFA for 10 minutes at room temperature, and permeabilized using 0.2% Triton-X-100 in PBS for 10 minutes at room temperature. Samples were washed with PBS, blocked in blocking buffer for >1 hour at room temperature, and incubated with primary antibodies (Table 4) for 16 hours at 4°C. Coverslips were thereafter washed thrice with washing buffer and incubated with Alexa Fluor conjugated secondary antibodies (Table 5) at room temperature for 1 hour. After samples were washed thrice with washing buffer and rinsed once with water, coverslips were mounted on microscope slides using DAPI Fluoromount-G mounting medium. Images were obtained using a fluorescent microscope (Nikon Eclipse Ti) or confocal microscope (Leica SP8 TCS DLS) using the software's NIS – Elements Viewer (Nikon) and LAS X Life Science (Leica), respectively. All images were analyzed and processed with the open access program FIJI.

3.2.6.2. Transmission electron microscopy (TEM)

3. Materials and Methods

Huh7-Lunet T7 cells were seeded one day prior to transfection on glass coverslips in 24-well plates at a density of 3×10^4 cells per well. At 18 h.p.t. cells were washed with PBS and fixed with EM fixative buffer for >30 minutes at room temperature. Fixed cells were washed thrice with 50 mM CaCo buffer, treated with 2% osmium tetroxide in 50 mM CaCo buffer for 40 minutes at 4°C, washed thrice with EM grade water, and subsequently incubated >16 hours in 0.5% uranyl acetate in water at 4°C. After 30 minutes of washing with EM grade water, samples were progressively dehydrated using 10% increment concentrations of ethanol (40% to 100%). Finally, samples were embedded in epoxy resin and polymerized for 48 hours at 60°C. Samples were thereafter trimmed, sectioned into 70-nm thick slices using a Leica EM UC6 Microtome and a diamond knife (Diatome), and collected on mesh grids (Plano GmbH). Counterstaining was performed using lead citrate and uranyl acetate. Cells were examined with a JEOL JEM-1400 transmission electron microscope (Jeol Ltd., Tokyo, Japan). Quantification of vesicle numbers and size per cell profile was done manually using the FIJI software package.

3.2.6.3. Correlative light-electron microscopy

Correlative light-electron microscopy was performed by transfecting Huh7-Lunet ZIKV RC cells with individual synZIKV constructs (see section 3.2.1.2.). Transfected cells were seeded into glass-bottom culture dishes containing photo-etched gridded coverslips (MatTek Corporation) at a density of 4.5×10^4 cells per dish. At 72 h.p.t. positions of positive cells were recorded using transmitted light with a differential interference contrast configuration. Cells were then fixed, processed, and analyzed as described above (see section 3.2.6.2., sections were collected on slotted grids (Plano GmbH)). Quantification of virion numbers per cell profile was done manually using the FIJI software package.

3.2.7. **Statistical analysis**

Statistical analyses of the results were performed in GraphPad Prism (Version 8). P-values were determined by using paired-ratio t-tests, one-way ANOVAS, and two-way ANOVAS. P-values are indicated as asterisks within the graphs (*, $p < 0.05$; **, $p < 0.01$; ***, $p < 0.001$; ****, $p < 0.0001$).

4. RESULTS

4.1. Generation of a replication-independent system to study the biogenesis of ZIKV replication organelles

Previous studies have shown that upon ZIKV infection the ER undergoes extensive expansion and is drastically remodeled giving rise to distinct membrane structures, referred to as vesicles, which are the presumed sites of viral replication^{298,299,301}. While former studies have identified several viral non-structural proteins, exhibiting the ability to induce membrane alterations, sole expression of individual proteins failed to phenocopy viral replication organelles (ROs). So far, studies investigating the effect of antiviral compounds and mutations on the virus replication cycle were limited to virus infection assays and viral replicon assays. Whether the antiviral effects observed were due to an impairment of RO formation remained an open question. To overcome this limitation, my first goal was to generate a system which induces ZIKV ROs independent from viral replication.

This chapter was published and following paragraphs are adapted from the reference [385].

4.1.1. Formation of ZIKV ROs is independent of the stem loop structures in the 5'UTR

With the aim of generating an expression system, supporting the Zika viral RO formation in a replication-independent manner, I created a ZIKV (strain H/PF/2013, GeneBank ID KJ776791) polyprotein expression construct, encoding the viral replicase (E_{TM} -NS1-NS5). Taking into account that ZIKV replication occurs in the cytoplasm of the host cell, I employed the T7 RNA polymerase-based system pTM³⁸³. This system allows the continual synthesis of viral RNA in the cytoplasm by using a transfected DNA plasmid as template. Furthermore, as transcription occurs directly in the cytoplasm undesired RNA modifications such as splicing, which would affect the viral protein synthesis, are eliminated. To promote a robust translation, the encephalomyocarditis virus (EMCV)-derived internal ribosome entry site (IRES)³⁸⁴ was added to the 5'end of the viral polyprotein. Given previous results within our group, showing that the sole expression of the dengue viral polyprotein (NS1-NS5) was not sufficient to induce the replication compartment, suggested a requirement of viral RNA elements located within the UTRs³⁸⁵. Based on these findings, both

4. Results

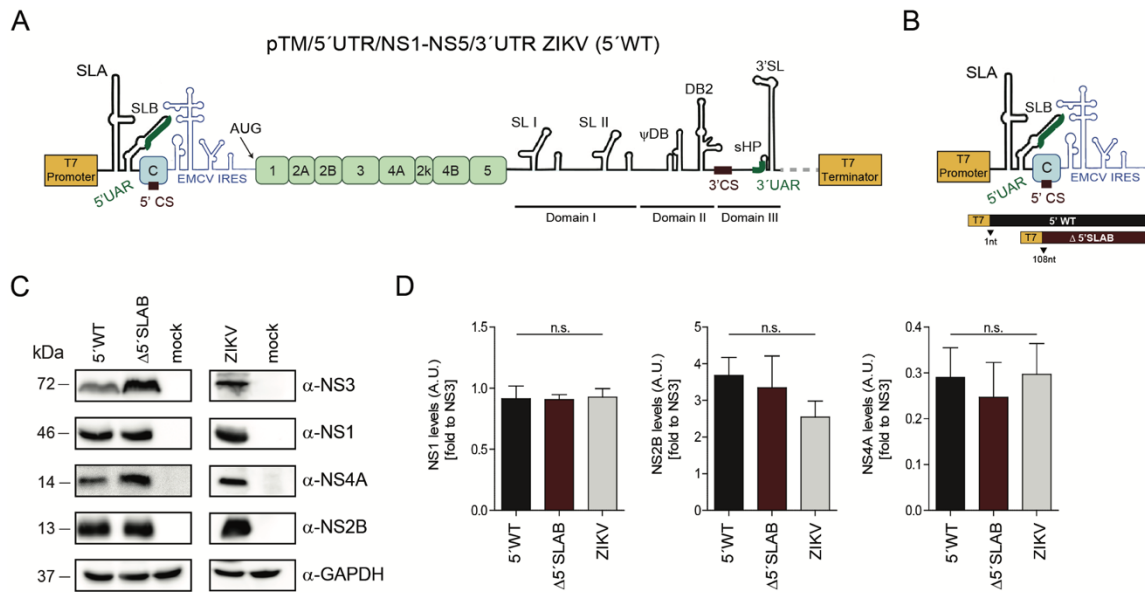


Figure 13. Expression and processing of the viral replicase is comparable between transfected and infected cells. (Adapted from [385])

(A) Design of the initial ZIKV expression construct (pTM/5'UTR/NS1-NS5/3'UTR). This construct is referred to as 5'WT. (B) Schematic representation of the 5'UTR indicating the deletion mutation (Δ 5'SLAB; nucleotides 1-107). (C) Immunoblot showing the expression of NS3, NS1, NS4A and NS2B upon transfection with indicated 5'UTR truncations (left panel). Polyprotein processing upon ZIKV infection (MOI=10) (right panel). GAPDH was used as loading control. (D) Relative polyprotein processing efficiency was calculated by densitometry normalizing the signals of NS1, NS2B, and NS4A to NS3 expression levels in each indicated construct. Values represent mean \pm SEM from three independent experiments. n.s., not significant.

UTRs were added to the initial construct of the ZIKV expression system, designated pTM/5'UTR/NS1-NS5/3'UTR (Figure 13a). To gain a better understanding of whether secondary RNA elements located within the 5'UTR are essential for ZIKV RO formation, I generated a deletion mutant lacking the SLA and SLB, of which the former corresponds to the RdRp binding site. This construct is designated pTM/ Δ 5'SLAB/NS1-NS5/3'UTR (Figure 13b). For characterization of these constructs with respect to polyprotein processing, protein abundance, subcellular localization of viral non-structural proteins, and their ability to induce ZIKV ROs, Huh7-Lunet T7 cells were transfected. To allow a direct comparative analysis, ZIKV infected Huh7-Lunet T7 cells were included as positive control and analyzed in parallel. Given my results, cells expressing individual 5'UTR constructs showed neither alterations in processing of the ZIKV polyprotein (Figure 13c) nor changes in the abundance of cleaved viral proteins when compared to ZIKV infected cells (Figure 13d). Furthermore, no changes were observed when comparing the subcellular localization of NS3, NS4B, and NS5 in transfected to infected cells. Like infected cells, NS3 and NS4B localized to the ER whereas NS5 localized to the nucleus, which was assessed by

4. Results

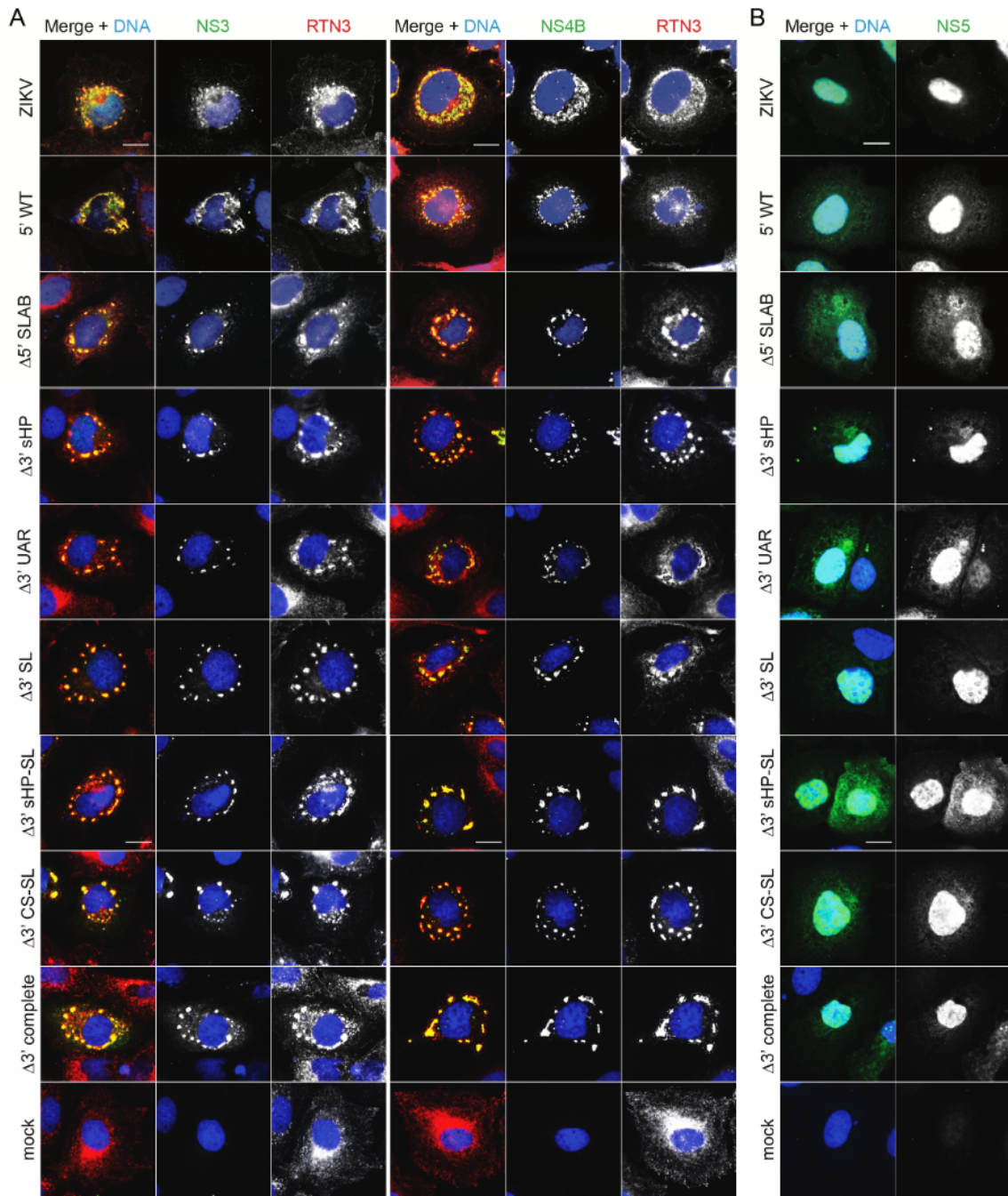


Figure 14. Deletion mutations in the 5' and 3'UTR do not affect subcellular localization of ZIKV NS proteins. (Adapted from [385])

Cells were either infected with ZIKV (upper row), transfected with the indicated constructs (row 2-9), or left untreated (bottom row). Cells were fixed for immunofluorescence analysis after 18 hours of transfections or 24 hours of ZIKV infection. **(A)** Subcellular localization of NS3 and NS4B was assessed by staining the ER using Reticulon 3 (RTN3). Scale bars: 10 μ M. **(B)** Nuclear localization of NS5 was assessed by staining cellular DNA with DAPI. Scale bar: 10 μ m.

staining RTN-3 (Figure 14a) and cellular DNA with DAPI (Figure 14b), respectively. To assess the ability of these constructs to induce vesicle packets (VPs), I next characterized the ultrastructure of transfected Huh7-Lunet T7 cells via transmission electron microscopy

4. Results

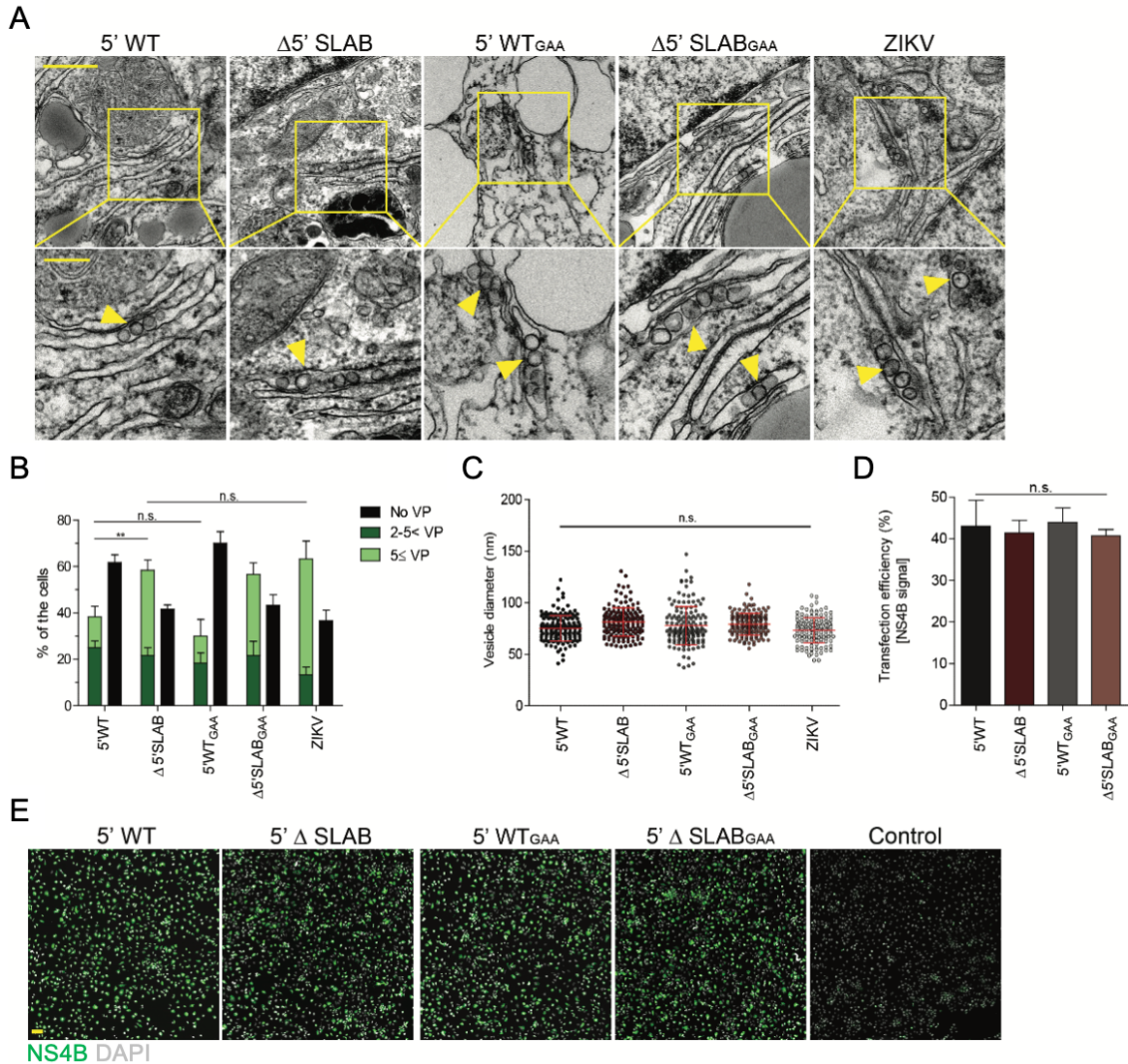


Figure 15. The ZIKV 5'UTR is dispensable for replication organelle biogenesis. (Adapted from [385])

(A) Thin-section TEM images of ROs induced upon transfection of indicated constructs. Cells were transfected or infected with ZIKV and, after 18 hours or 24 hours, respectively, fixed, processed, and embedded in resin for sectioning. Lower panels are the magnification of yellow square indicated area in the upper panel images. Scale bars: 500 nm (upper panel) and 200 nm (lower panel). (B) Cells were counted according to VP formation efficiency for each construct indicated. Means \pm SEM are represented from three independent quantifications. For each experiment 20 cells were counted. n.s., not significant (**, $p < 0.01$). (C) Diameters of vesicles were measured manually using Fiji software. Means \pm SEM are from three independent measurements. 50 vesicles were counted per experiment. n.s., not significant. (D) Transfection efficiencies were quantified according to NS4B staining by a custom-made macro for Fiji software. Error bars represent the SEM of three independent experiments. n.s., not significant. (E) IF images of NS4B staining showing the transfection efficiency for the indicated constructs. Scale bar: 100 μ m.

(TEM). For assessing the efficiency of individual constructs to induce VPs, three categories were defined as follows: cells with i) no VPs, ii) 2 to 5 VPs, and iii) more than 5 VPs. Cells containing only one vesicle were defined as false positive and therefore were not included in the quantifications. Although both constructs were able to induce vesicles in the lumen

4. Results

of the ER (Figure 15a), cells transfected with the 5'WT construct showed a 1.5-fold decrease in RO positive cells. Interestingly, the Δ 5'SLAB construct induced ROs to a similar extent as ZIKV infection (Figure 15b). Notably, size and morphology of induced VPs was not affected by the deletion mutation (Figure 15a+c), thus the plasmid induced VPs are morphologically indistinguishable from VPs found in infected cells. To exclude that the reduced number in VP positive cells for transfections with the 5'WT construct did not originate due to a reduced transfection efficiency, transfected Huh7-Lunet T7 cells were subjected to immunofluorescence-based visualization of NS4B (Figure 15e) and the subsequent quantification of positive cells (Figure 15d). In fact, transfection efficiencies were comparable among the tested constructs. To ensure, that this system induces VPs in a replication-independent manner, constructs resembling the replication-deficient NS5 mutant in which the RdRp active site is mutated (GAA), were generated. Ultrastructural characterization of Huh7-Lunet T7 cells transfected with RdRp mutant (GAA) constructs showed no significant difference in terms of percentage of cells forming VPs (Figure 15b), and further detailed analysis of induced VPs demonstrated that their size (Figure 15c) and morphology (Figure 15a) are comparable to those found in ZIKV infected cells. Taken together, my results show that ZIKV ROs can be phenocopied by expressing the ZIKV replicase (NS1-NS5) together with the 3'UTR. Furthermore, RO biogenesis does not require the active RdRp. Since the construct lacking the 5'SLAB element induced ROs to a similar extent as ZIKV infection, this construct served as template for subsequent experiments. This system (pTM/ Δ 5'SLAB/NS1-NS5/3'UTR) is referred to as Zika plasmid induced RO (pIRO-Z).

4.1.2. The essential role of the 3'UTR in the formation of ZIKV ROs

Given the results, showing that the 5'UTR is largely dispensable for the formation of ZIKV VPs, prompted me to further investigate RNA secondary elements located within the 3'UTR. The 3'UTR of the ZIKV RNA is generally divided into three domains, of which the domain III is the most conserved among flaviviruses and comprises the 3'SL which is indispensable for flavivirus replication. Therefore, I initially focused on the domain III by introducing deletion mutations into the pIRO-Z Δ 5'SLAB construct targeting the 3'sHP, 3'UAR, and 3'SL RNA structures (Figure 16a). Characterization of these newly generated constructs was performed as mentioned above using western blot analysis for polyprotein processing and protein abundance, immunofluorescence microscopy for subcellular localization and transfection efficiency, and TEM for VP formation. Given my results, deletions

4. Results

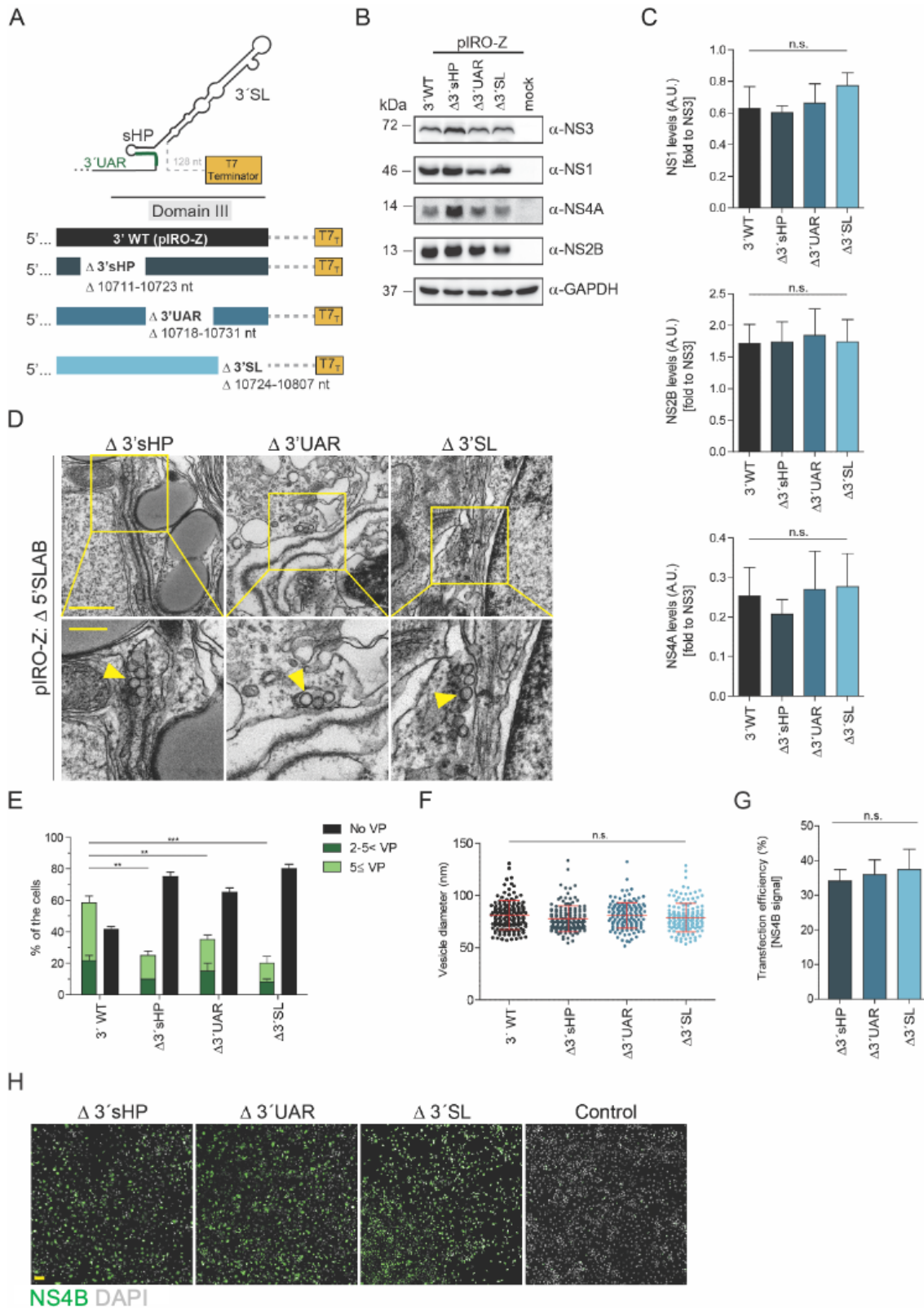


Figure 16. Role of RNA elements in the domain III of the ZIKV 3'UTR in replication organelle formation. (Adapted from [385])

(A) Schematic representation of 3'UTR domain III truncation mutations introduced into the pIRO-Z Δ5'SLAB construct. Numbers refer to the nucleotides that were deleted. (B) Huh7-Lunet T7 cells were either transfected with pIRO-Z 3'WT or indicated truncation mutations for 18 hours before being lysed and subjected to western blot analysis. Immunoblot shows the expression of NS3, NS1, NS4A, and NS2B. GAPDH was used as loading control. [Legend continues next page]

4. Results

(**C**) Relative polyprotein processing efficiency was calculated by densitometry normalizing the signals of NS1, NS2B, and NS4A to NS3 expression levels in each indicated construct. Values represent mean \pm SEM of three independent experiments. n.s., not significant. (**D**) TEM images of Huh7-Lunet T7 cells upon transfection of indicated constructs. Cells were transfected and after 18 hours fixed, processed, and resin-embedded for sectioning. Lower panels are the magnification of yellow square indicated area in the upper panel images. Scale bars: 500 nm (upper panel) and 200 nm (lower panel). (**E**) VP formation efficiency was quantified for each indicated construct. Means \pm SEM from three independent quantifications are shown. For each experiment 20 cells were counted. (*, $p < 0.05$) (**, $p < 0.01$). (**F**) Vesicle diameter measurements were performed manually using Fiji software. Means \pm SEM are from three independent measurements. 50 vesicles were counted per experiment. n.s., not significant. (**G**) Transfection efficiency rates were determined according to NS4B staining with a custom-made macro for Fiji software. Error bars represent the SEM of three independent experiments. n.s., not significant. (**H**) IF images of the signal from NS4B specific antibodies showing the transfection efficiencies for the indicated constructs. Scale bar: 100 μ m.

within the domain III of the 3'UTR did not affect the processing of the ZIKV polyprotein (Figure 16b), the abundance of cleaved viral proteins (Figure 16c), and the subcellular localization of NS3, NS4B and NS5 (Figure 14a+b). Interestingly, the ultrastructural analysis of pIRO-D (the same system for dengue) transfected Huh7-Lunet T7 cells showed that deletion of the 3'SL fully disrupted DENV VP formation³⁸⁵. In contrast, deletion of the 3'SL in the context of the pIRO-Z system did not suppress VP formation (Figure 16d), however, VPs were formed to a lesser extent (3-fold decrease) when compared to the parental construct (3'WT) (Figure 16e). This outcome suggests a differential requirement of RNA structures in the process of forming the viral VP. Along these lines, detailed analysis of the induced VPs demonstrated that none of the deletions affected the morphology or size (Figure 16f), which contrasts with the observations for dengue³⁸⁵. To ensure that the low numbers in VP positive cells (Figure 16e) did not originate due to a lower transfection efficiency, transfected Huh7-Lunet T7 were subjected to immunofluorescence-based visualization of NS4B, followed by the quantification of positive cells. The result shows comparable transfection efficiencies for all constructs tested (Figure 16g+h).

Given the difference between these two viruses, prompted me to introduce more extensive deletion mutations into the pIRO-Z Δ 5'SLAB construct by deleting the whole domain III and even the entire 3'UTR (Figure 17a). While processing of the ZIKV polyprotein (Figure 17b), the abundance of cleaved viral proteins (Figure 17c), and the subcellular localization of NS3, NS4B, and NS5 (Figure 14a+b) were not affected, ultrastructure analysis via TEM revealed that the extent of the introduced deletion mutation correlated with the reduction in VP positive cells (Figure 17e). However, these differences did not originate due to different transfection efficiencies, which were determined by immunofluorescence

4. Results

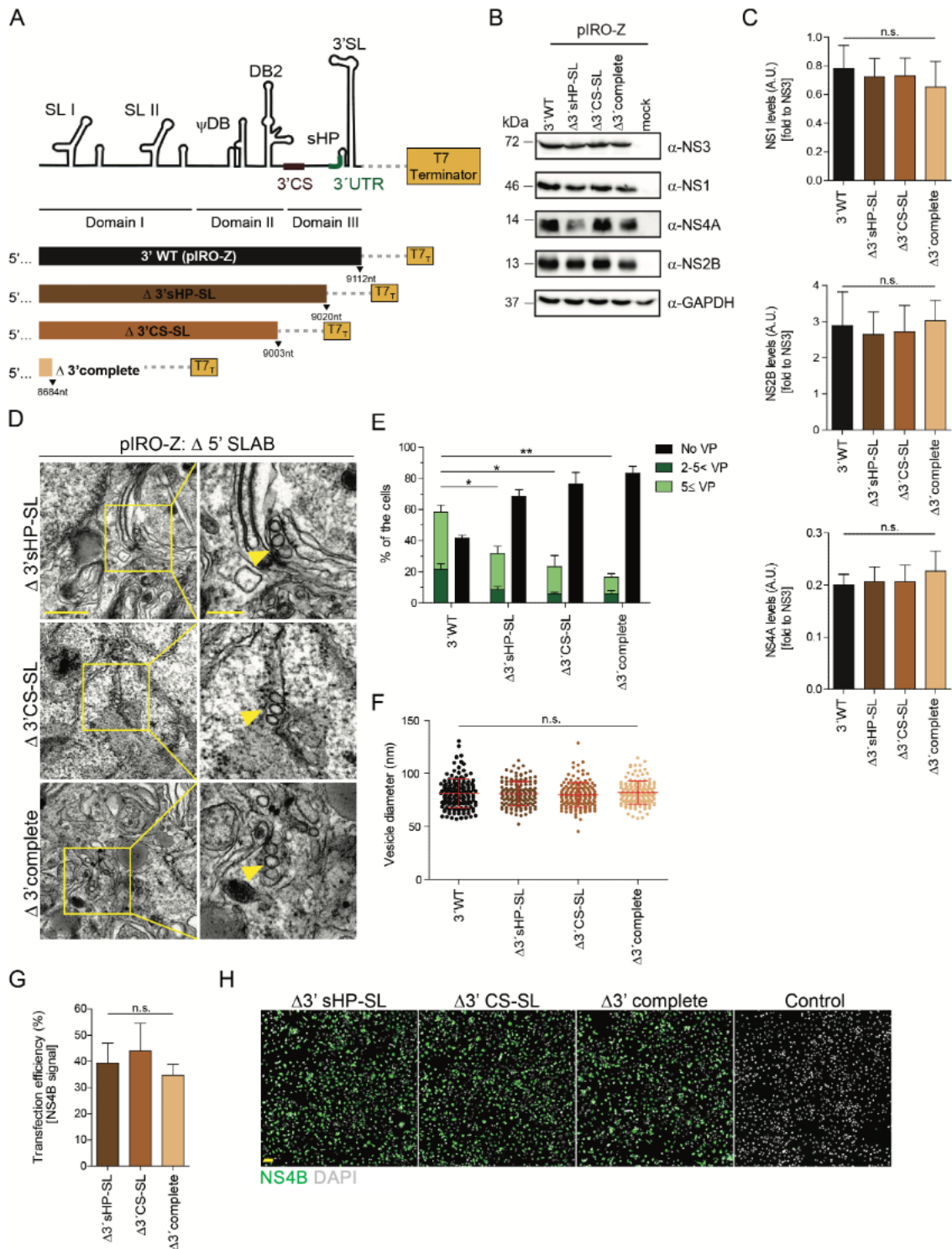


Figure 17. The ZIKV 3'UTR contributes to, but is not essential for, replication organelle formation. (Adapted from [385])

(A) Schematic representation of 3'UTR truncation mutations introduced into the pIRO-Z Δ 5'SLAB construct. Numbers refer to the last nucleotide according to the viral genome. (B) Huh7-Lunet T7 cells were either transfected with pIRO-Z 3'WT or indicated truncation mutations for 18 hours before being lysed and subjected to western blot analysis. Immunoblot shows the expression of NS3, NS1, NS4A, and NS2B. GAPDH was used as loading control. (C) Relative polyprotein processing efficiency was calculated by densitometry normalizing the signals of NS1, NS2B, and NS4A to NS3 expression levels in each indicated construct. Values represent mean \pm SEM of three independent experiments. n.s., not significant. [Legend continues next page]

4. Results

(**D**) TEM images of Huh7-Lunet T7 cells upon transfection of indicated constructs. Cells were transfected and after 18 hours fixed, processed, and resin-embedded for sectioning. Lower panels are the magnification of yellow square indicated area in the upper panel images. Scale bars: 500 nm (upper panel) and 200 nm (lower panel). (**E**) VP formation efficiency was quantified for each indicated construct. Means \pm SEM from three independent quantifications are shown. For each experiment 20 cells were counted. (*, $p < 0.05$) (**, $p < 0.01$). (**F**) Vesicle diameter measurements were performed manually using Fiji software. Means \pm SEM are from three independent measurements. 50 vesicles were counted per experiment. n.s., not significant. (**G**) Transfection efficiency rates were determined according to NS4B staining with a custom-made macro for Fiji software. Error bars represent the SEM of three independent experiments. n.s., not significant. (**H**) IF images of the signal from NS4B specific antibodies showing the transfection efficiencies for the indicated constructs. Scale bar: 100 μ m.

microscopy staining for NS4B followed by the quantification of positive cells (Figure 17g+h). Finally, ultrastructural analyses of the plasmid induced ZIKV VP showed that even with the full 3'UTR being deleted size or morphology remained unaffected (Figure 17d; Figure 17f). This outcome is contrary to the previously proposed model in which the length of the viral RNA determines the size of VPs. This suggests that ZIKV RO formation requires other viral or host factors.

4.1.3. Requirement of an authentic 3'end

Given the essential role of the 3'UTR in the formation of DENV RO, raised the question whether the biogenesis of ROs requires an authentic 3'end. So far, transcription of the described expression constructs was terminated via the plasmid encoded T7 terminator sequence³⁸⁶, causing an extension of 128 nucleotides which are unrelated to the viral RNA genome. To assess whether these additional nucleotides affect the formation of viral ROs, the parental construct pIRO-Z (Δ 5'SLAB/NS1-NS5/3'UTR) was modified by inserting the self-cleaving ribozyme of the hepatitis D virus (HDV) downstream of the 3'UTR (Figure 18a). The addition of the HDV ribozyme did not affect the processing of the ZIKV polyprotein (Figure 18b), the abundance of cleaved viral proteins (Figure 18c), the VP inducing efficiency (Figure 18e), and RO morphology (Figure 18d) and size (Figure 18f). This outcome is in contrast to the findings using the pIRO-D system, as addition of the HDV ribozyme significantly enhanced VP formation in Huh7-Lunet T7 cells transfected with the pIRO-D system³⁸⁵. Although the presence of the HDV ribozyme did not increase the efficiency of inducing viral ROs, subsequent experiments were performed using the HDV ribozyme modified pIRO-Z construct (Δ 5'SLAB/NS1-NS5/3'WT-Rib), to ensure authentic viral RNA transcripts upon transfection

4. Results

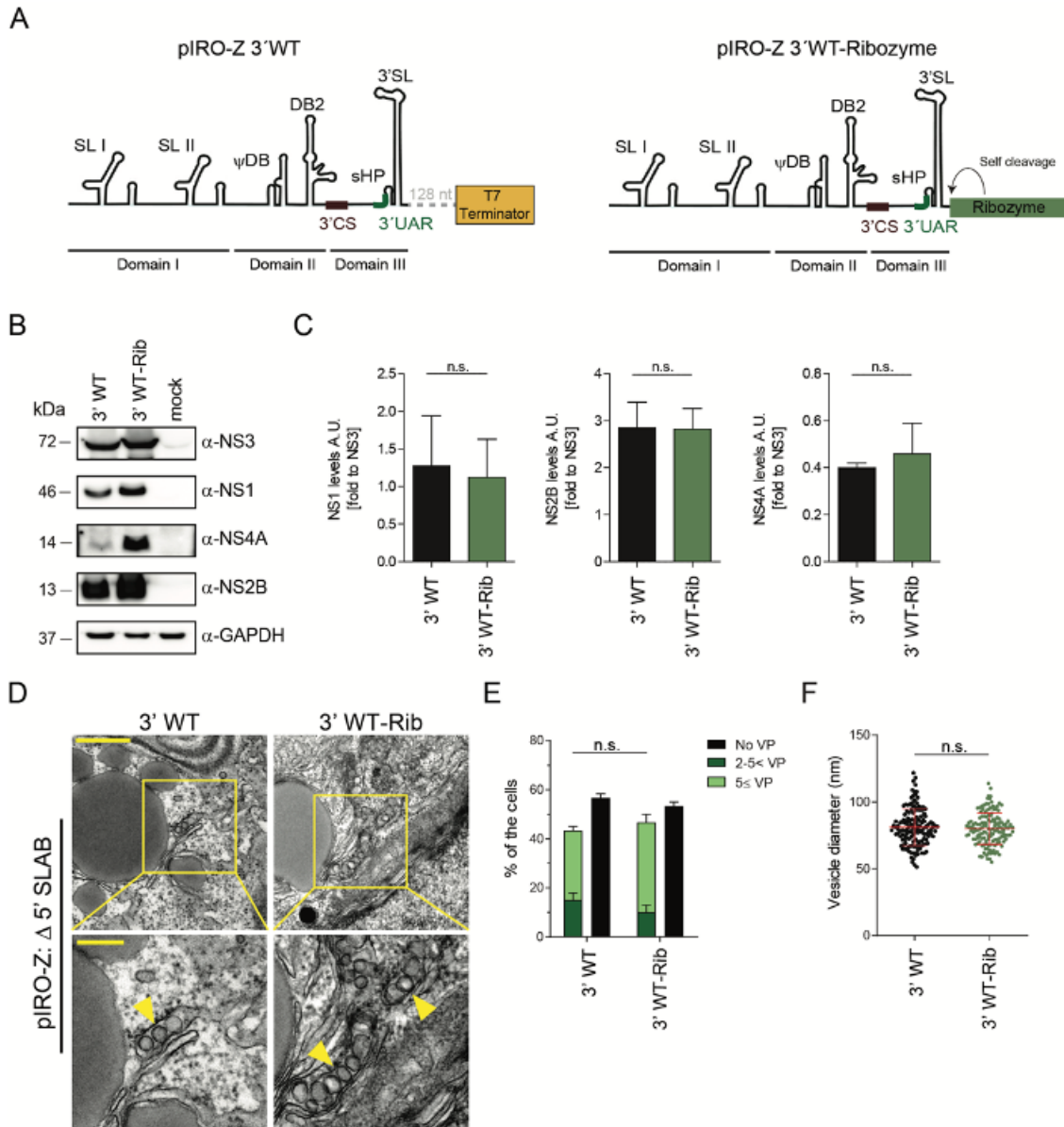


Figure 18. ZIKV replication organelle formation does not require an authentic 3' end. (Adapted from [385])

(A) Schematic representation of 3'WT and 3'WT-ribozyme piRO-Z Δ 5'SLAB construct. (B) Huh7-Lunet T7 cells were either transfected with piRO-Z 3'WT or piRO-Z 3'WT-ribozyme for 18 hours before being lysed and subjected to western blot analysis. Immunoblot shows the expression of NS3, NS1, NS4A, and NS2B. GAPDH was used as loading control. (C) Relative polyprotein processing efficiency was calculated by densitometry normalizing the signals of NS1, NS2B, and NS4A to NS3 expression levels in each indicated construct. Values represent mean \pm SEM of three independent experiments. n.s., not significant. (D) TEM images of Huh7-Lunet T7 cells upon transfection of indicated constructs. Cells were transfected and after 18 hours fixed, processed, and resin-embedded for sectioning. Lower panels are the magnification of yellow square indicated area in the upper panel images. Scale bars: 500 nm (upper panel) and 200 nm (lower panel). (E) VP formation efficiency was quantified for both constructs. Means \pm SEM from three independent quantifications are shown. For each experiment 20 cells were counted. n.s., not significant (F) Vesicle diameter measurements were performed manually using Fiji software. Means \pm SEM are from three independent measurements. 50 vesicles were counted per experiment. n.s., not significant.

4.2. pIRO-Z and its application to unravel the mode of action of a ZIKV NS4A inhibitor

After having established a system which phenocopies ZIKV ROs in the absence of viral replication^{385,387}, the pIRO-Z system was used to dissect the mode of action of an antiviral compound, referred to as SBI-0090799 (Figure 19a), which was provided by the Sanford Burnham Prebys Medical Discovery Institute in California, USA. At this point, experiments performed by Riva and colleagues have shown that SBI-0090799 exhibited an IC₅₀ value of 2.072 μ M and an IC₉₀ value of 5.19 μ M with respect to the African ZIKV strain MR766. Furthermore, they showed that SBI-0090799 is active against other ZIKV strains belonging to both, the African and Asian/American lineages. However, when tested against other members of the flavivirus genus, no antiviral activity was observed, suggesting a ZIKV specific inhibition of infection. By performing time-of-addition experiments Riva and colleagues found that the compound only significantly inhibited infection when added after viral inoculation. However, the molecular mechanisms of the mode of action of SBI-0090799 remained unclear. The second part aimed to determine whether the antiviral compound SBI-0090799 affects the formation of ZIKV replication organelles.

This chapter was published and following paragraphs are adapted from the reference [88].

4.2.1. SBI-0090799 and its antiviral activity against ZIKV-H/PF/2013

First, a CellTiter Glo cell viability assay was performed to determine a non-cytotoxic concentration for SBI-0090799. For this, Huh7-Lunet T7 cell monolayers were treated for 24 hours over a range of ten concentrations ranging from 80 μ M to 40 nM. The result shows that cell viability was not significantly affected at any concentration tested (Figure 19b, red line). As the pIRO-Z system is based on the genetic information of the Asian ZIKV strain H/PF/2013, the next step was to confirm the antiviral activity of SBI-0090799 against ZIKV-H/PF/2013. For this, Huh7-Lunet T7 cells were transfected with *in vitro* transcribed infectious ZIKV RNA encoding the sub-genomic replicon in which the structural proteins have been replaced with a *Renilla* luciferase reporter gene³⁷⁷. Directly after transfection, SBI-0090799 was provided at concentrations used for the cell viability assay. *Renilla* activity was monitored as a surrogate marker for viral replication at 24 hours. Transfected Huh7-Lunet T7 cells treated with DMSO were included as control. For

4. Results

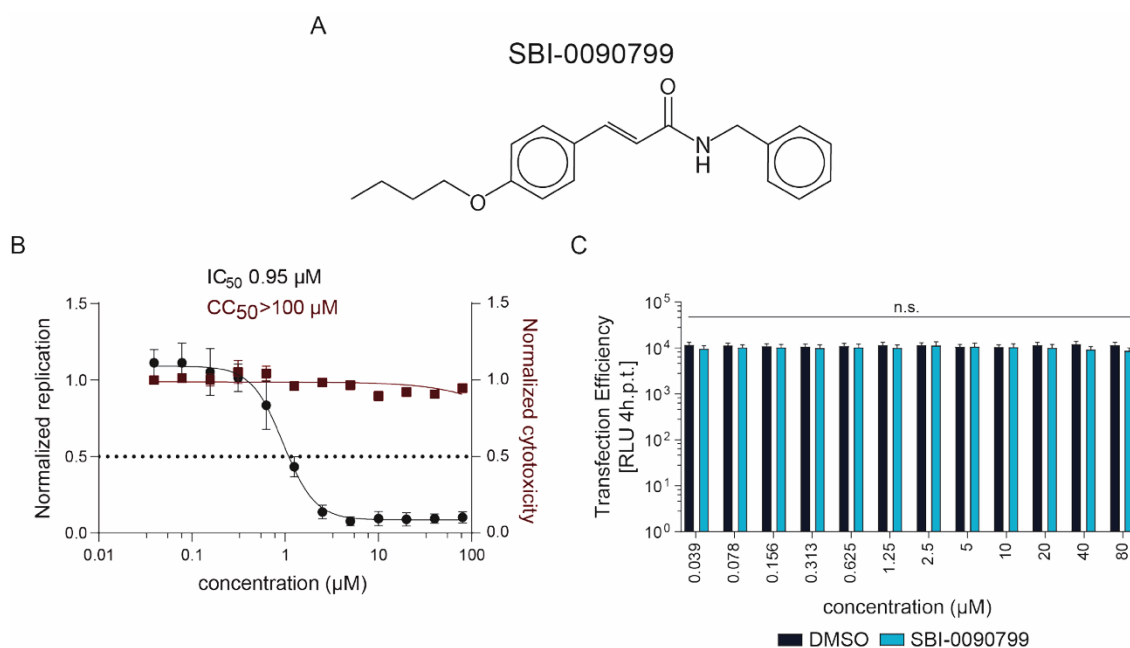


Figure 19. Assessment of antiviral activity and cytotoxicity of SBI-0090799. (Adapted from [88])

(A) Chemical structure of the antiviral compound SBI-0090799, which was identified in a large-scale high compound screen. (B+C) Effect of SBI-0090799 on the replication of the sgR2A H/PF/2013 (GeneBank ID KJ776791) replicon and viability of Huh7-Lunet T7 cells treated with various concentrations of the compound. Viral replication was assessed by measuring the *Renilla* luciferase activity 24 hours post transfection. The graph shows the percentage of replication (mean \pm SEM from three independent experiments) relative to the DMSO control. *Renilla* counts were normalized to 4 hours post transfection values reflecting transfection efficiency. The cell viability was determined by measuring ATP levels at 24 hours post treatment. The graph shows the percentage of ATP levels of compound treated cells (mean \pm SEM from three independent experiments) relative to DMSO treated control cells (triplicates per condition). n.s., not significant.

normalization, *Renilla* activity was assessed at 4 h.p.t. reflecting transfection efficiency (Figure 19c). The result shows that ZIKV-H/PF/2013 replication is SBI-0090799 sensitive in a dose-dependent manner (Figure 19b, black line), exhibiting an IC₅₀ value of 0.95 µM and an IC₉₀ value of 2.25 µM.

4.2.2. SBI-0090799 impairs the formation of ZIKV replication organelles

To study the effect of SBI-0090799 on the formation of ZIKV ROs (also known as vesicle packets (VPs)), Huh7-Lunet T7 cells were transfected with pIRO-Z in the presence of SBI-0090799 at a concentration of 12.5 µM, corresponding to \sim 6x the IC₉₀ value. As control, pIRO-Z transfected Huh7-Lunet T7 were treated with DMSO (0.125% v/v). The result shows that SBI-0090799 significantly decreased the mean number of VPs per cell profile

4. Results

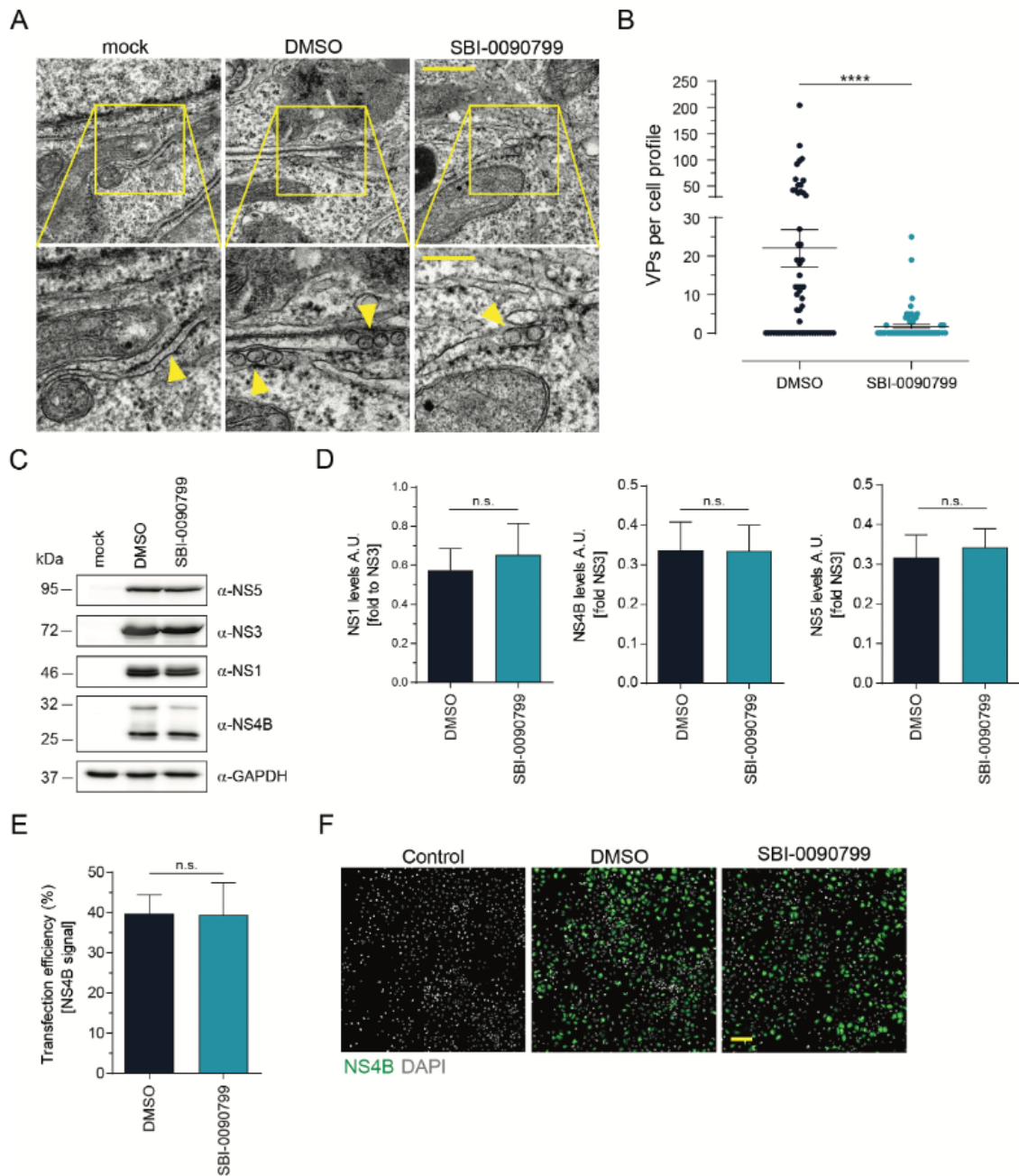


Figure 20. ZIKV replication organelle formation is suppressed by SBI-0090799. (Adapted from [88])

(A) Huh7-Lunet T7 cells transfected with pIRO-Z in the presence of either SBI-0090799 [12.5 μ M] or DMSO [0.125% v/v], for 18 hours were processed for transmission electron microscopy. Lower panels are the magnification of yellow-square indicated areas in the upper panel. Scale bars: 500nm and 200nm, in the upper and lower panel, respectively. Replication organelles are indicated by the yellow arrowhead. (B) Vesicle packets (VPs) inducing efficiency was determined by counting the number of VPs per cell profile. Per experiment a total of 20 cell profiles were analyzed. Means \pm SEM are shown from three independent experiments (****, $p < 0.0001$). (C) Immunoblot of Huh7-Lunet T7 cells transfected with the pIRO-Z construct in the presence of either SBI-0090799 [12.5 μ M] or DMSO [0.125% v/v] for 18 hours is shown. Polyprotein processing was assessed by probing for the non-structural proteins NS5, NS3, NS1 and NS4B. As loading control GAPDH was used. (D) Abundance of cleaved proteins was calculated by densitometry of the western blot signals for determining the relative polyprotein processing efficiency. Signals of NS1, NS4B or NS5 were normalized to NS3 expression levels in each sample. Values represent mean \pm SEM of three independent experiments. n.s., not significant. [Legend continues next page]

4. Results

(E) Immunofluorescence staining of NS4B was used to determine transfection efficiencies. Quantification was done automated using a custom-made macro for the FIJI software package. Error bars represent the SEM of three independent experiments. n.s., not significant. (F) Representative IF images of Huh7-Lunet T7 cells transfected with the pIRO-Z transfected cells in the presence of either SBI-0090799 [12.5 μ M] or DMSO [0.125% v/v] are shown upon NS4B staining. As staining control mock-transfected cells were included, that were treated with the compound. Nuclear DNA was stained with DAPI. Scale bar: 100 μ m.

when compared to the DMSO control (Figure 20b), without affecting the morphology (Figure 20a). To exclude that the antiviral compound had an effect on polyprotein processing and the abundance of ZIKV non-structural proteins Huh7-Lunet T7 cells were transfected and at 18 hours post transfection subjected to western blot analysis (Figure 20c). My results show that polyprotein processing (Figure 20c) and abundance of cleaved protein products (Figure 20d) were comparable to the control in which transfection occurred in the presence of DMSO, the solvent of the compound. Next, to exclude that SBI-0090799 affects transfection, transfected cells were subjected to immunofluorescence-based visualization of NS4B (Figure 20f), followed by the quantification of positive cells (Figure 20e). Additionally, to exclude that SBI-0090799 affects the subcellular localization of non-structural proteins, immunofluorescence-based visualization of NS3, NS4B or NS5 was performed (Figure 21). The result shows that NS3 and NS4B localized to the ER (Figure 21a) whereas NS5 localized to the nucleus (Figure 21b), which was visualized using RTN-3 and DAPI.

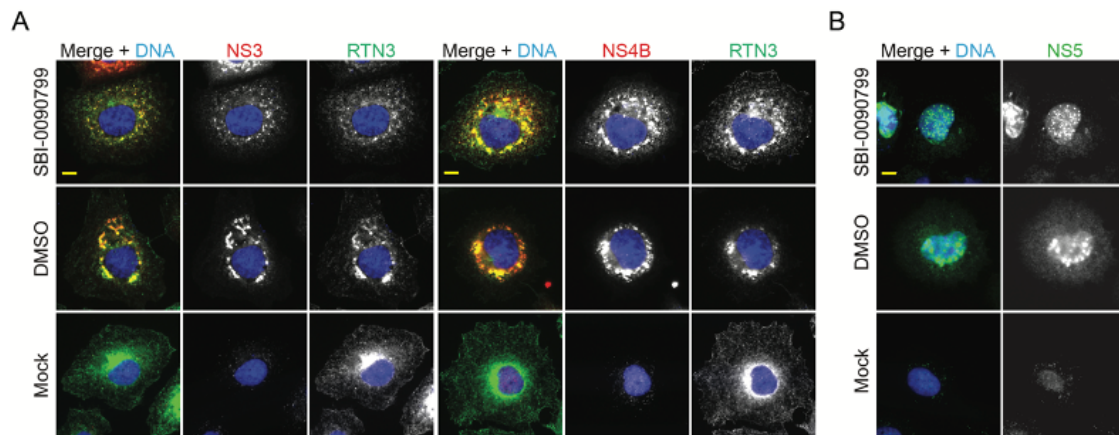
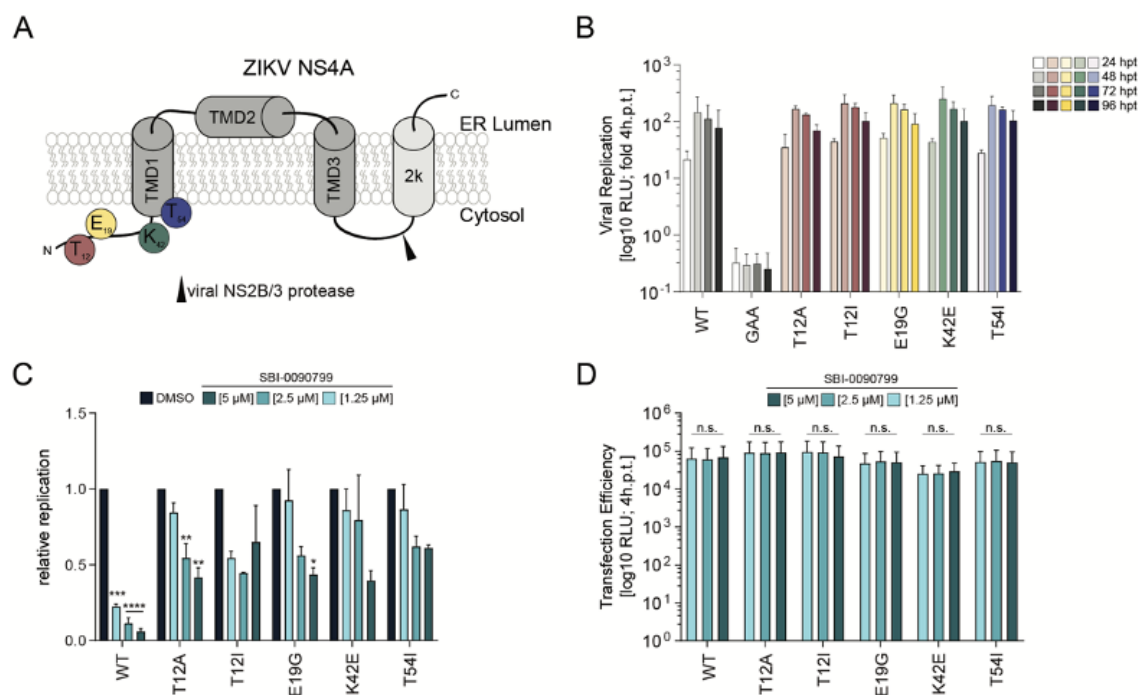


Figure 21. SBI-0090799 does not affect the subcellular localization of ZIKV NS proteins.

Huh7-Lunet T7 cells were transfected with the pIRO-Z construct in the presence of either SBI-0090799 [12.5 μ M] or DMSO [0.125% v/v] for 18 hours before. Cells were fixed for immunofluorescence analysis after 18 hours of transfection. (A) Subcellular localization of NS3 and NS4B was assessed by staining the ER using RTN3. Scale bars: 10 μ m. (B) Nuclear localization of NS5 was assessed by staining cellular DNA with DAPI. Scale bar: 10 μ m.

4. Results



4.2.3. Mutations within NS4A confer resistance to SBI-0090799 and restore RO formation

Passaging of ZIKV in the presence of the antiviral compound has shown that as early as passage 2, resistance mutations start to develop⁸⁸. Thereafter, viruses were sequenced identifying 4 mutations which all localized in the cytosolic N-terminal region of NS4A (Figure 22a). To exclude that these resistance mutations in general affect virus replication fitness, mutations were initially introduced into the ZIKV sub-genomic replicon. As positive and negative control, wild type and the replication deficient NS5 mutant (GAA) were included. Monitoring *Renilla* activity as surrogate for viral replication over a period of 96 hours showed no significant differences between WT and mutant NS4A ZIKV

4. Results

(Figure 22b). To investigate whether NS4A mutations provide resistance towards SBI-0090799, Huh7-Lunet T7 cells were transfected with *in vitro* transcribed RNA and immediately treated with the antiviral compound at a final concentration of 1.25 μM , 2.5 μM , or 5 μM . Virus replication was assessed at 24 hours post transfection by monitoring *Renilla* luciferase activity (Figure 22c). In fact, the result shows that all mutations within the cytosolic N-terminus of NS4A confer resistance to SBI-0090799, with a remaining replication efficacy given in Table 17. To exclude that observed differences between WT and mutant NS4A ZIKV did not originate due to different transfection efficiencies, *Renilla* activity was monitored at 4-hour value, representing the initial translation rate (Figure 22d).

Table 17. Relative replication of WT and NS4A mutant ZIKV replicons in the presence of various concentration of SBI-0090799. In color is given the severity of inhibition with red showing the strongest and blue the weakest inhibition.

SBI-0090799	WT	T12A	T12I	E19G	K42E	T54I
1.25 μM	0.23 \pm 0.02	0.85 \pm 0.07	0.55 \pm 0.05	0.93 \pm 0.21	0.86 \pm 0.14	0.87 \pm 0.17
2.5 μM	0.12 \pm 0.04	0.55 \pm 0.10	0.45 \pm 0.01	0.56 \pm 0.06	0.80 \pm 0.30	0.62 \pm 0.07
5 μM	0.06 \pm 0.02	0.42 \pm 0.07	0.65 \pm 0.24	0.44 \pm 0.05	0.40 \pm 0.06	0.61 \pm 0.02

Furthermore, to confirm that resistance also restores the formation of VPs, the above-mentioned mutations were introduced into the pIRO-Z system. While processing of the ZIKV polyprotein (Figure 23a), abundance of cleaved viral proteins (Figure 23b), and the transfection efficiency (Figure 23f+g) were not affected by the introduced mutations, ultrastructural analysis of Huh7-Lunet T7 cells transfected with respective pIRO-Z constructs revealed a rescue in the formation of ZIKV replication organelles (Figure 23c+e). In fact, the construct harboring the NS4A mutation K42E was the most potent mutant as its efficiency to induce ZIKV VPs was higher than the one observed for WT (Figure 23e). Of note, NS4A mutations did not have an effect on the size of induced replication organelles, which all had a diameter of approximately 80 nm (Figure 23d).

4. Results

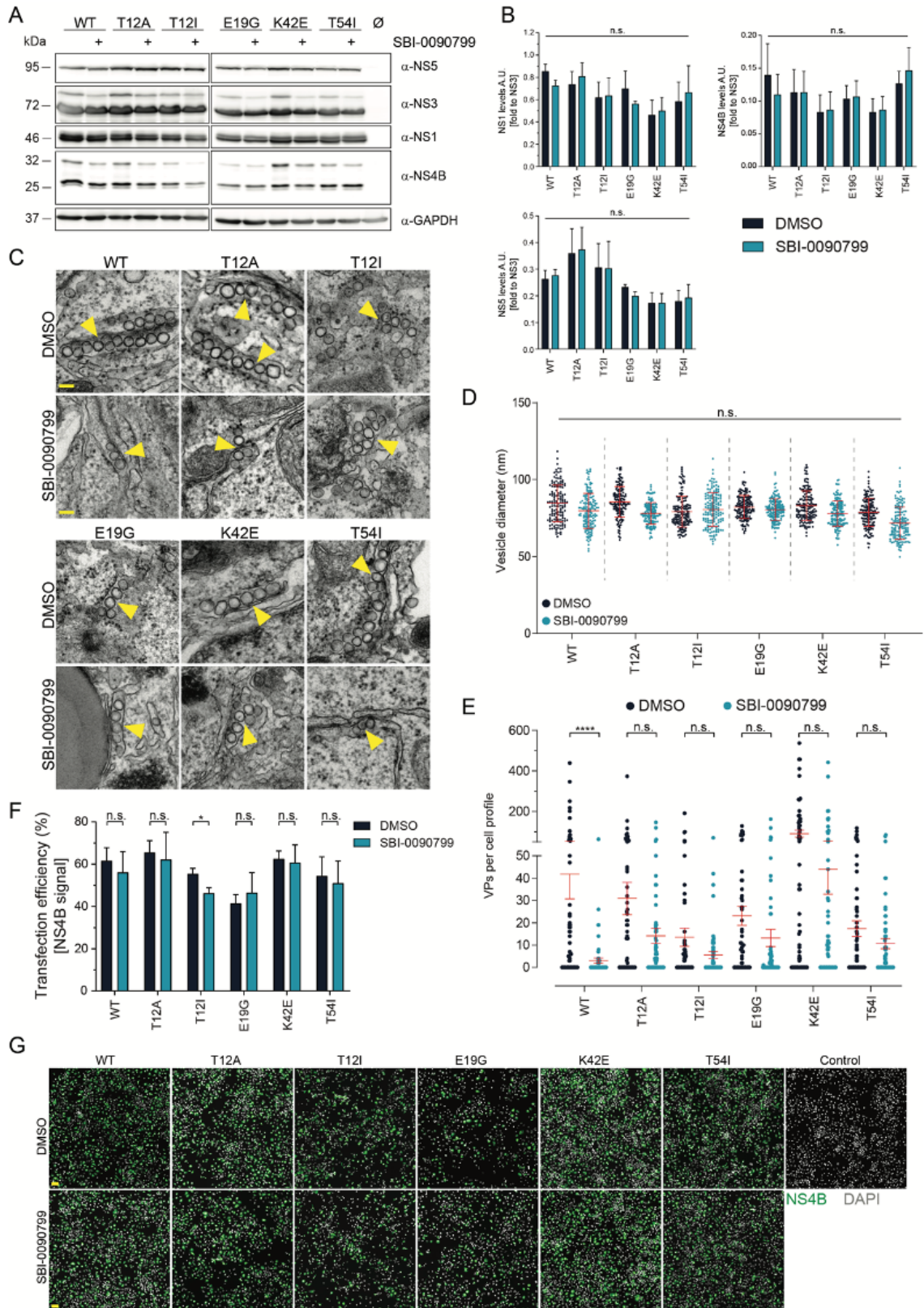


Figure 23. Mutations in NS4A restore ZIKV replication organelle formation in the presence of SBI-0090799. (Figure taken from [88])

(A) Immunoblot of cell lysates derived from transfected Huh7-Lunet T7 cells treated with either SBI-0090799 [12.5 μ M] or DMSO [0.125% v/v] for 18 hours. Polyprotein processing was assessed by probing for the non-structural proteins NS5, NS3, NS1 and NS4B. GAPDH was used as loading control. [Legend continues next page]

4. Results

(B) Abundance of cleaved proteins was calculated by densitometry of the western blot signals for determining the relative polyprotein processing efficiency. Signals of NS1, NS4B or NS5 were normalized to NS3 expression levels in each sample. Values represent mean \pm SEM of three independent experiments. n.s., not significant. **(C)** (Huh7-Lunet T7 cells transfected with pIRO-Z in the presence of either SBI-0090799 [12.5 μ M] or DMSO [0.125% v/v]. for 18 hours were processed for transmission electron microscopy. Lower panels are the magnification of yellow-square indicated areas in the upper panel. Scale bars: 500nm and 200nm, in the upper and lower panel, respectively. Replication organelles are indicated by the yellow arrowhead. **(D)** Vesicle diameter measurements were performed manually using Fiji software. Means \pm SEM are from three independent measurements. 50 vesicles were counted per experiment. n.s., not significant. **(E)** Vesicle packets (VPs) inducing efficiency was determined by counting the number of VPs per cell profile. Per experiment a total of 20 cell profiles were analyzed. Means \pm SEM are shown from three independent experiments (****. $p < 0.0001$). **(F)** Transfection efficiencies were determined by quantifying the number of NS4B containing cells using a custom-made macro for the FIJI software package. Error bars represent the SEM of three independent experiments (n.s., not significant; *, $P < 0.05$) **(G)** Representative IF images of Huh7-Lunet T7 cells transfected with the pIRO-Z transfected cells in the presence of either SBI-0090799 [12.5 μ M] or DMSO [0.125% v/v] are shown upon NS4B staining. As staining control mock-transfected cells were included, that were treated with the compound. Nuclear DNA was stained with DAPI. Scale bar: 100 μ m.

4.3. Cholesterol and its role during ZIKV entry and virus particle production

To date it is well established that flaviviruses share an intimate union with host cellular lipids at several steps during their infectious replication cycle. With respect to the mammalian host, previous studies have demonstrated that cholesterol plays a crucial role not only during virus entry but also during the assembly of new progeny viruses. In the context of viral entry, it was shown that WNV³⁴⁹ and ZIKV²⁸⁵ required cholesterol in host cellular target membranes, as experimental extraction of cholesterol using the solubilizing drug methyl-beta-cyclodextrin inhibited virus infection. While cholesterol in target membranes is dispensable for DENV infection, the presence of cholesterol within the viral envelope was found to be important, suggesting its role during viral fusion in late endosomes³⁴⁸. Within the last couple of years, lipidomic analyses^{322,323,329,330} of infected cells provided detailed insights into virus-induced changes revealing a fine-tuned and time-dependent interplay between the virus and its host. Regarding virus assembly, previous studies have highlighted that interference with the *de novo* synthesis of cholesterol using lipophilic statins, inhibitors of the HMG-CoA reductase, significantly reduced extracellular infectious titers of DENV and ZIKV by inhibiting virus assembly^{337,338}. While these studies have demonstrated that cellular cholesterol is an essential host factor, direct interactions between cholesterol and viral proteins have been scarcely studied.

This chapter will soon be published and following paragraphs are originally written by me.

4.3.1. ZIKV entry and particle production are cholesterol dependent

Given the aim to identify direct viral protein-cholesterol interactions and its requirement for the ZIKV replication cycle, prompted me to first confirm previous results, showing that ZIKV-H/PF/2013 requires cholesterol to complete its infectious replication cycle. For this, I experimentally manipulated cellular cholesterol levels by using on the one hand the solubilizing drug methyl- β -cyclodextrin³⁸⁸⁻³⁹¹ and on the other hand the lipophilic agent lovastatin which inhibits the HMG-CoA reductase thus preventing the *de novo* biosynthesis of cholesterol³⁹²⁻³⁹⁴. To identify non-cytotoxic concentrations for both drugs CellTiter Glo cell viability assays were performed. For this, VeroE6 or Huh7-Lunet naïve cells were seeded in 96-well plates and one day post seeding cell monolayers were treated with various

4. Results

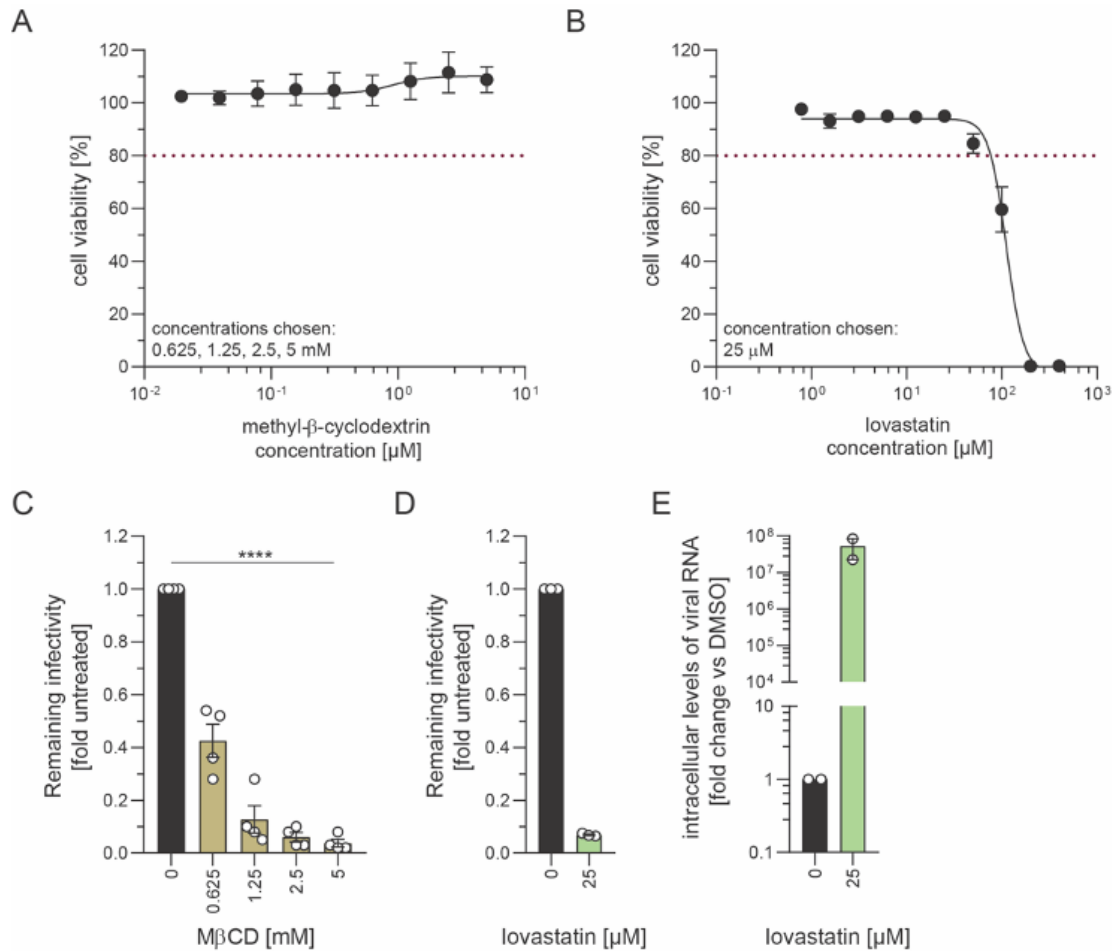


Figure 24. MβCD and lovastatin have antiviral activity against ZIKV.

(A+B) Cell viability was determined by measuring ATP levels after a 24- and 48-hours treatment using the (A) cholesterol solubilizing drug methyl-beta-cyclodextrin (MβCD) or (B) the MHG-CoA reductase inhibitor lovastatin. The graphs show the percentage of cells surviving (mean ±SEM) relative to the control (water or DMSO only). Each condition was analyzed in triplicates. Final concentrations used for subsequent experiments are indicated in the lower left corner. (C) VeroE6 cells were pretreated with various concentrations of MβCD for 3 hours at 37°C. Thereafter, cells were washed with delipidated media, followed by infection with ZIKV (MOI=3). Twenty-four hours post-infection, supernatants were collected and titrated by plaque assay. Bars represent the means of the remaining infectivity (ratio treated/untreated) from four independent experiments. (D) Huh7-Lunet naïve cells were infected with ZIKV (MOI=1) prior to treatment with lovastatin (25 μM). Newly produced virus was detected and quantified by plaque assay at 48 hours post infection. Bars represent the means of the remaining infectivity (ratio treated/untreated) from three independent experiments. (E) Cells from (D) were lysed and subjected to qRT-PCR analysis for quantification of intracellular levels of viral RNA. Bars represent the means from two independent experiments.

concentrations of MβCD and lovastatin, in a range of 5 mM down to 10 μM and 200 μM down to 0.4 μM, respectively (Figure 24a+b). For MβCD cell viability was assessed at 24 hours whereas for lovastatin cell viability was assessed at 48 hours post treatment. For subsequent experiments concentrations which caused less than 20% of reduction in ATP levels were chosen (Figure 24a+b). To investigate whether ZIKV infection is sensitive to

4. Results

cholesterol levels within target membranes, VeroE6 cell monolayers were treated for 3 hours at 4 different concentrations of M β CD prior to ZIKV infection (MOI=3). Relative infectivity was assessed at 24 hours post infection by titration of extracellular titers via plaque assays (Figure 24c). As control and for normalization, cells were infected and treated with water, the solvent of the drug. The result shows that ZIKV-H/PF/2013 infection is sensitive to M β CD in a dose dependent manner, thus, confirming previous findings showing that ZIKV infection is cholesterol dependent. Next, I investigated whether ZIKV replication or particle production rely on the *de novo* biosynthesis of cholesterol using the HMG-CoA reductase inhibitor lovastatin. For this, Huh7-Lunet naïve cells were seeded in 24-well plates and one day post seeding cells were infected with ZIKV-H/PF/2013 (MOI=1). To exclude defects on virus entry, lovastatin was added to the cell culture medium at 4 h.p.i. at a final concentration of 25 μ M. Virus particle production was assessed at 48 h.p.i. via plaque assays (Figure 24d) whereas virus replication was assessed by qRT-PCR quantifying intracellular levels of viral RNA (Figure 24e). In line with previous findings, inhibition of the *de novo* biosynthesis of cholesterol significantly reduced extracellular infectious titers when compared to DMSO treated cells. Notably, when comparing lovastatin treated cells with DMSO treated cells with respect to intracellular levels of viral RNA, revealed that lovastatin caused a remarkable increase (Figure 24e). These results suggest that *de novo* biosynthesis of cholesterol is rather required during virus assembly and egress than during virus replication. Taken together, these results show that cholesterol is involved at two steps of the Zika viral replication cycle - virus entry and virus particle production.

4.3.2. Probing ZIKV structural proteins for cholesterol interaction

Based on these results showing that cholesterol indeed is involved during ZIKV entry and particle production, I wondered whether ZIKV structural proteins have the ability to interact with host cellular cholesterol. To identify cholesterol binding viral proteins, I performed chemo-proteomics using a photoreactive and clickable cholesterol probe which has been used in previous studies to reveal protein-cholesterol interactions^{354,381,382} (Figure 25a). While the diazirine group at position 6 allows crosslinking to interacting proteins in close proximity ($<3\text{\AA}$)³⁸⁰ via ultraviolet irradiation, the alkyne group at the alkyl side chain is used for copper catalyzed azide-alkyne cycloaddition (CuAAC) to azide-biotin, thus allowing specific enrichment of proteins via lipid affinity purification. For probing viral proteins for their potential to bind to cholesterol Huh7-Lunet naïve cells were infected with ZIKV-

4. Results

H/PF/2013 (MOI=10). At 24 h.p.i. cells were labeled with 10 μ M of the photoreactive and clickable cholesterol probe. Crosslinking of the probe to viral proteins was facilitated by UV irradiation for 5 minutes. Thereafter, whole cell lysates were subjected to click chemistry for cycloaddition of azide-biotin to facilitate affinity purification using neutravidin resin beads. Enriched proteins were identified by western blot analysis using commercially available antibodies (Figure 25b). Although substantial amounts of viral proteins were detected in the input for both conditions – with and without ultraviolet irradiation; enrichment and purification of interacting viral proteins was highly specific for samples which were exposed to ultraviolet light (Figure 25c). Western blot analysis showed a significant enrichment for the structural prM protein. Notably, a significant enrichment of its cleaved form - the membrane embedded M domain, was also observed, indicating that mature virus particles could be associated with cholesterol (Figure 25c+d). Next to the structural protein prM, also three non-structural proteins, namely NS2B, NS4A, and NS4B were significantly enriched. However, no significant enrichment was observed for the structural protein capsid and envelope and the non-structural proteins NS1, NS3, and NS5, suggesting that no close association exists with cholesterol (Figure 25c+d).

4.3.3. Identification of potential cholesterol binding domains in the structural protein prM

Given my results showing that cholesterol is required for ZIKV entry and particle production and given my results that the structural protein prM interacts with the cholesterol probe I focused in my PhD on the interaction between the prM protein and cholesterol. For this, I next performed bioinformatic analysis aiming to identify potential cholesterol recognition amino acid consensus sequences (CRAC) and its “mirror” motif (CARC) which have been reported in previous studies^{395,396}. While the CRAC motif consists, from the N- to C-terminus, of an apolar residue (leucine [L] or valine [V]), up to five random amino acids, an aromatic residue (tyrosine [Y] or phenylalanine [F]), up to five random amino acids, and a basic residue (arginine [R] or lysine [K])³⁹⁷ (Figure 26a), its “mirror” motif CARC follows the same pattern in the opposite direction (Figure 26a). To this end, I have identified six potential cholesterol binding domains within the structural prM protein of which three are located within the soluble pr peptide and three are located within the membrane embedded M domain (Figure 26b+c). Considering that the prM protein gets cleaved in the trans Golgi

4. Results

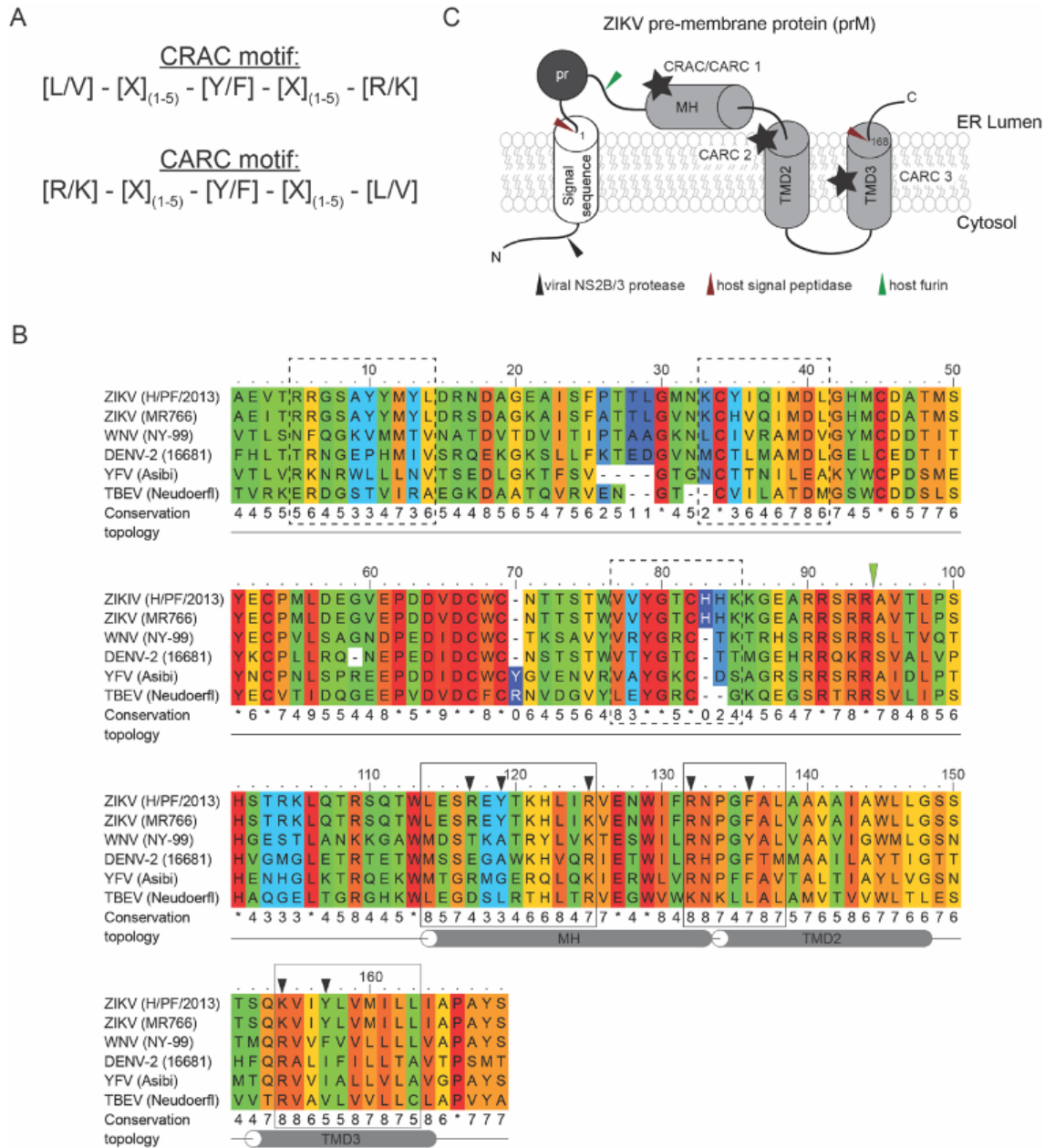


Figure 26. Identification of cholesterol binding domains in the prM protein of Zika.

(A) Cholesterol recognition amino acid consensus sequence (CRAC) and its “mirror” motif CARC. (B) Multiple-sequence alignment of prM proteins from different flaviviruses using the PRALINE multiple-sequence alignment toolbox. The residues are colored according to their degree of conservation, ranging from 1 (unconserved) to 10 (100% conserved; *). Potential cholesterol binding domains are indicated by boxes. Residues selected for mutagenesis are indicated by black arrowheads. (C) Schematic representation of the membrane topology of prM. The putative trans-membrane domains (TMD) and membrane-associated helix (MH) are represented as cylinders. The signal sequence is presented in white. Sites of proteolytic processing of the polyprotein are indicated. pr is represented in dark gray whereas M is represented in light gray.

network to obtain infectious virus particles, I set the focus on the cholesterol binding domains in the M domain, as this remains associated with virions upon release into the extracellular space. At this point of my PhD, little was known about the function of the prM

4. Results

protein in the virus replication cycle especially regarding its interplay with host cellular lipids.

Mapping the location of the three identified potential cholesterol binding domains in the membrane topology of the M domain revealed that one CRAC motif overlapped with one CARC motif within the membrane helix (MH), and two CARC motifs locate within the transmembrane domains (TMD) 2 and 3 (Figure 26c). Furthermore, multiple sequence alignment revealed that the two CARC motifs within the TMD2 and TMD3 are highly conserved among members of the flavivirus genus (Figure 26b), suggesting an important role during the flavivirus replication cycle.

4.3.4. Functional characterization of cholesterol binding domains within the M domain of the structural prM protein

Although CRAC and CARC motifs have been identified in a variety of proteins including the peripheral-type benzodiazepine receptor³⁹⁵, the tyrosine kinase receptor family³⁹⁸, the viral protein gp41 of the human immunodeficiency virus³⁹⁹ and the influenza M2 protein⁴⁰⁰, yet the sole presence of such motifs does not confer the ability of the protein to interact with cholesterol⁴⁰¹. To functionally characterize the cholesterol binding domains within the M domain, HA-tagged prM proteins were expressed, from wild type (WT) and mutants, in which the aromatic residue and the basic residue have been replaced with either alanine (A) or serine (S) and leucine (L), respectively (Figure 26b; Figure 27). To ensure correct membrane topology of prM upon expression in cells, the capsid anchor sequence was added at the N-terminus alongside with the tobacco 2A peptide sequence (Figure 27a). Since the expression of prM has been associated to trigger apoptotic cell death^{402,403}, cells counteract expression by immediate degradation of newly synthesized prM proteins. To overcome this limitation, transfected cells were treated with the proteasome inhibitor MG132 for three hours at a final concentration of 5 μ M. Thereafter cells were labeled with the photoreactive and clickable sterol probe at a final concentration of 10 μ M for one hour alongside with MG132. Crosslinking of the probe to proteins was facilitated by UV irradiation for 5 minutes. Thereafter, whole cell lysates were subjected to click chemistry with azide-biotin and cholesterol affinity purification was performed using neutravidin resin beads. Co-purified and enriched prM-HA proteins were analyzed by immunoblotting using a specific anti-HA antibody (Figure 27b). The resulting western blot shows that all, prM

4. Results

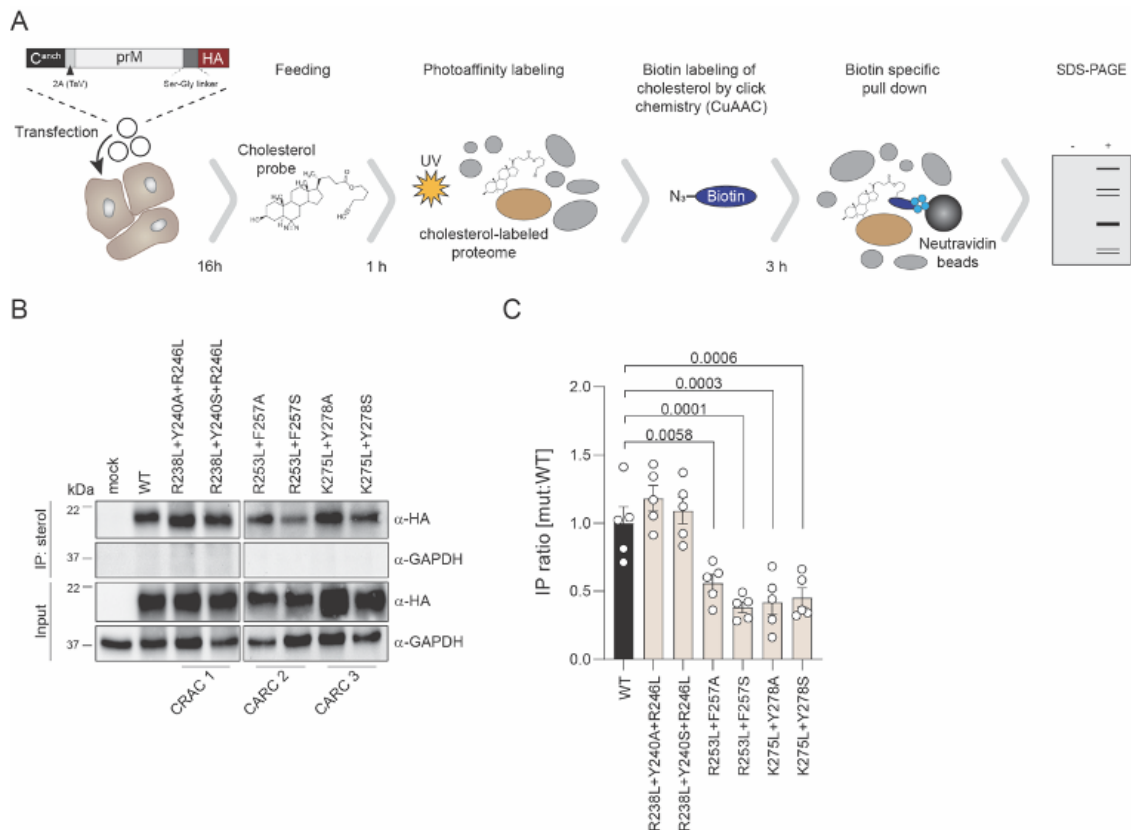


Figure 27. Mutagenesis of the cholesterol binding domains in the TMD2 and TMD3 of the M domain of the structural prM protein block cholesterol binding.

(A) Schematic representation of the experimental approach. Huh7-Lunet T7 cells were transfected with pTM prM-HA constructs for 18 h. Subsequently transfected cells were treated with 10 μ M trans-sterol probe alongside with the proteasome inhibitor MG132 for 1 hour. Crosslinking was achieved by UV irradiation. Thereafter, clarified cell lysates were subjected to biotinylation via click chemistry. Lipid specific pulldown was achieved using neutravidin conjugated resin beads. Co-purified proteins were subjected to western blot for analysis. (B) Co-purified prM-HA proteins from (A) were analyzed by immunoblotting using a HA-specific antibody. GAPDH was used as loading control. A representative result of five independent experiments is shown. (C) Relative sterol binding was calculated by densitometry of the HA signals normalized to input signals. Bars represent the means of the eluate/input signal ratio, normalized to WT, from five independent experiments. Error bars indicate SEM. P-values are given on the top.

WT and prM mutants, still interacted with the cholesterol probe. However, quantification of the chemiluminescence signal, normalizing it to initial expression levels (input), and calculating the fold change to WT showed a significant reduction of cholesterol binding of prM proteins with mutated CARC motifs located in the TMD2 and TMD3 (Figure 27c).

4.3.5. Atomistic molecular dynamics simulations confirm the interaction between the M protein and cholesterol

To further characterize the two cholesterol binding sites in molecular detail, atomistic molecular dynamics (MD) simulations of WT and mutant M proteins (CARC2:

4. Results

R253L+F257A, R253L+F257S; CARC3: K275L+Y278A, K275L+Y278S) were performed by Dr. Giray Enkavi, Dr. Waldemar Kulig, and Prof. Dr. Ilpo Vattulainen at the University of Helsinki in Finland. Since cryo-EM reconstructions of mature ZIKV particles have shown that M proteins exist as dimers which are regularly inserted into the viral lipid bilayer, atomistic MD simulations were performed with M protein dimers (Figure 30a). Furthermore, to assess whether different levels of cholesterol have an effect on the conformation of M protein dimers, the following CHOL:POPC ratios in bilayers were simulated: 0:100, 10:90, 20:80, and 30:70 (mol%:mol%). Measuring the radial distribution function of cholesterol shows that in all cholesterol-containing membranes, cholesterol accumulated next to the surface of the WT protein (Figure 30b). Moreover, analysis of the average three-dimensional occupancy of cholesterol atoms captured specific binding sites on the surface of the WT M protein (Figure 30c), which correspond to regions around the CARC2 and CARC3 motifs. In the 20:80 CHOL:POPC bilayer system, binding of cholesterol is highly specific to WT M protein dimers whereas mutants consistently show no specific binding (Figure 30d). To further assess the impact of the mutations on cholesterol binding, cholesterol binding curves were constructed via SCS (Figure 30e). Given the results, the curves clearly indicate a stronger and faster binding of cholesterol to WT than to mutant M proteins. In this context, mutants harboring the alanine substitution at the former aromatic residue showed the strongest effect. Taken together, these results suggest that the M domain interacts with cholesterol, and cholesterol interaction specificity is reduced by mutations in the CARC domains as well as affected by membrane cholesterol levels.

Moreover, detailed analysis of the MD simulation data demonstrated that neither high cholesterol concentrations nor mutations caused major conformational changes in the M protein in its transmembrane region, suggesting that cholesterol recognition rather depends on surface features of the M protein dimer. However, analysis of the simulation system using Linear Discriminant Analysis (LDA) revealed subtle differences in the conformation of the transmembrane region, which can discriminate between different membrane compositions. The LDA (Figure 28f) captures narrowing and widening of the transmembrane helices in response to changes in cholesterol levels. Although these conformational changes are small in individual M protein dimers, yet accumulation of small conformational changes could result in a larger effect for the whole virus.

4. Results

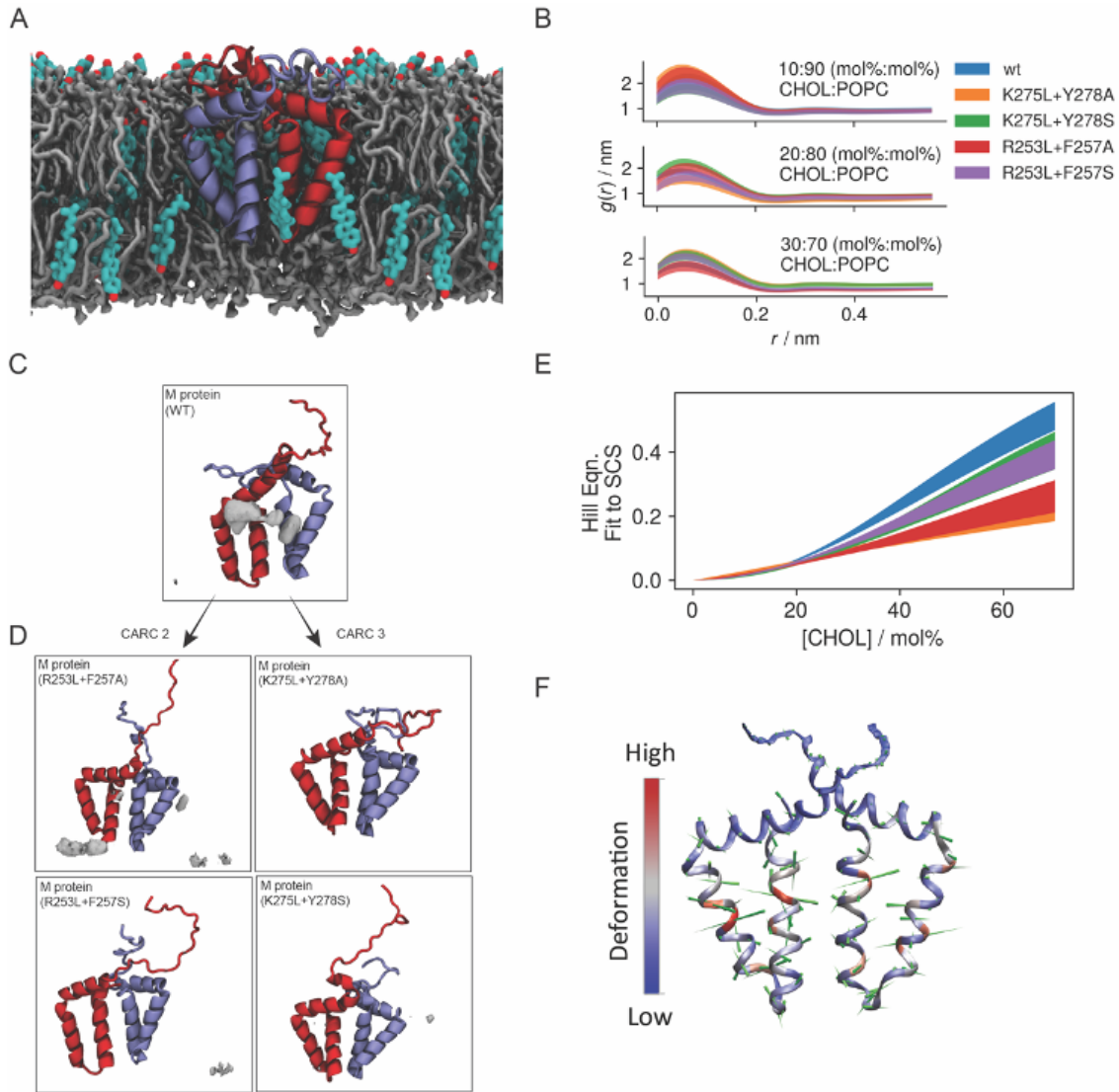


Figure 28. Atomistic molecular dynamics simulation.

(A) Snapshot of the molecular dynamics simulation of the predicted membrane topology of the M domain. (B) Two-Dimensional Radial distribution function of cholesterol with respect to the protein surface. (C) MD simulations capture high occupancy of cholesterol (0.16 isooccupancy surface) next to WT M protein surface in a 20:80 (mol%:mol%) CHOL:POPC membrane. (D) Cholesterol occupancy of given mutations targeting motifs CARC2 and CARC3 reveal nearly complete loss of cholesterol binding. (E) Hill Function fitted to the SCS values obtained for cholesterol-containing systems. WT M protein responds stronger and faster to increasing cholesterol concentration than all mutants, especially to K275L+Y278A and R253L+F257A. (F) The porcupine plot for the first LDA component. The deformations of protein C_α atoms were scaled by a factor of 10 for visual clarity and shown as green cones. The protein backbone is also coloured by the scale of deformation.

These data were produced by our collaborators at the University of Helsinki, Finland. Credits: Dr. Giray Enkavi, Dr. Waldemar Kulig, and Prof. Dr. Ilpo Vattulainen.

4. Results

4.3.6. Mutant CARC ZIKV are significantly impaired in spread

Given my results, showing that the M domain exhibits two functional cholesterol binding domains, I next wondered whether this interaction is essential during virus entry and virus particle assembly. For this, I introduced the above-mentioned mutations into the M domain in the context of the viral genome, using the reverse genetics system of Zika strain H/PF/2013 (synZIKV-H/PF/2013 and synZIKV-R2A-H/PF/2013)³⁷⁷. To avoid that mutant viruses revert back to wild type, amino acid substitutions were generated by modifying all three nucleotides. First, to assess whether mutations affect the replication kinetics of mutated ZIKV, Huh7-Lunet naïve cells were transfected with *in vitro* transcribed viral RNAs. *Renilla* luciferase activity was monitored as surrogate for virus replication in 24-hour intervals over a period of 120 hours (Figure 29a). Wild type and the replication deficient reporter viruses were included as positive and negative control, respectively. The results show that within the first 48 hours viral replication was comparable between mutant CARC and WT ZIKV, however, for timepoints where *Renilla* luciferase activity increases, due to viral spread (>72 hours), a significant reduction in *Renilla* activity was observed when comparing mutant CARC to WT ZIKV. To exclude that the observed differences in *Renilla* activity originated due to different transfection efficiencies, *Renilla* activity was measured at 4 h.p.t., showing similar translation rates for all constructs (Figure 29b). To confirm that the reduced *Renilla* activity correlates with an impairment of viral spread, transfected Huh7-Lunet naïve cells were seeded on glass coverslips, PFA fixed in the time period of 72-120 h.p.t., and subjected to fluorescence-based visualization of the structural protein envelope (Figure 29c). Quantification of envelope positive cells revealed that ZIKV exhibiting a mutated CARC1 or CARC3 motif were significantly attenuated, showing a reduction in positive cells of 30% and >60% at 120 h.p.t., respectively, when compared to WT ZIKV (Figure 29d). Although, mutant CARC1 ZIKV were showing a significant reduction in virus spread, yet in the cholesterol binding assays mutated CARC1 prM proteins did not show a reduction, suggesting a different mode of action by these amino acids. Hence, mutated CARC1 ZIKV were not further characterized. In contrast, mutant CARC2 ZIKV were only depicting a mild but not significant reduction (Figure 29d). Overall, these results show that the interaction between the M domain and cholesterol is required for efficient ZIKV propagation.

4. Results

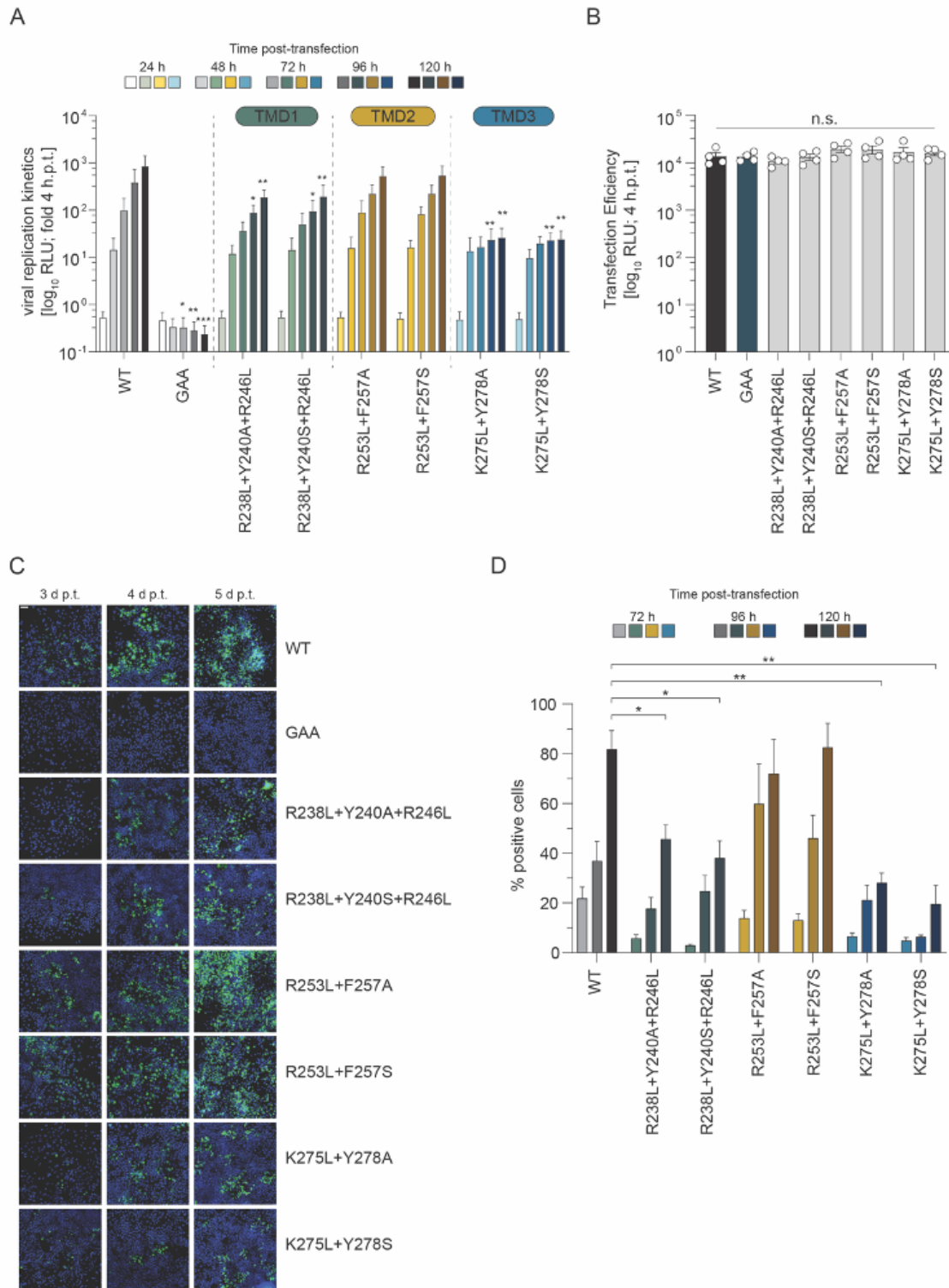


Figure 29. Mutagenesis of cholesterol binding domains within the M domain affects viral spread.

(A) Huh7-Lunet naïve cells were transfected with synZIKV-R2A constructs and *Renilla* luciferase activity was measured in 24-hour intervals over a period of 120 hours. Relative light units normalized to the 4-hour value are blotted from four independent experiments. Bars represent the means from four independent experiments. Error bars indicate SEM. (*, $p < 0.05$) (**, $p < 0.01$) (***, $p < 0.001$). (B). Transfection efficiency was assessed by monitoring *Renilla* luciferase activity at 4 hours post transfection. Bars represent the mean of four independent experiments. Error bars indicate SEM. n.s., not significant. [Legend continues on next page]

4. Results

(C) Viral spread was assessed by immunofluorescence microscopy at 72, 96, and 120 h.p.t. Transfected Huh7-Lunet naïve cells were seeded on glass coverslips and PFA fixed at given timepoints. Infected cells were identified by staining for the structural protein envelope. Representative pictures of four independent experiments are shown. Scale bar: 20 μm . (D) Quantification of positive cells from (C). Immunofluorescence microscopy pictures were analyzed using the Fiji software and by running a self-written macro. Percentage of positive cells are blotted. Bars represent the mean of four independent experiments. Error bars indicate SEM. (*, $p < 0.05$) (**, $p < 0.01$).

4.3.7. Mutant CARC2 ZIKV are sensitive to cholesterol levels in mammalian cells

As demonstrated in Section 4.3.1. ZIKV entry requires cholesterol in host cellular target membranes. Although cholesterol levels can be experimentally modified using the solubilizing drug M β CD, such treatments prevent infection by WT ZIKV, thus prohibiting a direct comparison between WT and cholesterol binding mutant Zika viruses. To overcome this limitation, I quantified the total cellular cholesterol content of several different mammalian cell lines, which are regularly used for studying the ZIKV replication cycle (Figure 30a). While the human cell lines Huh7-Lunet, JEG3, and A549 shared similar amounts of total cholesterol, the nonhuman primate cell line VeroE6 was significantly lower, corresponding to approximately 50% of the total cholesterol content of Huh7-Lunet cells (Figure 30a). Given this result, I next investigated the ability of mutant CARC2 ZIKV to infect VeroE6 cells. For this purpose, VeroE6 cells were seeded in 96-well plates and one day post seeding cells were infected with WT and mutant CARC2 ZIKV at an MOI of 3. At 24 h.p.i. cells were PFA fixed and subjected to fluorescence-based visualization of the two viral proteins NS4B and envelope (Figure 30b). As positive control, Huh7-Lunet naïve cells were seeded and infected in parallel. While I did not observe a significant difference in the infection ability on Huh7-Lunet naïve cells, mutant CARC2 ZIKV were significantly impaired in their ability to infect VeroE6 cells. In fact, quantification of positive cells revealed a reduction of approximately 99% (Figure 30c). To exclude that mutations within the M domain could cause structural conformational changes of the envelope protein, thus affecting binding and attachment, I next performed virus binding assays. To allow comparison of mutants with WT, I first analyzed whether extracellular infectious titers and secreted viral RNA were comparable between these two viruses. For this Huh7-Lunet naïve cells were transfected with *in vitro* transcribed viral RNAs, and virus containing supernatants were collected at 120 h.p.t. Viruses were concentrated via sucrose cushion and ultracentrifugation

4. Results

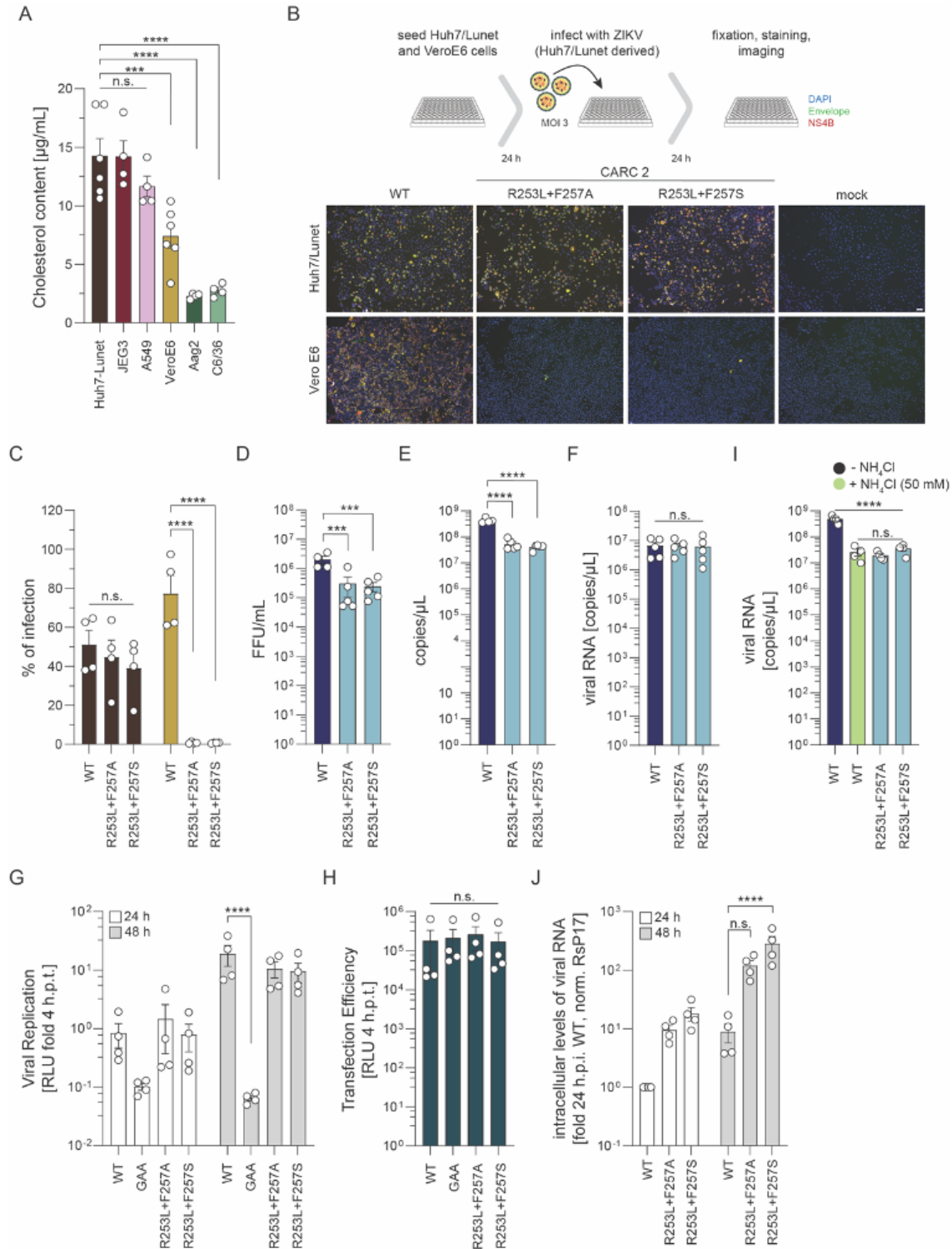


Figure 30. Functionality of the CARC2 motif in the M domain depends on cellular cholesterol levels.

(A) Quantification of total cholesterol amounts in the mammalian cell lines Huh7-Lunet naïve, JEG3, A549 and VeroE6, and the mosquito cell lines C6/36 and Aag2. Bars represent mean of up to six independent measurements. Error bars indicate SEM. (*, $p < 0.05$) (**, $p < 0.01$) (***, $p < 0.001$) (****, $p < 0.0001$). (B) Using immunofluorescence microscopy viral infectivity of mutant CARC2 ZIKV on VeroE6 cells was assessed. Huh7-Lunet naïve (positive control) and VeroE6 cells were seeded and infected with WT and mutant CARC2 ZIKV at a MOI of 3. Infection was assessed 24 hours post infection by staining the structural protein envelope (green) and the non-structural protein NS4B (red). [Legend continues next page]

4. Results

Representative pictures of four independent experiments are shown. Scale bar: 1 cm. **(C)** Quantification of positive cells from **(B)**. Percentage of positive cells are blotted. Bars represent the mean of four independent experiments. Error bars indicate SEM. n.s., not significant, (****, $p < 0.0001$). **(D)** Supernatant were collected 120 hours post transfection and concentrated via sucrose cushion and ultracentrifugation. Extracellular infectious titers were determined by TCID₅₀ assays. Bars represent the mean of 5 individual stock productions. Error bars indicate SEM. (***, $p < 0.0001$) **(E)** Secreted viral RNA was quantified from virus stocks produced in **(B)** by probe-based RT-qPCR. Bars represent mean of five independent experiments. Error bars indicate SEM. (****, $p < 0.0001$) **(F)** Virus binding to VeroE6 cells. VeroE6 cells were exposed for 1 ½ hours at 4°C to WT and mutant CARC2 ZIKV using the same genome copy number per cell, corresponding to a MOI of 2 calculated for WT. Thereafter, cells were extensively washed and total cellular and bound viral RNA was extracted. Virus RNA copies per exposed cell were quantified by probe-based qRT-PCR assays. Bars represent the mean of five independent experiments. Error bars indicate SEM. **(G)** Viral replication was monitored in VeroE6 cells by measuring *Renilla* luciferase activity at 24 and 48 hours post transfection. Relative light units normalized to the 4-hour value of four independent experiments are blotted. Error bars indicate SEM. (****, $p < 0.0001$). **(H)** Transfection efficiency was assessed by monitoring *Renilla* luciferase activity at 4 hours post transfection. Bars represent the mean of four independent experiments. Error bars indicate SEM. n.s., not significant. **(I)** Viral entry inhibition assay. VeroE6 cells were pretreated for 1 hour with ammonium chloride followed by virus binding for 1 ½ hours at 4°C using the same genome copy number per cell, corresponding to a MOI of 2 calculated for WT. Thereafter, cells were placed at 37°C for 1 hour (input) and 24 hours. Cells were washed and total cellular and bound viral RNA was extracted. Virus RNA copies per exposed cell were quantified by probe-based qRT-PCR assays. Bars represent the mean of five independent experiments. Error bars indicate SEM. n.s., not significant, (****, $p < 0.0001$) **(J)** Replication fitness of mutant CARC2 ZIKV in the mosquito cell line Aag2. Aag2 cells were seeded and infected with WT and mutant CARC2 ZIKV at a MOI of 0.1. Virus replication kinetics were assessed at 24 and 48 hours post infection by RT-qPCR. RSP17 was used for normalization. Bars represent the mean of two independent experiments. Error bars indicate SEM. n.s., not significant, (****, $p < 0.0001$).

and subsequently subjected to TCID₅₀ assays to determine extracellular infectious titers (Figure 30d), and probe-based qRT-PCR assays to determine extracellular levels of viral RNA (Figure 30e). In fact, extracellular infectious titers and viral RNA levels were significantly lower for CARC2 mutants when compared to WT ZIKV, showing 1log difference. Interestingly, virus specific infectivity (ratio of infectious virions to viral genomic RNA) was not affected. However, to ensure comparison between WT and mutant CARC2 ZIKV during binding assays, VeroE6 cell monolayers were exposed to equal genome copy numbers, corresponding to an MOI of 2 which was calculated for WT. Virus binding was performed on ice for 1 ½ hours followed by quantification of viral genome copy numbers associated with VeroE6 cells by performing probe-based qRT-PCR (Figure 30f). The result shows that virus binding was equally efficient for WT and mutant CARC2 ZIKV, suggesting that mutations within the M domain do not cause conformational changes in the envelope proteins. To further narrowing down which step during the viral life cycle is affected, I transfected VeroE6 cells with *in vitro* transcribed RNA, to overcome viral entry. Viral replication was assessed by monitoring the *Renilla* luciferase activity at 24 and 48 h.p.t., showing comparable levels of viral replication between mutant CARC2 and WT ZIKV

4. Results

(Figure 30g). Furthermore, to ensure that transfection efficiency was comparable among constructs, *Renilla* luciferase activity was measured at 4 h.p.t., showing similar translation rates among all constructs (Figure 30h). Taken together, these results suggest that the interaction between the M domain and cholesterol is required during virus uptake and/or release of the viral nucleocapsid into the cytoplasm from late endosomes.

So far, I have failed to investigate these two steps in particular. However, to confirm that escape from late endosomes is affected by the mutations in the CARC2 domain, I performed fusion inhibition assays. The acidic environment in late endosomes induces conformational changes in the structural protein envelope, releasing the fusion loop and therefore initiating the formation of the fusion pore. To inhibit the formation of the fusion pore in late endosomes, acidification was prevented by pre-treating VeroE6 cells with ammonium chloride (50 mM). After 1 hour of treatment, VeroE6 cell monolayers were exposed to equal genome copy numbers, corresponding to an MOI of 2. Virus binding was performed on ice for 1 ½ hours followed by a 45-minute incubation period at 37°C in the presence or absence of ammonium chloride. Infection was assessed by probe-based RT-qPCR at 24 h.p.i. (Figure 30i). In fact, quantification of intracellular viral RNA levels showed that treatment with ammonium chloride significantly reduced viral RNA copies when compared to the untreated control (Figure 30i). Interestingly, comparing intracellular viral RNA levels from mutant CARC2 ZIKV infected cells with WT infected cells treated with ammonium chloride no significant differences were found (Figure 30i). Although the step in the viral life cycle has not been directly addressed, mimicry and exclusion of viral steps have allowed me to identify that most probably virus escape from the endosome via fusion is defective in mutant CARC2 ZIKV. I hypothesize that based on its ability to interact with lipids, the M domain could mediate lipid sorting and/or exchange between the viral lipid bilayer and the endosomal membrane, thus contributing to the formation of the fusion pore.

4.3.8. Cholesterol is required during virus entry into mammalian but not insect cells

Unlike mammalian cells, insect cells are incapable of *de novo* synthesis of cholesterol due to the lack of essential enzymes involved in the cholesterol biosynthesis pathway^{404,405}. In accordance with this, quantification of cholesterol amounts in the two mosquito cells lines C6/36 and Aag2 showed over an 80% reduction when compared to Huh7-Lunet naïve

4. Results

cells (Figure 30a). However, I cannot exclude that cholesterol might be a cross contaminant derived from the medium, as the cell culture medium for mosquito cells contain FBS. To date, flavivirus infection in mosquito cells was found to occur at the plasma membrane^{406,407}. Furthermore, lipidomic profiles of ZIKV infected mosquito cells³²³ and cryo-electron tomography studies on purified virus particles have highlighted that the major lipid involved in the mosquito cell is phosphatidylethanolamine (PE), which was also incorporated into the lipid pocket in the viral envelope³²⁷. Based on previous findings, indicating that entry and the dependence on lipids differ between ZIKV hosts, led me to investigate whether the ability to infect mosquito cells was affected in mutant CARC2 ZIKV. For this, *A. aegypti* cells (Aag2) were infected with an MOI of 0.1 and at 24 and 48 h.p.i. viral replication was assessed via qRT-PCR (Figure 30j). Despite using a similar MOI, my results show that mutant CARC2 ZIKV were significantly enhanced in viral replication when compared to WT. Overall, these results show that lipid interactions, the abundance of various lipid species, and host specific lipids determine the ability of ZIKV to successfully establish an infection. In this context, I was able to show that the interaction between the M domain and cholesterol is required during virus entry into mammalian cells, whereas this interaction is negligible for the insect cells.

4.3.9. Mutant CARC3 Zika virions are defective in assembly

To further dissect the role of cholesterol binding to the CARC3 motif in the M domain in the ZIKV replication cycle, I next investigated the release of infectious virus particles and secretion of viral RNA. While for WT and CARC2 ZIKV, infectious virus titers were ranging from 10^2 to 10^5 FFU/mL (Figure 31a) and high levels of viral RNA were detected in supernatants (Figure 31b), a reduction of up to 80,000-fold in extracellular infectious titers (Figure 31a) and reduced amounts of secreted viral RNA were found for mutant CARC3 ZIKV (Figure 31b). To further investigate whether the reduction in extracellular titers and viral RNA levels was due to an impaired virus egress, intracellular virus particles were recovered by three consecutive freeze-thaw cycles. Recovered virus particles were thereafter subjected to TCID50 analysis (Figure 31c), showing still a reduction of up to 44,000-fold when compared to WT. Next, to assess whether mutant CARC3 ZIKV are defective in virus assembly, I used a correlative light electron microscopy (CLEM) approach to specifically analyze ZIKV transfected cells. For this a ZIKV reporter cell line was generated which

4. Results

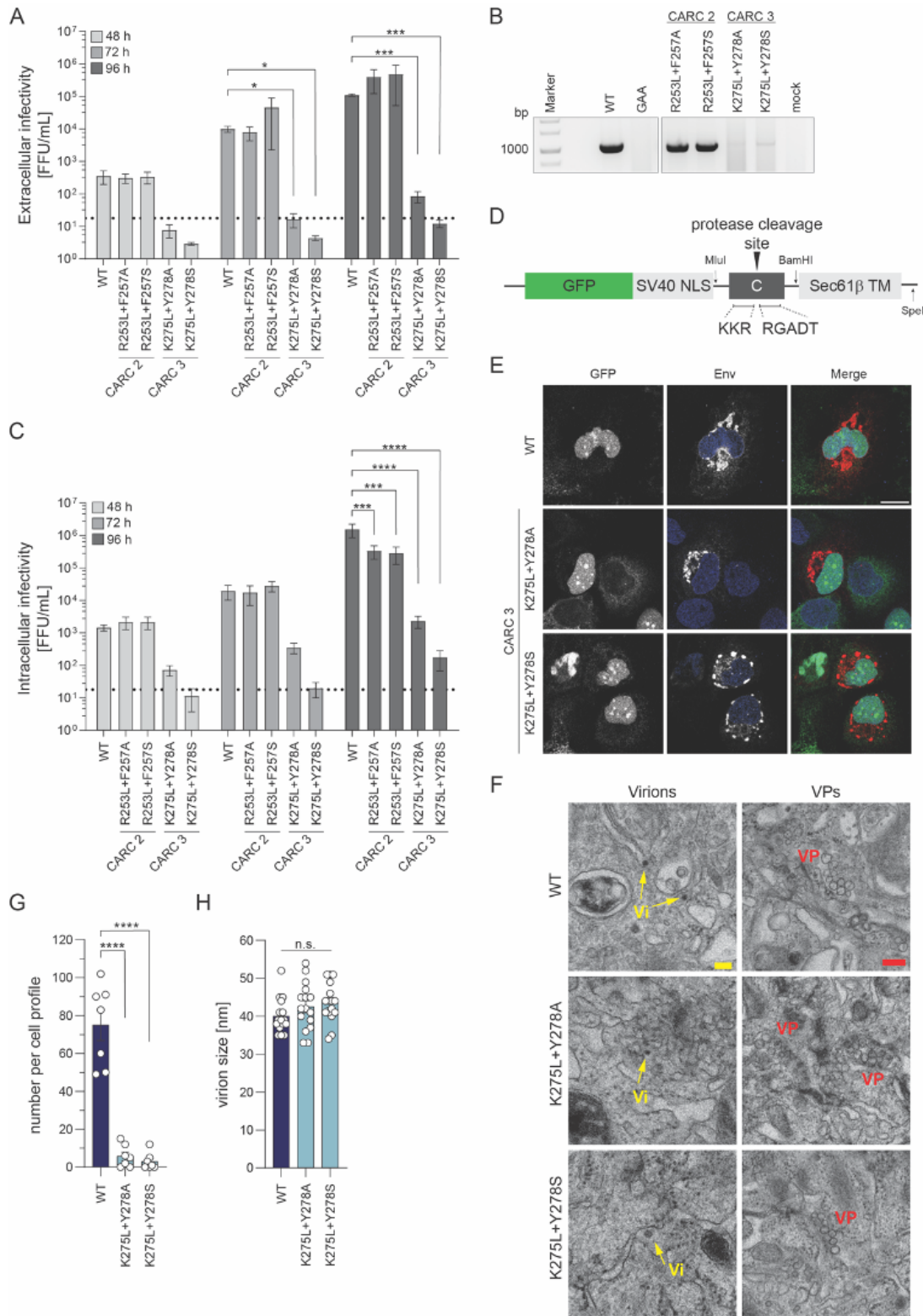


Figure 31. Mutagenesis of the CARC3 domain affects virus assembly.

(A) Extracellular infectious titers determined by TCID₅₀ assays. Huh7-Lunet cells were transfected with synZIKV-H/PF/2013 viral RNA and supernatants were collected at 48, 72, and 96 h.p.t. Bars represent mean of four independent experiments. Error bars indicate SEM. (*, $p < 0.05$) (***, $p < 0.001$). (B) At 96 h.p.t. supernatants from (A) were used for extracting viral RNA. Lane 1: 1kb DNA ladder. The RNA from mock- (Lane 6) and NS5-deficient (GAA; Lane 3) transfected cells served as negative control. A region within the structural genes (1000 bp) is amplified for WT (Lane 2). Only little amount of RNA was detected for mutant CARC3 ZIKV transfected cells (Lane 4+5). [Legend continues next page]

4. Results

(C) Intracellular infectivity was assessed by TCID₅₀ assay. Within the same experiment from (A) transfected cells were scraped and lysed by repeated freeze-thaw cycles for recovering intracellular particles. Clarified supernatants were subjected to TCID₅₀ analysis. Bars represent mean of three independent experiments. Error bars indicate SEM. (***, $p < 0.001$) (****, $p < 0.0001$). (D) Schematic representation of the constructs used for generating ZIKV reporter cell line. (E) ZIKV reporter cells were transfected with synZIKV WT and synZIKV mutant CARC3 RNAs. At 72 h.p.t. cells were processed for immunofluorescence microscopy for validation of the reporter's functionality. Envelope was stained as viral marker. Scale bar: 20 μm . (F) ZIKV reporter cells were transfected with synZIKV WT and synZIKV mutant CARC3 RNAs. At 72 h.p.t. cells were processed for TEM analysis. Representative images of seven analyzed cells are shown. Scale bar: 200 nm. Vi: virions; VP: vesicle packet. (G) Within seven cell profiles mean number of virions was counted. Bars represent the mean of seven analyzed cells from one experiment. Error bars indicate SEM. (****, $p < 0.0001$). (F) Size of identified virions from (E). Error bars indicate SEM. n.s. not significant.

under normal conditions expresses a GFP which resides in the ER due to its C-terminal anchor sequence KDEL (Figure 31d). Upon ZIKV infection, however, the viral protease recognizes the capsid cleavage site which connects the GFP to the KDEL sequence, thus cleaving GFP which thereafter locates into the nucleus as it comprises a NLS sequence (Figure 31e). This approach was used as transfection efficiency is below 10%. For this, Huh7-Lunet ZIKV reporter cells were transfected with *in vitro* transcribed viral RNA and at 72 h.p.t. positive cells were mapped, and samples were further processed for TEM. Analysis of up to 7 positive cells, has shown that all constructs induced the ultrastructural rearrangements as previously reported³⁰¹. However, while virus particles were frequently found in WT transfected cells with a mean number of 75 particles per cell profile (Figure 31g), a size of 40 ± 4.41 nm (Figure 31h) and located within the lumen of the ER and *trans*-Golgi network (Figure 31f), virus particles were rarely detected for mutant CARC3 transfected cells. Structures resembling virus particles were observed which matched in size (43.6 ± 5 nm and 42.5 ± 6 nm for K275L+Y278A and K275L+Y278S, respectively (Figure 31h) and sub-cellular localization (Figure 31f), yet the mean number per cell profile was significantly lower when compared to WT (Figure 31g). Taken together, these results demonstrate that the interaction between cholesterol and the CARC3 motif in the M domain is required for efficient virus particle production.

4.3.10. Evidence that the CARC3 motif is required for the recruitment of capsid to virus assembly sites

To exclude the possibility that mutations within the CARC motifs affect polyprotein or furin processing, lysates derived from transfected Huh7-Lunet naïve cells were immunoblotted with antibodies against the structural proteins and the viral protease NS3, as internal

4. Results

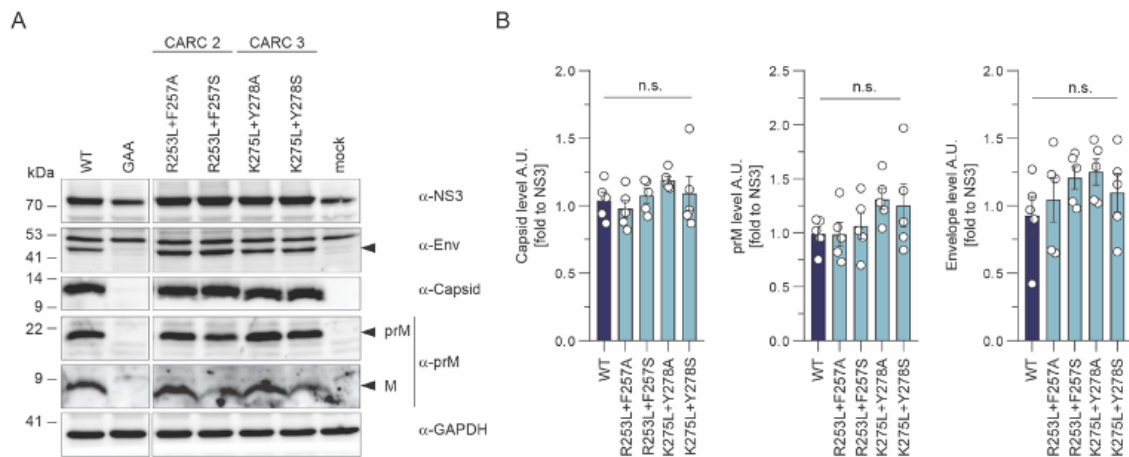


Figure 32. Polyprotein processing and protein abundance.

(A) Huh7-Lunet cells were transfected with respective synZIKV constructs and at 48 h.p.t. lysed and subsequently subjected to western blot analysis. Polyprotein processing was determined by probing capsid, prM, envelope, and NS3. GAPDH was used as loading control. (B) Relative polyprotein processing efficiency was calculated by densitometry of western blots and normalizing signals of capsid, prM and envelope to NS3 expression levels in each sample. Values represent mean \pm SEM of five independent experiments. n.s. not significant.

control, and GAPDH as loading control (Figure 32a). Western blot analysis showed that the overall protein abundance and processing of the ZIKV polyprotein was comparable between WT and mutant CARC3 viruses (Figure 32b). The difference in signal intensity for the M protein between WT and CARC mutants could be explained by reduced binding of primary antibodies, as mutations could affect epitopes. However, looking more closely at the structural protein capsid, revealed that CARC3 mutant viruses exhibit differential amounts of two capsid species when compared to WT (Figure 33a). The capsid protein is encoded by the N-terminus of the viral polyprotein and is sequentially processed by the host signal peptidase and the viral protease giving rise to two capsid species: a premature membrane-anchored form (capsid 1-122 aa) and a mature, cytosolic form (1-104 aa)^{125,408}. While the former associates with lipid droplets (LDs)¹⁶⁸, thus, is presumed to contribute to virus particle assembly^{168,409}, the latter is imported into the nucleus which determines host specific infectivity⁴¹⁰. Given my results, showing a differential processing of the capsid protein, resulting in an increase of cytosolic cleaved capsid and a decrease in membrane associated capsid (Figure 33b), prompted me to investigate whether mutations within the M domain affects the subcellular distribution of capsid proteins. As decrease in premature capsid was observed, I specifically analyzed capsid signals coinciding with envelope at lipid droplets to address virus particle production (Figure 33c). In fact, quantification of total colocalization events of capsid and envelope at LDs revealed that in CARC3 mutant transfected cells the

4. Results

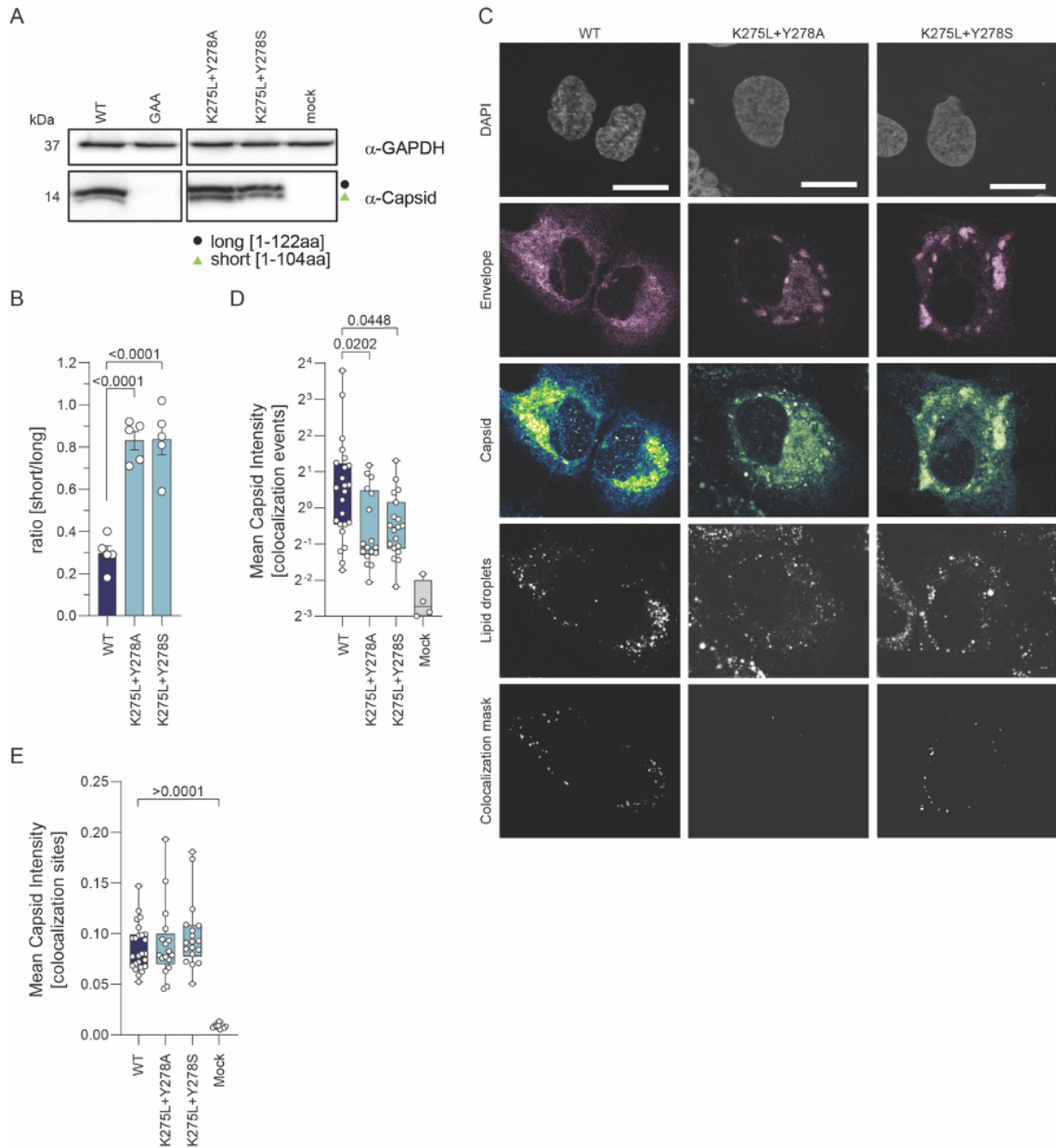


Figure 33. Cholesterol interaction with the M domain recruit capsid proteins to virus assembly sites.

(A) Whole cell lysates were collected at 48 h.p.t. and subjected to western blot analysis. Capsid cleavage was assessed and normalized to the loading control GAPDH. Size of proteins are indicated on the left. (B) Quantification of capsid processing was calculated by densitometry. Signals were normalized to GAPDH. Bars represent the means of the cleaved/uncleaved signal ratio from five independent experiments. Error bars indicate SEM. P-values are given on top. (C) Subcellular localization of virus capsid proteins was assessed by immunofluorescence microscopy. Transfected Huh7-Lunet naïve cells were seeded on glass coverslips and PFA fixed at 48 h.p.t. Infected cells were identified by staining for the structural proteins: envelope and capsid. Colocalization of capsid with lipid droplets (LDs) was assessed by probing LDs with BODIPY. Representative pictures of two independent experiments are shown. Scale bar: μm . (D) Quantification of colocalization events between C-E-LDs. Immunofluorescence microscopy pictures were analyzed using the cell profiler software and by running a self-written macro. Number of events are blotted. Bars represent the mean of two independent experiments. Error bars indicate SEM. P-values are given on the top. (E) Quantification of capsid signal intensity at colocalization events from (D).

4. Results

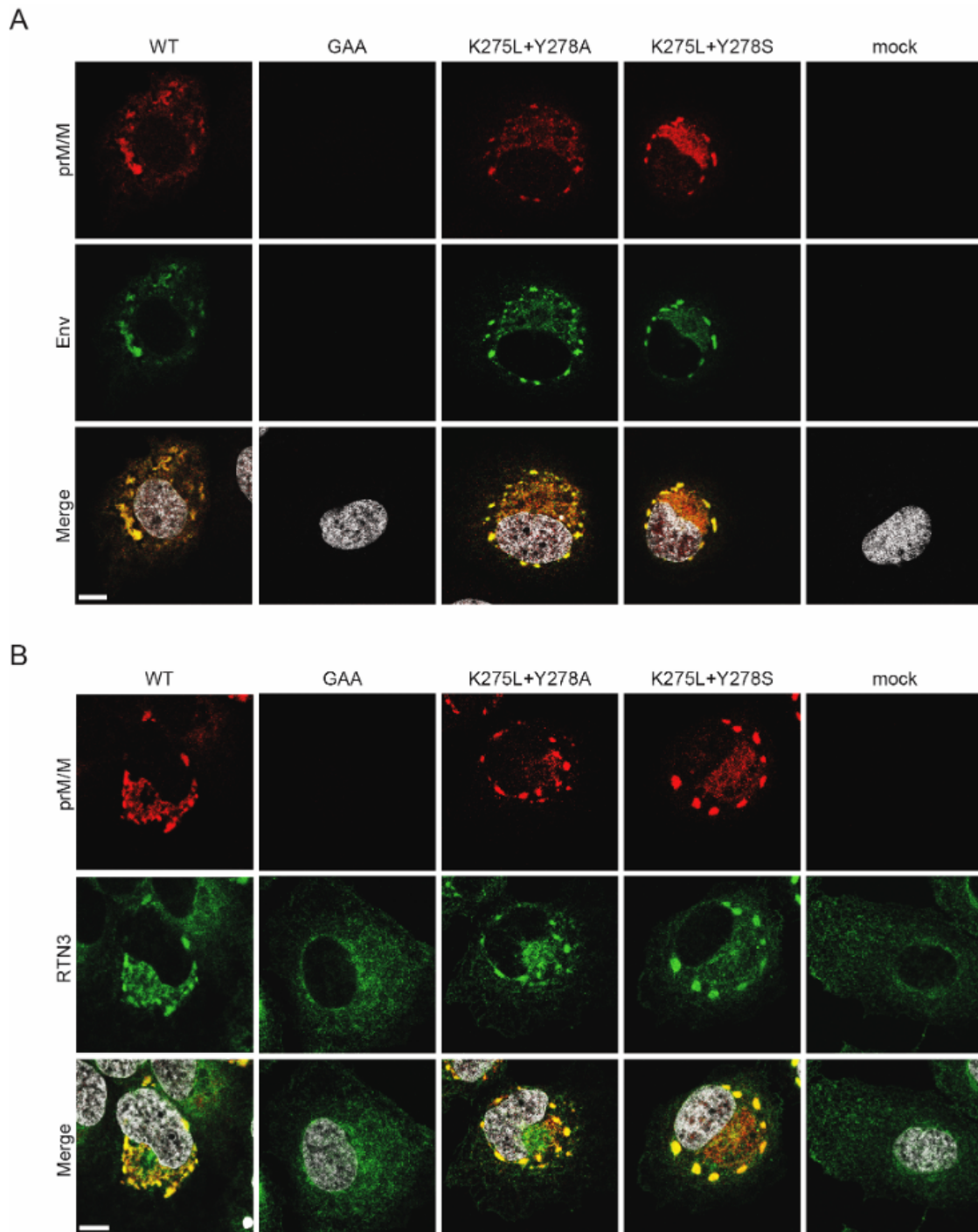


Figure 34. Subcellular localization of prM and E proteins.

Huh7-Lunet naïve cells were transfected with respective synZIKV constructs and seeded on glass coverslips. At 48 h.p.t. cells were PFA fixed and subjected to immunofluorescence analysis staining for prM and envelope (A) or prM and RTN3 (reticulon-3), which served as ER marker (B). Scale bar: 20 μ m.

overall number was significantly lower when compared to WT transfected cells (Figure 33d). However, measuring the mean intensity of capsid signal at these colocalization sites showed no significant differences (Figure 33e).

4. Results

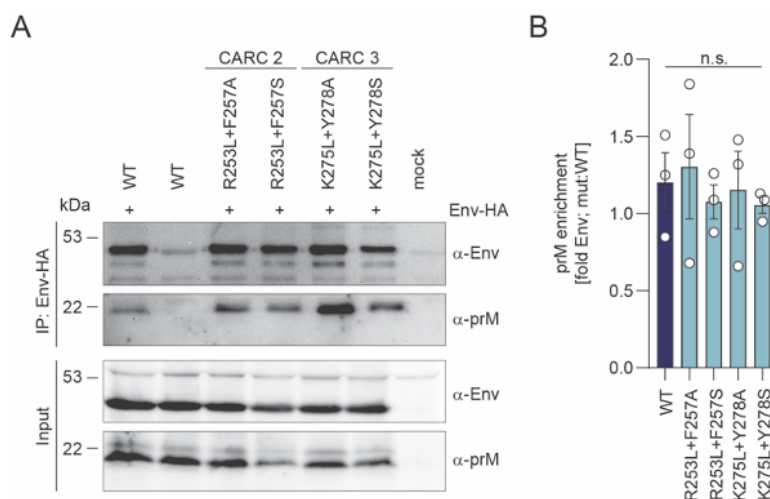


Figure 35. Mutations in the M domain of the prM protein do not affect the prM-Env interaction.

(A) HEK 293T cells were transfected with pcDNA3.1 constructs encoding the prM-E proteins. At 18 h.p.t. cells were lysed and subsequently subjected to co-immunoprecipitation assays. Co-purified prM proteins were analyzed by immunoblotting using a polyclonal prM-specific antibody. Pulldown of envelope was confirmed by immunoblotting using a polyclonal Env antibody. A representative result of three independent experiments is shown (B) Relative prM binding was calculated by densitometry of the signals normalized to input signals. Bars represent the means of the eluate/input signal ratio, normalized to WT, from three independent experiments. Error bars indicate SEM. n.s., not significant.

To exclude that the introduced mutations could affect the subcellular distribution of prM and E proteins, immunofluorescence microscopy was performed. For this Huh7-Lunet naïve cells were transfected with individual CARC mutants and at 48 h.p.t. fixed and stained with anti-prM, anti-E or anti-RTN3 antibodies (Figure 34), the latter serving as marker for the ER. For all ZIKV positive cells prM was distributed throughout the cytoplasm with occasional enriched puncta, which could correspond to protein accumulates within convoluted membranes. Colocalization of prM and E proteins (Figure 34a) and distribution of prM proteins in the ER (Figure 34b) were found to be similar. Furthermore, as the interaction between prM and E is crucial for virus particle formation, I addressed the question whether the mutations within the CARC3 domain interrupt this interaction by performing co-immunoprecipitations. For this HEK 293T cells were transfected with pCDNA3.1 constructs encoding the prM-E proteins. My results show that co-immunoprecipitation of prM with E was successful for all mutants tested (Figure 35a). Furthermore, quantification of the chemiluminescence signal, normalizing it to E pulldown, and calculating the fold change to WT showed no significant changes (Figure 35b). Overall, these results confirm that mutations within the CARC3 motif does neither affect polyprotein and furin processing, total protein abundance, the subcellular localization of prM proteins, nor the interaction

4. Results

between the two structural protein E and prM. Given my results I hypothesize that the M domain together with cholesterol generates a platform to which capsid is recruited and anchored while virus particles are being formed.

5. DISCUSSION

5.1. A new system to study flavivirus RO formation independent of viral RNA replication

ZIKV, like other flaviviruses, has evolved strategies that modify the host cell morphology during viral infection to support its replication. Over the course of its life cycle, ZIKV consecutively infects mosquitos and humans and other primates^{4,54,411}. According to previous research, flaviviruses share an intimate union with the host endomembranous network, which, after infection, undergoes significant expansion and rearrangements which are described as invaginations into the lumen of the ER, also known as vesicle packets, which are the presumed sites for viral replication³⁰¹. Although several non-structural proteins have been identified to be crucial for the formation of flavivirus ROs, single expression of these NS proteins failed to induce viral replication compartments. Their contribution to this formation is most likely due to their ability to induce lipid bilayer asymmetry^{317,412} and membrane curvature^{197,198,307}, both of which are necessary for RO biogenesis. Detailed analysis and assessment of mutations or antiviral drugs and their impact on viral RO formation, as they already impair viral replication, was not possible in prior research since they were restricted to infection- and replicon-based experiments. Given this limitation a system was needed that provides the opportunity to explicitly explore one of the first steps of the ZIKV replication cycle which is assumed to occur upon initial translation but most likely before bulk RNA replication. The main goal of my first PhD project therefore was to create such an expression system that supports the formation of ZIKV replication compartments without the need for viral RNA replication.

To create such an expression system, the viral replicase (NS1-NS5) together with the 5' and 3'UTR were initially cloned into a cytoplasmic transcription-translation plasmid that is controlled by a T7 RNA polymerase⁴¹³ and an EMCV IRES⁴¹⁴, respectively, ensuring continuous and robust production of viral RNAs and viral proteins. Functional characterization of this expression system showed comparable viral protein levels and cleavage (Figure 13), as well as the induction of ROs that are morphologically indistinguishable to those found in ZIKV-infected cells³⁸⁵ (Figure 15).

5. Discussion

With the aim to identify viral factors required for ZIKV RO biogenesis, the initial expression construct (pTM 5'UTR/NS1-NS5/3'UTR) was modified by introducing deletion mutations into both UTRs to specifically investigate the role of secondary RNA elements in this process. Comparative analysis of individual expression constructs demonstrated that the 5'UTR is largely dispensable for ZIKV RO formation (Figure 15). Interestingly, deletion of both stem loops (SLA and SLB) (pTM Δ 5'SLAB/NS1-NS5/3'UTR) increased RO inducing efficiency when compared to the construct containing the entire 5'UTR³⁸⁵, resembling the percentage of RO positive cells found upon ZIKV infection (Figure 15).

Aside from the 5'UTR, secondary RNA elements within the 3'UTR were analyzed by introducing deletion mutations into the parental pIRO construct (pTM Δ 5'SLAB/NS1-NS5/3'UTR). Initially the focus was set on the highly conserved domain III, as it contains the 3'SL structure which is essential for flavivirus replication¹⁶²⁻¹⁶⁵. Functional characterization of 3'UTR deletion mutant constructs revealed that the 3'UTR is to some extent an important determinant for RO biogenesis, as the percentage of cells forming ZIKV ROs significantly decreased (Figure 16). Interestingly, comparison of ZIKV with DENV, with respect to the 3'SL deletion mutation, revealed that DENV RO biogenesis was suppressed³⁸⁵ whereas ZIKV RO biogenesis was still taking place (Figure 16). Notably, the loss of RO formation for dengue was restored when the 3'SL of ZIKV was added³⁸⁵. This rescue suggests that for DENV RO biogenesis either a viral or host factor binds to conserved regions within the 3'SL or a stable SL structure per se is required at the 3'end serving as structural component for RO formation. This result shows that although both viruses are closely related different host and viral factors are involved during viral RO biogenesis.

Since ZIKV RO formation was found to be less sensitive to secondary RNA elements within the domain III of its 3'UTR, more extensive deletion mutations were introduced to investigate whether the 3'UTR in general is a crucial factor in the formation of ZIKV ROs. Although the formation was not suppressed, the efficiency significantly decreased the greater the deletion mutation was (Figure 17). In fact, the greatest decrease was observed for the most extensive deletion mutation (pTM Δ 5'UTR/NS1-NS5/ Δ 3'complete). My results show that ZIKV RO formation can be enhanced by providing the viral 3'UTR, however, the 3'UTR is not the key determinant for ZIKV RO biogenesis as it was shown for dengue. This outcome is consistent with earlier research on the hepatitis C virus (HCV), which showed that expression of the minimal viral replicase (NS3-NS5B) results in the

5. Discussion

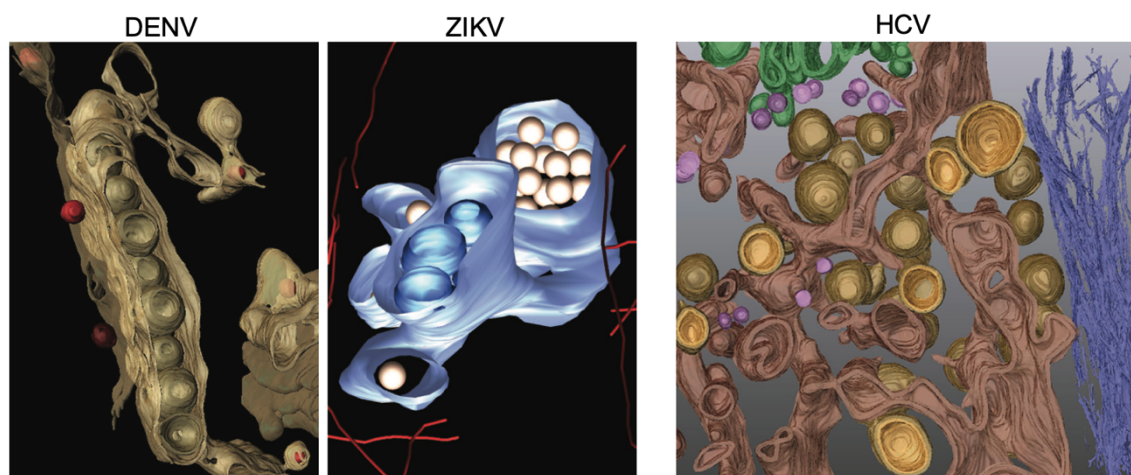


Figure 36. Replication organelles of the flavivirus and hepatitis virus.

Three-dimensional architecture of the replication compartments of dengue virus (DENV), Zika virus (ZIKV), and hepatitis C virus (HCV). The endoplasmic reticulum is shown for DENV in brown, for ZIKV in blue, and for HCV in dark brown. For DENV and ZIKV, the virus-induced vesicles are light brown and dark blue, respectively. The exterior membranes of HCV double-membrane vesicles (DMVs) are shown in light brown, and the interior membrane in orange. DENV and ZIKV particles are illustrated in red and gold, respectively. Single-membrane vesicles, the Golgi apparatus, and cytoskeletal filaments are illustrated in blue, green, and violet, respectively, in the tomogram of HCV. (Figure taken from [416])

formation of HCV ROs^{300,415}, also known as double-membrane vesicles (DMVs) (Figure 36). As DMVs and VPs have different morphologies⁴¹⁶, it is suggested that different mechanisms are involved in the process of forming the viral replication compartment. However, it was discovered that both HCV and ZIKV require phosphatidylinositol-4-phosphate (PI4P) for viral replication, demonstrating that various host metabolites are used alike by various viruses. The phosphatidylinositol-4-kinase- α (PI4K α) is recruited to DMVs by the two non-structural proteins NS5A and NS5B in the context of HCV, which correlates with elevated levels of PI4P and causes changes in the lipid content of membranes^{412,417}. In the case of ZIKV, PI4P is also highly enriched at ROs, and it has been shown that PI4KIII β inhibition effectively inhibits viral replication⁴¹⁸. Even though ZIKV and DENV are closely related and their ROs share morphological features (e.g., size and shape), PI4P was found to be dispensable for DENV RO formation^{417,419}. This emphasizes the various needs of host factors or mechanisms involved in the process of forming respective viral ROs.

Finally, ultrastructural analyses of the plasmid induced ROs from DENV and ZIKV revealed a remarkable distinction: whereas the size of Zika ROs was unchanged (Figure 15; Figure 16; Figure 17), dengue RO size was severely affected by deletion mutations within the 5' and 3'UTR³⁸⁵. My results for ZIKV are contrary to previous observations, where the

5. Discussion

size of the viral ROs for the Flock house virus⁴²⁰, Tomato bushy stunt virus⁴²¹, and Semliki Forest virus (SFV)⁴²², was found to depend on the length of the viral RNA. This implies that the architecture of ZIKV ROs is determined by other host and/or viral factors. Up until now, partial expression of the SFV⁴²³ and TBEV^{424,425} replicase was sufficient to induce RO-like structures, but they were morphologically different from those seen in replicating cells. Along these lines, the greatest benefit of the recently developed pIRO-Z system (pTM Δ 5'SLAB/NS1-NS5/3'WT-Rib) is its ability to induced ROs that are morphologically identical to those found in ZIKV-infected cells.

However, further research is required to completely comprehend the molecular mechanism(s) and host as well as viral factors involved in the formation of flavivirus ROs. For instance, as they have all received little research, RNA-protein interactomes, lipidomic profiles of flavivirus ROs, and protein-protein interactomes within ROs could all be created. Overall, understanding the molecular factors involved in one of the initial stages of the viral replication cycle could help towards the development of much-needed antiviral drugs.

5.2. *De novo* formation of the ZIKV RO is suppressed by the novel NS4A inhibitor SBI-0090799

Arthropod-borne viruses (arboviruses) are recognized as serious threats to global health, as billions of people are living at risk of infection. For emerging/re-emerging arboviral illnesses including dengue⁴²⁶, chikungunya⁴²⁷, West Nile⁴²⁸, and Zika⁴²⁹, the frequency and magnitude of outbreaks have substantially grown over the past 50 years. The viral target population considerably rises⁴³⁰ as a result of the rapid spread of the vectors into more temperate regions^{430,431} brought on by global warming, human population growth, urbanization, and globalization. ZIKV is recognized as a priority disease in the medical community⁴³² as a result of its emergence in the Americas in 2015/16 and its association with neurological disorders and neonatal malformations. With the continuous silent spread and mutagenesis of the Zika virus, there is an increased risk of a larger and more severe outbreak. All of this emphasizes how critical it is to develop antivirals and vaccines to combat this re-emerging infectious disease.

5. Discussion

Despite the fact that multiple prospective ZIKV antiviral medication candidates have been found in prior research using drug repurposing screens⁸¹⁻⁸³, their clinical application has unfortunately been unsuccessful⁴³³. With the aim to identify promising chemical candidates for developing antivirals against ZIKV, a large-scale high-content screening approach was performed by the Sanford Burnham Prebys Medical Discovery Institute, located in La Jolla, California, USA. Using this approach, the novel chemical compound (2E)-N-benzyl-3-(4-butoxyphenyl)prop-2-enamide (SBI-0090799) was identified as an antiviral against ZIKV⁸⁸.

To dissect the mode of action of SBI-0090799 a replicon-based assay was performed, revealing a dose-dependent reduction in viral replication (Figure 19). Whether the decline in viral replication corresponds with a decline in RO inducing efficacy, the newly established pIRO-Z system was functionally assessed in the presence and absence of SBI-0090799. The ability of the pIRO-Z system to induce viral ROs was dramatically reduced in the presence of the drug, despite the fact that SBI-0090799 had no effect on polyprotein cleavage, protein abundance, or subcellular localization of non-structural proteins (Figure 20; Figure 21).

SBI-0090799's hypothesized molecular mechanism for inhibiting RO formation most likely involves blocking NS4A's activity to alternate membranes. The fact that drug resistance mutations accumulated in the cytosolic N-terminal region of this protein provides the basis for the proposed mechanism. In the context of the pIRO system, analysis of these drug-resistant mutations revealed restoration of RO inducing efficacy to a degree comparable to control cells (Figure 22; Figure 23). When the NS4A proteins from Zika and dengue were compared structurally, it was discovered that the first 48 amino acid residues are part of a disordered cytosolic region that is described to fold into a helix upon lipid contact, supporting its function in membrane rearrangements^{434,435}. Although SBI-009079 had no effect on the oligomerization of NS4A proteins⁸⁸, it is hypothesized that SBI-009079 interferes with NS4A, either preventing it from inducing ER membrane curvature or inhibiting NS4A from binding viral or cellular factors. However, more research is required to completely comprehend the structural and functional effects of SBI-0090799 on NS4A. Chemically altering the compound, by adding a diazirine group for crosslinking and alkyne group for click chemistry, would enable its use in chemo-proteomic approaches and therefore provide further detailed insights. The question of whether mutations in NS4A have an impact on viral fitness *in vivo* and transmission by the mosquito vector remains to be investigated.

5. Discussion

It's interesting to note that, in addition to host factors that are used alike by HCV and ZIKV, SBI-0090799 and HCV NS5A inhibitors share a number of similarities. As an illustration, the first generation of HCV NS5A inhibitors were discovered in 2009 and completely inhibited HCV at a concentration of 15 μM ⁴³⁶. Extensive structure-activity relationship studies, however, resulted in the generation of molecules with >10,000-fold greater potency and the development of today's clinically authorized drugs (e.g., daclatasvir and ledipasvir)⁴³⁷. HCV NS5A, like ZIKV NS4A, lacks enzymatic activity but has been recognized as a crucial viral factor for HCV replication. While ZIKV ROs could not be produced by NS4A alone, DMVs, the membrane replication compartment of HCV, can be induced by the sole expression of NS5A. Along these lines, it has been demonstrated that daclatasvir and its derivatives prevent the formation of DMVs, which is comparable to the activity of SBI-0090799 on ZIKV. Overall, using the knowledge gained from the development of HCV NS5A inhibitors could be extremely useful in optimizing the identified ZIKV inhibitor and eventually resulting in its clinical use.

5.3. The interaction between the M domain of the prM protein and host cellular cholesterol drives ZIKV entry and particle assembly

Ever since ZIKV first appeared in the Americas and was linked to serious neurological disorders, numerous efforts have been undertaken to comprehend the viral replication cycle and to pinpoint critical host and viral factors. While noteworthy research transcriptomics^{438–440}, proteomics⁴⁴¹, and lipidomics^{322,323} have shed light on the relationships between ZIKV and its host cell, specific interactions between virus proteins and host cellular lipids are still largely unknown. In order to close this information gap, I performed chemo-proteomics in ZIKV-infected human cells and discovered that the structural protein prM and its cleaved product, the M domain, interact with cholesterol (Figure 25). I was able to demonstrate through bioinformatic analysis that the prM protein has a total of six possible cholesterol binding domains, three of which are located in the soluble pr peptide and three of which are located in the mature M domain (Figure 26). I was able to show how the photo-cross-linking efficiency of the cholesterol probe to prM was significantly decreased (~50%) by leucine and alanine/serine substitutions of the cholesterol binding motifs CRAC2 [R-X₃-F] and CRAC3 [K-X₂-Y] (Figure 27). Although this probe has been used to discover

5. Discussion

cholesterol-binding proteins *in vitro*, it cannot accurately represent quantities of protein-cholesterol complexes as it is a qualitative method for determining a protein's affinity for cholesterol. Other techniques, such as crystallography, should be used to better determine which amino acid residue in the M protein is in contact with cholesterol.

Atomistic molecular dynamics (MD) simulations that simulated M protein dimers embedded into a 20:80 (mol%:mol%) CHOL:POPC lipid bilayer supported my chemo-proteomic findings (Figure 30). The results of MD simulations demonstrated that the WT M protein's surface has a particular binding site of cholesterol atoms. These sites were discovered to be close to the CARC2 and CARC3 motifs. It's interesting that no specific cholesterol binding was found when MD simulations were run using mutant M protein dimers (Figure 30). It should be noted that mutations only slightly altered the conformation of the protein, which can be described as rotation of helix 2 with respect to helix 3. Overall, MD simulations support the assumption that the M protein recruits cholesterol and that the loss of cholesterol binding caused by the substitution of amino acids in the CRAC motifs reduces the ability of cholesterol recruitment.

The fact that members of the flavivirus genus share the cholesterol-binding domains in the TMD2 and TMD3 of the M domain (Figure 26), argues in favor of a critical function in the flavivirus replication cycle. In fact, compared to WT, CRAC mutants with amino acid substitutions in the context of the Zika viral genome displayed fitness disadvantages (Figure 29). According to analysis of replication kinetics, wild type quickly outgrew CARC3 mutant viruses, but CARC2 mutants only showed a minor, insignificant decline in virus fitness (Figure 29). Despite the fact that CARC1 mutants were significantly attenuated, these amino acid substitutions did not result in a loss of cholesterol association when they were functionally characterized (Figure 27), suggesting that the mode of action might be cholesterol independent. The difference in fitness between the CARC2 and CARC3 mutant viruses could be attributed to the high levels of cholesterol found in Huh7-Lunet naïve cells, which raises the probability of cholesterol interactions with M proteins. Along this note, MD simulations demonstrated that partial restoration of the cholesterol interactions for CARC2 mutants occurred at high cholesterol levels (30 mol%). It is safe to say that I have successfully identified the M domain as a cholesterol interactor with two functional cholesterol binding domains in its two transmembrane domains, which are essential for the ZIKV replication cycle.

5. Discussion

ZIKV, like other viruses including Influenza A virus (IAV)³⁸², WNV³⁴⁹, chikungunya virus (CHIKV)⁴⁴², Ebola virus⁴⁴³, and SARS-CoV-2⁴⁴⁴, enters its host target cell via clathrin-mediated endocytosis^{284,285}. Upon binding to cell surface receptors, viruses are internalized and subsequently traffic in clathrin-coated endocytic vesicles, from where they escape via the formation of a fusion pore. At present, it is well established that the formation of primary endocytic vesicles is a cholesterol-dependent process^{391,445}; as a result, cholesterol solubilizing drugs such as methyl- β -cyclodextrin have been proven to have antiviral activity by inhibiting virus infection^{285,345,442,444,446,447}. In this context, fusion activity for WNV was considerably enhanced when cholesterol was present in target membranes³⁴⁹. More recently, it was discovered that IAV fusion required cholesterol as well, mostly through the HA surface protein of the virus, which facilitates the mixing of lipids between membranes³⁸².

Since I have observed only mild defects of CARC2 mutant viruses in the human hepatoma cell line Huh7-Lunet, I next investigated whether the ability of CARC2 mutant viruses to infect cells is sensitive to levels of cholesterol provided by the host target cell. Accordingly, I have shown that the African green monkey kidney cell line VeroE6 has an estimate of 50% lower cholesterol content when compared to Huh7-Lunet cells (Figure 30). Indeed, the ability of CARC2 mutant viruses to infect VeroE6 cells was significantly compromised, indicating that the cholesterol interaction is required during initial stages of the viral infectious replication cycle (binding, uptake, or fusion) (Figure 30). I discovered that the conformation of the E protein, which control virus attachment and binding to host cell surface receptors, was unaffected by the mutation of the M domain (Figure 30). Next, I was able to demonstrate that the viral replication fitness of CARC2 mutant and WT viruses was equivalent after overcoming entry steps through electroporation (Figure 30). Last but not least, it was possible to mimic the observed phenotype of CARC2 mutant viruses in wild type viruses by either pretreating cells with M β CD (Figure 24), thereby lowering the concentrations of cholesterol in target membranes, or by preventing virus fusion by treating infected cells with the endocytic inhibitor ammonium chloride (Figure 30). Interestingly, I have showed that cholesterol binding was not required during infection in insect cells by infecting the mosquito cell line Aag2 with equal MOI (Figure 30). In contrast to WT, replication fitness was improved in CARC2 mutants. As insects are deficient in *de novo* biosynthesis of cholesterol, mosquitos rely on dietary sources to complete the gonotrophic cycle⁴⁴⁸⁻⁴⁵¹. According to my results, entrance mechanisms are regulated by various lipid species

5. Discussion

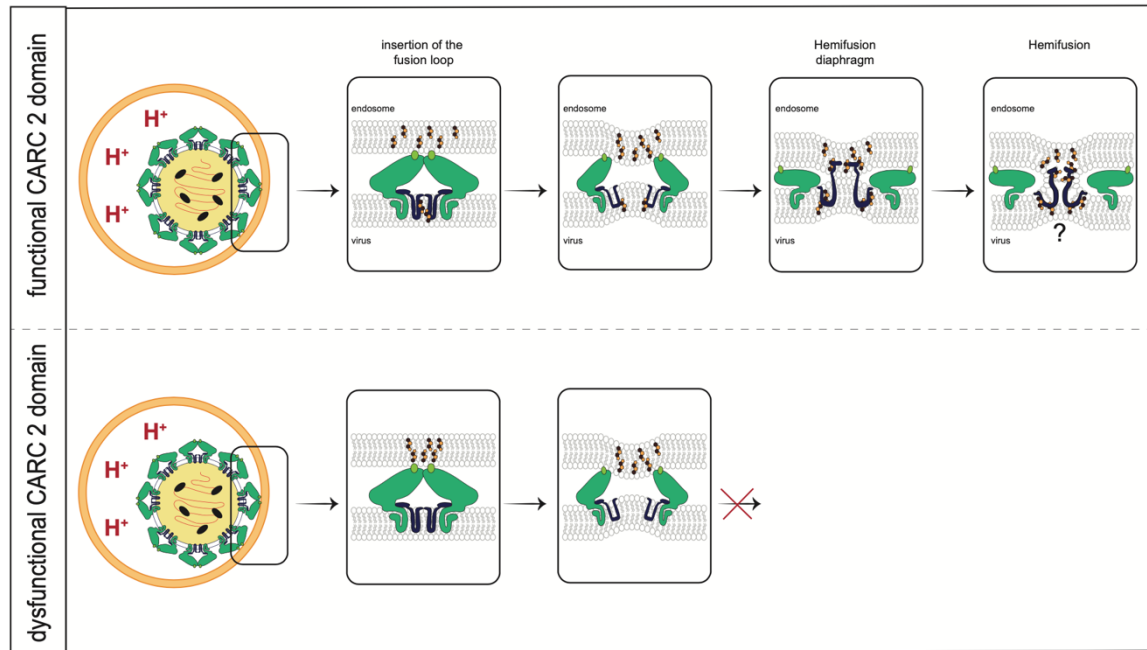


Figure 37. Proposed function of the M domain in virus entry.

ZIKV enters its host cell via clathrin-mediated endocytosis. As the endosome traffics a vacuolar ATPase pumps protons into the interior, causing its acidification. Acidification triggers irreversible conformational changes in the ectopic envelope protein, uncovering the fusion loop which is subsequently inserted into the endosomal membrane initiating the formation of the fusion pore. During the hemifusion event the M domain might facilitate lipid mixing due to its ability to bind lipids such as cholesterol. In the case of mutant CARC2 ZIKV viruses, lipid mixing is not occurring retaining the virus particles in the endosome. (Figure drawn with Adobe)

depending on the host. I demonstrated that in the case of ZIKV, cholesterol interaction is negligible in the mosquito host but of utmost importance during entry into mammalian cells. My findings suggest that this interaction most likely mediates the escape from late endosomes by aiding in the formation of the fusion pore. I speculate that the M domain may facilitate the mixing of lipids between membranes based on its ability to interact with lipids (Figure 37). With the continuous spread of mosquito vectors, as a result of climate change, and human population growth, insect specific viruses, which are currently not known to infect humans, could acquire evolutionary adaptive mutations, facilitating cholesterol interactions and ultimately leading to species jumps. In this respect, lipidomic profiles of viral particles isolated from mosquitos and mammalian cells together with investigation of insect-specific viruses may offer valuable information into the molecular mechanisms governing infection of various host species.

Within the last couple of years, research has provided valuable insights into the molecular mechanism of how ZIKV particles are being formed²⁰⁵, and cryo-electron tomography has

5. Discussion

provided atomistic resolution of immature and mature virus particles^{167,179,326}. The discovery by Zhang and colleagues, which demonstrated that viral RNA, the viral protease NS2B/3, and the polyprotein C-prM-E are recruited to virus assembly sites via the non-structural protein NS2A, is what led to the current understanding of how ZIKV particles are produced²⁰⁵. Upon polyprotein processing by the viral protease NS2B/3, mature capsid proteins are released into the cytoplasm where they bind to viral RNA via the positively charged interface (helix $\alpha 4$), forming the nucleocapsid¹⁶⁷. It was discovered through structural analysis of the capsid protein that its N-terminus (helix $\alpha 1$) interacts with the inner leaflet of the virus lipid membrane due to its highly hydrophobic character^{167,168}. The inner layer of the viral lipid envelope and the capsid density are interacting, as demonstrated by cryo-electron tomography and subtomogram averaging of immature virus particles, particular at regions where the transmembrane domains of envelope and M proteins are located¹⁷⁹. These data imply that capsid may interact with the envelope and/or the M protein, however, no proof of such an interaction has yet been provided. Although parts of the molecular mechanism have been revealed, there are still open questions remaining such as how is the nucleocapsid recruited and how is it ensured that the nucleocapsid is enveloped during the budding event.

My research adds to the molecular understanding of how the nucleocapsid is recruited and enveloped by the lipid bilayer containing prM and E proteins. The kinetics of CARC3 mutant and WT viruses' replication were compared, and the results revealed that CARC3 mutant viruses were greatly attenuated because of defects in the production of infectious virus particles (Figure 31). In fact, transmission electron microscopy analysis of transfected cells revealed that the average number of virus particles per cell profile was significantly lower, although the size of putative virus particles remained unaffected (Figure 31). As virus assembly has been shown to involve NS2A, NS2B/3 which processes the polyprotein C-prM-E, releasing mature capsid proteins, I next investigated the cleavage of the structural proteins. Although polyprotein processing and total protein abundance were comparable between CARC3 mutants and WT ZIKV (Figure 32), CARC3 mutant transfected cells showed differential cleavage of the capsid protein with increased levels of the mature form (Figure 33). To date, immature capsid proteins (helix $\alpha 1$ - $\alpha 5$) have been found to associate with lipid droplets and are thought to contribute to virus particle assembly and morphogenesis^{168,409}. The shorter form of the capsid protein (helix $\alpha 1$ - $\alpha 4$) is released into the cytosol where it binds to viral RNA to form the nucleocapsid or interferes with host cellular

5. Discussion

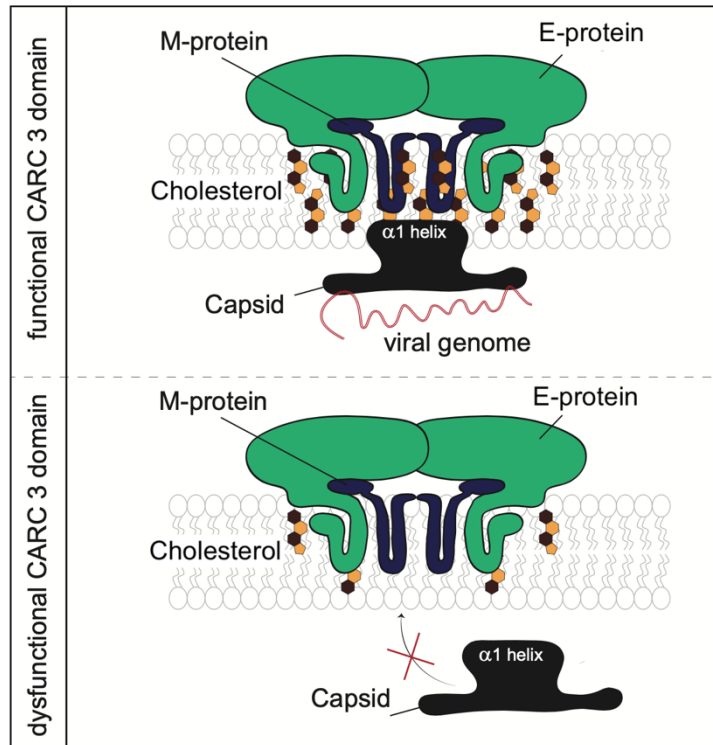


Figure 38. Proposed function of the M domain in virus assembly.

At the rough ER, new ZIKV particles are assembled. The capsid protein is expressed in the cytosolic region of the ER membrane, where it assembles into homodimers. The nucleocapsid is formed when the viral RNA interacts with the positively charged interphase (helix $\alpha 4$). On the luminal side of the ER, prM and E protein simultaneously form heterodimers. A lipid raft is created in this instance by the M domain, which actively recruits cholesterol. This lipid raft serves as an anchoring platform for the structural and non-structural proteins involved in the assembly of virus particles. Because the lipid raft is no longer formed in CARC3 mutants, recruitment of capsid to assembly sites is no longer possible, resulting in ineffective virus particle production. (Figure drawn with Adobe)

processes¹⁷¹. In response to this observation, co-localization events of capsid-envelope-lipid droplets were examined, and it was discovered that the number of total events had significantly decreased while the mean intensity of capsid signal at these sites remained constant (Figure 33). Of note, despite changes in capsid cleavage and subsequent subcellular localization, prM and E protein distribution within cells did not change (Figure 34).

Based on my results and other publications, I propose the model that the M domain interacts with cholesterol to form a lipid raft, which acts as an anchoring platform for structural and non-structural proteins involved in virus particle assembly (Figure 38). In this context, bioinformatic analysis of capsid, NS2A, and NS2B revealed that these proteins do comprise potential cholesterol binding domains in their hydrophobic alpha helices, which are inserted or spanning the ER membrane, respectively. I have shown that the interaction

5. Discussion

reported by Prasad and colleagues instead pertain to protein-lipid interactions rather than protein-protein interactions¹⁷⁹.

Bringing together my results, I am able to show that the ZIKV life cycle is dependent on its interaction with host cellular cholesterol. Interfering with the *de novo* synthesis of cholesterol and manipulation of cholesterol content in target membranes within the mammalian host, has demonstrated that cholesterol is an essential host factor mediating ZIKV entry and particle production. In addition, I have offered novel mechanistic perspectives to viral protein-lipid interactions and how these affect the infectious viral replication cycle. To better understand human illnesses and virus species jumps, more research on related flaviviruses and insect flaviviruses may be helpful. In order to tackle this infectious disease and potential future new emerging infectious diseases, it may be possible to design innovative antiviral drugs that interfere with virus replication by understanding the mechanism(s) involved in virus entrance and assembly.

6. BIBLIOGRAPHY

1. ICTV. International Committee on the Taxonomy of Viruses (ICTV). The Universal Virus Database of the ICTV. <https://ictv.global/taxonomy>. Published 2009.
2. Pierson TC, Diamond MS. The emergence of Zika virus and its new clinical syndromes. *Nature*. 2018;560(7720):573-581. doi:10.1038/s41586-018-0446-y
3. Pierson TC, Diamond MS. The continued threat of emerging flaviviruses. *Nat Microbiol*. 2020;5:796-812. doi:10.1038/s41564-020-0714-0
4. Dick GWA, Kitchen SF, Haddow AJ. Zika virus (I). Isolations and serological specificity. *Trans R Soc Trop Med Hyg*. 1952;46(5):509-520.
5. Marchette NJ, Garcia R, Rudnick A. Isolation of Zika virus from *Aedes aegypti* mosquitoes in Malaysia. *Am J Trop Med Hyg*. 1969;18(3):411-415. doi:10.1056/NEJMp1002530
6. Grard G, Caron M, Mombo IM, et al. Zika Virus in Gabon (Central Africa) - 2007: A New Threat from *Aedes albopictus*? *PLoS Negl Trop Dis*. 2014;8(2):e2681. doi:10.1371/journal.pntd.0002681
7. Ledermann JP, Guillaumot L, Yug L, et al. *Aedes hensilli* as a Potential Vector of Chikungunya and Zika Viruses. *PLoS Negl Trop Dis*. 2014;8(10):e3188. doi:10.1371/journal.pntd.0003188
8. MacNamara FN. Zika virus: A report on three cases of human infection during an epidemic of jaundice in Nigeria. *Trans R Soc Trop Med Hyg*. 1954;48(2). doi:10.1016/0035-9203(54)90006-1
9. Haddow AD, Schuh AJ, Yasuda CY, et al. Genetic characterization of Zika virus strains: Geographic expansion of the Asian lineage. *PLoS Negl Trop Dis*. 2012;6(2):e1477. doi:10.1371/journal.pntd.0001477
10. Musso D, Gubler DJ. Zika virus. *Clin Microbiol Rev*. 2016;29:487-524. doi:10.1128/CMR.00072-15
11. Pettersson JHO, Bohlin J, Dupont-Rouzeyrol M, et al. Re-visiting the evolution, dispersal and epidemiology of Zika virus in Asia article. *Emerg Microbes Infect*. 2018;7(79):2-8. doi:10.1038/s41426-018-0082-5
12. Olson JG, Ksiazek TG, Suhandiman G, Triwibowo V. Zika virus, a cause of fever in Central Java, Indonesia. *Trans R Soc Trop Med Hyg*. 1981;75(3):389-393. doi:10.1016/0035-9203(81)90100-0
13. Clarke DH, Casals J. Techniques for hemagglutination and hemagglutination-inhibition with arthropod-borne viruses. *Am J Trop Med Hyg*. 1958;7(5):561-573. doi:10.4269/ajtmh.1958.7.561
14. Mettler NE, Clarke DH, Casals J. Hemagglutination inhibition with arboviruses: relationship between titers and source of erythrocytes. *Appl Microbiol*. 1971;22(3):377-379. doi:10.1128/aem.22.3.377-379.1971
15. Calisher C harle. H, Karabatsos N, Dalrymple JM, et al. Antigenic relationships between flaviviruses as determined by cross-neutralization tests with polyclonal antisera. *J Gen Virol*. 1989;70(1):37-43. doi:10.1099/0022-1317-70-1-37
16. Kuno G. Serodiagnosis of Flaviviral Infections and Vaccinations in Humans. In: *Advances in Virus Research*. Vol 61. ; 2003:3-65. doi:10.1016/s0065-3527(03)61001-8
17. Duffy MR, Chen T-H, Hancock WT, et al. Zika Virus Outbreak on Yap Island, Federated States of Micronesia. *N Engl J Med*. 2009;360(24):2536-2543. doi:10.1056/nejmoa0805715
18. Lanciotti RS, Kosoy OL, Laven JJ, et al. Genetic and serologic properties of Zika virus associated with an epidemic, Yap State, Micronesia, 2007. *Emerg Infect Dis*. 2008;14(8):1232-1239. doi:10.3201/eid1408.080287
19. Musso D, Nilles EJ, Cao-Lormeau VM. Rapid spread of emerging Zika virus in the Pacific area. *Clin Microbiol Infect*. 2014;20(10):O595-O596. doi:10.1111/1469-0691.12707
20. Cao-Lormeau V-M, Roche C, Teissier A, et al. Zika virus, French Polynesia, South

6. Bibliography

- Pacific, 2013. *Emerg Infect Dis.* 2014;20(6):1085-1086. doi:10.3201/eid2006.140138
21. Cao-Lormeau V-M, Blake A, Mons S, et al. Guillain-Barré syndrome outbreak caused by ZIKA virus infection in French Polynesia. *Lancet.* 2016;387(10027):1531-1539. doi:10.1016/S0140-6736(16)00562-6.
 22. Simon O, Acket B, Forfait C, et al. Zika virus outbreak in New Caledonia and Guillain-Barré syndrome: a case-control study. *J Neurovirol.* 2018;24:362-368. doi:10.1007/s13365-018-0621-9
 23. Pyke AT, Daly MT, Cameron JN, et al. Imported Zika Virus Infection from the Cook Islands into Australia, 2014. *PLoS Curr.* 2014;6. doi:10.1371/currents.outbreaks.4635a54dbffba2156fb2fd76dc49f65e
 24. Tognarelli J, Ulloa S, Villagra E, et al. A report on the outbreak of Zika virus on Easter Island, South Pacific, 2014. *Arch Virol.* 2016;161:665-668. doi:10.1007/s00705-015-2695-5
 25. Campos GS, Bandeira AC, Sardi SI. Zika virus outbreak, Bahia, Brazil. *Emerg Infect Dis.* 2015;21(10):1885-1886. doi:10.3201/eid2110.150847
 26. Gorshkov K, Shiryayev SA, Fertel S, et al. Zika virus: Origins, pathological action, and treatment strategies. *Front Microbiol.* 2019;9(3252):1-17. doi:10.3389/fmicb.2018.03252
 27. Mlakar J, Korva M, Tul N, et al. Zika Virus Associated with Microcephaly. *N Engl J Med.* 2016;374(10):951-958. doi:10.1056/NEJMoa1600651
 28. Rasmussen SA, Jamieson DJ, Honein MA, Petersen LR. Zika Virus and birth defects — reviewing the evidence for causality. *N Engl J Med.* 2016;374(20):1981-1987. doi:10.1056/NEJMsr1604338
 29. Freitas DA, Souza-Santos R, Carvalho LMA, et al. Congenital Zika syndrome: A systematic review. *PLoS One.* 2020;15(12):e0242367. doi:10.1371/journal.pone.0242367
 30. Paixao ES, Cardim LL, Costa MCN, et al. Congenital Zika Syndrome: A Nationwide Cohort Study in Brazil, 2015-2018. *N Engl J Med.* 2022;386(8):757-767. doi:10.1056/NEJMoa2101195
 31. WHO. WHO statement on the third meeting of the International Health Regulations Emergency Committee on Zika virus and observed increase in neurological disorders and neonatal malformations. [https://www.who.int/en/news-room/detail/14-06-2016-who-statement-on-the-third-meeting-of-the-international-health-regulations-\(2005\)-\(ihr\(2005\)\)-emergency-committee-on-zika-virus-and-observed-increase-in-neurological-disorders-and-neonatal-malformations](https://www.who.int/en/news-room/detail/14-06-2016-who-statement-on-the-third-meeting-of-the-international-health-regulations-(2005)-(ihr(2005))-emergency-committee-on-zika-virus-and-observed-increase-in-neurological-disorders-and-neonatal-malformations).
 32. WHO. Zika Virus Disease - India. <https://www.who.int/emergencies/disease-outbreak-news/item/zika-virus-disease-india>.
 33. WHO. Zika virus. <https://www.who.int/news-room/fact-sheets/detail/zika-virus>.
 34. Agarwal A, Chaurasia D. The expanding arms of Zika virus : An updated review with recent Indian outbreaks. *Rev Med Virol.* 2021;31(e2145):1-9. doi:10.1002/rmv.2145
 35. PAHO. Zika Cumulative Cases. https://www3.paho.org/hq/index.php?option=com_content&view=article&id=12390:zika-cumulative-cases&Itemid=42090&lang=en#gsc.tab=0.
 36. Baud D, Gubler DJ, Schaub B, Lanteri MC, Musso D. An update on Zika virus infection. *Lancet.* 2017;390:2099-2109. doi:10.1016/S0140-6736(17)31450-2
 37. Gubler DJ, Vasilakis N, Musso D. History and Emergence of Zika Virus. *J Infect Dis.* 2017;216(S10):S860-S867. doi:10.1093/infdis/jix451
 38. CDC. About Dengue: What You Need to Know. <https://www.cdc.gov/dengue/about/index.html>.
 39. WHO. Dengue and severe dengue. <https://www.who.int/news-room/fact-sheets/detail/dengue-and-severe-dengue>.
 40. Messina JP, Kraemer MUG, Brady OJ, et al. Mapping global environmental suitability for Zika virus. *Elife.* 2016;5:e15272. doi:10.7554/eLife.15272
 41. Cardoso CW, Paploski IAD, Kikutí M, et al. Outbreak of Exanthematous Illness Associated with Zika, Chikungunya, and Dengue Viruses, Salvador, Brazil. *Emerg Infect Dis.* 2015;21(12):2274-2276.
 42. Furtado JM, Espósito DL, Klein TM, Teixeira-Pinto T, Fonseca BA. Uveitis Associated with Zika Virus Infection. *N Engl J Med.* 2016;375(4). doi:10.1056/NEJM1603618

6. Bibliography

43. Meltzer E, Leshem E, Lustig Y, Gottesman G, Schwartz E. The Clinical Spectrum of Zika Virus in Returning Travelers. *Am J Med.* 2016;129(10):1126-1130. doi:10.1016/j.amjmed.2016.04.034
44. Weitzel T, Cortes CP. Images in Clinical Tropical Medicine Zika Virus infection presenting with postauricular lymphadenopathy. *Am J Trop Med Hyg.* 2016;95(2):255-256. doi:10.4269/ajtmh.16-0096
45. Brasil P, Pereira JP, Moreira ME, et al. Zika Virus Infection in Pregnant Women in Rio de Janeiro. *N Engl J Med.* 2016;375(24):2321-2334. doi:10.1056/NEJMoa1602412
46. Basarab M, Bowman C, Aarons EJ, Cropley I. Zika virus. *Br Med J.* 2016;352(i1049):1-7. doi:10.1136/bmj.i1049
47. Galindo-Fraga A, Ochoa-Hein E, Sifuentes-Osornio J, Ruiz-Palacios G. Zika Virus: A New Epidemic on Our Doorstep. *Rev Invest Clin.* 2015;67:329-332.
48. Lessler J, Chaisson LH, Kucirka LM, et al. Assessing the global threat from Zika virus. *Science (80-).* 2016;353(6300):aaf8160-1-10. doi:10.1126/science.aaf8160
49. Oliveira Melo AS, Malinger G, Ximenes R, Szejnfeld PO, Alves Sampaio S, Bispo De Filippis AM. Zika virus intrauterine infection causes fetal brain abnormality and microcephaly: Tip of the iceberg? *Ultrasound Obstet Gynecol.* 2016;47:6-7. doi:10.1002/uog.15831
50. Oehler E, Watrin L, Larre P, et al. Zika virus infection complicated by Guillain-Barré syndrome – case report, French Polynesia, December 2013. *Euro Surveill.* 2014;19(9):20720. <http://www.eurosurveillance.org/ViewArticle.aspx?ArticleId=20720%0AArticle>.
51. European Centre for Disease Prevention and Control. Zika virus epidemic in the Americas: potential association with microcephaly and Guillain-Barré syndrome (1st update). 2016.
52. European Centre for Disease Prevention and Control. Rapid risk assessment: Microcephaly in Brazil potentially linked to the Zika virus epidemic. 2015:1-12. <https://ecdc.europa.eu/sites/portal/files/media/en/publications/Publications/zika-microcephaly-Brazil-rapid-risk-assessment-Nov-2015.pdf>.
53. Besnard M, Eyrolle-Guignot D, Guillemette-Artur P, et al. Congenital cerebral malformations and dysfunction in fetuses and newborns following the 2013 to 2014 Zika virus epidemic in French Polynesia. *Euro Surveill.* 2016;21(13):30181. doi:10.2807/1560-7917.ES.2016.21.13.30181
54. Dick GWA. Zika virus (II). Pathogenicity and physical properties. *Trans R Soc Trop Med Hyg.* 1952;46(5):521-534.
55. Yuki N. Infectious origins of, and molecular mimicry in, Guillain-Barré and Fisher syndromes. *Lancet Infect Dis.* 2001;1(1):29-37. doi:10.1016/S1473-3099(01)00019-6
56. Wim Ang C, Jacobs BC, Laman JD. The Guillain-Barré syndrome: A true case of molecular mimicry. *Trends Immunol.* 2004;25(2):61-66. doi:10.1016/j.it.2003.12.004
57. Lebeau G, Frumence E, Turpin J, et al. Zika E glycan loop region and Guillain-Barré syndrome-related proteins: A possible molecular mimicry to be taken in account for vaccine development. *Vaccines.* 2021;9(283). doi:10.3390/vaccines9030283
58. Romi F, Helgeland G, Gilhus NE. Heat-shock proteins in clinical neurology. *Eur Neurol.* 2011;66:65-69. doi:10.1159/000329373
59. Nakatani Y, Hotta S, Utsunomiya I, et al. Cav2.1 voltage-dependent Ca²⁺ channel current is inhibited by serum from select patients with Guillain-Barré syndrome. *Neurochem Res.* 2009;34:149-157. doi:10.1007/s11064-008-9735-4
60. Parra B, Lizarazo J, Jiménez-Arango JA, et al. Guillain-Barré Syndrome Associated with Zika Virus Infection in Colombia. *N Engl J Med.* 2016;375(16):1513-1523. doi:10.1056/NEJMoa1605564
61. Acosta-Ampudia Y, Monsalve DM, Castillo-Medina LF, et al. Autoimmune neurological conditions associated with Zika virus infection. *Front Mol Neurosci.* 2018;11. doi:10.3389/fnmol.2018.00116
62. Bhagat R, Kaur G, Seth P. Molecular mechanisms of Zika virus pathogenesis: An update. *Indian J Med Res.* 2021;154:433-445. doi:10.4103/ijmr.IJMR_169_20
63. Miner JJ, Diamond MS. Zika Virus Pathogenesis and Tissue Tropism. *Cell Host Microbe.*

6. Bibliography

- 2017;21(2):134-142. doi:10.1016/j.chom.2017.01.004
64. Sarno M, Sacramento GA, Khouri R, et al. Zika Virus Infection and Stillbirths: A Case of Hydrops Fetalis, Hydranencephaly and Fetal Demise. *PLoS Negl Trop Dis*. 2016;10(2):e0004517. doi:10.1371/journal.pntd.0004517
65. Hirsch AJ, Roberts VHJ, Grigsby PL, et al. Zika virus infection in pregnant rhesus macaques causes placental dysfunction and immunopathology. *Nat Commun*. 2018;9(263). doi:10.1038/s41467-017-02499-9
66. Rabelo K, de Souza LJ, Salomão NG, et al. Zika Induces Human Placental Damage and Inflammation. *Front Immunol*. 2020;11(2146):1-15. doi:10.3389/fimmu.2020.02146
67. Oliveira-Szejnfeld PS, Levine D, Oliveira Melo AS, et al. Congenital Brain abnormalities and Zika Virus: What the Radiologist Can Expect to See Prenatally and Postnatally. *Radiology*. 2016;281(1):203-218.
68. Vue D, Tang Q. Zika Virus Overview: Transmission, Origin, Pathogenesis, Animal Model and Diagnosis. *Zoonoses*. 2021;1(14). doi:10.15212/zoonoses-2021-0017
69. Wen Z, Song H, Ming G-L. How does Zika virus cause microcephaly? *Genes Dev*. 2017;31:849-861. doi:10.1101/gad.298216.117
70. Dang J, Tiwari SK, Lichinchi G, et al. Zika Virus Depletes Neural Progenitors in Human Cerebral Organoids through Activation of the Innate Immune Receptor TLR3. *Cell Stem Cell*. 2016;19:258-265. doi:10.1016/j.stem.2016.04.014
71. Onorati M, Li Z, Liu F, et al. Zika Virus Disrupts Phospho-TBK1 Localization and Mitosis in Human Neuroepithelial Stem Cells and Radial Glia. *Cell Rep*. 2016;16:2576-2592. doi:10.1016/j.celrep.2016.08.038
72. Tang H, Hammack C, Ogden SC, et al. Zika virus infects human cortical neural progenitors and attenuates their growth. *Cell Stem Cell*. 2016;18:587-590. doi:10.1016/j.stem.2016.02.016
73. Li C, Xu D, Ye Q, et al. Zika Virus Disrupts Neural Progenitor Development and Leads to Microcephaly in Mice. *Cell Stem Cell*. 2016;19:120-126. doi:10.1016/j.stem.2016.04.017
74. Souza BSF, Sampaio GLA, Pereira CS, et al. Zika virus infection induces mitosis abnormalities and apoptotic cell death of human neural progenitor cells. *Sci Rep*. 2016;6(39775):1-13. doi:10.1038/srep39775
75. Cugola FR, Fernandes IR, Russo FB, et al. The Brazilian Zika virus strain causes birth defects in experimental models. *Nature*. 2016;534:267-271. doi:10.1038/nature18296
76. Garcez PP, Loiola EC, Madeiro da Costa R, et al. Zika virus impairs growth in human neurospheres and brain organoids. *Science (80-)*. 2016. doi:10.1126/science.aaf6116
77. Nguyen HN, Qian X, Song H, Ming GL. Neural stem cells attacked by Zika virus. *Cell Res*. 2016;26:753-754. doi:10.1038/cr.2016.68
78. CDC. Zika Virus Treatment. <https://www.cdc.gov/zika/symptoms/treatment.html>.
79. PAHO, WHO. Epidemiological Update - Zika Virus Infection. 2015:1-7. <https://www.paho.org/hq/dmdocuments/2016/2015-oct-16-cha-zika-virus-epi-update.pdf>.
80. Bernatchez JA, Tran LT, Li J, Luan Y, Siqueira-Neto JL, Li R. Drugs for the Treatment of Zika Virus Infection. *J Med Chem*. 2020;63:470-489. doi:10.1021/acs.jmedchem.9b00775
81. Barrows NJ, Campos RK, Powell ST, et al. A Screen of FDA-Approved Drugs for Inhibitors of Zika Virus Infection. *Cell Host Microbe*. 2016;20:259-270. doi:10.1016/j.chom.2016.07.004
82. Adcock RS, Chu Y, Golden JE, Chung D. Evaluation of anti-Zika virus activities of broad-spectrum antivirals and NIH clinical collection compounds using a cell-based, high-throughput screen assay. *Antiviral Res*. 2017;138:47-56. doi:10.1016/j.antiviral.2016.11.018
83. Pascoalino BS, Courtemanche G, Cordeiro MT, Gil LHV, Freitas-Junior LH. Zika antiviral chemotherapy: identification of drugs and promising starting points for drug discovery from an FDA- approved library [version 1; peer review: 2 approved]. *F1000Research*. 2016;5(2523):1-17. doi:10.12688/f1000research.9648.1
84. Xu M, Lee EM, Wen Z, et al. Identification of small-molecule inhibitors of Zika virus infection and induced neural cell death via a drug repurposing screen. *Nat Med*.

6. Bibliography

- 2016;22(10):1101-1109. doi:10.1038/nm.4184
85. Zou G, Xu HY, Qing M, Wang Q, Shi P. Development and characterization of a stable luciferase dengue virus for high-throughput screening. *Antiviral Res.* 2011;91:11-19. doi:10.1016/j.antiviral.2011.05.001
 86. Puig-Basagoiti F, Deas TS, Ren P, Tilgner M, Ferguson DM, Shi P. High-Throughput Assays Using a Luciferase-Expressing Replicon, Virus-Like Particles, and Full-Length Virus for West Nile Virus Drug Discovery. *Antimicrob Agents Chemother.* 2005;49(12):4980-4988. doi:10.1128/AAC.49.12.4980-4988.2005
 87. Qing M, Liu W, Yuan Z, Gu F, Yong P. A high-throughput assay using dengue-1 virus-like particles for drug discovery. *Antiviral Res.* 2010;86:163-171. doi:10.1016/j.antiviral.2010.02.313
 88. Riva L, Goellner S, Biering SB, et al. The Compound SBI-0090799 Inhibits Zika Virus Infection by Blocking De Novo Formation of the Membranous Replication Compartment. *J Virol.* 2021;95(22):e0099621. doi:10.1128/jvi.00996-21
 89. Zhang Q-Y, Li X-D, Liu S-Q, Deng C-L, Zhang B, Ye H-Q. Development of a stable Japanese encephalitis virus replicon cell line for antiviral screening. *Arch Virol.* 2017;162:3417-3423. doi:10.1007/s00705-017-3508-9
 90. Lo MK, Tilgner M, Shi P-Y. Potential High-Throughput Assay for Screening Inhibitors of West Nile Virus Replication. *J Virol.* 2003;77(23):12901-12906. doi:10.1128/JVI.77.23.12901-12906.2003
 91. Ng CY, Gu F, Phong WY, et al. Construction and characterization of a stable subgenomic dengue virus type 2 replicon system for antiviral compound and siRNA testing. *Antiviral Res.* 2007;76:222-231. doi:10.1016/j.antiviral.2007.06.007
 92. Jones CT, Patkar CG, Kuhn RJ. Construction and applications of yellow fever virus replicons. *Virology.* 2005;331:247-259. doi:10.1016/j.virol.2004.10.034
 93. Khromykh AA, Westaway EG. Subgenomic Replicons of the Flavivirus Kunjin: Construction and Applications. *J Virol.* 1997;71(2):1497-1505.
 94. Kojima A, Yasuda A, Asanuma H, et al. Stable High-Producer Cell Clone Expressing Virus-Like Particles of the Japanese Encephalitis Virus E Protein for a Second-Generation Subunit Vaccine. *J Virol.* 2003;77(16):8745-8755. doi:10.1128/JVI.77.16.8745-8755.2003
 95. Scholle F, Girard YA, Zhao Q, Higgs S, Mason PW. trans -Packaged West Nile Virus-Like Particles: Infectious Properties In Vitro and in Infected Mosquito Vectors. *J Virol.* 2004;78(21):11605-11614. doi:10.1128/JVI.78.21.11605-11614.2004
 96. Ribeiro de Almeida Queiroz S, Joaquim Silva Júnior JV, Nazaré Montiero Rangel da Silva A, Gomes de Oliveira Carvalho A, José da Silva Santos J, Vega Gonzales Gil LH. Development and characterization of a packaging cell line for pseudo-infectious yellow fever virus particle generation. *Rev Soc Bras Med Trop.* 2018;51(1):66-70. doi:10.1590/0037-8682-0220-2017
 97. Matsuda M, Yamanaka A, Yato K, et al. High-throughput neutralization assay for multiple flaviviruses based on single-round infectious particles using dengue virus type 1 reporter replicon. *Sci Rep.* 2018;8(16624):1-8. doi:10.1038/s41598-018-34865-y
 98. Garg H, Sedano M, Plata G, Punke EB, Joshi A. Development of Virus-Like-Particle Vaccine and Reporter Assay for Zika Virus. *J Virol.* 2017;91(e00834-17):1-16. doi:10.1128/JVI.00834-17
 99. Lim SP, Wang Q-Y, Noble CG, et al. Ten years of dengue drug discovery: Progress and prospects. *Antiviral Res.* 2013;100:500-519. doi:10.1016/j.antiviral.2013.09.013
 100. Zou J, Shi PY. Strategies for Zika drug discovery. *Curr Opin Virol.* 2019;35:19-26. doi:10.1016/j.coviro.2019.01.005
 101. Byler KG, Ogungbe IV, Setzer WN. In-silico screening for anti-Zika virus phytochemicals. *J Mol Graph Model.* 2016;69:78-91. doi:10.1016/j.jmkgm.2016.08.011
 102. Shiryayev SA, Farhy C, Pinto A, et al. Characterization of the Zika virus two-component NS2B-NS3 protease and structure-assisted identification of allosteric small-molecule antagonists. *Antiviral Res.* 2017;143:218-229. doi:10.1016/j.antiviral.2017.04.015
 103. Yuan S, Chan JF-W, Den-Haan H, et al. Structure-based discovery of clinically approved drugs as Zika virus NS2B-NS3 protease inhibitors that potently inhibit Zika virus infection

6. Bibliography

- in vitro and in vivo. *Antiviral Res.* 2017;145:33-43. doi:10.1016/j.antiviral.2017.07.007
104. Stephen P, Baz M, Boivin G, Lin SX. Structural Insight into NS5 of Zika Virus Leading to the Discovery of MTase Inhibitors. *J Am Chem Soc.* 2016;138(50):16212-16215. doi:10.1021/jacs.6b10399
 105. Elfiky AA, Elshemey WM. Molecular dynamics simulation revealed binding of nucleotide inhibitors to ZIKV polymerase over 444 nanoseconds. *J Med Virol.* 2018;90:13-18. doi:10.1002/jmv.24934
 106. Pattnaik A, Palermo N, Sahoo BR, et al. Discovery of a non-nucleoside RNA polymerase inhibitor for blocking Zika virus replication through in silico screening. *Antiviral Res.* 2018;151:78-86. doi:10.1016/j.antiviral.2017.12.016
 107. Ramharack P, Soliman MES. Zika virus NS5 protein potential inhibitors: an enhanced in silico approach in drug discovery. *J Biomol Struct Dyn.* 2018;36(5):1118-1133. doi:10.1080/07391102.2017.1313175
 108. Yin Z, Patel SJ, Wang W-L, et al. Peptide inhibitors of dengue virus NS3 protease. Part 2: SAR study of tetrapeptide aldehyde inhibitors. *Bioorganic Med Chem Lett.* 2006;16:40-43. doi:10.1016/j.bmcl.2005.09.049
 109. Yin Z, Patel SJ, Wang W-L, et al. Peptide inhibitors of dengue virus NS3 protease. Part 1: Warhead. *Bioorganic Med Chem Lett.* 2006;16:36-39. doi:10.1016/j.bmcl.2005.09.062
 110. Nitsche C, Behnam MAM, Steuer C, Klein CD. Retro peptide-hybrids as selective inhibitors of the Dengue virus NS2B-NS3 protease. *Antiviral Res.* 2012;94:72-79. doi:10.1016/j.antiviral.2012.02.008
 111. Li K, Ji Q, Jiang S, Zhang N. Advancement in the Development of Therapeutics Against Zika Virus Infection. *Front Cell Infect Microbiol.* 2022;12(946957):1-7. doi:10.3389/fcimb.2022.946957
 112. Weaver SC, Costa F, Garcia-Blanco MA, et al. Zika virus: History, emergence, biology, and prospects for control. *Antiviral Res.* 2016;130:69-80. doi:10.1016/j.antiviral.2016.03.010
 113. Halstead SB. Dengvaxia sensitizes seronegatives to vaccine enhanced disease regardless of age. *Vaccine.* 2017;35:6355-6358. doi:10.1016/j.vaccine.2017.09.089
 114. Elong Ngonon A, Shresta S. Cross-Reactive T Cell Immunity to Dengue and Zika Viruses: New Insights Into Vaccine Development. *Front Immunol.* 2019;10(1316):1-9. doi:10.3389/fimmu.2019.01316
 115. European Medicines Agency. Japanese encephalitis virus. <https://www.ema.europa.eu/en/medicines/human/EPAR/ixiaro>.
 116. Paul-Ehrlich-Institut. Tick borne encephalitis vaccine. <https://www.pei.de/EN/medicinal-products/vaccines-human/tick-borne-encephalitis/tick-borne-encephalitis-node.html>.
 117. Paul-Ehrlich-Institut. Yellow Fever Vaccines. <https://www.pei.de/EN/medicinal-products/vaccines-human/yellow-fever/yellow-fever-node.html>.
 118. Gubler DJ. Dengue and dengue hemorrhagic fever in the Americas. *P R Health Sci J.* 1987;6(2):107-111.
 119. Gubler DJ. Dengue and dengue hemorrhagic fever. *Clin Microbiol Rev.* 1998;11(3):480-496.
 120. Winch PJ, Leontsini E, Rigau-Pérez JG, Ruiz-Pérez M, Clark GG, Gubler DJ. Community-based dengue prevention programs in Puerto Rico: Impact on knowledge, behavior, and residential mosquito infestation. *Am J Trop Med Hyg.* 2002;67(4):363-370. doi:10.4269/ajtmh.2002.67.363
 121. WHO. Vector control operations framework for Zika virus. 2016. http://who.int/whopes/Long-lasting_insecticidal_nets_April_2016.pdf.
 122. Wise De Valdez MR, Nimmo D, Betz J, et al. Genetic elimination of dengue vector mosquitoes. *Proc Natl Acad Sci U S A.* 2011;108(12):4772-4775. doi:10.1073/pnas.1019295108
 123. Ritchie SA, Townsend M, Paton CJ, Callahan AG, Hoffmann AA. Application of wMelPop Wolbachia Strain to Crash Local Populations of Aedes Aegypti. *PLoS Negl Trop Dis.* 2015;9(7):e0003930. doi:10.1371/journal.pntd.0003930
 124. Barrera R, Amador M, Acevedo V, Caban B, Felix G, Mackay AJ. Use of the CDC

6. Bibliography

- Autocidal Gravid Ovitrap to Control and Prevent Outbreaks of *Aedes aegypti* (Diptera: Culicidae). *J Med Entomol.* 2014;51(1):145-154.
125. Kuno G, Chang G-JJ. Full-length sequencing and genomic characterization of Bagaza, Kedougou, and Zika viruses. *Arch Virol.* 2007;152:687-696. doi:10.1007/s00705-006-0903-z
126. Chambers TJ. Flaviviruses: General Features. In: *Encyclopedia of Virology.* ; 2008. doi:10.1016/B978-012374410-4.00621-X
127. Ye Q, Liu Z-Y, Han J-F, Jiang T, Li X-F, Qin C-F. Genomic characterization and phylogenetic analysis of Zika virus circulating in the Americas. *Infect Genet Evol.* 2016;43:43-49. doi:10.1016/j.meegid.2016.05.004
128. Baronti C, Piorkowski G, Charrel RN, Boubis L, Leparac-Goffart I, De Lamballerie X. Complete Coding Sequence of Zika Virus from a French Polynesia Outbreak in 2013. *Genome Announc.* 2014;2(3):e00500-14. doi:10.1128/genomeA.00500-14.
129. Stocks CE, Lobigs M. Signal Peptidase Cleavage at the Flavivirus C-prM Junction: Dependence on the Viral NS2B-3 Protease for Efficient Processing Requires Determinants in C, the Signal Peptide, and prM. *J Virol.* 1998;72(3):2141-2149. doi:10.1128/jvi.72.3.2141-2149.1998
130. Rodriguez AK, Muñoz AL, Segura NA, Rangel HR, Bello F. Molecular characteristics and replication mechanism of dengue, Zika and chikungunya arboviruses, and their treatments with natural extracts from plants: An updated review. *EXCLI J Exp Clin Sci.* 2019;18:988-1006. doi:10.17179/excli2019-1825
131. Chambers TJ, Grakoui A, Rice CM. Processing of the yellow fever virus nonstructural polyprotein: a catalytically active NS3 proteinase domain and NS2B are required for cleavages at dibasic sites. *J Virol.* 1991;65(11):6042-6050. doi:10.1128/jvi.65.11.6042-6050.1991
132. Lin C, Amberg SM, Chambers TJ, Rice CM. Cleavage at a novel site in the NS4A region by the yellow fever virus NS2B-3 proteinase is a prerequisite for processing at the downstream 4A/4B signalase site. *J Virol.* 1993;67(4):2327-2335. doi:10.1128/JVI.67.4.2327-2335.1993.
133. Lobigs M. Flavivirus premembrane protein cleavage and spike heterodimer secretion require the function of the viral proteinase NS3. *Proc Natl Acad Sci U S A.* 1993;90(13):6218-6222. doi:10.1073/pnas.90.13.6218
134. Falgout B, Markoff L. Evidence that flavivirus NS1-NS2A cleavage is mediated by a membrane-bound host protease in the endoplasmic reticulum. *J Virol.* 1995;69(11):7232-7243. doi:10.1128/jvi.69.11.7232-7243.1995
135. Molloy SS, Bresnahan PA, Leppla SH, Klimpel KR, Thomas G. Human furin is a calcium-dependent serine endoprotease that recognizes the sequence Arg-X-X-Arg and efficiently cleaves anthrax toxin protective antigen. *J Biol Chem.* 1992;267(23):16396-16402. doi:10.1016/s0021-9258(18)42016-9
136. Nakayama K. Furin: A mammalian subtilisin/Kex2p-like endoprotease involved in processing of a wide variety of precursor proteins. *Biochem J.* 1997;327:625-635. doi:10.1042/bj3270625
137. Brierley I, Dos Ramos FJ. Programmed ribosomal frameshifting in HIV-1 and the SARS-CoV. *Virus Res.* 2006;119:29-42. doi:10.1016/j.virusres.2005.10.008
138. Clyde K, Harris E. RNA Secondary Structure in the Coding Region of Dengue Virus Type 2 Directs Translation Start Codon Selection and Is Required for Viral Replication. *J Virol.* 2006;80(5):2170-2182. doi:10.1128/jvi.80.5.2170-2182.2006
139. Kieft JS. Viral IRES RNA structures and ribosome interactions. *Trends Biochem Sci.* 2008;33(6):274-283. doi:10.1016/j.tibs.2008.04.007
140. Liu Y, Wimmer E, Paul A V. Cis-acting RNA elements in human and animal plus-strand RNA viruses. *Biochim Biophys Acta.* 2009;1789:495-517. doi:10.1016/j.bbagr.2009.09.007
141. Simon AE, Miller WA. 3' cap-independent translation enhancers of plant viruses. *Annu Rev Microbiol.* 2013;67:21-42. doi:10.1146/annurev-micro-092412-155609
142. Filomatori C V., Lodeiro MF, Alvarez DE, Samsa MM, Pietrasanta L, Gamarnik A V. A 5' RNA element promotes dengue virus RNA synthesis on a circular genome. *Genes Dev.*

6. Bibliography

- 2006;20(16):2238-2249. doi:10.1101/gad.1444206
143. Clyde K, Barrera J, Harris E. The capsid-coding region hairpin element (cHP) is a critical determinant of dengue virus and West Nile virus RNA synthesis. *Virology*. 2008;379:314-323. doi:10.1016/j.virol.2008.06.034
 144. Vogt DA, Andino R. An RNA element at the 5'-end of the poliovirus genome functions as a general promoter for RNA synthesis. *PLoS Pathog*. 2010;6(6):e1000936. doi:10.1371/journal.ppat.1000936
 145. Wu B, Pogany J, Na H, Nicholson BL, Nagy PD, White KA. A discontinuous RNA platform mediates RNA virus replication: Building an integrated model for RNA-based regulation of viral processes. *PLoS Pathog*. 2009;5(3):e1000323. doi:10.1371/journal.ppat.1000323
 146. Goto H, Muramoto Y, Noda T, Kawaoka Y. The Genome-Packaging Signal of the Influenza A Virus Genome Comprises a Genome Incorporation Signal and a Genome-Bundling Signal. *J Virol*. 2013;87(21):11316-11322. doi:10.1128/jvi.01301-13
 147. Keane SC, Heng X, Lu K, et al. Structure of the HIV-1 RNA packaging signal. *Science (80-)*. 2015;348(6237):917-921. doi:10.1126/science.aaa9266
 148. Morales L, Mateos-Gomez PA, Capiscol C, del Palacio L, Enjuanes L, Sola I. Transmissible Gastroenteritis Coronavirus Genome Packaging Signal Is Located at the 5' End of the Genome and Promotes Viral RNA Incorporation into Virions in a Replication-Independent Process. *J Virol*. 2013;87(21):11579-11590. doi:10.1128/jvi.01836-13
 149. Alvarez DE, Lodeiro MF, Ludueña SJ, Pietrasanta LI, Gamarnik A V. Long-Range RNA-RNA Interactions Circularize the Dengue Virus Genome. *J Virol*. 2005;79(11):6631-6643. doi:10.1128/jvi.79.11.6631-6643.2005
 150. Nicholson BL, White KA. Functional long-range RNA-RNA interactions in positive-strand RNA viruses. *Nat Rev Microbiol*. 2014;12:493-504. doi:10.1038/nrmicro3288
 151. Shetty S, Stefanovic S, Mihailescu MR. Hepatitis C virus RNA: Molecular switches mediated by long-range RNA-RNA interactions? *Nucleic Acids Res*. 2013;41(4):2526-2540. doi:10.1093/nar/gks1318
 152. Zhang B, Dong H, Stein DA, Iversen PL, Shi PY. West Nile virus genome cyclization and RNA replication require two pairs of long-distance RNA interactions. *Virology*. 2008;373:1-13. doi:10.1016/j.virol.2008.01.016
 153. Friebe P, Harris E. Interplay of RNA Elements in the Dengue Virus 5' and 3' Ends Required for Viral RNA Replication. *J Virol*. 2010;84(12):6103-6118. doi:10.1128/jvi.02042-09
 154. Friebe P, Shi P-Y, Harris E. The 5' and 3' Downstream AUG Region Elements Are Required for Mosquito-Borne Flavivirus RNA Replication. *J Virol*. 2011;85(4):1900-1905. doi:10.1128/jvi.02037-10
 155. Khromykh AA, Meka H, Guyatt KJ, Westaway EG. Essential Role of Cyclization Sequences in Flavivirus RNA Replication. *J Virol*. 2001;75(14):6719-6728. doi:10.1128/jvi.75.14.6719-6728.2001
 156. Chapman EG, Moon SL, Wilusz J, Kieft JS. RNA structures that resist degradation by Xrn1 produce a pathogenic dengue virus RNA. *Elife*. 2014;3:e01892. doi:10.7554/eLife.01892
 157. Funk A, Truong K, Nagasaki T, et al. RNA Structures Required for Production of Subgenomic Flavivirus RNA. *J Virol*. 2010;84(21):11407-11417. doi:10.1128/jvi.01159-10
 158. Villordo SM, Filomatori C V., Sánchez-Vargas I, Blair CD, Gamarnik A V. Dengue Virus RNA Structure Specialization Facilitates Host Adaptation. *PLoS Pathog*. 2015;11(1):e1004604. doi:10.1371/journal.ppat.1004604
 159. de Borja L, Villordo SM, Marsico FL, et al. RNA structure duplication in the dengue virus 3' UTR: Redundancy or host specificity? *MBio*. 2019;10:e02506-18. doi:10.1128/mBio.02506-18
 160. Manzano M, Reichert ED, Polo S, et al. Identification of cis-acting elements in the 3'-untranslated region of the dengue virus type 2 RNA that modulate translation and replication. *J Biol Chem*. 2011;286(25):22521-22534. doi:10.1074/jbc.M111.234302
 161. Romero TA, Tumban E, Jun J, Lott WB, Hanley KA. Secondary structure of dengue virus

6. Bibliography

- type 4 3' untranslated region: Impact of deletion and substitution mutations. *J Gen Virol.* 2006;87(11):3291-3296. doi:10.1099/vir.0.82182-0
162. Davis WG, Basu M, Elrod EJ, Germann MW, Brinton MA. Identification of cis-Acting Nucleotides and a Structural Feature in West Nile Virus 3'Terminus RNA That Facilitate Viral Minus Strand RNA Synthesis. *J Virol.* 2013;87(13):7622-7636. doi:10.1128/jvi.00212-13
163. Elghonemy S, Davis WG, Brinton MA. The majority of the nucleotides in the top loop of the genomic 3'terminal stem loop structure are cis-acting in a West Nile virus infectious clone. *Virology.* 2005;331:238-246. doi:10.1016/j.virol.2004.11.008
164. Yu L, Markoff L. The Topology of Bulges in the Long Stem of the Flavivirus 3' Stem-Loop Is a Major Determinant of RNA Replication Competence. *J Virol.* 2005;79(4):2309-2324. doi:10.1128/jvi.79.4.2309-2324.2005
165. Zeng L, Falgout B, Markoff L. Identification of Specific Nucleotide Sequences within the Conserved 3'SL in the Dengue Type 2 Virus Genome Required for Replication. *J Virol.* 1998;72(9):7510-7522. doi:10.1128/jvi.72.9.7510-7522.1998
166. Villordo SM, Alvarez DE, Gamarnik A V. A balance between circular and linear forms of the dengue virus genome is crucial for viral replication. *Rna.* 2010;16(12):2325-2335. doi:10.1261/rna.2120410
167. Tan TY, Fibriansah G, Kostyuchenko VA, et al. Capsid protein structure in Zika virus reveals the flavivirus assembly process. *Nat Commun.* 2020;11(895):1-13. doi:10.1038/s41467-020-14647-9
168. Shang Z, Song H, Shi Y, Qi J, Gao GF. Crystal Structure of the Capsid Protein from Zika Virus. *J Mol Biol.* 2018;430:948-962. doi:10.1016/j.jmb.2018.02.006
169. Amberg SM, Nestorowicz A, McCourt DW, Rice CM. NS2B-3 proteinase-mediated processing in the yellow fever virus structural region: in vitro and in vivo studies. *J Virol.* 1994;68(6):3794-3802. doi:10.1128/jvi.68.6.3794-3802.1994
170. Morando MA, Barbosa GM, Cruz-Oliveira C, Da Poian AT, Almeida FCL. Dynamics of Zika Virus Capsid Protein in Solution: The Properties and Exposure of the Hydrophobic Cleft Are Controlled by the α -Helix 1 Sequence. *Biochemistry.* 2019;58:2488-2498. doi:10.1021/acs.biochem.9b00194
171. Hou S, Kumar A, Xu Z, et al. Zika Virus Hijacks Stress Granule Proteins and Modulates the Host Stress Response. *J Virol.* 2017;91:e00474-17.
172. Guo M, Hui L, Nie Y, Tefsen B, Wu Y. ZIKV viral proteins and their roles in virus-host interactions. *Sci China Life Sci.* 2021;64(5):709-719. doi:10.1007/s11427-020-1818-4
173. Sirohi D, Chen Z, Sun L, et al. The 3.8Å resolution cryo-EM structure of Zika Virus. *Science (80-).* 2016;352(6284):467-470. doi:10.1126/science.aaf5316.
174. Pierson TC, Diamond MS. Degrees of maturity: The complex structure and biology of flaviviruses. *Curr Opin Virol.* 2012;2:168-175. doi:10.1016/j.coviro.2012.02.011
175. Nambala P, Su WC. Role of Zika virus prM protein in viral pathogenicity and use in vaccine development. *Front Microbiol.* 2018;9(1797):1-6. doi:10.3389/fmicb.2018.01797
176. Li G, Bos S, Tsetsarkin KA, et al. The roles of prM-E proteins in historical and epidemic Zika virus-mediated infection and neurocytotoxicity. *Viruses.* 2019;11(157):1-21. doi:10.3390/v11020157
177. Lin HH, Yip BS, Huang LM, Wu SC. Zika virus structural biology and progress in vaccine development. *Biotechnol Adv.* 2018. doi:10.1016/j.biotechadv.2017.09.004
178. Kostyuchenko VA, Zhang Q, Tan JL, Ng T-S, Lok S-M. Immature and Mature Dengue Serotype 1 Virus Structures Provide Insight into the Maturation Process. *J Virol.* 2013;87(13):7700-7707. doi:10.1128/jvi.00197-13
179. Prasad VM, Miller AS, Klose T, et al. Structure of the immature Zika virus at 9Å resolution. *Nat Struct Mol Biol.* 2017;24(2):184-186. doi:10.1038/nsmb.3352
180. Stadler K, Allison SL, Schalich J, Heinz FX. Proteolytic activation of tick-borne encephalitis virus by furin. *J Virol.* 1997;71(11):8475-8481. doi:10.1128/jvi.71.11.8475-8481.1997
181. Yu IM, Zhang W, Holdaway HA, et al. Structure of the immature dengue virus at low pH primes proteolytic maturation. *Science (80-).* 2008;319(5871):1834-1837.

6. Bibliography

- doi:10.1126/science.1153264
182. Yu I-M, Holdaway HA, Chipman PR, Kuhn RJ, Rossmann MG, Chen J. Association of the pr Peptides with Dengue Virus at Acidic pH Blocks Membrane Fusion. *J Virol*. 2009;83(23):12101-12107. doi:10.1128/jvi.01637-09
 183. Seidah NG, Mayer G, Zaid A, et al. The activation and physiological functions of the proprotein convertases. *Int J Biochem Cell Biol*. 2008;40:1111-1125. doi:10.1016/j.biocel.2008.01.030
 184. Yuan L, Huang XY, Liu ZY, et al. A single mutation in the prM protein of Zika virus contributes to fetal microcephaly. *Science (80-)*. 2017;358:933-936. doi:10.1126/science.aam7120
 185. Hasan SS, Sevvana M, Kuhn RJ, Rossmann MG. Structural biology of Zika virus and other flaviviruses. *Nat Struct Mol Biol*. 2018;25:13-20. doi:10.1038/s41594-017-0010-8
 186. Sapparapu G, Fernandez E, Kose N, et al. Neutralizing human antibodies prevent Zika virus replication and fetal disease in mice. *Nature*. 2016;540:443-447. doi:10.1038/nature20564
 187. Stettler K, Beltramello M, Espinosa DA, et al. Specificity, cross-reactivity, and function of antibodies elicited by Zika virus infection. *Science (80-)*. 2016;353(6301):823-826. doi:10.1126/science.aaf8505
 188. Tai W, He L, Wang Y, et al. Critical neutralizing fragment of Zika virus EDIII elicits cross-neutralization and protection against divergent Zika viruses. *Emerg Microbes Infect*. 2018;7(7):1-13. doi:10.1038/s41426-017-0007-8
 189. Dai L, Song J, Lu X, et al. Structures of the Zika Virus Envelope Protein and Its Complex with a Flavivirus Broadly Protective Antibody. *Cell Host Microbe*. 2016;19:696-704. doi:10.1016/j.chom.2016.04.013
 190. Kostyuchenko VA, Lim EXY, Zhang S, et al. Structure of the thermally stable Zika virus. *Nature*. 2016;533:425-428. doi:10.1038/nature17994
 191. Giraldo MI, Xia H, Aguilera-Aguirre L, et al. Envelope protein ubiquitination drives entry and pathogenesis of Zika virus. *Nature*. 2020;585:414-419. doi:10.1038/s41586-020-2457-8
 192. Shan C, Xia H, Haller SL, et al. A Zika virus envelope mutation preceding the 2015 epidemic enhances virulence and fitness for transmission. *Proc Natl Acad Sci U S A*. 2020;117(33):20190-20197. doi:10.1073/PNAS.2005722117
 193. Fontes-Garfias CR, Shan C, Luo H, et al. Functional Analysis of Glycosylation of Zika Virus Envelope Protein. *Cell Rep*. 2017;21:1180-1190. doi:10.1016/j.celrep.2017.10.016
 194. Xu X, Song H, Qi J, et al. Contribution of intertwined loop to membrane association revealed by Zika virus full-length NS1 structure. *EMBO J*. 2016;35(20):2170-2178. doi:10.15252/embj.201695290
 195. Song H, Qi J, Haywood J, Shi Y, Gao GF. Zika virus NS1 structure reveals diversity of electrostatic surfaces among flaviviruses. *Nat Struct Mol Biol*. 2016;23(5):456-458. doi:10.1038/nsmb.3213
 196. Ci Y, Liu ZY, Zhang NN, et al. Zika NS1-induced ER remodeling is essential for viral replication. *J Cell Biol*. 2020;219(2):1-13. doi:10.1083/jcb.201903062
 197. Akey DL, Brown WC, Dutta S, et al. Flavivirus NS1 structures reveal surfaces for associations with membranes and the immune system. *Science (80-)*. 2014;343(6173):881-885. doi:10.1126/science.1247749
 198. Brown WC, Akey DL, Konwerski JR, et al. Extended surface for membrane association in Zika virus NS1 structure. *Nat Struct Mol Biol*. 2016;23(9):865-867. doi:10.1038/nsmb.3268
 199. Puerta-Guardo H, Glasner DR, Espinosa DA, et al. Flavivirus NS1 Triggers Tissue-Specific Vascular Endothelial Dysfunction Reflecting Disease Tropism. *Cell Rep*. 2019;26:1598-1613. doi:10.1016/j.celrep.2019.01.036
 200. Liu J, Liu Y, Nie K, et al. Flavivirus NS1 protein in infected host sera enhances viral acquisition by mosquitoes. *Nat Microbiol*. 2016;1:1-11. doi:10.1038/nmicrobiol.2016.87
 201. Liu Y, Liu J, Du S, et al. Evolutionary enhancement of Zika virus infectivity in *Aedes aegypti* mosquitoes. *Nature*. 2017;545:482-486. doi:10.1038/nature22365
 202. Zhang X, Xie X, Zou J, et al. Genetic and biochemical characterizations of Zika virus NS2A protein. *Emerg Microbes Infect*. 2019;8:585-602. doi:10.1080/22221751.2019.1598291

6. Bibliography

203. Xie X, Gayen S, Kang C, Yuan Z, Shi P-Y. Membrane Topology and Function of Dengue Virus NS2A Protein. *J Virol.* 2013;87(8):4609-4622. doi:10.1128/jvi.02424-12
204. Márquez-Jurado S, Nogales A, Ávila-Pérez G, Iborra FJ, Martínez-Sobrido L, Almazán F. An Alanine-to-Valine substitution in the residue 175 of Zika virus NS2A protein affects viral RNA synthesis and attenuates the virus in vivo. *Viruses.* 2018;10(547):1-21. doi:10.3390/v10100547
205. Zhang X, Xie X, Xia H, et al. Zika virus NS2A-mediated virion assembly. *MBio.* 2019;10:e02375-19. doi:10.1128/mBio.02375-19
206. Ngan NTT, Kim S-J, Lee JY, Myoung J. Zika virus proteins NS2A and NS4A are major antagonists that reduce IFN- β promoter activity induced by the MDA5/RIG-I signaling pathway. *J Microbiol Biotechnol.* 2019;29(10):1665-1674. doi:10.4014/jmb.1909.09017
207. Xing H, Xu S, Jia F, et al. Zika NS2B is a crucial factor recruiting NS3 to the ER and activating its protease activity. *Virus Res.* 2020;275(197793):1-11. doi:10.1016/j.virusres.2019.197793
208. Li Y, Zhang Z, Phoo WW, et al. Structural Insights into the Inhibition of Zika Virus NS2B-NS3 Protease by a Small-Molecule Inhibitor. *Structure.* 2018;26:555-564. doi:10.1016/j.str.2018.02.005
209. Phoo WW, Li Y, Zhang Z, et al. Structure of the NS2B-NS3 protease from Zika virus after self-cleavage. *Nat Commun.* 2016;7(13410):1-8. doi:10.1038/ncomms13410
210. Lei J, Hansen G, Nitsche C, Klein CD, Zhang L, Hilgenfeld R. Crystal structure of Zika virus NS2B-NS3 protease in complex with a boronate inhibitor. *Science (80-).* 2016;353(6298). doi:10.1126/science.aag2419
211. Xu S, Ci Y, Wang L, et al. Zika virus NS3 is a canonical RNA helicase stimulated by NS5 RNA polymerase. *Nucleic Acids Res.* 2019;47(16):8693-8707. doi:10.1093/NAR/GKZ650
212. Chan JFW, Chik KKH, Yuan S, et al. Novel antiviral activity and mechanism of bromocriptine as a Zika virus NS2B-NS3 protease inhibitor. *Antiviral Res.* 2017;141:29-37. doi:10.1016/j.antiviral.2017.02.002
213. Zou J, Xie X, Wang Q-Y, et al. Characterization of Dengue Virus NS4A and NS4B Protein Interaction. *J Virol.* 2015;89(7):3455-3470. doi:10.1128/jvi.03453-14
214. Nemésio H, Palomares-Jerez F, Villalaín J. NS4A and NS4B proteins from dengue virus: Membranotropic regions. *Biochim Biophys Acta.* 2012;1818:2818-2830. doi:10.1016/j.bbamem.2012.06.022
215. Cortese M, Mulder K, Chatel-Chaix L, et al. Determinants in Nonstructural Protein 4A of Dengue Virus Required for RNA Replication and Replication Organelle Biogenesis. *J Virol.* 2021;95(21):e01310-21. doi:10.1128/jvi.01310-21
216. Hu Y, Dong X, He Z, et al. Zika virus antagonizes interferon response in patients and disrupts RIG-I-MAVS interaction through its CARD-TM domains. *Cell Biosci.* 2019;9(46):1-15. doi:10.1186/s13578-019-0308-9
217. Ma J, Ketkar H, Geng T, et al. Zika virus non-structural protein 4A blocks the RLR-MAVS signaling. *Front Microbiol.* 2018;9(1350):1-10. doi:10.3389/fmicb.2018.01350
218. Xia H, Luo H, Shan C, et al. An evolutionary NS1 mutation enhances Zika virus evasion of host interferon induction. *Nat Commun.* 2018;9(414):1-13. doi:10.1038/s41467-017-02816-2
219. Wu Y, Liu Q, Zhou J, et al. Zika virus evades interferon-mediated antiviral response through the co-operation of multiple nonstructural proteins in vitro. *Cell Discov.* 2017;3(17006):1-14. doi:10.1038/celldisc.2017.6
220. Wang B, Tan XF, Thurmond S, et al. The structure of Zika virus NS5 reveals a conserved domain conformation. *Nat Commun.* 2017;8(14763):1-6. doi:10.1038/ncomms14763
221. Zhao B, Yi G, Du F, et al. Structure and function of the Zika virus full-length NS5 protein. *Nat Commun.* 2017;8(14762):1-9. doi:10.1038/ncomms14762
222. Butcher SJ, Grimes JM, Makeyev E V, Bamford DH, Stuart DI. A mechanism for initiating RNA-dependent RNA polymerization. *Nature.* 2001;410:235-240.
223. Bügl H, Fauman EB, Staker BL, et al. RNA Methylation under Heat Shock Control. *Mol Cell.* 2000;6:349-360.
224. Grant A, Ponia SS, Tripathi S, et al. Zika Virus Targets Human STAT2 to Inhibit Type I

6. Bibliography

- Interferon Signaling. *Cell Host Microbe*. 2016;19:882-890. doi:10.1016/j.chom.2016.05.009
225. Kumar A, Hou S, Airo AM, et al. Zika virus inhibits type-I interferon production and downstream signaling. *EMBO Rep*. 2016;17(12):1766-1775. doi:10.15252/embr.201642627
226. De Maio FA, Risso G, Iglesias NG, et al. The Dengue Virus NS5 Protein Intrudes in the Cellular Spliceosome and Modulates Splicing. *PLoS Pathog*. 2016;12(8):e1005841. doi:10.1371/journal.ppat.1005841
227. Jorge FA, Thomazella M V., Moreira D de C, Lopes LDG, Teixeira JJ V., Bertolini DA. Evolutions and upcoming on Zika virus diagnosis through an outbreak: A systematic review. *Rev Med Virol*. 2020;30(e2105):1-13. doi:10.1002/rmv.2105
228. Akoua-Koffi C, Diarrassouba S, Bénéié VB, et al. [Investigation surrounding a fatal case of yellow fever in Côte d'Ivoire in 1999]. *Bull Soc Pathol Exot*. 2001;94(3):227-230.
229. Diallo D, Sall AA, Diagne CT, et al. Zika virus emergence in mosquitoes in Southeastern Senegal, 2011. *PLoS One*. 2014;9(10):e109442. doi:10.1371/journal.pone.0109442
230. Boorman JPT, Porterfield JS. A simple technique for infection of mosquitoes with viruses transmission of Zika virus. *Trans R Soc Trop Med Hyg*. 1956;50(3):238-242. doi:10.1016/0035-9203(56)90029-3
231. Cornet M, Robin Y, Adam C, Valade M, Calvo MA. Comparison between experimental transmission of yellow fever and Zika viruses in *Aedes aegypti*. *Cah ORSTOM, Ser Entomol Medicale Parasitol*. 1979;27(1):47-53.
232. Li MZI, Wong PSJ, Ng LC, Tan CH. Oral Susceptibility of Singapore *Aedes* (*Stegomyia*) *aegypti* (Linnaeus) to Zika Virus. *PLoS Negl Trop Dis*. 2012;6(8):e1792. doi:10.1371/journal.pntd.0001792
233. Foy BD, Kobylinski KC, Foy JLC, et al. Probable Non-Vector-borne Transmission of Zika Virus, Colorado, USA. *Emerg Infect Dis*. 2011;17(5):880-882. doi:10.3201/eid1705.101939
234. D'Ortenzio E, Matheron S, Yazdanpanah Y, et al. Evidence of Sexual Transmission of Zika Virus. *N Engl J Med*. 2016;374(22):2195-2198. doi:10.1056/nejmc1603617
235. Besnard M, Lastère S, Teissier A, Cao-Lormeau VM, Musso D. Evidence of perinatal transmission of Zika virus, French Polynesia, December 2013 and February 2014. *Eurosurveillance*. 2014;19(13):20751. doi:10.2807/1560-7917.ES2014.19.13.20751
236. Calvet G, Aguiar RS, Melo ASO, et al. Detection and sequencing of Zika virus from amniotic fluid of fetuses with microcephaly in Brazil: a case study. *Lancet Infect Dis*. 2016;16:653-660. doi:10.1016/S1473-3099(16)00095-5
237. Musso D, Nhan T, Robin E, et al. Potential for Zika virus transmission through blood transfusion demonstrated during an outbreak in French Polynesia, November 2013 to February 2014. *Eurosurveillance*. 2014;19(14):20761. doi:10.2807/1560-7917.ES2014.19.14.20761
238. Barjas-Castro ML, Angerami RN, Cunha MS, et al. Probable transfusion-transmitted Zika virus in Brazil. *Transfusion*. 2016;56(7):1684-1688. doi:10.1111/trf.13681
239. Prisant N, Bujan L, Benichou H, et al. Zika virus in the female genital tract. *Lancet Infect Dis*. 2016;16:1000-1001. doi:10.1016/S1473-3099(16)30193-1
240. Nicastri E, Castilletti C, Liuzzi G, Iannetta M, Capobianchi MR, Ippolito G. Persistent detection of Zika virus RNA in semen for six months after symptom onset in a traveller returning from Haiti to Italy, February 2016. *Eurosurveillance*. 2016;21(32):30314. doi:10.2807/1560-7917.ES.2016.21.32.30314
241. Barzon L, Pacenti M, Franchin E, et al. Infection dynamics in a traveller with persistent shedding of Zika virus RNA in semen for six months after returning from Haiti to Italy, January 2016. *Eurosurveillance*. 2016;21(32):30316. doi:10.2807/1560-7917.ES.2016.21.32.30316
242. Barzon L, Trevisan M, Sinigaglia A, Lavezzo E, Palù G. Zika virus: From pathogenesis to disease control. *FEMS Microbiol Lett*. 2016;363(18):1-17. doi:10.1093/femsle/fnw202
243. van der Eijk AA, van Genderen PJ, Verdijk RM, et al. Miscarriage Associated with Zika Virus Infection. *N Engl J Med*. 2016;375(10):1-3. doi:10.1056/nejmc1608225
244. Cordeiro MT, Pena LJ, Brito CA, Gil LH, Marques ET. Positive IgM for Zika virus in the cerebrospinal fluid of 30 neonates with microcephaly in Brazil. *Lancet*. 2016;387:1811-

6. Bibliography

1812. doi:10.1016/S0140-6736(16)30253-7
245. de Araújo TVB, Rodrigues LC, de Alencar Ximenes RA, et al. Association between Zika virus infection and microcephaly in Brazil, January to May, 2016: preliminary report of a case-control study. *Lancet Infect Dis.* 2016;16:1356-1363. doi:10.1016/S1473-3099(16)30318-8
246. Guedes DRD, Paiva MHS, Donato MMA, et al. Zika virus replication in the mosquito *Culex quinquefasciatus* in Brazil. *Emerg Microbes Infect.* 2017;6:e69. doi:10.1038/emi.2017.59
247. Monteiro VVS, Navegantes-Lima KC, De Lemos AB, et al. *Aedes-chikungunya* virus interaction: Key role of vector midguts microbiota and its saliva in the host infection. *Front Microbiol.* 2019;10(492):1-13. doi:10.3389/fmicb.2019.00492
248. Thaker SK, Chapa T, Garcia G, et al. Differential Metabolic Reprogramming by Zika Virus Promotes Cell Death in Human versus Mosquito Cells. *Cell Metab.* 2019;29:1206-1216. doi:10.1016/j.cmet.2019.01.024
249. Franz AWE, Kantor AM, Passarelli AL, Clem RJ. Tissue barriers to arbovirus infection in mosquitoes. *Viruses.* 2015;7:3741-3767. doi:10.3390/v7072795
250. Castillo-Macías A, Salinas-Carmona MC, Torres-López E. Immunology of viral infections with a high impact in Mexico: Dengue, Chikungunya, and Zika. *Med Univ.* 2018;19(77):198-207. doi:10.1016/j.rmu.2017.09.001
251. Wu P, Yu X, Wang P, Cheng G. Arbovirus lifecycle in mosquito : acquisition , propagation and transmission. *Expert Rev Mol Med.* 2019;21(e1):1-6. doi:10.1017/erm.2018.6
252. Daep CA, Muñoz-Jordán JL, Eugenin EA. Flaviviruses, an expanding threat in public health: focus on dengue, West Nile, and Japanese encephalitis virus. *J Neurovirol.* 2014;20:539-560. doi:10.1007/s13365-014-0285-z
253. Öhlund P, Lundén H, Blomström AL. Insect-specific virus evolution and potential effects on vector competence. *Virus Genes.* 2019;55:127-137. doi:10.1007/s11262-018-01629-9
254. Hamel R, Dejarnac O, Wichit S, et al. Biology of Zika Virus Infection in Human Skin Cells. *J Virol.* 2015;89(17):8880-8896. doi:10.1128/jvi.00354-15
255. Routhu NK, Byrareddy SN. Host-Virus Interaction of ZIKA Virus in Modulating Disease Pathogenesis. *J Neuroimmune Pharmacol.* 2017;12:219-232. doi:10.1007/s11481-017-9736-7
256. Khaiboullina SF, Ribeiro FM, Uppal T, Martynova E V., Rizvanov AA, Verma SC. Zika virus transmission through blood tissue barriers. *Front Microbiol.* 2019;10(1465):1-13. doi:10.3389/fmicb.2019.01465
257. Kim JA, Seong RK, Son SW, Shin OS. Insights into ZIKV-Mediated Innate Immune Responses in Human Dermal Fibroblasts and Epidermal Keratinocytes. *J Invest Dermatol.* 2019;139:391-399. doi:10.1016/j.jid.2018.07.038
258. Sun X, Hua S, Chen HR, et al. Transcriptional Changes during Naturally Acquired Zika Virus Infection Render Dendritic Cells Highly Conducive to Viral Replication. *Cell Rep.* 2017;21:3471-3482. doi:10.1016/j.celrep.2017.11.087
259. Foo S-S, Chen W, Chan Y, et al. Asian Zika virus strains target CD14+ blood monocytes and induce M2-skewed immunosuppression during pregnancy. *Nat Microbiol.* 2017;2:1558-1570. doi:10.1038/s41564-017-0016-3
260. Michlmayr D, Andrade P, Gonzalez K, Balmaseda A, Harris E. CD14+ CD16+ monocytes are the main target of Zika virus infection in peripheral blood mononuclear cells in a paediatric study in Nicaragua. *Nat Microbiol.* 2017;2:1462-1470. doi:10.1038/s41564-017-0035-0
261. Nowakowski TJ, Pollen AA, Di Lullo E, Sandoval-Espinosa C, Bershteyn M, Kriegstein AR. Expression analysis highlights AXL as a candidate zika virus entry receptor in neural stem cells. *Cell Stem Cell.* 2016;18:591-596. doi:10.1016/j.stem.2016.03.012
262. Wells MF, Salick MR, Wiskow O, et al. Genetic Ablation of AXL Does Not Protect Human Neural Progenitor Cells and Cerebral Organoids from Zika Virus Infection. *Cell Stem Cell.* 2016;19:703-708. doi:10.1016/j.stem.2016.11.011
263. Meertens L, Labeau A, Dejarnac O, et al. Axl mediates ZIKA virus entry in human glial cells and modulates innate immune responses. *Cell Rep.* 2017;18:324-333.

6. Bibliography

- doi:10.1016/j.celrep.2016.12.045
264. Stefanik M, Formanova P, Bily T, et al. Characterisation of Zika virus infection in primary human astrocytes. *BMC Neurosci.* 2018;19(5):1-8. doi:10.1186/s12868-018-0407-2
265. Rosenberg AZ, Yu W, Hill DA, Reyes CA, Schwartz DA. Placental pathology of Zika virus: Viral infection of the placenta induces villous stromal macrophage (Hofbauer Cell) proliferation and hyperplasia. *Arch Pathol Lab Med.* 2017;141:43-48. doi:10.5858/arpa.2016-0401-OA
266. Schwartz DA. Viral infection, proliferation, and hyperplasia of Hofbauer cells and absence of inflammation characterize the placental pathology of fetuses with congenital Zika virus infection. *Arch Gynecol Obstet.* 2017;295:1361-1368. doi:10.1007/s00404-017-4361-5
267. Simoni MK, Jurado KA, Abrahams VM, Fikrig E, Guller S. Zika virus infection of Hofbauer cells. *Am J Reprod Immunol.* 2017;77:e12613. doi:10.1111/aji.12613
268. Tabata T, Pettitt M, Puerta-Guardo H, et al. Zika Virus Targets Different Primary Human Placental Cells, Suggesting Two Routes for Vertical Transmission. *Cell Host Microbe.* 2016;20:155-166. doi:10.1016/j.chom.2016.07.002
269. Bayer A, Lennemann NJ, Ouyang Y, et al. Type III Interferons Produced by Human Placental Trophoblasts Confer Protection against Zika Virus Infection. *Cell Host Microbe.* 2016;19:705-712. doi:10.1016/j.chom.2016.03.008
270. Tabata T, Pettitt M, Puerta-Guardo H, Michlmayr D, Harris E, Pereira L. Zika Virus Replicates in Proliferating Cells in Explants from First-Trimester Human Placentas, Potential Sites for Dissemination of Infection. *J Infect Dis.* 2018;217(8):1202-1213. doi:10.1093/infdis/jix552
271. Cheng F, Silva SR da, Huang I-C, Jung JU, Gao S-J. Suppression of Zika Virus Infection and Replication in Endothelial Cells and Astrocytes by PKA Inhibitor PKI 14-22. *J Virol.* 2018;92:e02019-17.
272. Bagasra O, Addanki KC, Goodwin GR, Hughes BW, Pandey P, McLean E. Cellular Targets and Receptor of Sexual Transmission of Zika Virus. *Appl Immunohistochem Mol Morphol.* 2017;25(10):679-686. doi:10.1097/PAL.0000000000000580
273. Salam AP, Horby P. Isolation of viable Zika virus from spermatozoa. *Lancet Infect Dis.* 2018;18:144. doi:10.1016/S1473-3099(18)30020-3
274. Kumar A, Jovel J, Lopez-Orozco J, et al. Human sertoli cells support high levels of zika virus replication and persistence. *Sci Rep.* 2018;8(5477):1-11. doi:10.1038/s41598-018-23899-x
275. Siemann D, Strange D, Maharaj P, Shi PY, Verma S. Zika Virus Infects Human Sertoli Cells and modulates the integrity of the in vitro blood-testis barrier model. *J Virol.* 2017;91:e00623-17.
276. Roach T, Alcendor DJ. Zika virus infection of cellular components of the blood-retinal barriers: Implications for viral associated congenital ocular disease. *J Neuroinflammation.* 2017;14(43):1-12. doi:10.1186/s12974-017-0824-7
277. Lee I, Bos S, Li G, et al. Probing molecular insights into Zika virus – host interactions. *Viruses.* 2018;10(233):1-26. doi:10.3390/v10050233
278. Pujhari S, Brustolin M, Macias VM, et al. Heat shock protein 70 (Hsp70) mediates Zika virus entry, replication, and egress from host cells. *Emerg Microbes Infect.* 2019;8(1):8-16. doi:10.1080/22221751.2018.1557988
279. Tan CW, Huan Hor CH, Kwek S Sen, et al. Cell surface α 2,3-linked sialic acid facilitates Zika virus internalization. *Emerg Microbes Infect.* 2019;8(1):426-437. doi:10.1080/22221751.2019.1590130
280. Khongwichit S, Sornjai W, Jitobaom K, et al. A functional interaction between GRP78 and Zika virus E protein. *Sci Rep.* 2021;11(393):1-18. doi:10.1038/s41598-020-79803-z
281. Vazquez C, Jurado KA. Playing Favorites: Integrin α v β 5 Mediates Preferential Zika Infection of Neural Stem Cells. *Cell Stem Cell.* 2020;26:133-135. doi:10.1016/j.stem.2020.01.007
282. Srivastava M, Zhang Y, Chen J, et al. Chemical proteomics tracks virus entry and uncovers NCAM1 as Zika virus receptor. *Nat Commun.* 2020;11(3896):1-10. doi:10.1038/s41467-020-17638-y

6. Bibliography

283. Persaud M, Martinez-Lopez A, Buffone C, Porcelli SA, Diaz-Griffero F. Infection by Zika viruses requires the transmembrane protein AXL, endocytosis and low pH. *Virology*. 2018;518:301-312. doi:10.1016/j.virol.2018.03.009
284. Owczarek K, Chykunova Y, Jassoy C, Maksym B, Rajfur Z, Pyrc K. Zika virus: Mapping and reprogramming the entry. *Cell Commun Signal*. 2019;17(41):1-19. doi:10.1186/s12964-019-0349-z
285. Li M, Zhang D, Li C, et al. Characterization of Zika Virus Endocytic Pathways in Human Glioblastoma Cells. *Front Microbiol*. 2020;11(242):1-19. doi:10.3389/fmicb.2020.00242
286. Harrison SC. Viral membrane fusion. *Nat Struct Mol Biol*. 2008;15(7):690-698. doi:10.1038/nsmb.1456
287. Kaufmann B, Rossmann MG. Molecular mechanisms involved in the early steps of flavivirus cell entry. *Microbes Infect*. 2011;13:1-9. doi:10.1016/j.micinf.2010.09.005
288. Smit JM, Moesker B, Rodenhuis-Zybert I, Wilschut J. Flavivirus cell entry and membrane fusion. *Viruses*. 2011;3:160-171. doi:10.3390/v3020160
289. Stiasny K, Fritz R, Pangerl K, Heinz FX. Molecular mechanisms of flavivirus membrane fusion. *Amino Acids*. 2011;41:1159-1163. doi:10.1007/s00726-009-0370-4
290. Saiz JC, Vázquez-Calvo Á, Blázquez AB, Merino-Ramos T, Escribano-Romero E, Martín-Acebes MA. Zika virus: The latest newcomer. *Front Microbiol*. 2016;7(496):1-19. doi:10.3389/fmicb.2016.00496
291. Barrows NJ, Campos RK, Liao KC, et al. Biochemistry and Molecular Biology of Flaviviruses. *Chem Rev*. 2018;118(8):4448-4482. doi:10.1021/acs.chemrev.7b00719
292. Jackson RJ, Hellen CUT, Pestova T V. The mechanism of eukaryotic translation initiation and principles of its regulation. *Nat Rev Mol Cell Biol*. 2010;10:113-127. doi:10.1038/nrm2838
293. Kozak M. Structural features in eukaryotic mRNAs that modulate the initiation of translation. *J Biol Chem*. 1991;266(30):19867-19870. doi:10.1016/s0021-9258(18)54860-2
294. Pestova T V., Kolupaeva VG. The roles of individual eukaryotic translation initiation factors in ribosomal scanning and initiation codon selection. *Genes Dev*. 2002;16:2906-2922. doi:10.1101/gad.1020902
295. Wichit S, Gumpangseth N, Hamel R, et al. Chikungunya and Zika viruses: Co-circulation and the interplay between viral proteins and host factors. *Pathogens*. 2021;10(448):1-27. doi:10.3390/pathogens10040448
296. Sanford TJ, Mears H V., Fajardo T, Locker N, Sweeney TR. Circularization of flavivirus genomic RNA inhibits de novo translation initiation. *Nucleic Acids Res*. 2019;47(18):9789-9802. doi:10.1093/nar/gkz686
297. Lichinchi G, Zhao BS, Wu Y, et al. Dynamics of Human and Viral RNA Methylation during ZIKA Virus Infection. *Cell Host Microbe*. 2016;20(5):666-673. doi:10.1016/j.chom.2016.10.002.Dynamics
298. Welsch S, Miller S, Romero-Brey I, et al. Composition and three-dimensional architecture of the Dengue virus replication and assembly sites. *Cell Host Microbe*. 2009;5:365-375. doi:10.1016/j.chom.2009.03.007
299. Gillespie LK, Hoenen A, Morgan G, Mackenzie JM. The endoplasmic reticulum provides the membrane platform for biogenesis of the flavivirus replication complex. *J Virol*. 2010;84(20):10438-10447. doi:10.1128/JVI.00986-10
300. Romero-Brey I, Bartenschlager R. Membranous replication factories induced by plus-strand RNA viruses. *Viruses*. 2014;6:2826-2857. doi:10.3390/v6072826
301. Cortese M, Goellner S, Acosta EG, et al. Ultrastructural characterization of Zika virus replication factories. *Cell Rep*. 2017;18:2113-2123.
302. Överby AK, Popov VL, Niedrig M, Weber F. Tick-Borne Encephalitis Virus Delays Interferon Induction and Hides Its Double-Stranded RNA in Intracellular Membrane Vesicles. *J Virol*. 2010;84(17):8470-8483. doi:10.1128/jvi.00176-10
303. Miorin L, Alborno A, Baba MM, D'Agaro P, Marcello A. Formation of membrane-defined compartments by tick-borne encephalitis virus contributes to the early delay in interferon signaling. *Virus Res*. 2012;163:660-666. doi:10.1016/j.virusres.2011.11.020
304. Uchida L, Espada-Murao LA, Takamatsu Y, et al. The dengue virus conceals double-

6. Bibliography

- stranded RNA in the intracellular membrane to escape from an interferon response. *Sci Rep.* 2014;4(7395):1-10. doi:10.1038/srep07395
305. Mackenzie JM, Jones MK, Young PR. Immunolocalization of the dengue virus nonstructural glycoprotein NS1 suggests a role in viral RNA replication. *Virology.* 1996;220(0307):232-240. doi:10.1006/viro.1996.0307
306. Youn S, Ambrose RL, Mackenzie JM, Diamond MS. Non-structural protein-1 is required for West Nile virus replication complex formation and viral RNA synthesis. *Viral J.* 2013;10(339):1-14. doi:10.1186/1743-422X-10-339
307. Płaszczycza A, Scaturro P, Neufeldt CJ, et al. A novel interaction between dengue virus nonstructural protein 1 and the NS4A-2K-4B precursor is required for viral RNA replication but not for formation of the membranous replication organelle. *PLOS Pathog.* 2019;15(5):e1007736.
308. Zhang L, Mohan PM, Padmanabhan R. Processing and localization of Dengue virus type 2 polyprotein precursor NS3-NS4A-NS4B-NS5. *J Virol.* 1992;66(12):7549-7554. doi:10.1128/jvi.66.12.7549-7554.1992
309. Mackenzie JM, Khromykh AA, Jones MK, Westaway EG. Subcellular localization and some biochemical properties of the flavivirus Kunjin nonstructural proteins NS2A and NS4A. *Virology.* 1998;245(VY989156):203-215. doi:10.1006/viro.1998.9156
310. Miller S, Kastner S, Krijnse-Locker J, Bühler S, Bartenschlager R. The non-structural protein 4A of dengue virus is an integral membrane protein inducing membrane alterations in a 2K-regulated manner. *J Biol Chem.* 2007;282(12):8873-8882. doi:10.1074/jbc.M609919200
311. Hung YF, Schwarten M, Schünke S, et al. Dengue virus NS4A cytoplasmic domain binding to liposomes is sensitive to membrane curvature. *Biochim Biophys Acta.* 2015;1848:1119-1126. doi:10.1016/j.bbame.2015.01.015
312. Hung YF, Schwarten M, Hoffmann S, Willbold D, Sklan EH, Koenig BW. Amino terminal region of dengue virus NS4A cytosolic domain binds to highly curved liposomes. *Viruses.* 2015;7:4119-4130. doi:10.3390/v7072812
313. Lee CM, Xie X, Zou J, et al. Determinants of Dengue Virus NS4A Protein Oligomerization. *J Virol.* 2015;89:6171-6183. doi:10.1128/jvi.00546-15
314. Mikulasova A, Gillespie LK, Ambrose RL, et al. A Putative Lipid-Associating Motif in the West Nile Virus NS4A Protein Is Required for Efficient Virus Replication. *Front Cell Dev Biol.* 2021;9(655606):1-13. doi:10.3389/fcell.2021.655606
315. Miller S, Sparacio S, Bartenschlager R. Subcellular localization and membrane topology of the dengue virus type 2 non-structural protein 4B. *J Biol Chem.* 2006;281(13):8854-8863. doi:10.1074/jbc.M512697200
316. Paul D, Romero-Brey I, Gouttenoire J, et al. NS4B Self-Interaction through Conserved C-Terminal Elements Is Required for the Establishment of Functional Hepatitis C Virus Replication Complexes. *J Virol.* 2011;85(14):6963-6976. doi:10.1128/jvi.00502-11
317. Zou J, Xie X, Lee LT, et al. Dimerization of Flavivirus NS4B Protein. *J Virol.* 2014;88(6):3379-3391. doi:10.1128/jvi.02782-13
318. Roosendaal J, Westaway EG, Khromykh A, Mackenzie JM. Regulated cleavages at the West Nile virus NS4A-2K-NS4B Junctions play a major role in rearranging cytoplasmic membranes and Golgi trafficking of the NS4A protein. *J Virol.* 2006;80(9):4623-4632. doi:10.1128/JVI.80.9.4623-4632.2006
319. Aktepe TE, Liebscher S, Prier JE, Simmons CP, Mackenzie JM. The Host Protein Reticulon 3.1A Is Utilized by Flaviviruses to Facilitate Membrane Remodelling. *Cell Rep.* 2017;21:1639-1654. doi:10.1016/j.celrep.2017.10.055
320. Neufeldt CJ, Cortese M, Scaturro P, et al. ER-shaping atlastin proteins act as central hubs to promote flavivirus replication and virion assembly. *Nat Microbiol.* 2019;4(12):2416-2429. doi:10.1038/s41564-019-0586-3
321. Evans AS, Lennemann NJ, Coyne CB. BPIFB3 Regulates Endoplasmic Reticulum Morphology To Facilitate Flavivirus Replication. *J Virol.* 2020;94:e00029-20.
322. Leier HC, Weinstein JB, Kyle JE, et al. A global lipid map defines a network essential for Zika virus replication. *Nat Commun.* 2020;11(3652):1-15. doi:10.1038/s41467-020-17433-9

6. Bibliography

323. Melo CFOR, De Oliveira DN, De Oliveira Lima E, et al. A lipidomics approach in the characterization of zika-infected mosquito cells: Potential targets for breaking the transmission cycle. *PLoS One*. 2016;11(10):e0164377. doi:10.1371/journal.pone.0164377
324. Mackenzie JM, Westaway EG. Assembly and Maturation of the Flavivirus Kunjin Virus Appear To Occur in the Rough Endoplasmic Reticulum and along the Secretory Pathway, Respectively. *J Virol*. 2001;75(22):10787-10799. doi:10.1128/jvi.75.22.10787-10799.2001
325. Sirohi D, Kuhn RJ. Zika Virus Structure, Maturation, and Receptors. *J Infect Dis*. 2017;216(S10):S935-S944. doi:10.1093/infdis/jix515
326. DiNunno NM, Goetschius DJ, Narayanan A, et al. Identification of a pocket factor that is critical to Zika virus assembly. *Nat Commun*. 2020;11(4953):1-8. doi:10.1038/s41467-020-18747-4
327. Renner M, Dejnirattisai W, Carrique L, et al. Flavivirus maturation leads to the formation of an occupied lipid pocket in the surface glycoproteins. *Nat Commun*. 2021;12(1238):1-9. doi:10.1038/s41467-021-21505-9
328. Stiasny K, Medits I, Roßbacher L, Heinz FX. Impact of structural dynamics on biological functions of flaviviruses. *FEBS J*. 2022;1-13. doi:10.1111/febs.16419
329. Perera R, Riley C, Isaac G, et al. Dengue virus infection perturbs lipid homeostasis in infected mosquito cells. *PLoS Pathog*. 2012;8(3):e1002584. doi:10.1371/journal.ppat.1002584
330. Martín-Acebes MA, Merino-Ramos T, Blázquez A-B, et al. The Composition of West Nile Virus Lipid Envelope Unveils a Role of Sphingolipid Metabolism in Flavivirus Biogenesis. *J Virol*. 2014;88(20):12041-12054. doi:10.1128/jvi.02061-14
331. Mercer J, Schelhaas M, Helenius A. Virus entry by endocytosis. *Annu Rev Biochem*. 2010;79:803-833. doi:10.1146/annurev-biochem-060208-104626
332. Marsh M, Helenius A. Virus entry: Open sesame. *Cell*. 2006;124(4):729-740. doi:10.1016/j.cell.2006.02.007
333. Mackenzie JM, Khromykh AA, Parton RG. Cholesterol Manipulation by West Nile Virus Perturbs the Cellular Immune Response. *Cell Host Microbe*. 2007;2:229-239. doi:10.1016/j.chom.2007.09.003
334. Zhang Z, He G, Filipowicz NA, et al. Host lipids in positive-strand RNA virus genome replication. *Front Microbiol*. 2019;10(FEB):1-18. doi:10.3389/fmicb.2019.00286
335. Soto-Acosta R, Mosso C, Cervantes-Salazar M, et al. The increase in cholesterol levels at early stages after dengue virus infection correlates with an augment in LDL particle uptake and HMG-CoA reductase activity. *Virology*. 2013;442:132-147. doi:10.1016/j.virol.2013.04.003
336. Rothwell C, LeBreton A, Young Ng C, et al. Cholesterol biosynthesis modulation regulates dengue viral replication. *Virology*. 2009;389:8-19. doi:10.1016/j.virol.2009.03.025
337. Martínez-Gutiérrez M, Castellanos JE, Gallego-Gómez JC. Statins reduce dengue virus production via decreased virion assembly. *Intervirology*. 2011;54:202-216. doi:10.1159/000321892
338. España E, Nam JH, Song EJ, Song D, Lee CK, Kim JK. Lipophilic statins inhibit Zika virus production in Vero cells. *Sci Rep*. 2019;9(11461):1-11. doi:10.1038/s41598-019-47956-1
339. Aktepe TE, Pham H, Mackenzie JM. Differential utilisation of ceramide during replication of the flaviviruses West Nile and dengue virus. *Virology*. 2015;484:241-250. doi:10.1016/j.virol.2015.06.015
340. Agnello V, Ábel G, Elfahal M, Knight GB, Zhang QX. Hepatitis C virus and other flaviviridae viruses enter cells via low density lipoprotein receptor. *Proc Natl Acad Sci U S A*. 1999;96(22):12766-12771. doi:10.1073/pnas.96.22.12766
341. Tsai B, Gilbert JM, Stehle T, Lencer W, Benjamin TL, Rapoport TA. Gangliosides are receptors for murine polyoma virus and SV40. *EMBO J*. 2003;22(17):4346-4355. doi:10.1093/emboj/cdg439
342. Roth SL, Whittaker GR. Promotion of vesicular stomatitis virus fusion by the endosome-specific phospholipid bis(monoacylglycero)phosphate (BMP). *FEBS Lett*. 2011;585:865-869.

6. Bibliography

- doi:10.1016/j.febslet.2011.02.015
343. Ewers H, Römer W, Smith AE, et al. GM1 structure determines SV40-induced membrane invagination and infection. *Nat Cell Biol.* 2010;12(1):11-18. doi:10.1038/ncb1999
344. Diwaker D, Mishra KP, Ganju L, Singh SB. Protein disulfide isomerase mediates dengue virus entry in association with lipid rafts. *Viral Immunol.* 2015;28(3). doi:10.1089/vim.2014.0095
345. Medigeschi GR, Hirsch AJ, Streblov DN, Nikolich-Zugich J, Nelson JA. West Nile Virus Entry Requires Cholesterol-Rich Membrane Microdomains and Is Independent of avb3 Integrin. *J Virol.* 2008;82(11):5212-5219. doi:10.1128/jvi.00008-08
346. Zhu YZ, Cao MM, Wang WB, et al. Association of heat-shock protein 70 with lipid rafts is required for Japanese encephalitis virus infection in Huh7 cells. *J Gen Virol.* 2012;93:61-71. doi:10.1099/vir.0.034637-0
347. Puerta-Guardo H, Mosso C, Medina F, Liprandi F, Ludert JE, del Angel RM. Antibody-dependent enhancement of dengue virus infection in U937 cells requires cholesterol-rich membrane microdomains. *J Gen Virol.* 2010;91:394-403. doi:10.1099/vir.0.015420-0
348. Carro AC, Damonte EB. Requirement of cholesterol in the viral envelope for dengue virus infection. *Virus Res.* 2013;174:78-87. doi:10.1016/j.virusres.2013.03.005
349. Moesker B, Rodenhuis-Zybert IA, Meijerhof T, Wilschut J, Smit JM. Characterization of the functional requirements of West Nile virus membrane fusion. *J Gen Virol.* 2010;91:389-393. doi:10.1099/vir.0.015255-0
350. Stiasny K, Koessl C, Heinz FX. Involvement of Lipids in Different Steps of the Flavivirus Fusion Mechanism. *J Virol.* 2003;77(14):7856-7862. doi:10.1128/jvi.77.14.7856-7862.2003
351. Lee C-J, Lin H-R, Liao C-L, Lin Y-L. Cholesterol Effectively Blocks Entry of Flavivirus. *J Virol.* 2008;82(13):6470-6480. doi:10.1128/jvi.00117-08
352. Brass AL, Huang IC, Benita Y, et al. The IFITM Proteins Mediate Cellular Resistance to Influenza A H1N1 Virus, West Nile Virus, and Dengue Virus. *Cell.* 2009;139:1243-1254. doi:10.1016/j.cell.2009.12.017
353. Savidis G, Perreira JM, Portmann JM, et al. The IFITMs Inhibit Zika Virus Replication. *Cell Rep.* 2016;15:2323-2330. doi:10.1016/j.celrep.2016.05.074
354. Das T, Yang X, Lee H, et al. S-Palmitoylation and Sterol Interactions Mediate Antiviral Specificity of IFITMs. *ACS Chem Biol.* 2022;17(8):2109-2120. doi:10.1021/acscchembio.2c00176
355. Li C, Deng YQ, Wang S, et al. 25-Hydroxycholesterol Protects Host against Zika Virus Infection and Its Associated Microcephaly in a Mouse Model. *Immunity.* 2017;46:446-456. doi:10.1016/j.immuni.2017.02.012
356. Zaitseva E, Yang ST, Melikov K, Pourmal S, Chernomordik L V. Dengue virus ensures its fusion in late endosomes using compartment-specific lipids. *PLoS Pathog.* 2010;6(10):e1001131. doi:10.1371/journal.ppat.1001131
357. Carocci M, Hinshaw SM, Rodgers MA, et al. The bioactive lipid 4-hydroxyphenyl retinamide inhibits flavivirus replication. *Antimicrob Agents Chemother.* 2015;59(1):85-95. doi:10.1128/AAC.04177-14
358. Heaton NS, Perera R, Berger KL, et al. Dengue virus nonstructural protein 3 redistributes fatty acid synthase to sites of viral replication and increases cellular fatty acid synthesis. *Proc Natl Acad Sci U S A.* 2010;107(40):17345-17350. doi:10.1073/pnas.1010811107
359. Martín-Acebes MA, Vázquez-Calvo Á, Saiz JC. Lipids and flaviviruses, present and future perspectives for the control of dengue, Zika, and West Nile viruses. *Prog Lipid Res.* 2016;64:123-137. doi:10.1016/j.plipres.2016.09.005
360. Villareal VA, Rodgers MA, Costello DA, Yang PL. Targeting host lipid synthesis and metabolism to inhibit dengue and hepatitis C viruses. *Antiviral Res.* 2015;124:110-121. doi:10.1016/j.antiviral.2015.10.013
361. Reddy T, Sansom MSP. The Role of the Membrane in the Structure and Biophysical Robustness of the Dengue Virion Envelope. *Structure.* 2016;24:375-382. doi:10.1016/j.str.2015.12.011
362. Goñi FM, Contreras FX, Montes LR, Sot J, Alonso A. Biophysics (and sociology) of

6. Bibliography

- ceramides. *Biochem Soc Symp.* 2005;72:177-188. doi:10.1042/bss0720177
363. Holopainen JM, Angelova MI, Kinnunen PKJ. Vectorial budding of vesicles by asymmetrical enzymatic formation of ceramide in giant liposomes. *Biophys J.* 2000;78:830-838. doi:10.1016/S0006-3495(00)76640-9
364. Zha X, Pierini LM, Leopold PL, Skiba PJ, Tabas I, Maxfield FR. Sphingomyelinase treatment induces ATP-independent endocytosis. *J Cell Biol.* 1998;140(1):39-47. doi:10.1083/jcb.140.1.39
365. Meertens L, Carnec X, Lecoin MP, et al. The TIM and TAM families of phosphatidylserine receptors mediate dengue virus entry. *Cell Host Microbe.* 2012;12:544-557. doi:10.1016/j.chom.2012.08.009
366. Richard AS, Zhang A, Park SJ, Farzan M, Zong M, Choe H. Virion-associated phosphatidylethanolamine promotes TIM1-mediated infection by Ebola, dengue, and West Nile viruses. *Proc Natl Acad Sci U S A.* 2015;112(47):14682-14687. doi:10.1073/pnas.1508095112
367. Untergasser A, Cutcutache I, Koressaar T, et al. Primer3-new capabilities and interfaces. *Nucleic Acids Res.* 2012;40(15):e115. doi:10.1093/nar/gks596
368. Graham FL, Smiley J, Russell WC, Nairn R. Characteristics of a human cell line transformed by DNA from human adenovirus type 5. *J Gen Virol.* 1977;36:59-72. doi:10.1099/0022-1317-36-1-59
369. Friebe P, Boudet J, Simorre J-P, Bartenschlager R. Kissing-Loop Interaction in the 3' End of the Hepatitis C Virus Genome Essential for RNA Replication. *J Virol.* 2005;79(1):380-392. doi:10.1128/jvi.79.1.380-392.2005
370. Blight KJ, McKeating JA, Rice CM. Highly Permissive Cell Lines for Subgenomic and Genomic Hepatitis C Virus RNA Replication. *J Virol.* 2002;76(24):13001-13014. doi:10.1128/jvi.76.24.13001-13014.2002
371. Appel N, Pietschmann T, Bartenschlager R. Mutational Analysis of Hepatitis C Virus Nonstructural Protein 5A: Potential Role of Differential Phosphorylation in RNA Replication and Identification of a Genetically Flexible Domain. *J Virol.* 2005;79(5):3187-3194. doi:10.1128/jvi.79.5.3187-3194.2005
372. Sheets R. History and characterization of the Vero cell line. *Vaccines Relat Prod Advis Comm.* 2000.
373. Giard DJ, Aaronson SA, Todaro GJ, et al. In vitro cultivation of human tumors: Establishment of cell lines derived from a series of solid tumors. *J Natl Cancer Inst.* 1973;51(5):1417-1423. doi:10.1093/jnci/51.5.1417
374. Peleg J. Growth of arboviruses in monolayers from subcultured mosquito embryo cells. *Virology.* 1968;35(4). doi:10.1016/0042-6822(68)90293-6
375. Lan Q, Fallon AM. Small heat shock proteins distinguish between two mosquito species and confirm identity of their cell lines. *Am J Trop Med Hyg.* 1990;43(6). doi:10.4269/ajtmh.1990.43.669
376. Singh KR. Cell cultures derived from larvae of *Aedes Albopictus* (Skuse) and *Aedes Aegypti* (L.). *Source Curr Sci.* 1967;36(19).
377. Münster M, Płaszczyc A, Cortese M, et al. A reverse genetics system for Zika virus based on a simple molecular cloning strategy. *Viruses.* 2018;10(368):1-17. doi:10.3390/v10070368
378. Moghimi SM, Symonds P, Murray JC, Hunter AC, Debska G, Szewczyk A. A two-stage poly(ethylenimine)-mediated cytotoxicity: Implications for gene transfer/therapy. *Mol Ther.* 2005;11(6):990-995. doi:10.1016/j.ymthe.2005.02.010
379. Bradford MM. A Rapid and Sensitive Method for the Quantitation of Microgram Quantities of Protein Utilizing the Principle of Protein-Dye Binding. *Anal Biochem.* 1976;72:248-254. doi:10.1006/abio.1976.9999
380. Hacke M, Björkholm P, Hellwig A, et al. Inhibition of Ebola virus glycoprotein-mediated cytotoxicity by targeting its transmembrane domain and cholesterol. *Nat Commun.* 2015;6(May). doi:10.1038/ncomms8688
381. Hulce JJ, Cognetta AB, Niphakis MJ, Tully SE, Cravatt BF. Proteome-wide mapping of cholesterol-interacting proteins in mammalian cells. *Nat Methods.* 2013;10(3):259-264. doi:10.1038/nmeth.2368

6. Bibliography

382. Hu B, Höfer CT, Thiele C, Veit M. Cholesterol Binding to the Transmembrane Region of a Group 2 Hemagglutinin (HA) of Influenza Virus Is Essential for Virus Replication, Affecting both Virus Assembly and HA Fusion Activity. *J Virol.* 2019;93(15). doi:10.1128/jvi.00555-19
383. Moss B, Mizukami T, Alexander WA, Fuerst TR. New mammalian expression vectors. *Nature.* 1990;348:91-92.
384. Palmenberg AC, Kirby EM, Janda MR, et al. The nucleotide and deduced amino acid sequences of the encephalomyocarditis viral polyprotein coding region. *Nucleic Acids Res.* 1984;12(6):2969-2985.
385. Cerikan B, Goellner S, Neufeldt CJ, et al. A Non-Replicative Role of the 3' Terminal Sequence of the Dengue Virus Genome in Membranous Replication Organelle Formation. *Cell Rep.* 2020;32(107859):1-32. doi:10.1016/j.celrep.2020.107859
386. Macdonald LE, Durbin RK, Dunn JJ, McAllister WT. Characterization of two types of termination signal for bacteriophage T7 RNA polymerase. *J Mol Biol.* 1994;238(2):145-158.
387. Goellner S, Cerikan B, Cortese M, Neufeldt CJ, Haselmann U, Bartenschlager R. Replication-Independent Generation and Morphological Analysis of Flavivirus Replication Organelles. *STAR Protoc.* 2020;1(3):100173. doi:10.1016/j.xpro.2020.100173
388. Yancey PG, Rodriguez W V., Kilsdonk EPC, et al. Cellular cholesterol efflux mediated by cyclodextrins: Demonstration of kinetic pools and mechanism of efflux. *J Biol Chem.* 1996;271(27):16026-16034. doi:10.1074/jbc.271.27.16026
389. Christian AE, Haynes MP, Phillips MC, Rothblat GH. Use of cyclodextrins for manipulating cellular cholesterol content. *J Lipid Res.* 1997;38(11):2264-2272. doi:10.1016/s0022-2275(20)34940-3
390. Ilangumaran S, Hoessli DC. Effects of cholesterol depletion by cyclodextrin on the sphingolipid microdomains of the plasma membrane. *Biochem J.* 1998;335(2):433-440. doi:10.1042/bj3350433
391. Rodal SK, Skretting G, Garred Ø, Vilhardt F, Deurs B Van, Sandvig K. Extraction of Cholesterol with Methyl- β -Cyclodextrin Perturbs Formation of Clathrin-coated Endocytic Vesicles. *Mol Biol Cell.* 1999;10:961-974. papers2://publication/uuid/B058F2B3-EDAD-4885-ABA3-C588CA3546F2.
392. Alberts AW. Discovery, biochemistry and biology of lovastatin. *Am J Cardiol.* 1988;62(15). doi:10.1016/0002-9149(88)90002-1
393. McKenney JM. Lovastatin: A new cholesterol-lowering agent. *Clin Pharm.* 1988;7(1). doi:10.1093/ajhp/45.2.410
394. Alberts AW. Lovastatin and simvastatin – inhibitors of hmg coa reductase and cholesterol biosynthesis. *Cardiol.* 1990;77. doi:10.1159/000174688
395. Li H, Papadopoulos V. Peripheral-type benzodiazepine receptor function in cholesterol transport. Identification of a putative cholesterol recognition/interaction amino acid sequence and consensus pattern. *Endocrinology.* 1998;139(12):4991-4997. doi:10.1210/endo.139.12.6390
396. Baier CJ, Fantini J, Barrantes FJ. Disclosure of cholesterol recognition motifs in transmembrane domains of the human nicotinic acetylcholine receptor. *Sci Rep.* 2011;1(X). doi:10.1038/srep00069
397. Fantini J, Barrantes FJ. How cholesterol interacts with membrane proteins: An exploration of cholesterol-binding sites including CRAC, CARC, and tilted domains. *Front Physiol.* 2013;4 FEB(February):1-9. doi:10.3389/fphys.2013.00031
398. Cannarozzo C, Fred SM, Girysh M, et al. Cholesterol-recognition motifs in the transmembrane domain of the tyrosine kinase receptor family: The case of TRKB. *Eur J Neurosci.* 2021;53(10):3311-3322. doi:10.1111/ejn.15218
399. Vishwanathan SA, Thomas A, Brasseur R, Epanand RF, Hunter E, Epanand RM. Large changes in the CRAC segment of gp41 of HIV do not destroy fusion activity if the segment interacts with cholesterol. *Biochemistry.* 2008;47(45):11869-11876. doi:10.1021/bi8014828
400. Schroeder C, Heider H, Möncke-Buchner E, Lin TI. The influenza virus ion channel and maturation cofactor M2 is a cholesterol-binding protein. *Eur Biophys J.* 2005;34(1):52-66.

6. Bibliography

- doi:10.1007/s00249-004-0424-1
401. Epand RM, Sayer BG, Epand RF. Caveolin scaffolding region and cholesterol-rich domains in membranes. *J Mol Biol.* 2005;345(2):339-350. doi:10.1016/j.jmb.2004.10.064
402. Catteau A, Kalinina O, Wagner MC, Deubel V, Courageo MP, Desprès P. Dengue virus M protein contains a proapoptotic sequence referred to as ApoptoM. *J Gen Virol.* 2003;84(10):2781-2793. doi:10.1099/vir.0.19163-0
403. Li H, Saucedo-Cuevas L, Yuan L, et al. Zika Virus Protease Cleavage of Host Protein Septin-2 Mediates Mitotic Defects in Neural Progenitors. *Neuron.* 2019;101(6):1089-1098.e4. doi:10.1016/j.neuron.2019.01.010
404. Perera H, Wijerathna T. Sterol Carrier Protein Inhibition-Based Control of Mosquito Vectors: Current Knowledge and Future Perspectives. *Can J Infect Dis Med Microbiol.* 2019;2019. doi:10.1155/2019/7240356
405. Grieneisen ML. Recent advances in our knowledge of ecdysteroid biosynthesis in insects and crustaceans. *Insect Biochem Mol Biol.* 1994;24(2):115-132. doi:10.1016/0965-1748(94)90078-7
406. Hase T, Summers PL, Eckels KH. Flavivirus entry into cultured mosquito cells and human peripheral blood monocytes. *Arch Virol.* 1989;104:129-143.
407. Vancini R, Kramer LD, Ribeiro M, Hernandez R, Brown D. Flavivirus infection from mosquitoes in vitro reveals cell entry at the plasma membrane. *Virology.* 2013;435(2):406-414. doi:10.1016/j.virol.2012.10.013
408. Byk LA, Gamarnik A V. Properties and Functions of the Dengue Virus Capsid Protein. *Annu Rev Virol.* 2016;3:263-281. doi:10.1146/annurev-virology-110615-042334
409. Samsa MM, Mondotte JA, Iglesias NG, et al. Dengue virus capsid protein usurps lipid droplets for viral particle formation. *PLoS Pathog.* 2009;5(10). doi:10.1371/journal.ppat.1000632
410. Mori Y, Okabayashi T, Yamashita T, et al. Nuclear Localization of Japanese Encephalitis Virus Core Protein Enhances Viral Replication. *J Virol.* 2005;79(6):3448-3458. doi:10.1128/jvi.79.6.3448-3458.2005
411. Haddow AJ, Williams MC, Woodall JP, Simpson DI, Goma LK. Twelve isolations of Zika virus from *Aedes (Stegomyia) Africanus* (Theobald) taken in and above a Uganda Forest. *Bull World Health Organ.* 1964;31:57-69.
412. Paul D, Bartenschlager R. Flaviviridae Replication Organelles: Oh, What a Tangled Web We Weave. *Annu Rev Virol.* 2015;2(1):289-310. doi:10.1146/annurev-virology-100114-055007
413. Studier FW, Moffatt BA. Use of bacteriophage T7 RNA polymerase to direct selective high-level expression of cloned genes. *J Mol Biol.* 1986;189:113-130. doi:10.1016/0022-2836(86)90385-2
414. Jang SK, Kräusslich HG, Nicklin MJ, Duke GM, Palmenberg AC, Wimmer E. A segment of the 5' nontranslated region of encephalomyocarditis virus RNA directs internal entry of ribosomes during in vitro translation. *J Virol.* 1988;62(8):2636-2643. doi:10.1128/jvi.62.8.2636-2643.1988
415. Berger C, Romero-Brey I, Radujkovic D, et al. Daclatasvir-like inhibitors of NS5A block early biogenesis of hepatitis C virus-induced membranous replication factories, independent of RNA replication. *Gastroenterology.* 2014;147(5):1094-1105. doi:10.1053/j.gastro.2014.07.019
416. Neufeldt CJ, Cortese M, Acosta EG, Bartenschlager R. Rewiring cellular networks by members of the Flaviviridae family. *Nat Rev Microbiol.* 2018;16:125-142. doi:10.1038/nrmicro.2017.170
417. Reiss S, Rebhan I, Backes P, et al. Recruitment and activation of a lipid kinase by hepatitis C virus NS5A is essential for integrity of the membranous replication compartment. *Cell Host Microbe.* 2011;9:32-45. doi:10.1016/j.chom.2010.12.002
418. Ci Y, Yang Y, Xu C, Qin CF, Shi L. Electrostatic Interaction Between NS1 and Negatively Charged Lipids Contributes to Flavivirus Replication Organelles Formation. *Front Microbiol.* 2021;12(641059):1-11. doi:10.3389/fmicb.2021.641059
419. Wang H, Perry JW, Lauring AS, Neddermann P, De Francesco R, Tai AW. Oxysterol-

6. Bibliography

- binding protein is a phosphatidylinositol 4-kinase effector required for HCV replication membrane integrity and cholesterol trafficking. *Gastroenterology*. 2014;146(5):1373-1385. doi:10.1053/j.gastro.2014.02.002
420. Ertel KJ, Benefield D, Castaño-Diez D, et al. Cryo-electron tomography reveals novel features of a viral rna replication compartment. *Elife*. 2017;6(e25940):1-24. doi:10.7554/eLife.25940
421. Kovalev N, de Castro Martín IF, Pogany J, et al. Role of Viral RNA and Co-opted Cellular ESCRT-I and ESCRT-III Factors in Formation of Tombusvirus Spherules Harboring the Tombusvirus Replicase. *J Virol*. 2016;90(7):3611-3626. doi:10.1128/jvi.02775-15
422. Kallio K, Hellström K, Balistreri G, Spuul P, Jokitalo E, Ahola T. Template RNA Length Determines the Size of Replication Complex Spherules for Semliki Forest Virus. *J Virol*. 2013;87(16):9125-9134. doi:10.1128/jvi.00660-13
423. Hellström K, Kallio K, Utt A, et al. Partially Uncleaved Alphavirus Replicase Forms Spherule Structures in the Presence and Absence of RNA Template. *J Virol*. 2017;91(18):e00787-17. doi:10.1128/jvi.00787-17
424. Miorin L, Romero-Brey I, Maiuri P, et al. Three-Dimensional Architecture of Tick-Borne Encephalitis Virus Replication Sites and Trafficking of the Replicated RNA. *J Virol*. 2013;87(11):6469-6481. doi:10.1128/jvi.03456-12
425. Yau W-L, Nguyen-Dinh V, Larsson E, Lindqvist R, Överby AK, Lundmark R. Model System for the Formation of Tick-Borne Encephalitis Virus Replication Compartments without Viral RNA Replication. *J Virol*. 2019;93(18):e00292-19. doi:10.1128/jvi.00292-19
426. Bhatt S, Gething PW, Brady OJ, et al. The global distribution and burden of dengue. *Nature*. 2013;496:504-507. doi:10.1038/nature12060
427. Mayer S V., Tesh RB, Vasilakis N. The emergence of arthropod-borne viral diseases: A global prospective on dengue, chikungunya and zika fevers. *Acta Trop*. 2017;166:155-163. doi:10.1016/j.actatropica.2016.11.020
428. Gubler DJ. The continuing spread of West Nile virus in the Western Hemisphere. *Clin Infect Dis*. 2007;45(8):1039-1046. doi:10.1086/521911
429. Puntasecca CJ, King CH, Labeaud AD. Measuring the global burden of Chikungunya and Zika viruses: A systematic review. *PLoS Negl Trop Dis*. 2021;15(3):e0009055. doi:10.1371/journal.pntd.0009055
430. Bellone R, Failloux AB. The Role of Temperature in Shaping Mosquito-Borne Viruses Transmission. *Front Microbiol*. 2020;11(584846):1-15. doi:10.3389/fmicb.2020.584846
431. Dohm DJ, O'Guinn ML, Turell MJ. Effect of environmental temperature on the ability of *Culex pipiens* (Diptera: Culicidae) to transmit West Nile virus. *J Med Entomol*. 2002;39(1):221-225. doi:10.1603/0022-2585-39.1.221
432. WHO. Prioritizing diseases for research and development in emergency contexts. <https://www.who.int/activities/prioritizing-diseases-for-research-and-development-in-emergency-contexts>.
433. Han Y, Mesplède T. Investigational drugs for the treatment of Zika virus infection: a preclinical and clinical update. *Expert Opin Investig Drugs*. 2018;27(12). doi:10.1080/13543784.2018.1548609
434. Kumar A, Kumar P, Giri R. Zika virus NS4A cytosolic region (residues 1–48) is an intrinsically disordered domain and folds upon binding to lipids. *Virology*. 2020;550:27-36. doi:10.1016/j.virol.2020.07.017
435. To J, Torres J. Trimerization of the N-Terminal tail of zika virus NS4A protein: A potential in vitro antiviral screening assay. *Membranes (Basel)*. 2021;11(335):1-13. doi:10.3390/membranes11050335
436. Lemm JA, O'Boyle D, Liu M, et al. Identification of Hepatitis C Virus NS5A Inhibitors. *J Virol*. 2010;84(1):482-491. doi:10.1128/jvi.01360-09
437. Romine JL, St. Laurent DR, Leet JE, et al. Inhibitors of HCV NS5A: From iminothiazolidinones to symmetrical stilbenes. *ACS Med Chem Lett*. 2011;2(3):224-229. doi:10.1021/ml1002647
438. Zanini F, Pu SY, Bekerman E, Einav S, Quake SR. Single-cell transcriptional dynamics of

6. Bibliography

- flavivirus infection. *Elife*. 2018;7:1-21. doi:10.7554/eLife.32942
439. Zhang F, Hammack C, Ogden SC, et al. Molecular signatures associated with ZIKV exposure in human cortical neural progenitors. *Nucleic Acids Res*. 2016;44(18):8610-8620. doi:10.1093/nar/gkw765
440. Tiwari SK, Dang J, Qin Y, Lichinchi G, Bansal V, Rana TM. Zika virus infection reprograms global transcription of host cells to allow sustained infection. *Emerg Microbes Infect*. 2017;6(4):e24-10. doi:10.1038/emi.2017.9
441. Scaturro P, Stukalov A, Haas DA, et al. An orthogonal proteomic survey uncovers novel Zika virus host factors. *Nature*. 2018;561(7722):253-257. doi:10.1038/s41586-018-0484-5
442. Bernard E, Solignat M, Gay B, et al. Endocytosis of chikungunya virus into mammalian cells: Role of clathrin and early endosomal compartments. *PLoS One*. 2010;5(7). doi:10.1371/journal.pone.0011479
443. Aleksandrowicz P, Marzi A, Biedenkopf N, et al. Ebola virus enters host cells by macropinocytosis and clathrin-mediated endocytosis. *J Infect Dis*. 2011;204(SUPPL. 3):957-967. doi:10.1093/infdis/jjr326
444. Sorice M, Misasi R, Riitano G, et al. Targeting Lipid Rafts as a Strategy Against Coronavirus. *Front Cell Dev Biol*. 2021;8(February):1-11. doi:10.3389/fcell.2020.618296
445. Parton RG, Richards AA. Lipid rafts and caveolae as portals for endocytosis: New insights and common mechanisms. *Traffic*. 2003;4(11):724-738. doi:10.1034/j.1600-0854.2003.00128.x
446. Saeed MF, Kolokoltsov AA, Albrecht T, Davey RA. Cellular entry of ebola virus involves uptake by a macropinocytosis-like mechanism and subsequent trafficking through early and late endosomes. *PLoS Pathog*. 2010;6(9). doi:10.1371/journal.ppat.1001110
447. Sun X, Whittaker GR. Role for Influenza Virus Envelope Cholesterol in Virus Entry and Infection. *J Virol*. 2003;77(23):12543-12551. doi:10.1128/jvi.77.23.12543-12551.2003
448. Caragata EP, Rancès E, Hedges LM, et al. Dietary Cholesterol Modulates Pathogen Blocking by Wolbachia. *PLoS Pathog*. 2013;9(6). doi:10.1371/journal.ppat.1003459
449. Clifton ME, Noriega FG. The fate of follicles after a blood meal is dependent on previtellogenic nutrition and juvenile hormone in *Aedes aegypti*. *J Insect Physiol*. 2012;58(7):1007-1019. doi:10.1016/j.jinsphys.2012.05.005
450. Marques J, Cardoso JCR, Felix RC, et al. Fresh-blood-free diet for rearing malaria mosquito vectors. *Sci Rep*. 2018;8(1):1-9. doi:10.1038/s41598-018-35886-3
451. Merritt RW, Dadd RH, Walker ED. Feeding Behavior, Natural Food, and Nutritional Relationships of Larval Mosquitoes. *Annu Rev Entomol*. 1992;37(1). doi:10.1146/annurev.en.37.010192.002025

7. APPENDIX

7.1. Abbreviations

A.	<i>Aedes</i>	DMSO	dimethyl sulfoxide
A	alanine	DMV	double-membrane vesicle
aa	amino acid	DNA	deoxyribonucleic acid
arbovirus	arthropod-borne virus	dNTP	deoxynucleotide triphosphate
ARCA	anti-reverse cap analog	dsRNA	double-stranded RNA
ATP	adenosine triphosphate	DTT	dithiothreitol
BRIFB3	BPI fold containing family N member 3	E	envelope protein
BSA	bovine serum albumin	<i>E. coli</i>	<i>Escherichia coli</i>
C	capsid protein	EDTA	ethylenediaminetetraacetic acid
CaCl ₂	calcium chloride	EGTA	ethylene glycol-bis(β-aminoethyl ether)-N,N,N',N'-tetraacetic acid
CaCo	cacodylate	eIF	eukaryotic initiation factor
CARC	cholesterol amino recognition consensus	EM	electron microscopy
cDNA	complementary DNA	EMCV	encephalomyocarditis virus
CHOL	cholesterol	ER	endoplasmic reticulum
cHP	capsid hair pin	F	phenylalanine
CIP	calf intestinal phosphatase	FBS	fetal bovine serum
CTP	cytidine triphosphate	FFU	focus forming unit
CuAAC	copper-catalyzed azide-alkyne cycloaddition	GAPDH	glyceraldehyde 3-phosphate dehydrogenase
CuSO ₄	copper (II) sulfate	GBS	Guillain-Barré syndrome
CS	cyclization sequence	GFP	green fluorescent protein
DAPI	4',6-Diamidino-2-phenylindol	GTP	guanosine triphosphate
DAR	downstream AUG region	H ₂ O ₂	hydrogen peroxide
DB	dumbbell	HA	hemagglutinin
DSC	downstream 5' cyclization sequence	HCV	hepatitis C virus
DC-SIGN	dendritic cell specific intercellular adhesion molecule-3-grabbing non-integrin	HDV	hepatitis D virus
DDM	dodecyl maltoside	HEPES	(4-(2-hydroxyethyl)-1-piperazineethanesulfonic acid)
DDT	dichlorodiphenyltrichloroethane	HMG-CoA	hydroxyl methyl glutaryl-CoA
DENV	dengue virus	h.p.e.	hours post electroporation
DL	delipidated	h.p.i.	hours post infection
DMEM	Dulbecco's Modified Eagle Medium	h.p.t.	hours post transfection
		HRP	horseradish peroxidase

7. Appendix

HSP	heat shock protein	PAC	photo-activated cholesterol
IFN	interferon	PAGE	polyacrylamide gel electrophoresis
IRES	internal ribosome entry site	PBS	phosphate buffered saline
IRF3	interferon regulatory factor 3	PCR	polymerase chain reaction
IVT	<i>in vitro</i> transcription	PE	phosphatidylethanolamine
JEV	Japanese encephalitis virus	PEI	polyethylenimine
K	lysine	PFA	paraformaldehyde
kb	kilo base pair	PFU	plaque forming units
KCl	potassium chloride	PHEIC	Public Health Emergency of International Concern
kDa	kilo Dalton	pIRO	plasmid induced replication organelle
KOH	potassium hydroxide	PI4K	phosphatidylinositol-4-kinase
L	leucine	PI4P	phosphatidylinositol-4-phosphate
LB	lysogeny broth	PK	pseudoknot
LD	lipid droplet	POPC	phosphocholine
LDA	Linear Discriminant Analysis	prM	precursor membrane protein
M	methionine	PVDF	polyvinylidene difluoride
MAVS	mitochondrial antiviral-signaling proteins	qRT-PCR	quantitative real-time PCR
M β CD	methyl- β -cyclodextrin	R	arginine
MD	molecular dynamics	RdRp	RNA-dependent RNA polymerase
MDA5	melanoma differentiation-associated protein 5	RIG-I	retinoic acid inducible gene I
MEM	Minimal Essential Medium	RIPA	radioimmunoprecipitation assay
MgCl ₂	Magnesium chloride	RNA	ribonucleic acid
MgSO ₄	Magnesium sulfate	rNTP	ribonucleoside triphosphate
MH	membrane helix	ROs	replication organelles
MOI	multiplicity of infection	rpm	rounds per minute
mRNA	messenger RNA	RsP17	ribosomal gene S17
MTase	methyltransferase	RT	reverse transcriptase
N	asparagine	RTN	reticulon
NaCl	sodium chloride	S	serine
NC	nucleocapsid	SDS	sodium dodecyl sulfate
NLS	nuclear localization sequence	SEM	standard error of the mean
nm	nanometer	sfRNAs	subgenomic flavivirus RNA
NPC	neuronal progenitor cell	SFV	Semliki forest virus
NS	non-structural	sgR2A	sub-genomic replicon encoding the <i>Renilla</i> luciferase and a self-cleaving 2A peptide
n.s.	not significant	sHP	short hairpin stem loop
ORF	open reading frame		

7. Appendix

SL	stem-loop
ssRNA	single-stranded RNA
STAT	signal transducer and activator of transcription
synZIKV	synthetic ZIKV
TAM	<u>T</u> yro3, <u>A</u> xl, and <u>M</u> er
TBK	TANK-binding kinase
TBP	tryptose B Phosphate
TBTA	tris[(1-benzyl-1H-1,2,3-triazol-4-yl) methyl]amine
TCID	tissue culture infectious dose
TEBV	tick borne encephalitis virus
TEM	transmission electron microscopy
TEMED	tetramethylethylenediamin
TIM	T cell, immunoglobulin, and mucin
TMD	transmembrane domain
U	Unit
UAR	upstream AUG region
UTP	uridine triphosphate
UTR	untranslated region
UV	ultraviolet
V	valine
V	voltage
VLP	virus-like particle
VPs	vesicle packets
vRNA	viral RNA
WHO	World Health Organization
WNV	West Nile virus
WT	wild type
Y	tyrosine
YFV	yellow fever virus
ZIKV	Zika virus

7.2. Additional projects

7.2.1. A pIRO-Z reporter system for CLEM analyses

To enable targeted analysis of transfected cells via correlative light-electron microscopy, the pIRO-Z system ($\Delta 5'$ SLAB/NS1-NS5/3'WT) was modified by inserting a fluorescent protein (mNeonGreen) upstream of the viral NS1 protein. Furthermore, by adding a 2A peptide along with an NLS-signal sequence to the fluorescent protein, it is auto-cleaved upon translation and directly imported into the nucleus (Figure S1a). To functionally characterize the reporter pIRO-Z system polyprotein processing and protein abundance were assessed via western blot, subcellular localization of non-structural proteins was assessed via immunofluorescent microscopy, and its ability to induce ZIKV replication compartments was assessed via TEM. To allow a direct comparative analysis to the parental construct, Huh7-Lunet T7 cells transfected with the pIRO-Z system ($\Delta 5'$ SLAB/NS1-NS5/3'WT) were analyzed in parallel. Given my results, cells expressing the reporter construct showed neither alterations in processing of the ZIKV polyprotein (Figure S1e) nor changes in the abundance of cleaved viral proteins when compared to ZIKV infected cells (Figure S1f). Furthermore, no changes were observed when comparing the subcellular localization of NS3 and NS4B in transfected cells. As described in the results (see section 4.1.1.), NS3 and NS4B localized to the ER which was assessed by staining RTN-3 (Figure S1d). Most importantly, comparing the pIRO-Z reporter construct to the parental construct with respect to its ability to induce ZIKV replication compartments demonstrated that the reporter induced ROs are of similar morphology and size as those found in pIRO-Z transfected cells (Figure S1b+c). However, until today this reporter construct lacks the HDV ribozyme at the 3'end, thus needs further optimization to ensure the production of authentic viral RNA transcripts upon transfection.

7. Appendix

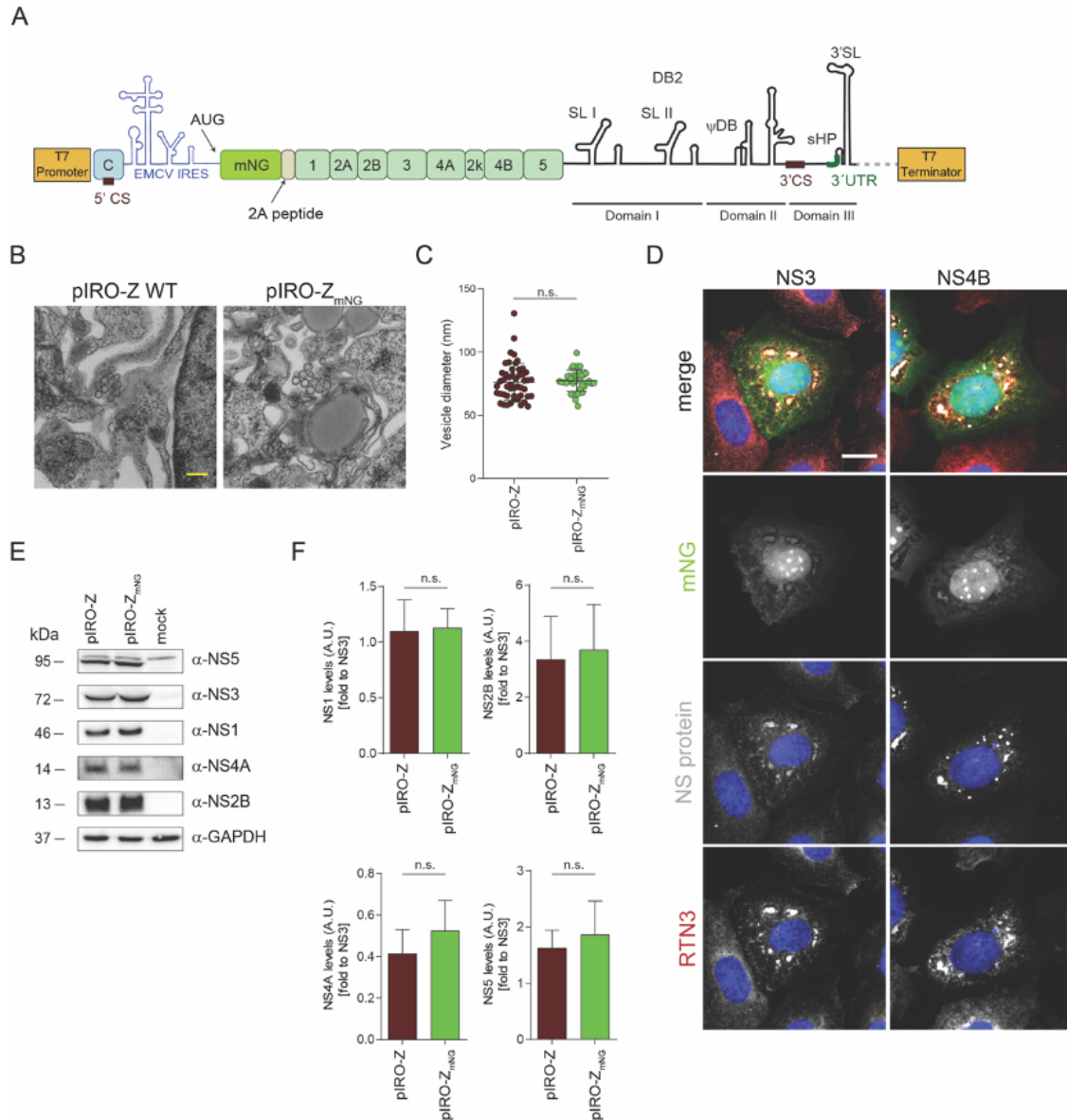


Figure S1. A reporter piRO construct for CLEM approaches.

(A) Schematic representation of the reporter piRO-Z construct. The fluorescent reporter protein (mNeonGreen = mNG) is cleaved off via a 2A-peptide sequence (C-terminal) and transported into the nucleus post-cleavage. (B) TEM images of Huh7-Lunet T7 cells upon transfection with $\Delta 5'$ SLAB or $\Delta 5'$ SLAB_{mNG} constructs. Cells were transfected and after 18 hours, fixed, processed, and resin-embedded for sectioning. Upper panel scale bar: 500 nm. Lower panel represents the magnification of red square indicated area in the upper panel images. Lower panel scale bar: 200 nm. (C) Vesicle diameter measurements were performed manually using Fiji software. Means \pm SEM are from one experiment. 50 vesicles were counted for $\Delta 5'$ SLAB whereas only 38 vesicles were counted for $\Delta 5'$ SLAB_{mNG} so far. n.s., not significant. (D) Cells were transfected with the indicated constructs and fixed for immunofluorescence analysis after 18 hours. RTN3 signal was used as ER maker. Scale bars: 10 μ m. (E) Huh7-Lunet T7 cells were either transfected with $\Delta 5'$ SLAB or $\Delta 5'$ SLAB_{mNG} for 18 hours before being lysed and subjected to western blot analysis. Immunoblot shows the expression of NS5, NS3, NS1, NS4A, and NS2B. GAPDH was used as loading control. (F) Relative polyprotein processing efficiency was calculated by densitometry normalizing the signals of NS1, NS2B, NS4A, and NS5 to NS3 expression levels in each indicated construct. Values represent mean \pm SEM of two independent experiments. n.s., not significant.

7.3. Supplementary information

7.3.1. Plasmids

Table S1. List of plasmids used and generated in this study.

No	Name	Description
Basic plasmids		
1	pWPI_BLR_empty	Lentiviral vector, EMCV promotor, blasticidin resistance
2	pWPI_Puro_empty	Lentiviral vector, EMCV promotor, puromycin resistance
3	pCMV-GagPol	Lentiviral packaging plasmid, encoding the replication machinery
4	pMD.G2	Lentiviral packaging plasmid, encoding surface protein (envelope)
5	pCDN3.1_empty	High-copy expression vector, CMV promotor
6	pTM1-2	High-copy expression vector, T7 promotor
ZIKV constructs		
7	pFK_synZIKV-H/PF/2013	Plasmid encoding full-length synthetic genome of ZIKV strain H/PF/2013; T7 promotor used for <i>in vitro</i> transcription ³⁷⁷
8	pFK_synZIKV-H/PF/2013_GAA	full-length synthetic ZIKV based on plasmid [7]; replication deficient NS5 mutant; T7 promotor used for <i>in vitro</i> transcription ³⁷⁷
9	ZV_R238L+Y240A+R246L	Full-length synthetic ZIKV based on plasmid [7] containing indicated mutation within prM
10	ZV_R238L+Y240S+R246L	Full-length synthetic ZIKV based on plasmid [7] containing indicated mutation within prM
11	ZV_R253L+F257A	Full-length synthetic ZIKV based on plasmid [7] containing indicated mutation within prM
12	ZV_R253L+F257S	Full-length synthetic ZIKV based on plasmid [7] containing indicated mutation within prM
13	ZV_K275L+Y278A	Full-length synthetic ZIKV based on plasmid [7] containing indicated mutation within prM
14	ZV_K275L+Y278S	Full-length synthetic ZIKV based on plasmid [7] containing indicated mutation within prM
15	pFK_synZIKV-H/PF/2013_R2A	Plasmid encoding full-length synthetic ZIKV RLuc reporter virus; T7 promotor used for <i>in vitro</i> transcription ³⁷⁷
16	pFK_synZIKV-H/PF/2013_R2A_GAA	full-length synthetic ZIKV based on plasmid [15]; replication deficient NS5 mutant; T7 promotor used for <i>in vitro</i> transcription ³⁷⁷
17	ZVR2A_R238L+Y240A+R246L	Full-length synthetic ZIKV RLuc reporter virus based on plasmid [15] containing indicated mutation within prM
18	ZVR2A_R238L+Y240S+R246L	Full-length synthetic ZIKV RLuc reporter virus based on plasmid [15] containing indicated mutation within prM
19	ZVR2A_R253L+F257A	Full-length synthetic ZIKV RLuc reporter virus based on plasmid [15] containing indicated mutation within prM
20	ZVR2A_R253L+F257S	Full-length synthetic ZIKV RLuc reporter virus based on plasmid [15] containing indicated mutation within prM
21	ZVR2A_K275L+Y278A	Full-length synthetic ZIKV RLuc reporter virus based on plasmid [15] containing indicated mutation within prM
22	ZVR2A_K275L+Y278S	Full-length synthetic ZIKV RLuc reporter virus based on plasmid [15] containing indicated mutation within prM
23	pFK_synZIKV-H/PF/2013_FP365	Plasmid encoding full-length synthetic ZIKV FP365 reporter virus; T7 promotor used for <i>in vitro</i> transcription ³⁷⁷
24	ZVFP635_R238L+Y240A+R246L	Full-length synthetic ZIKV FP365 reporter virus based on plasmid [23] containing indicated mutation within prM
25	ZVFP635_R238L+Y240S+R246L	Full-length synthetic ZIKV FP365 reporter virus based on plasmid [23] containing indicated mutation within prM

7. Appendix

26	ZVFP635_R253L+F257A	Full-length synthetic ZIKV FP365 reporter virus based on plasmid [23] containing indicated mutation within prM
27	ZVFP635_R253L+F257S	Full-length synthetic ZIKV FP365 reporter virus based on plasmid [23] containing indicated mutation within prM
28	ZVFP635_K275L+Y278A	Full-length synthetic ZIKV FP365 reporter virus based on plasmid [23] containing indicated mutation within prM
29	ZVFP635_K275L+Y278S	Full-length synthetic ZIKV FP365 reporter virus based on plasmid [23] containing indicated mutation within prM
30	pFK_sgR2A ZIKV-H/PF/2013	Subgenomic ZIKV replicon with RLuc reporter gene ³⁷⁷
31	pFK_sgR2A ZIKV-H/PF/2013_GAA	Subgenomic ZIKV replicon based on plasmid [30]; replication deficient NS5 mutant; T7 promoter used for in vitro transcription ³⁷⁷
32	sgR2A_ZV_Y42A+K47L	Subgenomic ZIKV replicon based on plasmid [30] containing indicated mutation within NS2B
33	sgR2A_ZV_Y42S+K47L	Subgenomic ZIKV replicon based on plasmid [30] containing indicated mutation within NS2B
34	sgR2A_ZV_Y52A+R55L	Subgenomic ZIKV replicon based on plasmid [30] containing indicated mutation within NS2B
35	sgR2A_ZV_Y52S+R55L	Subgenomic ZIKV replicon based on plasmid [30] containing indicated mutation within NS2B
36	sgR2A_ZV_T12A	Subgenomic ZIKV replicon based on plasmid [30] containing indicated mutation within NS4A ⁸⁸
37	sgR2A_ZV_T12I	Subgenomic ZIKV replicon based on plasmid [30] containing indicated mutation within NS4A ⁸⁸
38	sgR2A_ZV_E19G	Subgenomic ZIKV replicon based on plasmid [30] containing indicated mutation within NS4A ⁸⁸
39	sgR2A_ZV_K42E	Subgenomic ZIKV replicon based on plasmid [30] containing indicated mutation within NS4A ⁸⁸
40	sgR2A_ZV_T54I	Subgenomic ZIKV replicon based on plasmid [30] containing indicated mutation within NS4A ⁸⁸
41	sgR2A_ZV_K80L+F83A	Subgenomic ZIKV replicon based on plasmid [30] containing indicated mutation within NS4A
42	sgR2A_ZV_K80L+F83S	Subgenomic ZIKV replicon based on plasmid [30] containing indicated mutation within NS4A
43	sgR2A_ZV_K105L+Y110A	Subgenomic ZIKV replicon based on plasmid [30] containing indicated mutation within NS4B
44	sgR2A_ZV_K105L+Y110S	Subgenomic ZIKV replicon based on plasmid [30] containing indicated mutation within NS4B
45	sgR2A_ZV_R251L+Y254A	Subgenomic ZIKV replicon based on plasmid [30] containing indicated mutation within NS4B
46	sgR2A_ZV_R251L+Y254S	Subgenomic ZIKV replicon based on plasmid [30] containing indicated mutation within NS4B
47	sgR2A_ZV_Y262A+R266L	Subgenomic ZIKV replicon based on plasmid [30] containing indicated mutation within NS4B
48	sgR2A_ZV_Y262S+R266L	Subgenomic ZIKV replicon based on plasmid [30] containing indicated mutation within NS4B
49	pFK_sgmNG ZIKV-H/PF/2013	Subgenomic ZIKV replicon with mNeonGreen fluorescent protein
Expression constructs		
50	pcDNA3.1, prM-Env-HA WT	pcDNA3.1. containing prM-Envelope with Capsid anchor sequence, C-terminal HA-tag preceded by Ser-Gly linker
51	pcDNA3.1, prM-Env-HA_R253L+F257A	pcDNA3.1. containing prM-Envelope with Capsid anchor sequence, C-terminal HA-tag and the indicated mutation
52	pcDNA3.1, prM-Env-HA_R253L+F257S	pcDNA3.1. containing prM-Envelope with Capsid anchor sequence, C-terminal HA-tag and the indicated mutation
53	pcDNA3.1, prM-Env-HA_K275L+Y278A	pcDNA3.1. containing prM-Envelope with Capsid anchor sequence, C-terminal HA-tag and the indicated mutation
54	pcDNA3.1, prM-Env-HA_K275L+Y278S	pcDNA3.1. containing prM-Envelope with Capsid anchor sequence, C-terminal HA-tag and the indicated mutation

7. Appendix

55	pcDNA3.1. prM-Env WT	pcDNA3.1. containing prM-Envelope with Capsid anchor sequence
56	pcDNA3.1. prM-Env_R253L+F257A	pcDNA3.1. containing prM-Envelope with Capsid anchor sequence and containing the indicated mutations
57	pcDNA3.1. prM-Env_R253L+F257S	pcDNA3.1. containing prM-Envelope with Capsid anchor sequence and containing the indicated mutations
58	pcDNA3.1. prM-Env_K275L+Y278A	pcDNA3.1. containing prM-Envelope with Capsid anchor sequence and containing the indicated mutations
59	pcDNA3.1. prM-Env_K275L+Y278S	pcDNA3.1. containing prM-Envelope with Capsid anchor sequence and containing the indicated mutations
60	pTM prM -HA WT	pTM containing prM with Capsid anchor sequence and the tobacco 2A peptide, C-terminal HA-tag preceded by Ser-Gly linker
61	pTM prM-HA_R116L+Y118A+R124L	pTM containing prM with Capsid anchor sequence and the tobacco 2A peptide, C-terminal HA-tag and the indicated mutation
62	pTM prM-HA_R116L+Y118S+R124L	pTM containing prM with Capsid anchor sequence and the tobacco 2A peptide, C-terminal HA-tag and the indicated mutation
63	pTM prM-HA_R130L+F135A	pTM containing prM with Capsid anchor sequence and the tobacco 2A peptide, C-terminal HA-tag and the indicated mutation
64	pTM prM-HA_R130L+F135S	pTM containing prM with Capsid anchor sequence and the tobacco 2A peptide, C-terminal HA-tag and the indicated mutation
65	pTM prM-HA_K153L+Y156A	pTM containing prM with Capsid anchor sequence and the tobacco 2A peptide, C-terminal HA-tag and the indicated mutation
66	pTM prM-HA_K153L+Y156S	pTM containing prM with Capsid anchor sequence and the tobacco 2A peptide, C-terminal HA-tag and the indicated mutation
67	pTM NS2B-NS3-HA WT	pTM containing NS2B-NS3, C-terminal HA-tag preceded by Ser-Gly linker
68	pTM NS2B-NS3-HA_Y42A+K47L	pTM containing NS2B-NS3, C-terminal HA-tag and the indicated mutation
69	pTM NS2B-NS3-HA_Y42S+K47L	pTM containing NS2B-NS3, C-terminal HA-tag and the indicated mutation
70	pTM NS2B-NS3-HA_Y52A+R56L	pTM containing NS2B-NS3, C-terminal HA-tag and the indicated mutation
71	pTM NS2B-NS3-HA_Y52S+R56L	pTM containing NS2B-NS3, C-terminal HA-tag and the indicated mutation
72	pTM HA-NS4A WT	pTM containing NS4A, N-terminal HA-tag preceded by Ser-Gly linker
73	pTM HA-NS4A_K80L+F83A	pTM containing NS4A, N-terminal HA-tag and indicated mutation
74	pTM HA-NS4A_K80L+F83S	pTM containing NS4A, N-terminal HA-tag and indicated mutation
75	pTM 2kNS4B-HA WT	pTM containing 2kNS4B, C-terminal HA-tag preceded by Ser-Gly linker
76	pTM 2kNS4B-HA_K105L+Y110A	pTM containing 2kNS4B, C-terminal HA-tag and indicated mutation
77	pTM 2kNS4B-HA_K105L+Y110S	pTM containing 2kNS4B, C-terminal HA-tag and indicated mutation
78	pTM 2kNS4B-HA_R251L+Y254A	pTM containing 2kNS4B, C-terminal HA-tag and indicated mutation
79	pTM 2kNS4B-HA_R251L+Y254S	pTM containing 2kNS4B, C-terminal HA-tag and indicated mutation
80	pTM 2kNS4B-HA_Y262A+R266L	pTM containing 2kNS4B, C-terminal HA-tag and indicated mutation
81	pTM 2kNS4B-HA_Y262S+R266L	pTM containing 2kNS4B, C-terminal HA-tag and indicated mutation
ZIKV polyprotein constructs		
82	pIRO-Z_UTRWT_GDD	Low copy vector expressing the ZIKV polyprotein via T7 promoter, with complete 5' and 3'UTRs ³⁸⁵
83	pIRO-Z_UTRWT_GAA	Polyprotein expression plasmid based in plasmid [82]; NS5 inactivated mutant ³⁸⁵
84	pIRO-Z_5'ΔSLAB_GDD	Low copy vector expressing the ZIKV polyprotein via T7 promoter, modified 5'UTR (ΔSLAB); complete 3'UTR ³⁸⁵
85	pIRO-Z_5'ΔSLAB_GAA	Polyprotein expression plasmid based in plasmid [82]; NS5 inactivated mutant ³⁸⁵
86	pIRO-Z_5'ΔSLAB_3'ΔsHP_GDD	Polyprotein expression plasmid based in plasmid [82]; modified 3'UTR (ΔsHP) ³⁸⁵

7. Appendix

87	pIRO-Z_5'ΔSLAB_3'ΔsHP_GAA	Polyprotein expression plasmid based in plasmid [83]; modified 3'UTR (ΔsHP); NS5 inactivated mutant
88	pIRO-Z_5'ΔSLAB_3'ΔUAR_GDD	Polyprotein expression plasmid based in plasmid [82]; modified 3'UTR (ΔUAR) ³⁸⁵
89	pIRO-Z_5'ΔSLAB_3'ΔUAR_GAA	Polyprotein expression plasmid based in plasmid [83]; modified 3'UTR (ΔUAR); NS5 inactivated mutant
90	pIRO-Z_5'ΔSLAB_3'ΔSL_GDD	Polyprotein expression plasmid based in plasmid [82]; modified 3'UTR (ΔSL) ³⁸⁵
91	pIRO-Z_5'ΔSLAB_3'ΔSL_GAA	Polyprotein expression plasmid based in plasmid [83]; modified 3'UTR (ΔSL); NS5 inactivated mutant
92	pIRO-Z_5'ΔSLAB_3'ΔsHP-SL_GDD	Polyprotein expression plasmid based in plasmid [82]; modified 3'UTR (ΔsHP-SL) ³⁸⁵
93	pIRO-Z_5'ΔSLAB_3'ΔsHP-SL_GAA	Polyprotein expression plasmid based in plasmid [83]; modified 3'UTR (ΔsHP-SL); NS5 inactivated mutant
94	pIRO-Z_5'ΔSLAB_3'ΔCS-SL_GDD	Polyprotein expression plasmid based in plasmid [82]; modified 3'UTR (ΔCS-SL) ³⁸⁵
95	pIRO-Z_5'ΔSLAB_3'ΔCS-SL_GAA	Polyprotein expression plasmid based in plasmid [83]; modified 3'UTR (ΔCS-SL); NS5 inactivated mutant
96	pIRO-Z_5'ΔSLAB_3'Δcomplete_GDD	Polyprotein expression plasmid based in plasmid [82]; modified 3'UTR (Δcomplete) ³⁸⁵
97	pIRO-Z_5'ΔSLAB_3'Δcomplete_GAA	Polyprotein expression plasmid based in plasmid [83]; modified 3'UTR (Δcomplete); NS5 inactivated mutant
98	pIRO-Z_5'ΔSLAB_GDD_mNGreporter	Polyprotein expression plasmid based in plasmid [82]; reporter gene mNeonGreen upstream of coding sequence
99	pIRO-Z_5'ΔSLAB_GDD_3'WT-Ribozym	Polyprotein expression plasmid based in plasmid [82]; complete 3'UTR-Ribozym ³⁸⁵
100	pIRO-Z_Y42A+K47L	Polyprotein expression plasmid based in plasmid [99]; containing indicates NS2B-3 mutation
101	pIRO-Z_Y42S+K47L	Polyprotein expression plasmid based in plasmid [99]; containing indicates NS2B-3 mutation
102	pIRO-Z_Y52A+R56L	Polyprotein expression plasmid based in plasmid [99]; containing indicates NS2B-3 mutation
103	pIRO-Z_Y52S+R56L	Polyprotein expression plasmid based in plasmid [99]; containing indicates NS2B-3 mutation
104	pIRO-Z_K80L+F83A	Polyprotein expression plasmid based in plasmid [99]; containing indicates NS4A mutation
105	pIRO-Z_K80L+F83S	Polyprotein expression plasmid based in plasmid [99]; containing indicates NS4A mutation
106	pIRO-Z_T12A	Polyprotein expression plasmid based in plasmid [99]; containing indicates NS4A mutation ⁸⁸
107	pIRO-Z_T12I	Polyprotein expression plasmid based in plasmid [99]; containing indicates NS4A mutation ⁸⁸
108	pIRO-Z_E19G	Polyprotein expression plasmid based in plasmid [99]; containing indicates NS4A mutation ⁸⁸
109	pIRO-Z_K42E	Polyprotein expression plasmid based in plasmid [99]; containing indicates NS4A mutation ⁸⁸
110	pIRO-Z_T54I	Polyprotein expression plasmid based in plasmid [99]; containing indicates NS4A mutation ⁸⁸
111	pIRO-Z_K105L+Y110A	Polyprotein expression plasmid based in plasmid [99]; containing indicates NS4B mutation
112	pIRO-Z_K105L+Y110S	Polyprotein expression plasmid based in plasmid [99]; containing indicates NS4B mutation
113	pIRO-Z_R251L+Y254A	Polyprotein expression plasmid based in plasmid [99]; containing indicates NS4B mutation
114	pIRO-Z_R251L+Y254S	Polyprotein expression plasmid based in plasmid [99]; containing indicates NS4B mutation
115	pIRO-Z_Y262A+R266L	Polyprotein expression plasmid based in plasmid [99]; containing indicates NS4B mutation

7. Appendix

116	pIRO-Z_Y262A+R266L	Polyprotein expression plasmid based in plasmid [99]; containing indicates NS4B mutation
Constructs for lentiviral transduction		
117	pWPI_Puro_ZV-RC	pWPI containing the ZIKV reporter construct (cloned by F. Pahmeier)
118	pWPI_BLR_C-prM-Env TCP WT	pWPI containing the structural proteins of ZIKV, trans complementation system for particle production
119	pWPI_BLR_C-prM-Env TCP_R238L+Y240A+R246L	pWPI containing the structural proteins of ZIKV, trans complementation system for particle production; containing indicated mutations in prM
120	pWPI_BLR_C-prM-Env TCP_R238L+Y240S+R246L	pWPI containing the structural proteins of ZIKV, trans complementation system for particle production; containing indicated mutations in prM
121	pWPI_BLR_C-prM-Env TCP_R253L+F257A	pWPI containing the structural proteins of ZIKV, trans complementation system for particle production; containing indicated mutations in prM
122	pWPI_BLR_C-prM-Env TCP_R253L+F257S	pWPI containing the structural proteins of ZIKV, trans complementation system for particle production; containing indicated mutations in prM
123	pWPI_BLR_C-prM-Env TCP_K275L+Y278A	pWPI containing the structural proteins of ZIKV, trans complementation system for particle production; containing indicated mutations in prM
124	pWPI_BLR_C-prM-Env TCP_K275L+Y278A	pWPI containing the structural proteins of ZIKV, trans complementation system for particle production; containing indicated mutations in prM

7.3.2. Oligonucleotides

Table S2. List of oligos used in this study for qPCR and cloning.

Nr	Name	Sequence (5'-3')
Primers used for qRT-PCR		
1	Fluc_fw	CCCTGGTTCCTGGAACAATT
2	Fluc_rev	ATAGCTTCTGCCAACC GAAC
3	GAPDH_fw	GAAGGTGAAGGTCCGAGTC
4	GAPDH_rev	GAAGATGGTGATGGGATTTC
5	RPS17_fw	CACTCCGAGGTCCGTGGTAT
6	RPS17_rev	GGACACTTCGGGCACGTAGT
7	ZIKV_fw	ACTCAACGCAATCCTGGAAG
8	ZIKV_rev	AAGTACGATTTCCCCCAAGC
Probes used for qRT-PCR		
9	Fluc_probe	Cy5 - ATCGAGGTGGACATCACTTACGCT - BHQ3
10	GAPDH_probe	Cy5 - CAAGCTTCCCGTTCTCAGCCT - BHQ3
11	ZIKV_probe	FAM - TGGAGTTCAACTGACGGTCGTTGTG - BHQ1
Oligonucleotides used for sequencing		
12	Seq0 (binds in backbone)	ACGGGTTACTGATGATGA
13	Seq1 (binds in backbone)	GGATATGTTCTGCCAAGC
14	Seq2 (binds in IRES of pIRO-Z)	ACGTCTGTAGCGACCCTT
15	Seq3 (binds in prM)	ACGTCAACTTGGGTTGTG
16	Seq4 (binds in Env)	TTAGTGGACAGAGGCTGG
17	Seq5 (binds in Env)	TTACACGGCCCTTGCTG
18	Seq6 (binds in NS1)	GTTTCAAGAATGAAAAAC
19	Seq7 (binds in NS1)	GAATGGTGCTGCAGGGAG
20	Seq8 (binds in NS2A)	CTGGTCGACCCCATCAAC
21	Seq9 (binds in NS3)	GGAACATCCAGACTCTGC
22	Seq10 (binds in NS3)	GTGACGGATCATTCTGGA

7. Appendix

23	Seq11 (binds in NS3)	GATCATGCGGCCCTGAAG
24	Seq12 (binds in NS4B)	CCATTCTACGCATGGGAC
25	Seq13 (binds in NS5)	GGCCCTGGAATTCTACTC
26	Seq14 (binds in NS5)	ACTGGTCAGAGTGCCACT
27	Seq15 (binds in NS5)	CACGAGTCTGTACCAAAG
28	Seq16 (binds in NS5)	CCAGCTGAAAAAGGGAAG
29	Seq17 (binds in NS5)	GAAATGGACAGACATTCC
30	CMV_fw (provided by Seqlab)	CGCAAATGGGCGGTAGGCGTG
Oligonucleotides used for cloning ZIKV polyprotein constructs		
31	pTM_backbone_fw (+SphI)	GATCGCATGCCCTTATTAAGTCGATCGACG
32	pTM_backbone_rev (+AscI)	GATCGGCGCGCCCCCTATAGTGAGTCGTATTAATTTTC
33	sgR2A-H/PF/2013_fw (+AscI)	GATCGGCGCGCCAGTTGTTGATCTGTGTGAATCAGAC
34	sgR2A-H/PF/2013_rev (+SphI)	GATCGCATGCAGACCCATGGATTTCGCCAC
35	EMCV-IRES_fw (replacing RLuc; +NotI)	CCAGGGCGCGCAGACCACAACGGTTTCC
36	EMCV-IRES_rev (replacing RLuc; +NruI)	GATCTCGCGAGGTATTATCGTGTTTTTCAAAGG
37	IRES_rev (removing 2A site; +NruI)	ATTCAGTGCCATTTCGCGAGGTATTATCGTGTTTTTCAAAGGA
38	Etm-NS1_fw (removing 2A site; +NruI)	ACCTCGCGAATGGCACTGAATGGATCTATTTCCCTTATGTG
39	Etm-NS1_rev (removing 2A site; +AgeI)	GATCACCGGTCCCTCCAGGCTTCAA
40	IRES_rev (removing NruI site)	CAGTGCCATGGTATTATCGTGTTTTTCAAAGGAAAACCAC
41	Etm-NS1_fw (removing NruI site)	GATAATACCATGGCACTGAATGGATCTATTTCCCTTATGT
42	5'UTR_DSLAB_fw (+AscI)	ATAGGGGGCGCGCCATGAAAAACCCAAAAAAGAA
43	5'UTR_DSLAB_rev (+AvrII)	AAGACCCCTAGGAATGCTCGTCAAGAAGACA
44	3'UTR_deletions_fw (+XbaI)	AAGTTCTAGAGATGCAAGACTTGTGGC
45	3'UTR_DsHP_fw	ATATTGACGCGAGACTCCATGAGTTTCCACCACG
46	3'UTR_DsHP_rev	ATGGAGTCTCGCGTCAATATGCTGTTTTG
47	3'UTR_DUAR_fw	GCTGGGAAACATGAGTTTCCACCACGCTGG
48	3'UTR_DUAR_rev	AAACTCATGTTTCCAGCGTCAATATGCT
49	3'UTR_DSL_rev (+SphI)	AAAAGCATGCCTGGTCTTTCCCA
50	3'UTR_deletions_rev	GTGGTGTACGCTCGTCTTTGGTAT
51	3'UTR_DsHP-SL_rev (+SphI)	AAAAGCATGCCCCAGCGTCAATATGC
52	3'UTR_DCS-SL_rev (+SphI)	AAAAGCATGCGTTTTTGCCTTTTCCGG
53	3'UTR_Dcomplete_rev (+SphI)	AAAAGCATGCTTACAGCACTCCAGGTG
54	3'UTR_dG-Ribozyme_rev	CCTCGGAATGTTGCCAGCCGGCGCCAGCGAGGAGGCTGGG ACCATGCCGGCCAGACCCATGGATTTCGCCACAC
55	3'UTR_dG-Ribozyme_fw (+SphI)	CCGGCTGGGCAACATTCCGAGGGGACCGTCCCCTCGTAATG GCGAATGGGACGCATGCCCTTATTAAGTCGATCGACGATCC
56	IRES_overlap_mNG reporter_fw	CATGGCACTGGTGGCAAGGGCGAGGAGGATAACAT
57	IRES_overlap_mNG reporter rev	CCTTGCTCACCAGTGCCATGGTATTATCGTGTTTTTCAAAGG AAAACCA
58	pIRO-Z_overlap_mNG_fw	CCAAAAAGAAGAGAAAAGGTAAGAGCCGAGGGCAGGGGAA GTCT
59	pIRO-Z_overlap mNG_rev	TACCTTTCTCTCTTTTTTTGGCTTGTACAGCTCGTCCATGCC ATCACA
Oligonucleotides used for cloning ZIKV constructs		
60	pFK_fl_synZIKV_prM_fw (+NheI)	GAAGCGAAAGCTAGCAACAGTATCAACAG
61	pFK_fl_synZIKV_prM_R238L+Y240A+ R246L_rev	TTTCGACTAGAATCAAGTGCTTTGTGCTTCTAGTGATTC
62	pFK_fl_synZIKV_prM_R238L+Y240S+ R246L_rev	TTTCGACTAGAATCAAGTGCTTTGTGCTTCTAGTGATTC

7. Appendix

63	pFK_fl_synZIKV_prM_R253L+F257A_rev	TAACGCTGCGCCAGGGTTTAGGAATA
64	pFK_fl_synZIKV_prM_R253L+F257S_rev	TAACGCGCTGCCAGGGTTTAGGAATA
65	pFK_fl_synZIKV_prM_K275L+Y278A_rev	GACCAATGCTATGACTAGTTGGCTCGTT
66	pFK_fl_synZIKV_prM_K275L+Y278S_rev	GACCAAGCTTATGACTAGTTGGCTCGTT
67	pFK_fl_synZIKV_prM_rev (+SphI)	CATTTTCTTGGAGCATGCAAACCTTAGCGC
68	pFK_fl_synZIKV_prM_R238L+Y240A+R246L_fw	GAATCACTAGAAGCAACAAAGCACTTGATTCTAGTCGAAA
69	pFK_fl_synZIKV_prM_R238L+Y240S+R246L_fw	GAATCACTAGAAAGCACAAAGCACTTGATTCTAGTCGAAA
70	pFK_fl_synZIKV_prM_R253L+F257A_fw	TATTCCTAAACCCTGGCGCAGCGTTA
71	pFK_fl_synZIKV_prM_R253L+F257S_fw	TATTCCTAAACCCTGGCAGCGCGTTA
72	pFK_fl_synZIKV_prM_K275L+Y278A_fw	AACGAGCCAACCTAGTCATAGCATTGGTC
73	pFK_fl_synZIKV_prM_K275L+Y278S_fw	AACGAGCCAACCTAGTCATAAGCTTGGTC
74	pFK_sgR2A_ZIKV_NS2B_fw (+ClaI)	ACATCGATGGCAGTGCTGGTAGC
75	pFK_sgR2A_ZIKV_NS2B_rev (+BamHI)	GCGCGGATCCTTTTGTGACGTGCCAC
76	pFK_sgR2A_ZIKV_NS2B_Y42A+K48L_rev	CCACACTCAGTCCTGAGACCACTGCACTGACA
77	pFK_sgR2A_ZIKV_NS2B_Y42S+K48L_rev	CCACACTCAGTCCTGAGACCACCGAACTGACA
78	pFK_sgR2A_ZIKV_NS2B_Y52A+R56L_rev	GTCACCTGCCAGTTCAATAGCCATGTCCACA
79	pFK_sgR2A_ZIKV_NS2B_Y52S+R56L_rev	GTCACCTGCCAGTTCAATACTCATGTCCACA
80	pFK_sgR2A_ZIKV_NS4A_fw (+NaeI)	GTGTGCCGGCAGAGGTGTGGACCA
81	pFK_sgR2A_ZIKV_NS4A_rev (+RsrII)	CAGGCGGTCCGCGACAGTATGGCG
82	pFK_sgR2A_ZIKV_NS4A_K80L+F83A_rev	CACCATTCCAGCGCCCATCAACCCATATG
83	pFK_sgR2A_ZIKV_NS4A_K80L+F83S_rev	CACCATTCCACTGCCCATCAACCCATATG
84	pFK_sgR2A_ZIKV_NS4B_fw	GACTGGAAGCAGGCCTTACAA
85	pFK_sgR2A_ZIKV_NS4B_rev	CACTCTTAAGACGGACTATGTTCCA
86	pFK_sgR2A_ZIKV_NS4B_K105+Y110A_rev	CCCATGCAGCGAATGGCATCCCTAAACCCATA
87	pFK_sgR2A_ZIKV_NS4B_K105+Y110S_rev	CCCATGCAGTGAATGGCATCCCTAAACCCATA
88	pFK_sgR2A_ZIKV_NS4B_R251L+Y254A_rev	CCAGCCAAGGCGCTTCCCAAAAAAATGT
89	pFK_sgR2A_ZIKV_NS4B_R251L+Y254S_rev	CCAGCCAAGCTGCTTCCCAAAAAAATGT
90	pFK_sgR2A_ZIKV_NS4B_Y262A+R266L_rev	GCCAGCGTTCAATGTTACTGTTGCGATTAGA
91	pFK_sgR2A_ZIKV_NS4B_Y262S+R266L_rev	GCCAGCGTTCAATGTTACTGTTGCGATTAGA
92	pFK_sgR2A_ZIKV_NS2B_Y42A+K48L_fw	TGTCAGTGCAGTGGTCTCAGGACTGAGTGTGG
93	pFK_sgR2A_ZIKV_NS2B_Y42S+K48L_fw	TGTCAGTTCGGTGGTCTCAGGACTGAGTGTGG
94	pFK_sgR2A_ZIKV_NS2B_Y52A+R56L_fw	TGTGGACATGGCTATTGAACTGGCAGGTGAC
95	pFK_sgR2A_ZIKV_NS2B_Y52S+R56L_fw	TGTGGACATGAGTATTGAACTGGCAGGTGAC
96	pFK_sgR2A_ZIKV_NS4A_K80L+F83A_fw	CATAGGGTTGATGGGCGCTGGAATGGTG
97	pFK_sgR2A_ZIKV_NS4A_K80L+F83S_fw	CATAGGGTTGATGGGCGCTGGAATGGTG
98	pFK_sgR2A_ZIKV_NS4B_K105+Y110A_fw	TATGGGTTTAGGGATGCCATTTCGCTGCATGGG
99	pFK_sgR2A_ZIKV_NS4B_K105+Y110S_fw	TATGGGTTTAGGGATGCCATTTCAGTGCATGGG
100	pFK_sgR2A_ZIKV_NS4B_R251L+Y254A_fw	ACATTTTTTTTGGGAAGCGCCTTGGCTGG
101	pFK_sgR2A_ZIKV_NS4B_R251L+Y254S_fw	ACATTTTTTTTGGGAAGCAGCTTGGCTGG
102	pFK_sgR2A_ZIKV_NS4B_Y262A+R266L_fw	TCTAATCGCAACAGTAACATTGAACGCTGGC
103	pFK_sgR2A_ZIKV_NS4B_Y262S+R266L_fw	TCTAATCAGCACAGTAACATTGAACGCTGGC
104	pFK_sgR2A_backbone_fw (+KasI)	AGATGGGCGCCAACCTTTAAAGCT
105	pFK_sgR2A_backbone_rev (+EcoRI)	GAGTAGAATTCCAGGGCCGACATCTG
106	pFK_sgR2A_ZIKV_NS4A_T12A_fw	TGGGAGCACTGCCAGGA

7. Appendix

107	pFK_sgR2A_ZIKV_NS4A_T12A_rev	TCCTGGCAGTGCTCCCA
108	pFK_sgR2A_ZIKV_NS4A_T12L_fw	TGGGAATACTGCCAGGA
109	pFK_sgR2A_ZIKV_NS4A_T12L_rev	TCCTGGCAGTATTCCCA
110	pFK_sgR2A_ZIKV_NS4A_E19G_fw	CACATGACAGGGAGATTCCAGGA
111	pFK_sgR2A_ZIKV_NS4A_E19G_rev	TCCTGGAATCTCCCTGTTCATGTG
112	pFK_sgR2A_ZIKV_NS4A_K42E_fw	CTTACGAAGCCGCGGCG
113	pFK_sgR2A_ZIKV_NS4A_K42E_rev	CGCCGCGGCTTCGTAAAG
114	pFK_sgR2A_ZIKV_NS4A_T54L_fw	GGAGACCCTAGAGATCATTATGCTTTTGG
115	pFK_sgR2A_ZIKV_NS4A_T54L_rev	CCAAAAGCATAATGATCTCTAGGGTCTCC
116	pFK_sgmNG_ZIKV_fw (+NotI)	GGCTGCCAGGCGGCCGCATGGTGTAGCAAGGGCGAGGAGGAT
117	pFK_sgmNG_ZIKV_rev (+NruI)	CTCGGCTCTTCGCGACTTGTACAGCTCGTCCATGCCCA
Oligonucleotides used for cloning Expression constructs		
118	pTM_ZVproteins-HA_IRES_fw (+AvrII)	GACGAGCATTCCCTAGGGGTCTTTCC
119	pTM_prM-HA_IRES_rev	ACGTCCCCGCATGTTAGAAGACTTCCCCTGCCCTCGGCTCTC ATGGTATTATCGTGTTTTTCAAAGGAAAACCACG
120	pTM_prM-HA_fw	GAAGTCTTCTAACATGCGGGACGTGGAGGAAAATCCCCGGG CCCCGGCGCAGATACTAGTGTCCGAATTG
121	pTM_prM-HA_rev (+BamHI)	AATTAATTAGGGATCCCTAAGCGTAATCTGGAACATCGTATG GGTATGATCCGCTGTATGCCGGGGCAATCAG
122	pTM_NS2B/3-HA_IRES_rev	GGGCCAGCTCATGGTATTATCGTGTTTTTCAAAGGAAAACC ACGT
123	pTM_NS2B/3-HA_fw	CGATAATACCATGAGCTGGCCCCCTAGC
124	pTM_NS2B/3-HA_rev (SpeI)	AATTAATTAGACTAGTCTAAGCGTAATCTGGAACATCGTATG GGTATGATCCTCTTTTCCCAGCGGCAAACCTCC
125	pTM_HA-NS4A_IRES_rev	GTGGTTTTTCCTTTGAAAAACACGATAATACCATGTACCCATA CGATGTTCCAGATTACGCTGG
126	pTM_HA-NS4A_fw	CCATACGATGTTCCAGATTACGCTGGATCAGGAGCGGCTTTT GGAGTGATGG
127	pTM_HA-NS4A_rev (BamHI)	AATTAATTAGGGATCCTCATCTTTGCTTTTCTGGCTCAGGT
128	pTM_2kNS4B-HA_IRES_rev	GTGGTTTTTCCTTTGAAAAACACGATAATACCATGTCTCCCA GGAC
129	pTM_2kNS4B-HA_fw	CACGATAATACCATGTCTCCCCAGGACAACCAAATG
130	pTM_2kNS4B-HA_rev (BamHI)	AATTAATTAGGGATCCCTAAGCGTAATCTGGAACATCGTATG GGTATGATCCACGTCTCTTGACCAAGCCAGC
131	pTM_prM-Env_fw (+BamHI)	AAAAAGGATCCATGAGTGTCCGAATTGTTGGCCTCCT
132	pTM_prM-Env_rev (+EcoRI)	AAAAAGAATTCTTAAGCAGAGACAGCTGTGGATAAGAAGATC
133	pTM_prM-Env-HA_rev (+EcoRI)	AAAAAGAATTCTTAAGCGTAATCTGGAACATCGTATGGGTATG ATCCAGCAGAGACAGCTGTGGATAAGAAGATC
Oligonucleotides used for cloning lentiviral constructs		
134	TCP_fw (C-prM-E; +BamHI)	AGGCGCGCCGGATCCATGAAAAACCCAAAAAAGAAATCC GGAGGA
135	TCP_rev (C-prM-E; +MluI)	TTTACTAGTACGCGTTTAAGCAGAGACAGCTGTGGATAAG AAGATC

8. PUBLICATIONS AND PRESENTATIONS

8.1. Publications and Manuscripts in preparation

Goellner, S., Enkavi, G., Denolly, S., Eu, S., Prasad, V., Witte, L., Kulig, W., Kulig, W., Uckeley, Z., Haselmann, U., Lozach, P.Y., Brügger, B., Vattulainen, I., and Bartenschlager, R. *Cholesterol binding domains within the small membrane protein of Zika virus mediate virus entry and assembly*. In preparation

Riva, L., **Goellner, S.**, Biering, S.B., Huang, C.-T., Rubanov, A.N., Haselmann, U., Warnes, C.M., De Jesus, P.D., Martin-Sancho, L., Terskikh, A.V., Harris, E., Pinkerton, A.B., Bartenschlager, R., and Chanda, S.K. (2021). *The compound SBI-0090799 inhibits Zika virus infection by blocking de novo formation of the membranous replication compartment*. Journal of Virology

Goellner, S., Cerikan, B., Cortese, M., Neufeldt, C.J., Haselmann, U., and Bartenschlager, R. (2020). *Replication-independent generation and morphological analysis of flavivirus replication organelles*. STAR Protocols

Cerikan, B., **Goellner, S.**, Neufeldt, C.J., Haselmann, U., Mulder, K., Chatel-Chaix, L., Cortese, M., and Bartenschlager, R. (2020). *A non-replicative role of the 3' terminal sequence of the dengue virus genome in membranous replication organelle formation*. Cell Reports

8.2. Presentations

Keystone Positive-Strand RNA Viruses Meeting, June 18–23, 2022, Keystone, Colorado, USA

Goellner, S., Denolly, S., Enkavi, G., Kulig, W., Eu, S., Witte, L., Haselmann, U., Brügger, B., Vattulainen, I., and Bartenschlager, R. *Cholesterol binding domains in the Zika virus prM protein are essential for efficient virus propagation*. (Poster presentation)

31st Annual Meeting Society of Virology, March 30-April 2, 2022, Munich, Germany

Goellner, S., Witte, L., Denolly, S., Eu, S., Brügger, B., and Bartenschlager, R. *Cholesterol binding domains in the Zika virus prM protein are essential for efficient virus propagation*. (Oral presentations)

Keystone Positive-Strand RNA Viruses Meeting, June 9–13, 2019, Killarney, Ireland

Cerikan, B., **Goellner, S.**, Neufeldt, C.J., Haselmann, U., Cortese, M., and Bartenschlager, R. *An expression-based system to study dengue and Zika virus replication organelle formation independent from viral RNA replication*. (Poster presentation)